# Modelling the axial behaviour of marine wind turbine piles anchored in chalk

Mirna Doghman

Université de Lille

Ecole doctorale Sciences Pour l'Ingénieur - ED SPI

Laboratoire Génie Civil et géo-Environnement LGCgE

**Thèse**

Pour l'obtention du grade de

**Docteur de l'Université de Lille**

Discipline : Génie Civil

Par

**Mirna DOGHMAN**

# Modélisation du comportement axial des pieux d'éoliennes marines ancrés dans des massifs crayeux

# Modelling the axial behaviour of marine wind turbine piles anchored in chalk

Soutenu le 01 octobre 2021 devant le jury composé de :

| | | |
|---|---|---|
| TANG Anh Minh | Directeur de recherche, HDR, Ecole des Ponts ParisTech | Rapporteur |
| HATTAB Mahdia | Professeure, Université de Lorraine | Rapporteur |
| SHAHROUR Isam | Professeur, Université de Lille | Président |
| BURLON Sébastien | Directeur d'études, HDR, Terrasol | Examinateur |
| DUPLA Jean-Claude | Chargé de recherche, HDR, Ecole des Ponts ParisTech | Examinateur |
| HATEM-QUIRIN Alia | Ingénieur, Docteur, ARCADIS | Examinateur |
| DAMBLANS Guillaume | Ingénieur de recherche, France Énergies Marines | Invité |
| MROUEH Hussein | Professeur, Université de Lille | Directeur |

# Acknowledgment

***This PhD thesis takes part in the French national project SOLCYP+ benefited from France Energies Marines and State financing managed by the National Research Agency (ANR) under the Investments for the Future program bearing the reference SOLCYP+ANR-10-IEED-0006-18.***

I would like to express my gratitude to all the people that have contributed to the realisation of this thesis.

Foremost, I would like to thank my supervisor, Professor Hussein MROUEH for offering me the opportunity to carry out this doctoral work. Thank you for your trust, for your continuous encouragement, and for your guidance. My gratefulness goes also to Doctor Sébastien BURLON for sharing his knowledge, for his precious advices and for the fruitful discussions that kept me persistently enthusiastic about this research. Thank you for your moral support that helped me overcome the PhD challenges.

I would like to thank my PhD committee for accepting to be a part of this achievement by reading, reporting, and examining my work. Thanks to Prof. Anh Minh TANG, Prof. Mahdia HATTAB, Prof. Isam SHAHROUR, Dr. Jean-Claude DUPLA, Dr. Alia HATEM-QUIRIN and Eng. Guillaume DAMBLANS. I want to express my appreciation, a second time, to Prof. Isam SHAHROUR, the former director of LGCgE where I am affiliated, not only for giving me the honour of chairing my PhD committee, but also for his warm welcoming and for being available anytime to discuss about my work's difficulties.

Thank you to all the partners in the ANR project "SOLCYP+": Ecole des Ponts - ParisTech, France Energies Marines, Université Gustave Eiffel, Laboratoire 3SR, INNOSEA, FUGRO, ORSTED and EDF. My particular thanks go to Alain PUECH (FUGRO), and Christophe DANO (3SR) for the idea exchanges and data sharing.

Moreover, I would like to express my gratitude to all my colleagues at LGCgE. The past years were not only about making PhD, but they were also about making true friends with whom I've shared the ups and downs, the laughs and tears. A special thanks go to Dina, Nivine, Reda, Rim, Rania, Lara, Tarek and Ayoub. I also want to thank all the permanent lecturers/researchers and administrative staffs at LGCgE, whom I thank warmly especially Ammar. My thanks also

extend to my colleagues of lecturers and professors at Polytech'Lille with whom I worked with pleasure.

My acknowledgments would not be complete without expressing my profound gratitude and thankfulness to all my friends in Lebanon and in France, for all the support and enjoyment they've brought to my life. Thanks to Hiba, Dima, Rim, Eliane, Sara, Yara, Charbel and Joy. A special thanks go to Grece for always being there for me in times of sadness as in times of joy.

I heartily thank Anwar. His unconditional support and continuous motivation have provided the serenity, patience and peace during this PhD completion.

Finally, I am indebted to my family, my mom, my dad, my brother and my sisters. Without their unconditional love, support and confidence, I never would have been able to get this far and to succeed on and on. I have always been far away from home, but their care is always by my side. This PhD is dedicated to them. Thank you and I love you.

# Abstract

Design of axially loaded piles is widely considered in civil engineering works. Different types of loading are encountered, they can be either monotonic or cyclic. Forthcoming Offshore Windfarm projects will arise on both the French and English sides of the English Channel where chalk is found widespread. In order to meet the requirements of these projects, calculation methods developed to predict the pile response, in terms of displacements and bearing capacity evolution, should consider the following features: the unconventional behaviour of chalk and the impact of cyclic loading.

The first objective of this work is to evaluate the reliability of existing approaches for the estimation of pile capacity in chalk. The second objective is to provide a practical numerical modelling of the soil-pile interface with a simple behaviour law considering the influence of normal stress variation on the shear mechanism along the pile shaft, adapted for chalk and other soil types.

A comparison between the French perspective presented by the specifications of the French national standard NF P 94-262 and the UK perspective presented by the recommendations of CIRIA C574 is firstly conducted. This comparison is based on available results of static pile load tests recorded in the French database. The ratio of the calculated and the measured values of pile shaft resistance and pile base resistance is interpreted, and the scatter of each approach is studied. A special attention is paid to the evolution of the long-term capacity of driven piles in chalk, presented in the considered database.

Regarding the second objective of this thesis, a constitutive model based on elastoplasticity principles, with a single yield mechanism acting upon Mohr-Coulomb criterion, is proposed. The concept of the considered behaviour law implies the modification of the corresponding flow rule. The latter is directly defined on the base of experimental results of direct shear tests describing the evolution of the interface volumetric behaviour. The formulation of the constitutive model is firstly presented. Numerical expressions representing the experimental data are then proposed and calibrated on the results of monotonic and cyclic direct shear tests.

The constitutive model is implemented in the FLAC3D finite difference calculation code. It is then applied to a theoretical example considering monotonic loading. Corresponding results are compared with predictions of a conventional t-z calculation where the variation of normal stress is not considered. Afterwards, the developed behaviour law is combined with a skipped cycles

procedure in order to perform cyclic calculations. Corresponding results are presented and analysed.

Lying under the same objective, the last part of this thesis intends to provide a practical numerical prototype for modelling the pile response under axial loadings. Based on the finite element method, a one-dimensional approach is developed, and its formulation is presented. According to elastoplasticity principles, the calculation scheme follows a non-linear iterative procedure considering the soil-pile interface behaviour law developed in this thesis. The proposed approach is implemented in Fortran in a CodeBlocks file. It allows to perform a large number of cyclic sequences with a great reduction in computational time consumption. First calculations are performed and compared with previous results of FLAC3D predictions in order to validate the modelling procedure. Finally, several additional cyclic simulations are performed considering different cyclic characteristics and a large number of cycles.

# Résumé

La conception des pieux soumis à un chargement axial est largement considérée dans les ouvrages de génie civil. Différents types de chargement sont rencontrés, ils peuvent être monotones ou cycliques. Les récents projets d'éoliennes offshores sont implantés au large de la Manche, tant du côté français que anglais, où la craie se trouve très répandue. Afin de répondre aux exigences de ces projets, les méthodes de calcul disponibles pour prédire la réponse des pieux, en termes de déplacements et d'évolution de la capacité portante, devraient tenir compte des caractéristiques suivantes : le comportement non conventionnel de la craie et l'impact du chargement cyclique.

Le premier objectif de ce travail est d'évaluer la fiabilité des approches existantes pour l'estimation de la capacité portante des pieux dans la craie. Le deuxième objectif est de proposer une modélisation numérique pratique de l'interface sol-pieu avec une loi de comportement tenant compte de l'influence de la variation de la contrainte normale sur le mécanisme de cisaillement le long du pieu, adaptée pour la craie mais aussi par extension pour d'autres types de sol.

Une comparaison entre l'approche française présentée par les spécifications de la norme nationale française NF P 94-262 et la perspective britannique présentée par les recommandations du CIRIA C574 est d'abord abordée. Cette comparaison est basée sur les résultats disponibles des essais de chargement statique enregistrés dans la base de données française. Le rapport entre les valeurs calculées et mesurées de la résistance de frottement et de la résistance de pointe est interprété et la dispersion de chaque approche est étudiée. Une attention particulière est accordée à l'évolution de la capacité à long terme des pieux battus dans la craie, présentés dans la base de données considérée.

Concernant le deuxième objectif, un modèle de comportement basé sur les principes de l'élastoplasticité, avec un seul mécanisme de rupture suivant le critère de Mohr-Coulomb, est proposé. La notion de loi de comportement considérée implique la modification de la règle d'écoulement correspondante. Cette dernière est directement définie sur la base des résultats expérimentaux des essais de cisaillement direct décrivant l'évolution du comportement volumétrique de l'interface. La formulation du modèle constitutif est d'abord présentée. Des expressions numériques représentant les données expérimentales sont ensuite proposées et calibrées sur la base des résultats des essais de cisaillement direct monotone et cyclique.

Le modèle de comportement est implémenté dans le code de calcul de différence finie FLAC3D. Il est ensuite appliqué à un exemple théorique considérant une charge monotone. Les résultats correspondants sont comparés avec les prédictions d'un calcul t-z classique où la variation de la contrainte normale n'est pas prise en compte. Ensuite, la loi de comportement développée est combinée avec une procédure de sauts de cycles afin d'effectuer des calculs cycliques. Les résultats correspondants sont présentés et analysés.

Sous le même objectif, la dernière partie vise à fournir un prototype numérique pratique pour modéliser la réponse des pieux sous charges axiales. Suivant la méthode des éléments finis, une approche unidimensionnelle est développée et sa formulation est présentée. Selon les principes de l'élastoplasticité, le schéma de calcul suit une procédure itérative non linéaire considérant la loi de comportement d'interface sol-pieu développée dans cette thèse. L'approche proposée est implémentée dans Fortran. Il permet d'effectuer un grand nombre de séquences cycliques avec une grande réduction de la consommation de temps de calcul. Les premiers calculs sont effectués et comparés aux résultats antérieurs des prévisions de FLAC3D afin de valider la procédure de modélisation. Enfin, plusieurs simulations cycliques sont effectuées considérant différentes caractéristiques cycliques et un grand nombre de cycles.

# Table of Contents

# List of figures

# List of tables

# General Introduction

Piles are considered as foundation techniques that have been used for a long time in the field of civil engineering where the surface layers of the soil are not sufficiently resistant. In frequent cases such as buildings and bridges, piles are designed in the aim to support monotonic loading. Under this type of loading, two elements must be correctly estimated: the bearing capacity of the pile and the pile displacement.

Recently, under the impetus of expansion of the pile industry due to the development of high-rise structures, such as wind turbines and towers, and the exploitation of renewable offshore energy, a new type of loading has been developed. Having a repetitive nature, this type of loading, known as cyclic loading, may have a negative impact on the stability and the capacity of piles during their service life. Degradation of pile capacity and accumulation of displacements at the pile head during cycles are the main negative aspects encountered in the case of axial cyclic loading. These aspects are directly related to the degradation of the normal stress acting on the pile shaft. Hence, it is of great importance to accurately study and understand different mechanisms that take place at the chalk-pile interface. On one hand, the conventional pile design method, the t-z method, does not take into account the effect of variation in normal stress on the shear mechanism along the pile. On the other hand, constitutive laws, with corresponding flow rules, have been developed to simulate the overall behaviour of the soil-pile interface under cyclic loading. These laws seem to be sufficient to assess the mechanisms of deformation at the scale of either a soil sample or a structure only for a small number of cycles. Bearing in mind the large number of cycles that the piles of offshore projects can exposed to, the use of complex constitutive models, even simple models, in incremental calculations appears to be not applicable due to the extensive time consumption and the possible accumulation of numerical errors.

Chalk is widely extended across northern Europe and under the North Sea, including the continental shelf of France, Ireland, Denmark, Germany and the UK. It constitutes the geological formation for a large number of constructions in civil and petroleum engineering such as roads, railways, tunnels, onshore and offshore piles and oil drillings. From the end of sixties, researches concerning the mechanical behaviour of chalk have experienced a considerable development especially in the field of petroleum engineering. The main finding of these researches is the particularity and complexity of chalk. Indeed, it is known as an unconventional material presenting, for a given variety, a whole range of behaviours. It has the singularity of having an intermediate mechanical behaviour between that of soil and that of rock. Its high porosity, origin, mineralogy and type of microstructure are the direct responsible for this heterogeneousness.

The presence of chalk poses geotechnical challenges and difficulties for designers searching to achieve satisfactory performance of piles. Regarding this field, experience in chalk is considered limited, especially in the case of driven piles. During pile driving, the high-porosity structure of chalk experiences crushing and deterioration along the pile shaft. Hence, a low-strength and viscous annulus along the pile shaft is produced, through a "puttification" mechanism. This process is responsible for the low ultimate unit shaft resistances mobilised at the chalk-pile interface. However, the effect of time on the evolution of these ultimate shaft resistances is significant. Several tests have proven the progressive increase in the ultimate pile shaft resistance during time, corresponding to ageing effects. Despite that, ageing effect has not been considered in different recommendations of pile design in chalk.

In view of what has been already mentioned, this thesis pursues **two main axes**:

- A practical axis which consists in reviewing and assessing the reliability of current approaches of the estimation of pile capacity in chalk;
- A fundamental axis which consists in providing an efficient calculation tool for the modelling of soil-pile interface considering the effect of normal stress variation on the shear mechanism along the pile shaft, under axial monotonic and cyclic loadings, applicable for chalk and other soil types.

In order to achieve these objectives, this thesis is divided into five chapters, including the one dedicated to the bibliographic synthesis.

**The first chapter** attempts at first to establish a state of the art relative to the complex behaviour of chalk itself in addition to different phenomena and elements affecting its mechanical response. Afterwards, the second part of this chapter focuses on presenting a synthesis relative to piles behaviour in chalk under monotonic and cyclic axial loadings. On one hand, methods of prediction of piles capacity in chalk according to the French national standard for the designing of deep foundations NF P 94-262 (AFNOR 2012) are presented. On the other hand, different observations made during limited cyclic loadings performed on piles in chalk are described. Given that the stress levels adopted in laboratory tests since the sixties are considered relatively high regarding the range of interest of pile works, the last part of this chapter summarises different laboratory experimental tests performed more recently on chalk samples in the field of offshore developments. These experiments give an illustration of chalk behaviour around the pile and along the pile shaft during monotonic and cyclic loadings, considering stress state encountered in the field of offshore works.

The upcoming Offshore Windfarm projects that will take place on both the French and English sides of the English Channel and along the south-east coast of England rise the importance of

assessing the reliability of common practices. From this perspective, **the second chapter,** which comes within the framework of the first axis, intends to compare the French and English approaches developed for the estimation of pile bearing capacity in chalk. While different rules adopted in French perspective, according to the specifications of the French national standard NF P 94-262 (AFNOR 2012), are presented in chapter 1, this chapter begins by reviewing the UK perspective where the recommendations of CIRIA C574 (Lord et al. 2002), the official guide for pile design in chalk in the UK, are detailed. The comparison between considered recommendations is based on results of static pile load tests performed by the Laboratoire Central des Ponts et Chaussées (LCPC, now called IFSTTAR) at four sites located in the Paris Basin. After a detailed geotechnical description of each site, results of comparison between measured and calculated values are illustrated. Moreover, capacity-ageing trends of driven piles provided from the LCPC database are investigated.

Considering the second axis, **the third chapter** presents a constitutive law which is proposed to account for the effect of the variation of normal stress along the pile shaft, on the mobilised shear resistance. The proposed model is based on the principles of elastoplasticity with a single yield mechanism acting upon Mohr-Coulomb criterion. The corresponding flow rule is modified based on experimental data and the constitutive law is rewritten for the direct consideration of the volumetric behaviour of soil-pile interface. These experimental results of direct shear tests in terms of normal displacement in function of shear displacement in the case of monotonic loading, and in function of number of cycles in the case of cyclic loading, directly qualify the flow rule. At first, the formulation of the behaviour law is detailed. Combined with numerical expression presenting the evolution of the interface normal displacement, the developed constitutive law is then calibrated and tested considering experimental results of monotonic direct shear tests performed on a well-recognised material, the sand, and on recently available experimental results considering chalk samples. Afterwards, simulation results of cyclic tests done according to a numerical approach proposed for sand interfaces, named SOLCYP, are used to calibrate the model considering cyclic loading scheme.

**The fourth chapter,** which also makes part of the second axis, presents the implementation of the proposed constitutive law in a commercial finite difference software, FLAC3D (Itasca 2012), in order to assess the response of a theoretical pile subjected to axial tension loading taking into consideration the effect of normal stress variation. Firstly, considering axial tension monotonic loading, predictions of a conventional t-z calculation, with elastic perfectly-plastic t-z curves, are compared to predictions of FLAC3D calculations considering the default interface constitutive law incorporated in FLAC3D, in order to validate the modelling process

in the considered software. Subsequently, the influence of normal stress variation on the pile response is investigated by presenting results of calculations performed in FLAC3D according to the implemented constitutive law. At last, a skipped cycles method is developed in order to execute axial tension cyclic sequences and to assess the response of the pile regarding these applied loadings.

**The final chapter** of this thesis, included also in the second axis, presents the major contribution of this thesis which is the development of a 1D practical numerical approach for modelling the pile response under axial loading in a reasonable computational time. This approach is based on the finite element method where the pile is considered as a bar element, and it is discretised into *n* finite elements. The problem is treated following principles of elastoplasticity according to a non-linear iterative procedure combined with the constitutive law of soil-pile interface developed in chapter 3. The proposed approach is implemented in Fortran in order to provide a simple engineering tool for practical use. Calculation procedures considering monotonic loading, on one hand, and cyclic loading according to skipped cycles method, on the other hand, are detailed. Predictions of calculations performed using the developed tool are compared with preceding results of chapter 4. Additional tension cyclic simulations are done covering a large variety of cyclic characteristics and a high number of cycles in order to study the cyclic response of the pile by benefiting from the important economy in calculation time consumption provided by the developed tool.

# Chapter 1
# State of the art

## 1.1 Introduction

Knowledge and characterisation of the mechanical behaviour of chalk is, since a few decades, a subject of major interest in many countries of Europe, such as France, United Kingdom and Norway. This porous rock is widely encountered in several petroleum and civil engineering problems. It constitutes the substratum of a large number of constructions and structures, such as tunnels, onshore and offshore piles, and oil drillings. The design and the stability analysis of these works require a good knowledge of the mechanical behaviour of this material.

The mechanical behaviour of chalk is quite complex and particular. It presents, for a given variety, a whole range of rheological behaviour. It has the particularity of being a material with an intermediate mechanical behaviour between that of the soil and that of a rock. Generally, many factors intervene significantly in the chalk behaviour. Its big porosity, origin, mineralogy and type of microstructure are a part of numerous parameters that influence its behaviour.

The need to build on poor quality soils, on one hand, and the support of existing buildings and structures to limit their movement, on the other hand, has given rise to a wide range of foundation techniques. Piles are one of these techniques that have been used for a long time in the field of civil engineering.

In common cases such as buildings and bridges, piles are designed to support monotonic solicitations. The study of piles performance under this type of loading has already been the subject of many researches. This work has resulted in designing methods that have been introduced into different standards.

The recent expansion of the pile industry has been dominated by the evolution of construction types (wind turbines, high-rise towers, etc.) and by the exploitation of offshore energy resources. These developments have contributed to changing the type of loading transmitted to piles. These non-monotonic variable loadings, which can be described as "cyclic" loadings, can have a significant influence on the stability and behaviour of piles during their service life. Therefore, a particular attention should be paid to the evolution of the bearing capacity of the pile during cycles, and to the accumulation of displacements at the pile head.

Considering the particular behaviour of chalk and the effect of cyclic loading on the stability of piles, advancing understanding of different mechanisms taking place at the chalk-pile interface is very important in order to ensure a reliable design of piles in chalk.

From this perspective, the first part of this chapter presents a synthesis of chalk complex behaviour and the different phenomena and factors affecting its mechanical response. Considering the engineering practices in terms of piles in chalk, the second part describes the

behaviour of piles in chalk under monotonic and cyclic axial loadings. The last part illustrates the laboratory experimental tests that can give a representation of chalk-pile interface behaviour under cyclic and monotonic axial loading with corresponding stress levels that may encountered in the case of onshore and offshore pile works.

## 1.2 Chalk material

### 1.2.1 Definition

Dated from the period of the upper Cretaceous (Clayton 1983), more exactly of the period between Maastrichian and Campanian, the chalk is a white, sedimentary, porous carbonated rock, in fine texture, which distinguishes itself very clearly from limestone. Its white colour is due to its constitution almost exclusively made of calcium carbonate, in the state of calcite. Its percentage can exceed 90, even 95%.

According to Mortimore and Fielding (1990), chalk presents often certain variations in its mineralogical composition and its petrography. These variations are related to the geological history of chalk and reflect the heterogeneousness of its behaviour and its physical and mechanical properties. Between these variations we can find some variations of colours, green, yellow, grey, related to the presence of some secondary minerals in its mineralogical composition (clays, silica, etc), herself governing the hardness of the chalk. Sedimentologists agree to give the naming of "chalk" only to rocks among which the carbonated part is constituted by at least 50 % of tests of nanoplanktons. A chalk is said "pure" when the proportion of tests of calcite reaches an 80-85 % value (figure 1.1).

This variability makes chalk analysis very difficult with the need of a large number of precautions in the determination of physical and mechanical properties. In this field, the report CIRIA C574 (Lord et al. 2002) summarizes the properties of English chalks, the special Bulletin of the LCPC (LCPC 1973), the French Highways Agency, summarizes those of chalks of the North of France and Andersen (1995) recapitulates the researches conducted on chalks as oil reservoirs of the North Sea.

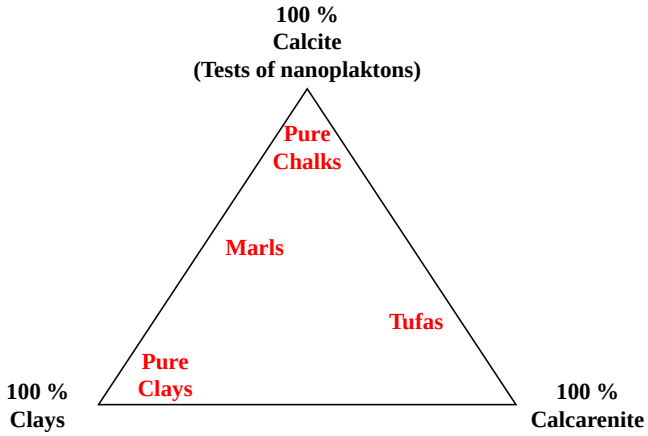


*Figure 1.1: Composition of sedimentary rocks chalks-marls-clays (Mortimore and Fielding 1990, Schroeder 2002)*

### 1.2.2 Mechanical behaviour of chalk

Mechanical behaviour of porous chalk has been widely studied. It has been demonstrated that its behaviour is very complex. It depends on many parameters, including porosity, saturation conditions, confinement pressure and time. Chalk presents a particularity to be a material with intermediate mechanical behaviour between that of a soil and that of a rock.

Time has a great influence on chalk behaviour. Therefore, deformations in chalk take place not only due to instantaneous applied stresses, but also due to time dependent mechanisms such as creep privileged by the viscous nature of chalk and the phenomenon of dissolution under stress due to the presence of water.

#### *1.2.2.1 Effect of porosity*

Chalk is a very porous rock. Its porosity is at the origin of its complex and specific behaviour regarding the various mechanical phenomena. Scholle (quoted by (Bell et al. 1999)) specified that chalk porosity could reach 70 to 80 % at the time of the deposition, and then decrease by consolidation and cementation (Clayton 1983) to reach average values between 25 and 40%, even until less than 5% (Jones et al. 1984). This observation shows the importance of the porous nature in the behaviour of chalk, evolving together with the solid matrix (consolidation, cementation) and the permeability.

The influence of porosity on the mechanical behaviour of chalk has been studied by several authors since the seventies (Doremus 1978, Engstrom 1992). On a wide range of chalks of the North Sea, Engstrom (1992) has shown that the Young's modulus E and the coefficient of Poisson ν can be correlated to the porosity of chalk. Evolution of Young's modulus is an

exponential function of the porosity (equation 1.1) and the Poisson's coefficient varies linearly with the porosity variation (equation 1.2):

$$E = 224800e^{-11.2n}\ (MPa) \tag{1.1}$$

$$\nu = 0.21n + 0.117 \tag{1.2}$$

Clayton (1983) and Matthews and Clayton (1993) have found similar results (figure 1.2). Monjoie et al. (1990) also found that for chalks of the North Sea, the Young's modulus and the elastic limit obtained during a triaxial compression depend on the initial porosity: chalks with weak porosity present average values of elastic limit and Young's modulus clearly larger than those observed for chalks with strong porosity. Therefore, according to Monjoie et al. (1990), we can distinguish between chalk with low porosity (< 37%), and chalk with high porosity (> 37%).

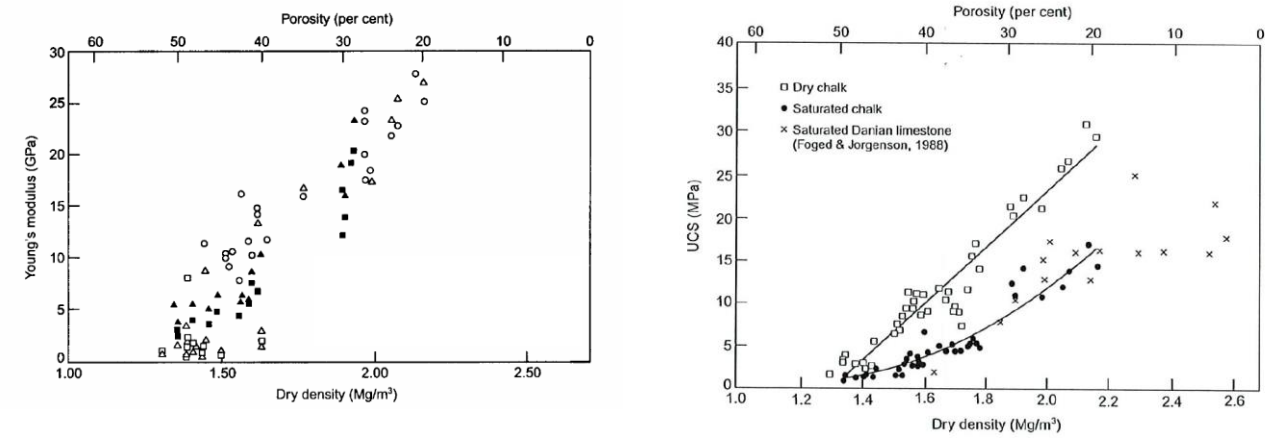


*Figure 1.2 : Effect of the chalk porosity on the Young's modulus and the unconfined compression strength (Matthews and Clayton, 1993)*

In addition, studies carried out by Risnes at al. (2005) and Kornes et al. (2008) have shown the influence of porosity on the whole mechanical behaviour of chalk using Brazilian test and triaxial test.

### *1.2.2.2 Effect of water*

The effect of water on the behaviour of chalk is known for a long time and is illustrated by the progressive loss of chalk resistance with a high degree of saturation. Starting from the end of sixties, several studies, concerning the decrease in chalk resistance during saturation, have been done by the LCPC (Masson 1973). This important aspect has also been considered by Dessene (1971).

The interstitial water softened the chalk, and this aspect can be demonstrated by simple compression test. The ratio between the resistances at dry and saturated state, ($R_{c,dry}/R_{c,saturated}$), highlighted this behaviour. The variation of these parameters, studied by Matthews and Clayton (1993), is presented in figure (1.3). The slope between the simple compressive strength at dry and saturated state, approximately equal to 2, shows the decrease of chalk resistance in presence of water.

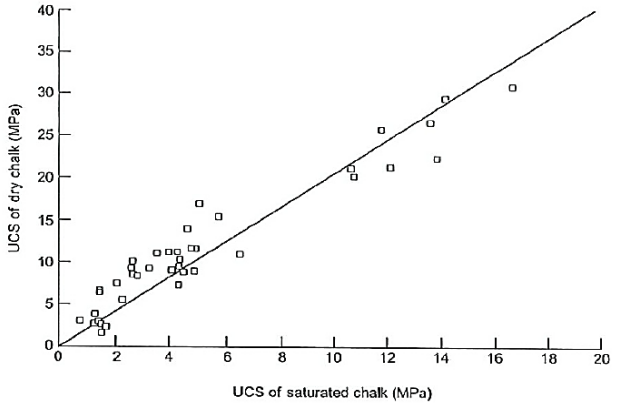


*Figure 1.3 : Comparison between unconfined compression strength at dry and saturated state of intact chalk (Matthews and Clayton 1993)*

Considering the influence of the degree of water saturation, several authors have demonstrated that the elastic properties of chalk, such as Young's modulus, unconfined compressive strength and elastic limit, are dependent on this parameter. Papamichos et al. (1997) observed that the unconfined compression strength (figure 1.4) decreases with the increase of the degree of saturation, whereas the Poisson's coefficient and the angle of friction remain more or less constant. Using Brazilian test, Talesnick et al. (2001) have also shown a decrease in the traction resistance with the increase in the degree of saturation (figure 1.5).

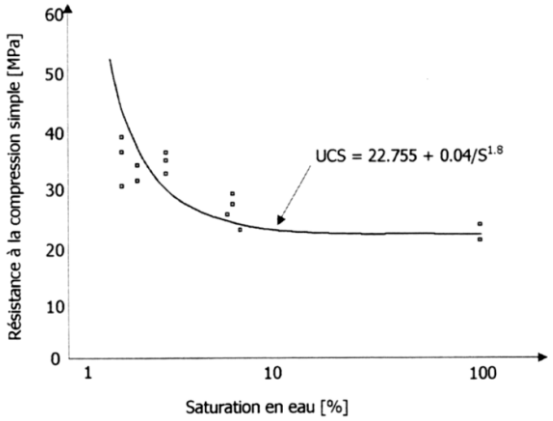


*Figure 1.4 : Effect of water on the chalk unconfined compression strength, Brazilian test (Papamichos et al. 1997)*

Several hydrostatic tests, on the Lixhe chalk, have been perfomed by Schroeder et al. (2000), for various degrees of saturation in water. The results of these tests, presented in figure (1.6), show that the "pore collapse" limit decreases as the degree of saturation in water increases.

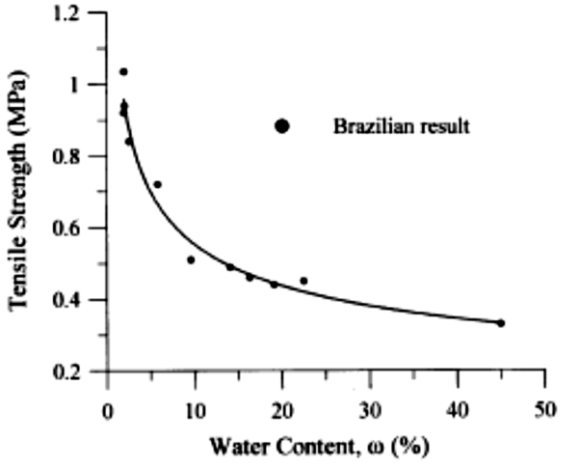


*Figure 1.5 : Effect of water on the chalk tensile strength, Brazilian test (Talesnick et al. 2001)*

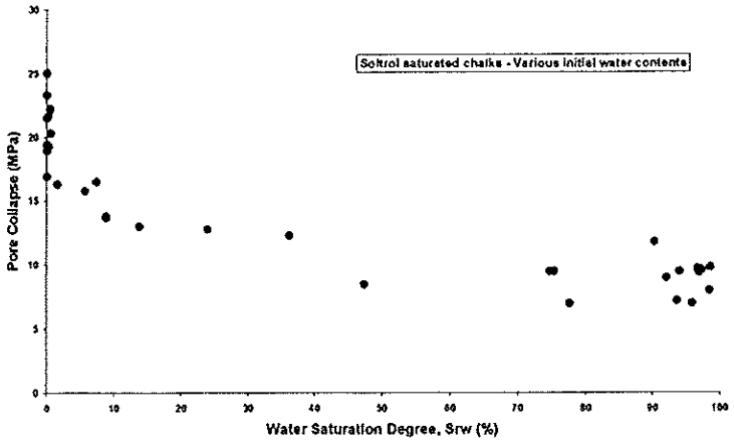


*Figure 1.6 : The "Pore collapse" limits for various degrees of saturation in water (Schroeder et al. 2000)*

- *Phenomenon of Dissolution-Recrystallization under stress*

Besides the important effect of water on the mechanical properties of chalk as explained above, it has also a chemical role. This role is illustrated by the process of dissolution-recrystallization. This phenomenon is an alteration process of calcareous rocks rich in calcite, such as chalk (Newman 1983, Piau and Maury 1994, Lord et al. 1998, Risnes and Flaageng 1999, Gutierrez et al. 2000).

The term of dissolution refers to the process by which a solution is formed afterward solid chalk being dissolved in water. During the invasion of pores by water, these pores get enlarged. As for the recrystallisation, it occurs when chalk solute transfers from liquid solution to a pure solid

crystalline. Therefore, water-chalk interaction by the mean of chemical effect can be due to the dissolution of calcite in contact with grains as well as to the recrystallisation associated in places where the energy of deformation is lower. The dissolution-recrystallisation phenomenon can intervene in the creep mechanism where time acts as an important factor in order to activate the chemical effect.

### *1.2.2.3 Mechanical time independent behavior of chalk*

The mechanical behaviour of chalk has been the subject of several studies performed on different types of chalk using a large number of laboratory tests: simple compression, odometer, hydrostatic and triaxial tests (Leddra and Jones 1989, Monjoie et al. 1990, Gourri 1991, Siwak 1994, Dahou 1995, Homand and Shao 2000, Schroeder 2002, De Gennaro et al. 2003, Priol 2005, Xie 2005, Priol et al. 2007, Lafrance 2016). According to a review done by Hickman (2004), it has been observed experimentally that chalk can exhibit different independent plastic yield mechanisms: (1) pore collapse, (2) shear failure, and (3) tensile failure.

Under hydrostatic conditions, an important phenomenon of chalk behaviour is identified, "Pore collapse", related to the collapse of the chalk porous network. Pore collapse is a volumetric yield mechanism and it occurs at high mean stresses (Hickman 2004). Therefore, this phenomenon can take place at high depths, for example chalk reservoirs at the Northern Sea. Figure 1.7 presents results of isotropic behaviour of Lixhe chalk under both loading procedures, applied step loading (Xie 2005) and controlled loading rate (Homand and Shao 2000). Homand and Shao (2000) identified the evolution of confining pressure (figure 1.7) in three zones describing chalk behaviour. The first phase corresponds to a quasi-linear elastic behaviour up to a value of confining pressure defining the degradation threshold of the material. This phase presents an elastic and reversible response. In the second phase, the presence of a strong plastic compaction is the result of a progressive collapse of the porous structure by breaking of bridges between grains and the growth of the contact area between grains leading to an increase of the material compressibility. The last phase shows a densification of the chalk by a hardening strain due to the important decrease of chalk porosity. According to Monjoie et al. (1990), it is caused by the break of the physico-chemical connections leading to sliding between grains. It should be noted that this evolution can be observed in results of odometer test (Siwak 1994, Schroeder 1995, 2002).

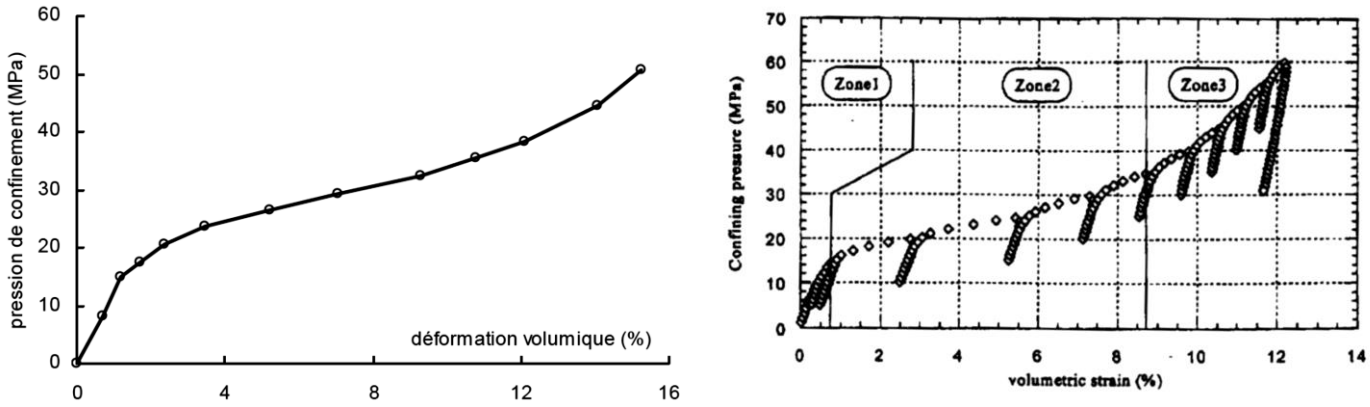


*Figure 1.7 : Hydrostatic tests under applied step loading and controlled loading rate of Lixhe chalk (Homand and Shao 2000, Xie 2005)*

Generally, the "Pore collapse" phenomenon comes along by a brutal irreversible reduction in chalk porosity (Monjoie and Schroeder 1989, Dahou 1995, Homand and Shao 2000) . Thus, it should be noted that the plastic deformations are more important as the chalk is porous and the threshold of "Pore collapse" varies from a chalk to another depending on the initial porosity as well as on the conditions of saturation (Monjoie et al. 1990, Xie 2005). For example, hydrostatic tests done by Siwak (1994) on different chalk types with different values of porosity, figure 1.8, can confirm this idea. Several threshold values have been obtained depending on chalk origin. Another example can be referred to hydrostatic test realised by Dahou (1995) on Lezennes chalk where the elastic limit has a value of approximately 13 MPa, different from others threshold values of different chalk mentioned before.

The second failure mechanism of chalk, shear failure, is a deviatoric yielding in which solid rock grains rotate and/or slide past each other on internal surfaces (Hickman 2004). It occurs at relatively low mean stress. Thus, it is noticeable more often at chalk outcrops and chalk at shallow depths.

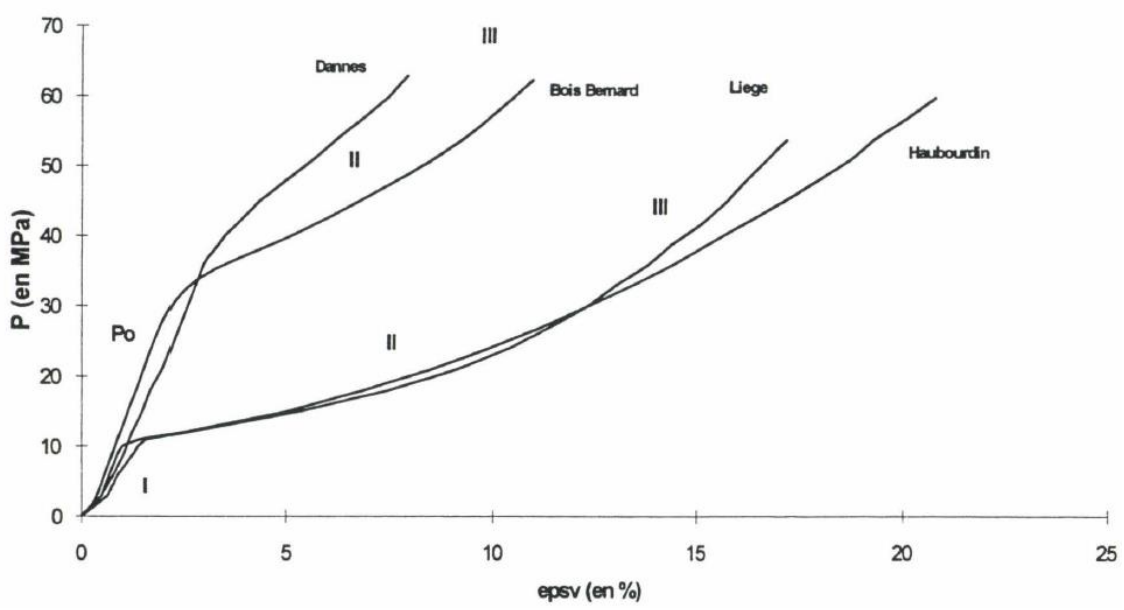


*Figure 1.8 : Monotonic hydrostatic tests on different types of chalk (Siwak 1994)*

Considering the deviatoric behaviour of chalk, it has been found that results obtained on different chalks are in a good agreement. Following the classical draining loading path under constant confining pressure (Siwak 1994, Dahou 1995, Schroeder 2002, Priol 2005, Xie 2005, Lafrance 2016), two distinct behaviours of chalk, depending on the applied confining pressure value, have been noticed. As shown in figure 1.9, under low confining pressure (< 10 Mpa), the Haubourdin chalk presents brittle to softening elastoplastic behaviour with peak resistances. Otherwise, under high confining pressure, a ductile to hardening elastoplastic behaviour dominates.

Likewise, figure 1.10 presents results from triaxial tests realised on North Sea chalk (Schroeder 2002). Two different behaviours can also be noticed. As shown in figure 1.10, at low confinement pressure (2.5 MPa and 5 MPa), the North Sea chalk exhibits brittle behaviour with a peak. When the confinement pressure increases (from 5 MPa), the deviator-axial strain curves exhibit a ductile behaviour. The rupture becomes more and more plastic, reflecting an elastoplastic type of behaviour with hardening. The "pseudo-elastic" phase is reduced and disappears beyond a confinement of 25 MPa. At confinement of 25 MPa, the chalk was probably already plasticised by isotropic loading. Therefore, it worth noting that the elastic limit becomes negligible when the confining pressure exceeds the elastic limit in isotropic compression.

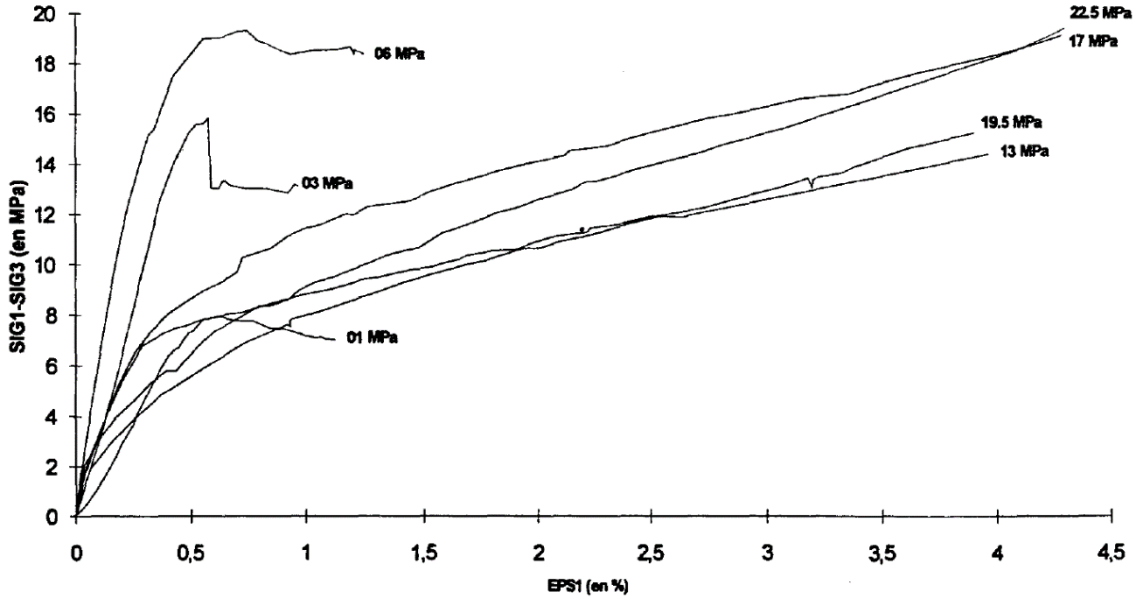


*Figure 1.9 : Behaviour of the Haubourdin chalk, North France at different confining pressure (Siwak 1994)*

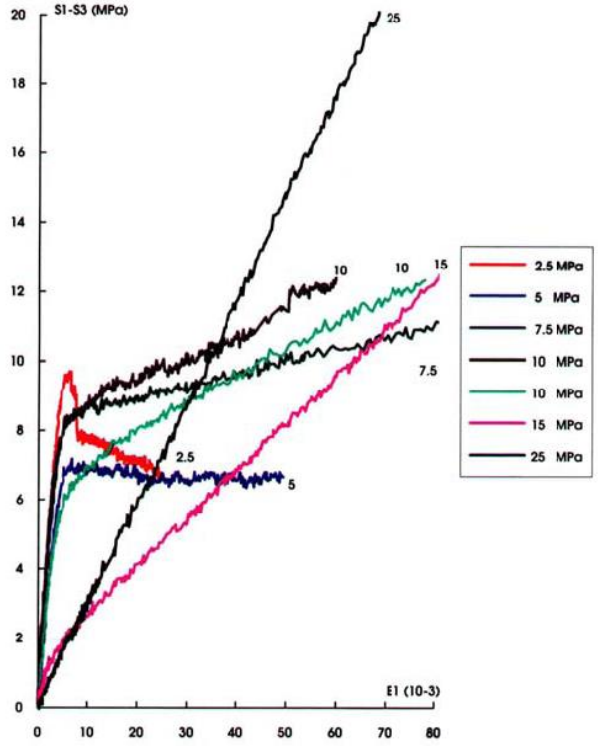


*Figure 1.10 : Triaxial compression tests with different confining pressures on North Sea chalk (Schroeder 2002)*

Same observations have been noticed during triaxial compression tests conducted on Lixhe chalk saturated with Soltrol by Homand & Shao (2000) (figure 1.11).

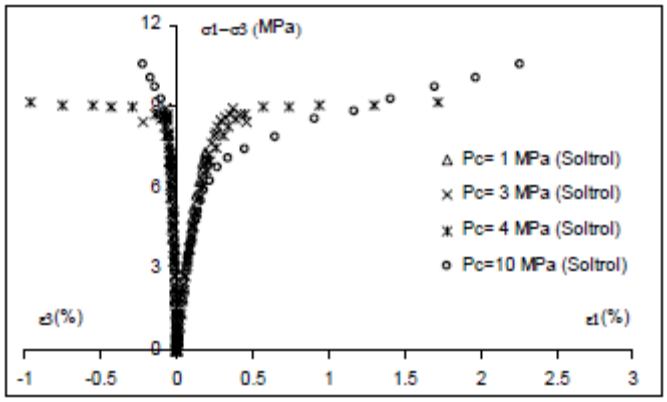


*Figure 1.11 : Triaxial compression tests with different confining pressures on Lixhe chalk (Homand and Shao 2000)*

Due to the high porosity of chalks, the plastic volumetric deformation of this material is often contracting. In addition, contractancy level is highly dependent on the confining pressure and porosity.

Tensile failure is a failure mechanism in which rock grains pull apart from each other when one of the normal stress components in the rock becomes sufficiently small or tensile (Hickman 2004). Like other strengths of chalk, i.e., isotropic stress and shear strength, tensile strength depends on the porosity value. It decreases as the porosity increases.

### *1.2.2.4 Mechanical time dependent behavior of chalk*

Under static stresses or repeated loading, chalk is considered as an evolving material. Time is reported as an important parameter when explaining some aspects of the mechanical behaviour of chalk.

Different studies on chalk, in different laboratories, have shown that this material presents a significant creep under constant load (Dahou 1995). In fact, creep is a physical phenomenon that causes delayed irreversible deformation of the material subjected to a constant stress. The typical creep curve (figure 1.12) exhibits three phases. The first phase, known as Primary or Transient creep, presents a rapid decrease of deformation rate with time after an initial instantaneous deformation. In the second phase, known as Stationary or Steady State creep, the deformation rate remains substantially constant over time. The third phase, known as Tertiary or Accelerating Creep, presents rapid failure under high stresses.

Uniaxial creep tests, done by Monjoie and Schroeder (1989), have shown that when the applied stresses are greater than 0.7 $R_c$ ($R_c$: compression resistance of chalk), the viscoplastic deformation rapidly increases leading to rupture. Dahou (1995) studied the creep of a chalk from northern France. The tests followed isotropic and deviatoric paths. Results of triaxial creep

tests on the chalk of Lezennes showed the absence of accelerating creep. Creep behaviour of this chalk, at different confining pressures and under various applied deviatoric stresses, is governed by the transient creep only (figure 1.13). This is related to the applied stress which greatly influences the type of encountered creep.

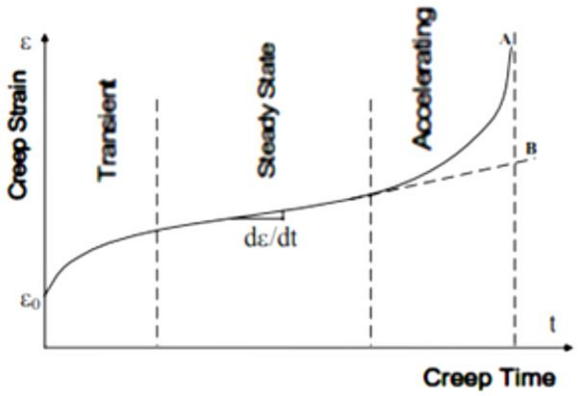


*Figure 1.12 : Typical Creep Curve*

In addition, Xie (2005) showed for the Lixhe chalk that under a very high confining pressure, tertiary creep has no occurrence, contrary to the case where a low confinement is applied. Under low confining pressure, the increase of deviatoric stress allows to distinguish between different creep phases (figure 1.14).

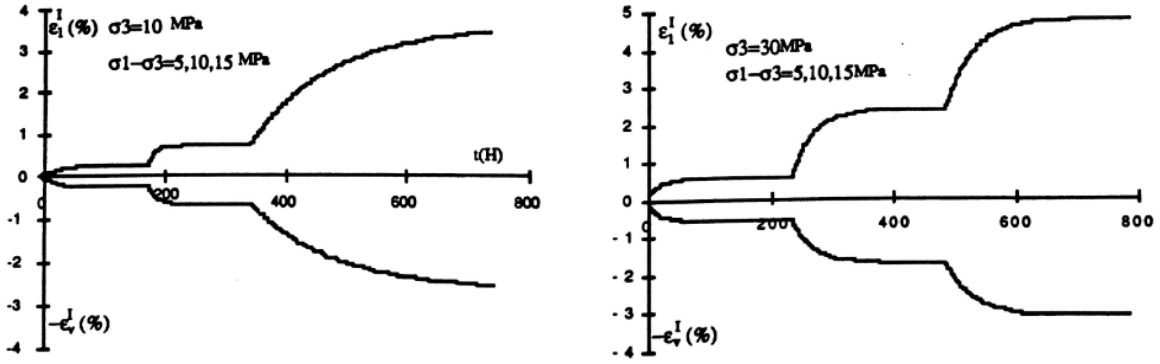


*Figure 1.13 : Triaxial creep tests performed on Lezennes chalk, North France under different confining pressures (Dahou 1995)*

Therefore, the observation of tertiary creep for chalk depends entirely on the state of stress of the material. Since creep corresponds to the viscous side of the behaviour, the viscosity of the chalk has been the subject of many studies (Dahou 1995, Schroeder 2002, De Gennaro et al. 2003, Priol 2005, Nguyen 2009).

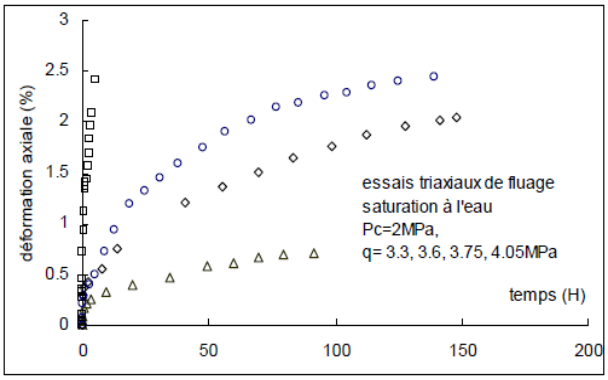


*Figure 1.14 : Triaxial creep tests on Lixhe chalk under different deviatoric stresses (Xie 2005)*

As for the effect of water on the phenomenon of creep, Lafrance (2016) has studied the effect of relative humidity on the long-term behaviour of different chalks. She concluded that as the relative humidity increases, the amplitude of viscoplastic deformations drastically increases, and it leads to an increase in the rate of delayed deformation.

## 1.3 Chalk in engineering works

### 1.3.1 Chalk classification

Like other weak rocks, chalk shows large difficulty in obtaining samples for laboratory testing. Authors reported the difficulties of sampling intact samples of significant volume, by means of usual methods (Pasturel 1968, Spink and Norbury 1989). In order to classify chalk and to assess its engineering performance, in the field of deep foundations for civil engineering works, different in-situ tests have been developed and used. According to the French standard NF P94-262 (AFNOR 2012), based on results from Static Penetrometer Test (CPT) and Pressuremeter Test (PMT), three categories of chalk, soft, weathered and sound can be encountered, (table 1.1).

*Table 1.1 : Chalk classification (AFNOR 2012)*

| Chalk | $p_l^*$ (MPa) | $q_c$ (MPa) |
|---|---|---|
| **Soft** | < 0,7 | < 5 |
| **Weathered** | 0,7 to 3 | 5 to 15 |
| **Sound** | ≥ 3 | ≥ 15 |

CIRIA's "Engineering in chalk" (Lord et al. 2002) provides a detailed description of chalk and a classification for engineering purposes based on dry density, aperture, filling and spacing of discontinuities. Globally chalks are classified in structureless class D chalk and structured

chalks. Structured chalks are characterised by their density (low, medium, high, very high) and their grade (A, B, C) according to their fracturing state.

## 1.3.2 Behaviour of piles in chalk under monotonic axial loading

### *1.3.2.1 Experimental observations*

Piles are structural elements used as deep foundations for several civil engineering works. They are suggested when shallow foundations cannot ensure the stability of the superstructure because of the weakness of the ground layers at the top surface or the importance of the transmitted loads.

As presented in the following expressions, the bearing capacity of a pile under monotonic axial loading in compression, $R_c$, is considered the sum of the mobilised resistance at the soil-pile interface, i.e. the shaft resistance $R_s$, and the mobilised resistance at the pile base, i.e. the base resistance $R_b$. In tension, pile bearing capacity is only equal to the mobilised shaft resistance.

$$R_c = R_b + R_s \text{ and } R_t = R_s \tag{1.3}$$

$$R_b = A_b * q_b \tag{1.4}$$

$$R_s = P_s \int_0^L q_s(z)dz \tag{1.5}$$

$A_b$ is the area of the pile base and $q_b$ is the ultimate base resistance.

$P_s$ is the pile perimeter, L is the length of pile in the ground and $q_s$ is the shaft resistance at level z.

Several methods exist in the literature for determining these two parameters, the shaft and the base resistance. These methods are based on geotechnical data provided by laboratory or in-situ tests, depending on the ground type.

Some methods are based on the knowledge of intrinsic mechanical properties of soil, c and $\phi$ (Caquot and Kerisel 1966). The difficulty in applying these methods lies in the measurement of the mechanical characteristics that are generally estimated from laboratory tests. Such methods are not suitable for all soil types. For example, they are applicable in the case of clay and hard rocks that can undergo such treatment without being altered. Other types of soil because of their structure, alteration, etc. cannot be collected in intact form. Regarding this difficulty in the case of chalk, results from in-situ tests, Pressuremeter test (PMT) and Static

Penetrometer test (CPT), are used. Parameters extracted from these tests are the limit pressure $p_l$ or the cone resistance $q_c$.

### *1.3.2.2 Methods for predicting the bearing capacity of piles*

#### *1.3.2.2.1 Pressuremeter Method (PMT)*

The Fasicule 62 Title V (MELT 1993) has been adopted since 1993 by the Ministry of Equipment. It includes rules for calculating pile capacity from Pressuremeter and Penetrometer tests. However, many static pile load tests have been carried out since 1990 and have not been considered in the development of Fasicule 62-V rules (MELT 1993). Bustamante and Gianeselli (2006) used these pile tests and older tests, available in the LCPC (Laboratoire Central des Ponts et Chaussées) database, to propose new rules for calculating pile resistance. More recently, the old calculation rules as well as those presented by Bustamante and Gianeselli (2006) have been revised by Burlon et al. (2014a). The objective of this revision is the implementation of the Eurocode 7 into the French practice. In this section, the new rules implemented in the French national standard for the designing of deep foundations NF P 94-262 (AFNOR 2012) are presented. The rules set out in this standard are based on the work of Burlon et al. (2014a). Between the 174 full-scale static load tests, taken from the LCPC database and used to calibrate the PMT model, 24 tests have been performed on piles in chalk. Out of 24 piles, 4 were bored piles, 4 screw piles, 12 driven piles and 4 driven sheet pile walls (Frank 2017).

**a. Shaft resistance $q_s$:**

The value of the shaft resistance is calculated according to the following general expression:

$$q_s(z) = \alpha_{pile-soil} * f_{soil}(p_l^*) \tag{1.6}$$

Where $p_l^*$ is the net limit pressure (PMT), $\alpha_{pile\text{-}soil}$ is a dimensionless parameter depending on the type of pile and the type of soil (table 1.2) and $f_{soil}$ is a function depending on the soil type and limit pressure $p_l^*$. The expression of $f_{soil}$ is given by equation 1.7. a, b and c are parameters depending on the soil type. For chalk a = 0.007, b = 0.07 and c = 1.3.

$$f_{soil}(p_l^*) = (a * p_l^* + b) * \left(1 - e^{-cp_l^*}\right) \tag{1.7}$$

Figure 1.15 illustrates the evolution of the shaft resistance $q_s$ in function of the net limit pressure $p_l^*$ for various pile categories encountered in different chalk type. It should be noted that the numbers mentioned in the figure legend refer to the pile categories presented in table 1.2.

*Table 1.2 : Values of $\alpha_{pile\text{-}soil}$ for chalk (Pressuremeter method)*

| **Pile class** | **Pile category** | **$\alpha_{pile\text{-}soil}$** |
|---|---|---|
| **C1: Bored piles** | 1. No support | 1.8 |
| | 2. With slurry | 1.8 |
| | 3. Permanent casing | 0.5 |
| | 4. Recoverable casing | 1.7 |
| | 5. Dry Bored Pile/ or Slurry Bored Pile with Grooved Sockets | - |
| **C2: CFA piles** | 6. CFA pile | 2.1 |
| **C3: Screw piles** | 7. Screw cast in place pile | 1.7 |
| | 8. Screw piles with casing | 1 |
| **C4: Closed-ended driven piles** | 9. Pre-cast or Pre-stressed Concrete Driven Pile | 1 |
| | 10. Coated Driven Steel Pile (coating concrete, mortar, grout) | 1.9 |
| | 11. Driven cast-in-place pile | 2.1 |
| | 12. Driven steel pile, closed-ended | 0.4 |
| **C5: Open-ended driven piles** | 13. Driven steel pile, open-ended | 0.5 |
| **C6: Driven H piles** | 14. Driven H pile | 0.4 |
| | 15. Driven grouted H pile | 2.4 |
| **C7: Driven sheet pile walls** | 16. Driven sheet pile | 0.4 |
| **C8: Micropiles** | 17. Micropile I (gravity pressure) | - |
| | 18. Micropile II (low pressure) | - |
| | 19. Micropile III (high pressure) | 2.4 |
| | 20. Micropile IV (high pressure with TAM) | 3.1 |

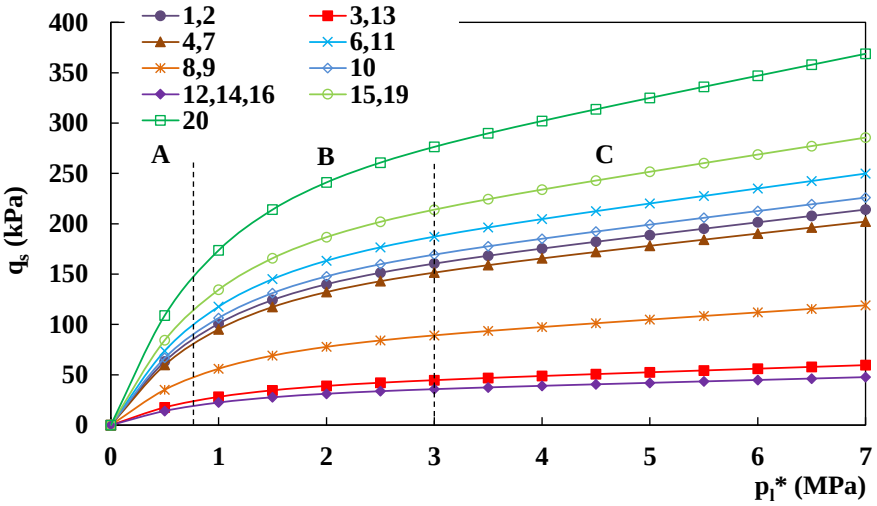


*Figure 1.15 : Evolution of $q_s$ values in function of $p_l$* for different pile category*

Table 1.3 groups the maximum values of shaft resistance that can be obtained in chalk for different pile categories.

*Table 1.3 : Values of $q_{s,max}$ for design from PMT and CPT results*

| Pile class | Pile category | $q_{s,max}$ (kPa) |
|---|---|---|
| **C1: Bored piles** | 1. No support | 200 |
| | 2. With slurry | 200 |
| | 3. Permanent casing | 50 |
| | 4. Recoverable casing | 170 |
| | 5. Dry Bored Pile/ or Slurry Bored Pile with Grooved Sockets | – |
| **C2: CFA piles** | 6. CFA pile | 200 |
| **C3: Screw piles** | 7. Screw cast in place pile | 170 |
| | 8. Screw piles with casing | 90 |
| **C4: Closed-ended driven piles** | 9. Pre-cast or Pre-stressed Concrete Driven Pile | 90 |
| | 10. Coated Driven Steel Pile (coating concrete, mortar, grout) | 200 |
| | 11. Driven cast-in-place pile | 260 |
| | 12. Driven steel pile, closed-ended | 50 |
| **C5: Open-ended driven piles** | 13. Driven steel pile, open-ended | 50 |
| **C6: Driven H piles** | 14. Driven H pile | 50 |
| | 15. Driven grouted H pile | 320 |
| **C7: Driven sheet pile walls** | 16. Driven sheet pile | 50 |
| **C8: Micropiles** | 17. Micropile I (gravity pressure) | – |
| | 18. Micropile II (low pressure) | – |
| | 19. Micropile III (high pressure) | 320 |
| | 20. Micropile IV (high pressure with TAM) | 440 |

**b. Base resistance $q_b$:**

The value of the base resistance is calculated according to the following general expression:

$$q_b = k_p * p^*_{le} \tag{1.8}$$

Where, $p^*_{le}$ is the equivalent net limit pressure and it is calculated according to equation 1.9. $k_p$ is the Pressuremeter bearing capacity factor. It is related to the effective installation height $D_{ef}$ determined from the equation 1.10.

$$p^*_{le} = \frac{1}{3a+b}\int_{L-b}^{L+3a} p^*_l(z)dz \quad \text{With a} = \max\{\frac{B}{2}; 0.5\} \quad \text{b} = \min\{a;h\} \tag{1.9}$$

Where, L is the pile length, B is the pile diameter and h is the height of the pile installed in the bearing layer.

$$D_{ef} = \frac{1}{p^*_{le}}\int_{L-h_D}^{L} p^*_l(z)dz \tag{1.10}$$

With $h_D$=10*B

- If $D_{ef}$/B is bigger than 5, then $k_p = k_{pmax}$;
- If $D_{ef}$/B is smaller than 5, then $k_p = 1 + \left(k_{pmax} - 1\right) * \frac{\frac{D_{ef}}{B}}{5}$;

Values of $k_{pmax}$ are given in table 1.4.

*Table 1.4 : Values of $k_{pmax}$ for different pile classes*

| **Pile class** | **C1** | **C2** | **C3** | **C4** | **C5** | **C6** | **C7** | **C8** |
|---|---|---|---|---|---|---|---|---|
| **$k_{pmax}$** | 1.45 | 1.6 | 2.35 | 2.3 | 1.4 | 1.7 | 1 | 1.45 |

### *1.3.2.2.2 Penetrometer Method (CPT)*

During the drafting of the new French standard for pile design according to Eurocode 7, a revision of the first model for bearing capacity of piles from CPT results has been done. This first model has been calibrated using data from LCPC database by Bustamante and Gianeselli (1981, 1982). The revised model "CPT 2012" has been implemented in the new French standard for the application of Eurocode 7 to deep foundations NF P 94-262 (AFNOR 2012). However, the proposed rules for the prediction of the bearing capacity of piles from CPT results are more uncertain than the rules from the Pressuremeter method. The small number of full-scale load tests available with CPT results compared to PMT results is considered the main reason behind this uncertainty. Results of only 42 full-scale static load tests available in the database have

been used for the calibration of the "CPT 2012" model (Frank 2017). According to Bustamante et al. (2009), the Pressuremeter method has showed its reliability for a large number of soil types and it remains the most versatile site investigation tool. As for the chalk, the Pressuremeter method has the advantage of being always applicable regardless of the degree of chalk alteration (Bustamante et al. 1980).

**a. Shaft resistance $q_s$:**

The value of the shaft resistance is calculated according to the following general expression:

$$q_s(z) = \alpha_{pile-soil} * f_{soil}[q_c(z)] \quad (1.11)$$

In this equation, $\alpha_{pile\text{-}soil}$ is a dimensionless parameter depending on type of pile and type of soil (table 1.5) and $f_{soil}$ is a function depending on the type of soil and the cone resistance values from the CPT test noted $q_c$. The expression of $f_{soil}$ is given in equation 1.12. a, b and c are parameters depending on soil type. For chalk a = 0.0015, b = 0.1 and c = 0.25.

$$f_{soil}(q_c) = (a * q_c + b) * (1 - e^{-cq_c}) \quad (1.12)$$

Figure 1.16 illustrates the evolution of the shaft resistance $q_s$ in function of cone resistance $q_c$ for various pile categories encountered in different chalk type. It should be noted that the numbers mentioned in the figure legend refer to the pile categories presented in table 1.5.

*Table 1.5 : Values of $\alpha_{pile\text{-}soil}$ for chalk (Penetrometer method)*

| Pile class | Pile category | $\alpha_{pile\text{-}soil}$ |
|---|---|---|
| **C1: Bored piles** | 1. No support | 0.80 |
| | 2. With slurry | 0.80 |
| | 3. Permanent casing | 0.25 |
| | 4. Recoverable casing | 0.75 |
| | 5. Dry Bored Pile/ or Slurry Bored Pile with Grooved Sockets | - |
| **C2: CFA piles** | 6. CFA pile | 0.95 |
| **C3: Screw piles** | 7. Screw cast in place pile | 0.75 |
| | 8. Screw piles with casing | 0.45 |
| **C4: Closed-ended driven piles** | 9. Pre-cast or Pre-stressed Concrete Driven Pile | 0.45 |
| | 10. Coated Driven Steel Pile (coating concrete, mortar, grout) | 0.85 |
| | 11. Driven cast-in-place pile | 0.95 |
| | 12. Driven steel pile, closed-ended | 0.20 |
| **C5: Open-ended driven piles** | 13. Driven steel pile, open-ended | 0.25 |
| **C6: Driven H piles** | 14. Driven H pile | 0.20 |
| | 15. Driven grouted H pile | 1.10 |
| **C7: Driven sheet pile walls** | 16. Driven sheet pile | 0.20 |
| **C8: Micropiles** | 17. Micropile I (gravity pressure) | - |
| | 18. Micropile II (low pressure) | - |
| | 19. Micropile III (high pressure) | 1.10 |
| | 20. Micropile IV (high pressure with TAM) | 1.40 |

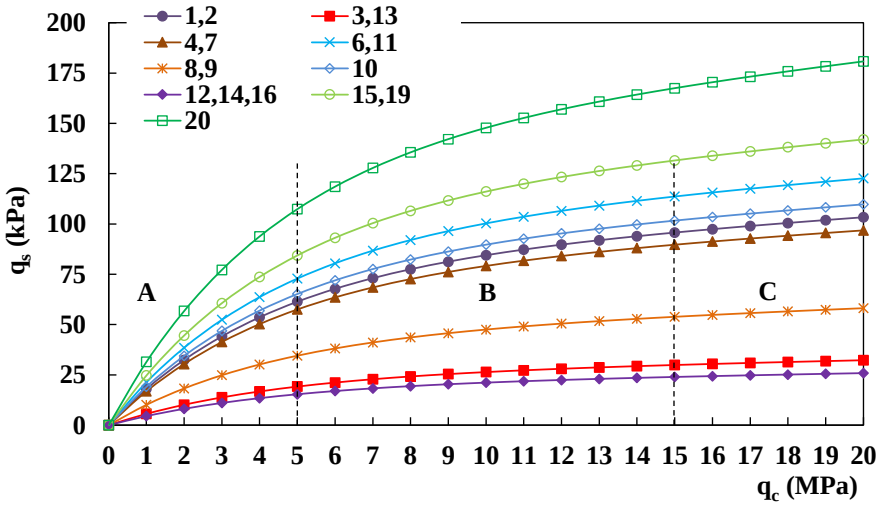


*Figure 1.16 : Evolution of $q_s$ values in function of $q_c$ for different pile category*

**b. Base resistance $q_b$:**

The value of the base resistance is calculated according to equation 1.13. In this equation, $q_{ce}$ is the equivalent penetration resistance of the cone. It is determined according to equation 1.14 where $q_{cc}$ corresponds to the corrected penetrometer profile, L to the pile length, B to the pile diameter and h to the height of the pile installed in the bearing layer.

$$q_b = k_c * q_{ce} \tag{1.13}$$

$$q_{ce} = \frac{1}{3a+b}\int_{L-b}^{L+3a} q_{cc}(z)dz \text{ with a = max } \{\frac{B}{2}; 0.5\} \quad \text{b = min } \{a; h\} \tag{1.14}$$

The parameter $k_c$ in equation 1.13 corresponds to the penetrometer bearing capacity factor and depends on the effective installation height $D_{ef}$ given by equation 1.15.

$$D_{ef} = \frac{1}{q_{ce}}\int_{L-h_D}^{L} q_c(z)dz \tag{1.15}$$

With $h_D$=10*B
According to the following rules, the parameter $k_c$ is determined:

- If $D_{ef}$/B is bigger than 5, then $k_c = k_{cmax}$;
- If $D_{ef}$/B is smaller than 5, then $k_c = 0.15 + (k_{cmax} - 0.15) * \frac{\frac{D_{ef}}{B}}{5}$;

Values of $k_{cmax}$ are given in table 1.6.

*Table 1.6 : Values of $k_{c,max}$ for different pile classes*

| **Pile class** | **C1** | **C2** | **C3** | **C4** | **C5** | **C6** | **C7** | **C8** |
|---|---|---|---|---|---|---|---|---|
| **$K_{cmax}$** | 0.3 | 0.3 | 0.4 | 0.4 | 0.15 | 0.35 | 0.15 | 0.3 |

### *1.3.2.3 Parameters affecting pile capacity under monotonic loading*

#### *1.3.2.3.1 Method of pile installation*

Method of pile installation can have a significant effect on its bearing capacity. In fact, pile bearing capacity is affected by changes in stress states and surrounding soil condition parameters that occur during and after installation. During pile driving, the soil undergoes deformations and alterations in the area around the pile. This type of installation then causes friction degradation, which is a mechanism often related to the degradation of soil parameters at interface level, such as friction angle and radial effective stress.

In chalk, silt and clay-sized particles are generated after pile driving, where this operation easily causes crushing and deterioration of chalk structures. Thus, de-structuration and crushing of hollow calcium carbonate particles beneath the advancing pile tip produces low-strength, viscous material, identified as “putty chalk”, that spreads along the pile (Florentin et al. 1961, Lake 1975, Bustamante et al. 1998, Lord et al. 2002). This low-strength putty, in direct contact with the pile, limits the radial effective stresses and shear resistances that can act on the pile shaft (Hobbs and Atkinson 1993, Lord et al. 2002).

These observations have been recently confirmed by some researchers who have tested open-ended steel tube piles driven in low to medium density chalk (Ciavaglia et al. 2017). An annulus of remoulded chalk (figure 1.17) has been encountered around the pile with approximately 20-40 mm of thickness.


*Figure 1.17 : Side view of a pile after being driving in low to medium density chalk, (Ciavaglia et al. 2017)*

Generally, installation of the pile by the mean of drilling doesn’t have the same effect on the surrounding soil. Drilled pile causes a lower degree of disturbance. In terms of bearing capacity, by comparing two piles of same characteristics, it seems that pile installed by drilling has a higher bearing capacity than the pile installed by driving.

### *1.3.2.3.2 Time dependency*

Advantageous time effects on pile shaft resistance have been reported in sands and clays (Jardine et al. 2006, Karlsrud et al. 2014, Gavin et al. 2015). Similarly, several researchers have studied the effect of time after pile driving in chalk. An increase in the pile capacity in chalk over time has been reported. Pasturel (1968) has reported an increase of 117% in the dynamic driving resistance over 10 days pause during a campaign of pile load tests, within the LCPC, on precast concrete pile driven in weathered chalk for the Bridge of Oissel. Within the same

laboratory, Bustamante et al. (1980) have reported an increase of about 30% in the pile capacity over nine months during static load tests performed on three different piles, precast concrete, steel cylindrical and steel H, driven in chalk. Vijayvergia et al. (1977) have reported an increase of about 80% in the dynamic driving resistance within 60 days pause in an offshore project. Skov and Denver (1989), and Lahrs and Kallias (2013) have also observed similar time effects. The most recent cases have been reported by Ciavaglia et al. (2017),and Buckley et al. (2020, 2018b, 2018a). Ciavaglia et al. (2017) have interpreted the results of three tension tests performed on the same 762 mm diameter tubular steel pile driven into low to medium density grade A/B chalk at St Nicholas at Wade, Kent, UK. These results have shown an increase of up to 700% in the pile shaft resistance during re-tests conducted over 4 months from pile driving. Buckley et al. (2018b) described the results of several static tension tests conducted on three 139 mm diameter open steel tubes driven in low to medium density chalk in a quarry close to St Nicholas at wade. Results have indicated a set-up factor, or shaft capacity increasing factor, of 5.2 after 246 days from driving.

In the frame of the same load testing project of driven piles into in low to medium density chalk in a quarry close to St Nicholas at wade, another type of well instrumented piles has been investigated. Two closed-ended instrumented Imperial college piles (ICPs) of 102 mm diameter have been jacked into chalk (Buckley et al. 2018a). These intrumented piles allowed the tracking of the effective stress regime along the pile shaft during pile installation, equalisation period and load testing. Althougth these piles developed an overall average shaft resistance of 50 kPa, during installation, exceeding the CIRIA driven pile static capacity recommendation of 20 kPa (Lord et al. 2002), and the developed average shaft resistances of 16 kPa for open-ended driven piles in the same site (Buckley et al. 2018b), they have presented a strong contrast with the open-ended tested piles regarding ageing trends. Tension load tests showed shaft capacity reducing with time after installation, dropping by 20% for the first pile after 23 days and 18% for the second pile after 80 days. Also, long-term tracking showed total radial shaft stresses reducing by more marked proportions, dropping by 26% and 34% respectively. Corresponding authors reffered the diffrence between ageing trens to geometry and (or) installation method.

Considering Offshore piles, a full-scale dynamic and static testing campaign has been held on steel open-ended tubes driven through glacial tills and structured low-medium density chalk at a Baltic Sea windfarm, the Wikinger windfarm (Buckley et al. 2020). Six 1.37 m diameter piles have been driven in pairs at three different locations. After 12-15 weeks from installation, one pile from each pair has been tested statically while the adjacent twin pile has undergone an instrumented re-strike. Buckley at al. (2020) compared the mobilised shaft resistance at end of

driving (EOD), at beginning of re-strike (BOR) and during static tensile tests. Figure 1.18 presents the compressive shaft resistance at EOD and BOR for tested piles in locations where chalk dominates glacial tills.

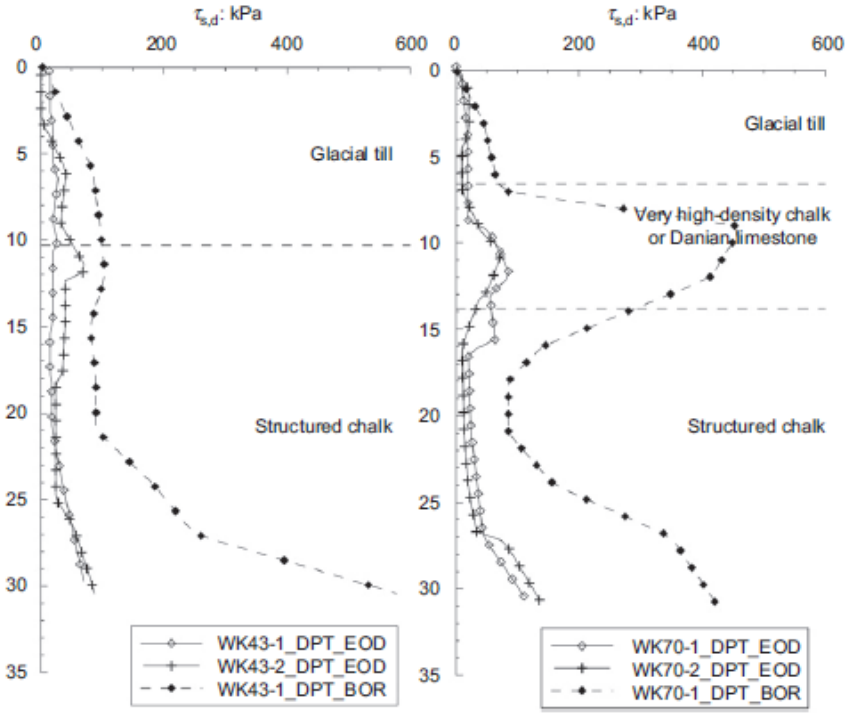


*Figure 1.18 : Shaft resistance at end of driving and beginning of re-strike, (Buckley et al. 2020)*

Shaft capacities have developed set-up factors between 5.3 and 5.2 from re-strike tests, where 86% and 96% of the total shaft capacities has been developed within the respective piles chalk layer. Considering the tension pile load tests, ultimate failure could not been achieved, therefore a special extrapolation has been adopted in order to determine the tensile static shaft capacities. The obtained shaft capacities have shown overall set-up factors of 4.4 and 4.9 compared to values mobilised at the EOD. It has been also noticed that for the first location, tensile shaft capacity was 13% higher than the measured BOR shaft capacity, while for the second location it was 23% higher.

According to Lord et al. (2002), the increase of pile shaft capacity in chalk, also known as field set-up, may be attributed to pore pressure dissipation and possible re-cementing of remoulded chalk annulus around the pile shaft. Buckley et al. (2018b) suggested that this set-up phenomenon in chalk may also be due to redox chemical reactions. However, the absence of set-up shown by the ICP piles which are mainly oxidisable molybdenum steel jacked piles demonstrates that physiochemical effects and re-cementing cannot be the main ageing mechanism (Buckley et al. 2018a).

Several empirical relationships have been subjected in the literature to quantify the increase in the bearing capacity of driven piles , as a function of time, in clays and sands. Buckley et al. (2018b) suggested that the hyperbolic relationship (equation 1.16), proposed by Tan et al. (2004) for sand, seems to be appropriate to represent the results obtained during pile testing in chalk (figure 1.19).

$$Q(t) = Q_u \left\{ m + (1-m) \left[ \frac{t/T_{50}}{1 + \left(t/T_{50}\right)} \right] \right\} \tag{1.16}$$

Where, $Q_u$ is the ultimate capacity, $T_{50}$ is the time required to achieve 50% of $Q_u$ and m is an empirical coefficient (around 0.2) applied to improve the fit at the early age.

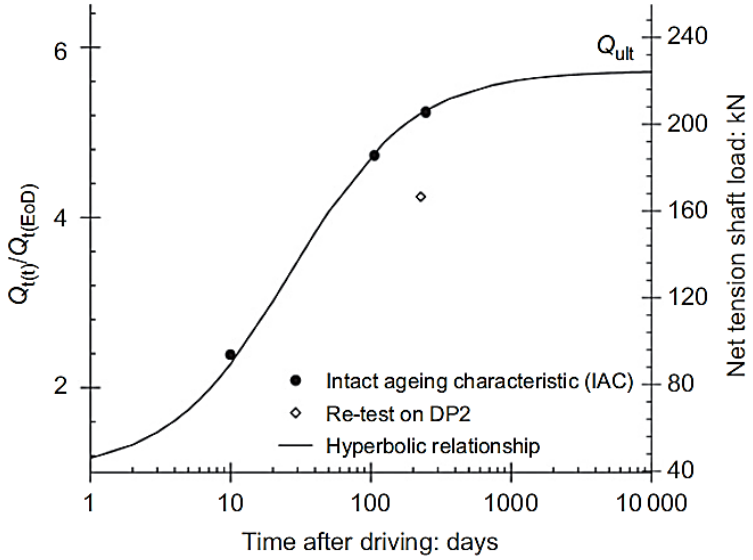


*Figure 1.19 : Shaft capacity growth with time (Buckley et al. 2018b)*

Jardine and Standing (2012) insisted on the importance of distinguishing between "virgin", no pre-tested, and pre-tested piles when studying the effect of time on bearing capacity. In fact, re-testing pre-failed piles affects the set-up phenomenon and is often consisedered as misleading. If a pile has been pre-loaded to failure, the rate of improvement of the bearing capacity over time remains modest compared to an equivalent virgin pile in sands and clays. This aspect has also been noticed for chalk. As shown in figure 1.19, the capacity of the pre-failed pile is 32% lesser than the capacity of the equivalent "virgin" pile over the age of 10-227 day.

Tests carried out on offshore piles have also shown same ageing trends over time (Buckley et al. 2020). They have presented similarly shaped set-up curves obtained for onshore piles totally immerged in chalk (figure 1.19). These trends have been strongly dependent on the degree of penetration of piles in chalk.

## 1.3.3 Behaviour of piles in chalk under cyclic axial loading

### *1.3.3.1 Definition and description of cyclic loading*

Cyclic loading, in its ideal case, is a variable loading mode that has a character of repeatability with regularity in amplitude and frequency. These cyclic loadings can be induced by environmental actions (wind, waves), by industrial actions (rail traffic, rolling loads), or by a combination of environmental and industrial actions. In reality, this type of loadings are irregular and random phenomena by nature, regarding both parameters, amplitude and frequency. For the sake of simplification, as part of calculations and modelling, these loadings are idealised and presented in the form of series of cycles having a regularity in amplitude and frequency.

Applied cyclic loadings can be described by using the following parameters, presented in figure (1.20):

- $Q_{max}$: Maximum cyclic loading;
- $Q_{min}$: Minimum cyclic loading;
- $Q_{mean}$: Mean cyclic loading ($Q_{mean}= (Q_{max}+Q_{min})/2$);
- $Q_{cyc}$: Amplitude of cyclic loading ($Q_{cyc}= (Q_{max}-Q_{min})/2$);
- T: Period of cyclic loading;
- N: Number of cycles;

Depending on these parameters, two types of cyclic loadings can be defined: “one-way” and “two-way” cyclic loading. The first type includes repetitive cyclic loadings. These repetitive loadings can be tension or compression loadings. The second type includes no-repetitive cyclic loadings. The maximum and minimum loadings are of opposite signs and the pile undergoes successions of cycles of compression and traction.

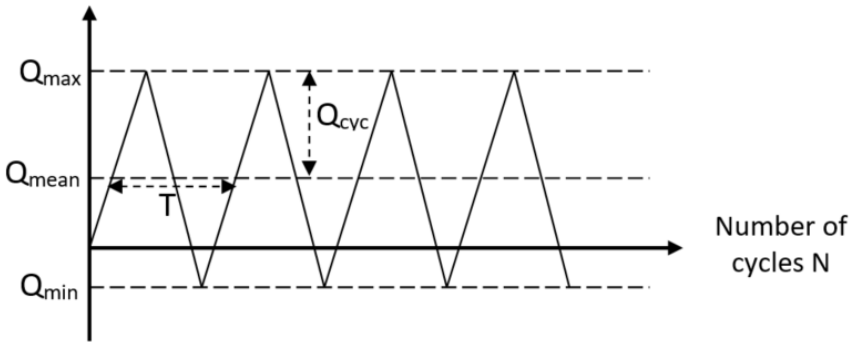


*Figure 1.20 : Characteristics of cyclic loading*

### *1.3.3.2 Stability diagram*

For different combinations of mean cyclic loading $Q_{mean}$ and cyclic amplitude $Q_{cyc}$, pile can exhibit three different responses to axial cyclic loading. Many field experiments carried out on piles in sand and clay have shown these three possible responses: stable, meta-stable and unstable. These three classifications are related to both possible numbers of cycles, N, and permanent cyclic displacement that can occur at the pile head. Using these three responses and in order to predict the nature of a pile behaviour under axial cyclic loading, for a given load combination ($Q_{mean}$, $Q_{cyc}$), the concept of cyclic stability diagram has been introduced by Poulos (1988). This diagram has been largely used to evaluate the axial cyclic response of a pile as a function of the number of cycles and cyclic loadings (figure 1.21). $P_0$ is the mean load, $P_c$ is the amplitude of cyclic load, $Q_c$ is the static compressive capacity and $Q_t$ is the static tensile capacity. This diagram is decomposed into three zones: zone (A) defines the stable behavior, zone (B) defines the meta-stable behavior and zone (C) defines the unstable behavior. Using the stability diagram, it is possible to determine if the applied cyclic load can be critical or not for the pile. Cyclic stability diagrams are valid for a given pile type and a given soil type.

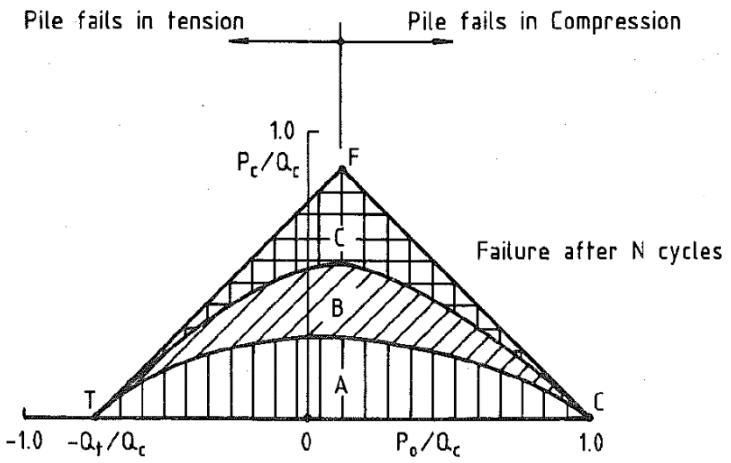


*Figure 1.21 : Main features of a cyclic stability diagram, (Poulos 1988)*

Buckley et al. (2018b) used the stability diagram to characterise cyclic behaviour of axially loaded piles driven in chalk (figure 1.22). Several open steel tubes driven in low to medium density chalk have undergone one-way tension cyclic loading.

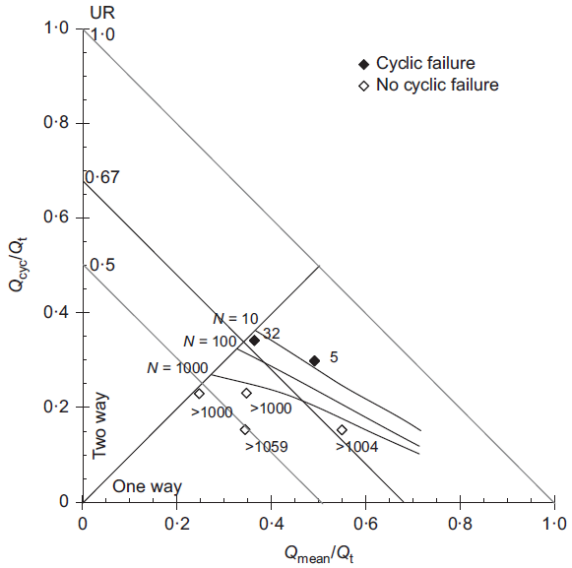


*Figure 1.22 : Cyclic loading interaction diagram for tests on piles in chalk, (Buckley et al. 2018b)*

Based on the working definitions of Jardine and Standing (2012) and Rimoy et al. (2013) in the case of open tube piles driven in dense sand, Buckley et al. (2018b) defined the different three pile responses as follows:

- Stable (S): no failure over 1000 cycles. Accumulation of cyclic displacement is slow over a large number of cycles and tends to stabilise with cycling. The final displacement is always less than 0.01D (D is the pile diameter), the rate of displacement accumulation is less than 1 mm/1000 cycles and the cyclic stiffness shows negligible loss. Operational shaft capacity and foundation serviceability are not affected by cycling.
- Meta-stable (MS): failure may occur with a number of cycles falling between 100 and 1000 cycles. Final displacement of 0.01D to 0.1D develops with a rate of displacement accumulation between 1mm/1000 cycles and 1mm/10 cycles. Operational shaft capacity and foundation serviceability losses are goverened by the numbers of applied cycles.
- Unstable (US): failure occur with a number of cycles less than 100, generating a large accumulated displacement greater than 0.1D or a rate of accumulation of displacement greater than 1mm/10 cycles. Potential marked losses in operational shaft capacity may occur and the foundations may become unserviceable.

Each cyclic loading is placed on this diagram according to its corresponding combination ($Q_{mean}$, $Q_{cyc}$). The cyclic stability diagram contains two diagonals. The first one with $Q_{mean} = Q_t$ indicates the static bearing capacity of the pile, and in this case the tensile static bearing capacity. The second one with $Q_{mean} = Q_{cyc}$ separates the two-way cyclic loadings ($Q_{mean} < Q_{cyc}$) and the one-way cyclic loadings ($Q_{mean} > Q_{cyc}$). The distance between the point of the cyclic

loading and the first diagonal indicates the drop in the bearing capacity of the pile during cyclic loading.

Regarding the limited database related to cyclic axial loadings conducted on piles in chalk, one-way cyclic tension tests done by Buckley et al. (2018b) remain the only available large dataset wich provide a first systematic study of axial cyclic response of piles driven in chalk. Further limited cyclic investigations have also been performed on two closed-ended ICP piles jacked into chalk of the same testing site (Buckley et al. 2018a). Limited packages of one-way axial cyclic loading have been applied after static tension tests to failure. Total number of 20 cycles has been performed. It has been decomposed into two successive packages of 10 cycles each, with different cyclic characteristics. Additional limited cyclic tests have been recently conducted on an offshore steel open-ended piles (Buckley et al. 2020) according to the same loading procedure followed for the ICPs piles.

Table 1.7 presents the cyclic (non-dynamic) programme tested on aged piles in chalk, using four virgin piles after 247 to 255 days from driving (Buckley et al. 2018b). These piles have undergone static post-cyclic testing to evaluate the effect of cycling loading on their static behaviour.

*Table 1.7 : Summary of cyclic testing programme, (Buckley et al. 2018b)*

| Test pile | Test code | Pile age: days | Mode | Comment |
|---|---|---|---|---|
| DP1 | DP1-CY1 | 253 | Cyclic | Low-Level cyclic test on previously untested pile |
| | DP1-CY2 | 253 | Cyclic | Second cyclic test immediately after DP1-CY1 |
| | DP1-TPC | 253 | Static | 'Quick' static test post cyclic failure |
| DP4 | DP4-CY1 | 249 | Cyclic | Low-Level cyclic test on previously untested pile |
| | DP4-TPC | 249 | Static | 'Quick' static test post DP4-CY1 |
| | DP4-CY2 | 255 | Cyclic | Second cyclic test on DP4 (Retest) |
| DP5 | DP5-CY1 | 254 | Cyclic | Low-Level cyclic test on previously untested pile |
| | DP5-CY2 | 254 | Cyclic | Second cyclic test immediately after DP5-CY1 |
| | DP5- TPC | 254 | Static | 'Quick' static test post cyclic failure |
| DP7 | DP7-CY1 | 247 | Cyclic | Cyclic test on previously untested pile |
| | DP7-TPC | 247 | Static | 'Quick' static test post cyclic failure |

Table 1.8 summarises results of different cyclic loading tests (Buckley et al. 2018b). Based on the three different categories defined above, tested piles show a variety of responses from non

failing stable behaviour with a numbers of cycles greater than 1000 to failing unstable behaviour with low numbers of cycles generating reductions of pile static capacity.The two tests (DP1-CY2, DP5-CY2) have exhibited unstable response reaching a numbers of cycles far less than 100. Regarding the numbers of cycles reached during testing, the four tests (DP1-CY1,DP4-CY1, DP5-CY1, DP7-CY1) have shown a stable response reaching more than 1000 cycles without generating a noticeable loss in static capacity. As for the accumulation of displacement, this was not the case for these four tests. Response of different piles in terms of accumulated displacement will be discussed in section (1.3.3.3.1). Based on the two criteria that define different responses of pile, numbers of cycles and accumulated displacement, the test DP4-CY2 has shown a fully stable response.

*Table 1.8 : Summary of cyclic loading test results, (Buckley et al. 2018b)*

| **Test code** | **One way axial cyclic loading** | | | | | | | |
|---|---|---|---|---|---|---|---|---|
| | **$Q_{min}$ kN** | **$Q_{max}$ kN** | **$Q_t$ kN** | **$Q_{cyc}/Q_t$** | **$Q_{mean}/Q_t$** | **UR: $Q_{max}/Q_t$** | **N cycles** | **Class** |
| DP1-CY1 | 40 | 103 | 207.2 | 0.15 | 0.34 | 0.5 | >1059 | MS/S |
| DP1-CY2 | 40 | 164 | 207.2 | 0.3 | 0.49 | 0.79 | 5 | US |
| DP4-CY1 | 82 | 145 | 207.0 | 0.15 | 0.55 | 0.7 | >1004 | MS/S |
| DP4-CY2 | 49 | 146 | 207.3 | 0.23 | 0.47 | 0.7 | >1003 | S |
| DP5-CY1 | 4 | 99 | 207.3 | 0.23 | 0.25 | 0.48 | >1000 | MS/S |
| DP5-CY2 | 5 | 146 | 207.3 | 0.34 | 0.36 | 0.71 | 32 | US |
| DP7-CY1 | 24 | 120 | 206.8 | 0.23 | 0.35 | 0.58 | >1000 | MS/S |

### *1.3.3.3 Effects of axial cyclic loading on pile response in chalk*

#### *1.3.3.3.1 Accumulation of displacements*

Accumulation of permanent displacements is one of the important and main effects of axial cyclic loading on pile response. This accumulation may occur at the pile head and throughout the pile shaft and can lead to failure if its value is very high. This phenomenon has been observed during many in-situ and laboratory tests on piles in clay and sand. These tests have shown that displacements accumulate over cycles. Values and rate of displacements accumulation are function of several parameters that can affect pile response under axial cyclic loading, such as type of cycling loading (one-way, two-way) and loading characteristics ($Q_{mean}$, $Q_{cyc}$, etc). If the maximum applied cyclic loading exceeds a threshold value, the rate of permanent displacement accumulation increases with the numbers of cycles. Below this value,

permanent accumulated displacements are very low with a rate of accumulation that decreases during cycles and may not occur if the maximum load is very small. For example, after analysing results from in-situ cyclic tests conducted on steel piles in loose sand, Puech (1982) has mentioned that when the maximum applied load is greater than $0.5R_s$, accumulation of permanent displacements accelerates with numbers of cycles. However, below this value, the rate of accumulation decreases with the number of cycles.

Figures 1.23a, 1.23b, 1.23c and 1.23d present the evolution of permanent displacement, normalised by the pile diameter D, according to the number of cycles N, for the un-failing tests (table 1.8) performed on driven piles in chalk (Buckley et al. 2018b). These curves follow approximately constant logarithmic gradients when N exceeds 20 cycles. Buckley et al. (2018b) have proposed the numerical expression presented in equation 1.17 in order to characterise the power law trends. Equation 1.17 gives a description of the evolution of permanent displacement in function of number of cycles. In this equation, A and B are non-dimensional fitting parameters. Similarly, figure 1.23e presents the trend of permanent displacement evolution for the cyclic test CP4-CY2 which has been tested under static tensile loading until failure after its first axial cyclic loading. This re-test has presented the same behaviour as the non-failing tests but in more staggered trend.

$$\frac{S_{acc}}{D} = AN^B \tag{1.17}$$

Plots of the two remaining failing tests are presented in figure 1.24. Regarding the definition of instability mentioned above, these two tests present an unstable behaviour failing at low N values. Test DP1-CY2 accumulated displacements of 2.3 to 3.5 mm/cycle until failing at five cycles. Before reaching nine cycles, the test DP5-CY2 accumulated displacements below 0.1mm/cycle but after that more rapid accumulation took place leading to failure in 32 cycles.

Using these results, Buckley et al. (2018b) have demonstrated the combined effects of cyclic amplitude $Q_{cyc}$ and mean cyclic loading $Q_{mean}$ by considering accumulated displacements developed after 3, 10, 20, 100, 300 and 600 cycles. These permanent accumulated displacements have been plotted on cyclic stability interaction diagrams where contours corresponding to $S_{acc}/D$ ratios of 0.2%, 0.5% and 2.0% are represented for these one-way cyclic tests. Figures 1.25a and 1.25b present cases of N = 3 cycles and N = 600 cycles. Obviously, achieving a final displacement between 0.5% D and 2% D, responses of the four non-failing tests can be classified as meta-stable.

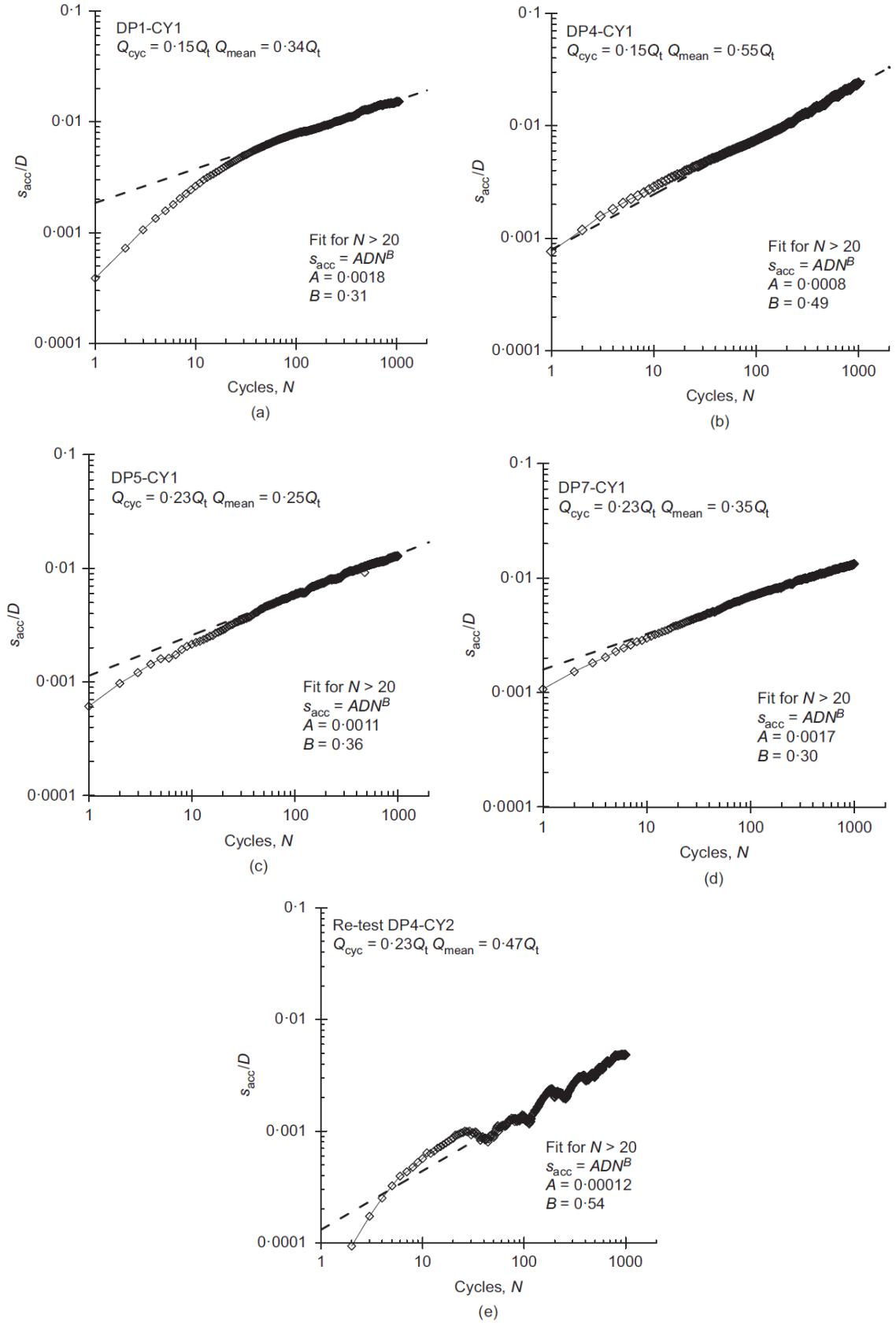


*Figure 1.23 : Permanent accumulated cyclic displacement normalised by pile diameter for un-failed tests, (Buckley et al. 2018b)*

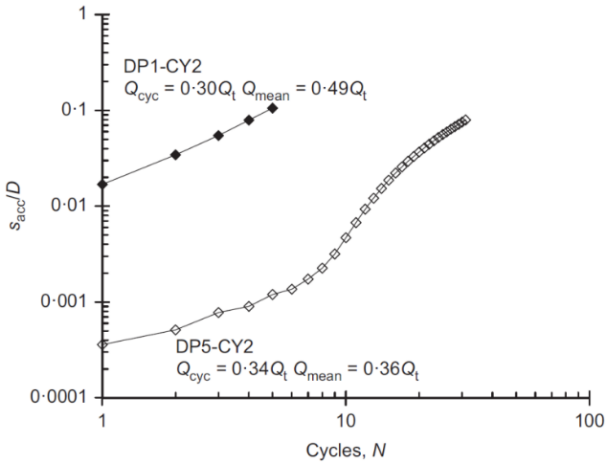


*Figure 1.24 : Permanent accumulated cyclic displacement normalised by pile diameter for failed tests, (Buckley et al. 2018b)*

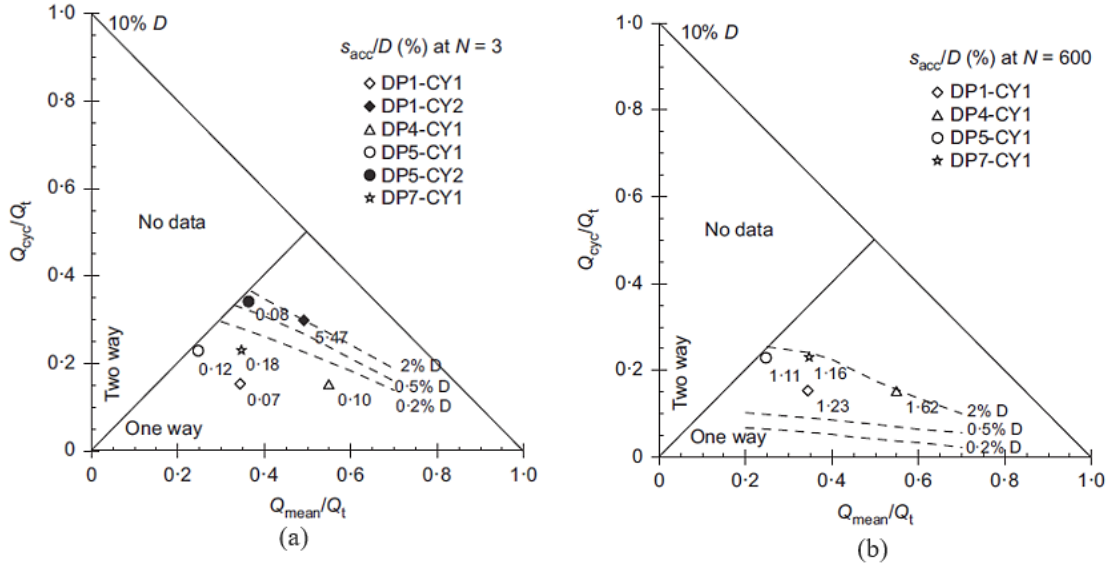


*Figure 1.25 : Cyclic interaction charts showing accumulated displacements (normalised by pile diameter) at: (a) N= 33; (b) N= 600, (Buckley et al. 2018b)*

Figure 1.26 illustrates the evolution of permanent pile head displacement according to number of cycles for ICP piles (Buckley et al. 2018a). These trends showed either metastable or unstable responses, considering that the maximum shaft loadings have reached 0.7-0.9 times the static tension failure loading. In general, these piles have not shown marked sensitivity to high-level one-way cyclic loading as has been detected in the cyclic tests on open-ended driven piles (Buckley et al. 2018b).

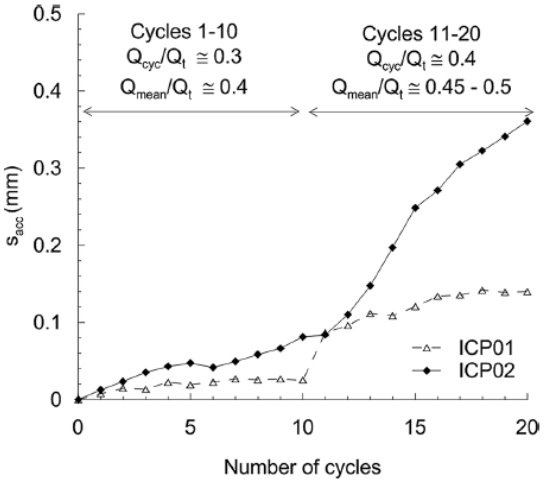


*Figure 1.26 : Evolution of permanent pile head displacement with number of cycles (Buckley et al. 2018a)*

The Offshore pile has also presented a similar evolution of accumulated permanent displacements where the rate of accumulation has increased by increasing the loading ratio (Buckley et al. 2020).

#### *1.3.3.3.2 Cyclic degradation of limit shaft resistance and base resistance*

Another effect of cycling loading is the degradation of shaft and base resistance of the pile. Several in-situ and laboratory tests have confirmed these phenomena either during pile testing in clay or in sand. As a result, bearing capacity of the pile and stiffness of the soil undergo a degradation leading to rupture over cycles. Poulos (1981) has realised cyclic tests on pile models installed in clay. Increasing pile bearing capacity degradation has been observed over cycles. In order to quantify the degree of limit shaft capacity degradation, Poulos (1981) defined a limit shaft capacity degradation factor, $D_\tau$, which is the ratio between limit shaft resistance after cyclic loading and limit shaft resistance before cyclic loading. Evolution of this factor in function of the amplitude of cyclic displacement is presented in figure 1.27. As it can be noticed, degradation factor increases with the numbers of cycles. According to Poulos (1982), the degradation of limit shaft resistance is due to the variation of interstitial pressure in the zone situated at the soil-pile interface, and rearrangement of grains and their deterioration as cycles progress.

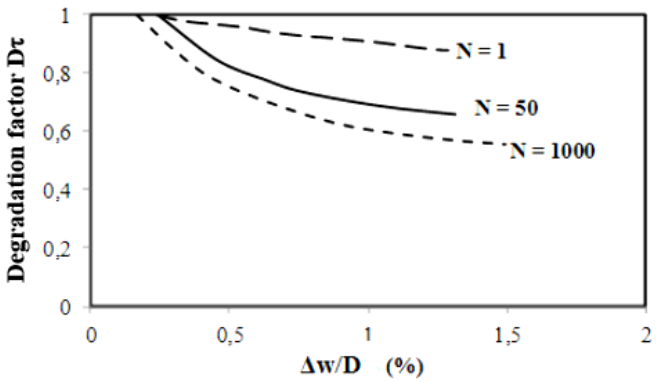


*Figure 1.27 : The limit shaft capacity degradation factor of model piles in clay, (Poulos 1981)*

Results of tests conducted on piles installed in loose sand have been reported by Puech (1982). A reduction in the radial stresses around the pile has been observed as the cycles continue. A compaction of soil around the pile may be the reason of such reduction according to Puech (1982). Loss in radial stresses contribute to a degradation in limit skin friction leading finally to rupture over cycles. This observation has been also reported by Poulos (1984) after conducting experiments on pile models in sand. A reduction in the volume of the soil-pile interface has been observed over cycles leading to loss in radial stresses and therefore in the limit skin friction throughout the pile shaft.

Occurrence of these phenomena is after all related to the type and level of imposed cyclic loading. Therefore, the pile can support a large number of cycles without failing under a low level of loading and especially under one-way cyclic loading where two-way cyclic loading has more negative and severe impact on pile response.

As for chalk, the effect of axial cyclic loading on the capacity degradation of pile has been reported by Buckley et al. (2018b) in function of the evolution of global cyclic secant stiffness during each cyclic test listed in table 1.8. Using the definition of loading and unloading terms of stiffness, $k_l$ and $k_u$, determined by Rimoy et al. (2013), Buckley et al. (2018b) have evaluated the secant stiffness evolution. Results of the four un-failed tests are presented in figure 1.28a. Values of loading stiffness were normalised by the first cycle value. Two of these tests showed an increase under continued cycling reaching about 35 % gains at N=1000 cycles. For the two others un-failed tests, it can be seen a decrease in the stiffness up to 200 cycles, followed by an increasing reaching almost 1.05 times the initial value at N=1000 cycles. Mentioning that the re-test DP4-CY2 completed 6 days after the first cyclic test DP4-CY1 and a following tension test to failure, showed a similar trend with a gentler degradation than the initial cyclic test of the same pile. Although the response of the four un-failed piles has been classified as meta-

stable regarding accumulated displacements, it should be classified as stable in terms of reaching 1000 cycles without experience failure or remarkable loss in operational tension capacity and stiffness. However, the re-test DP4-CY2 has been considered as stable regarding the two conditions.

Trends of the two failed tests, presented in figure 1.28b, showed a degradation of stiffness by over 60% prior to final failure. One of these tests failed with sudden stiffness loss after relatively few cycles, while the other conserved most of its initial stiffness until within approximately four cycles of final failure which occurred at 32 cycles.

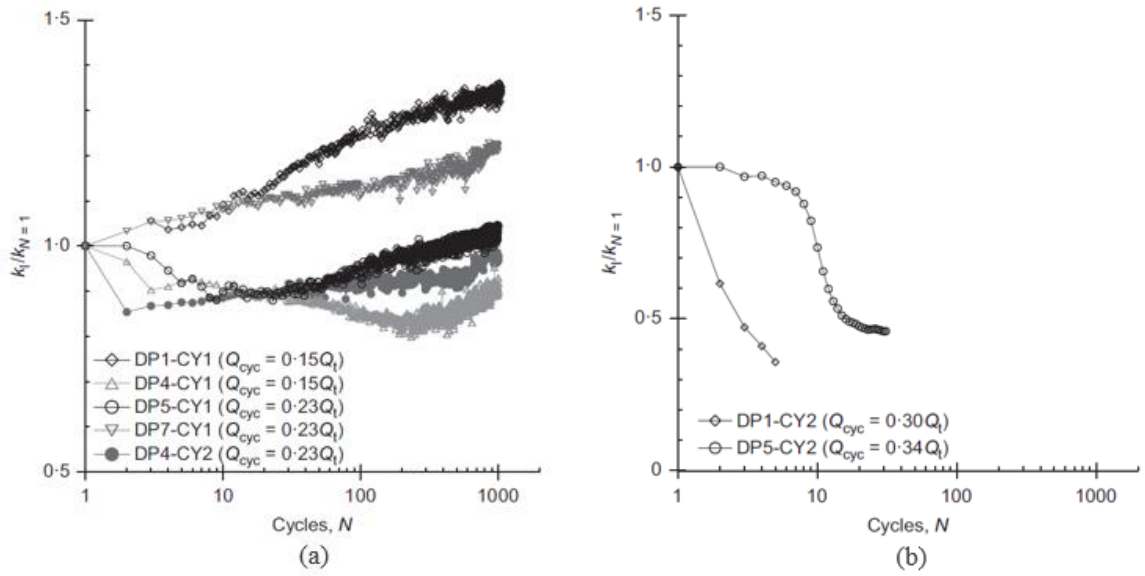


*Figure 1.28 : Global axial loading stiffness from tests on driven piles in chalk: (a) un-failed tests; (b) failed tests, (Buckley et al. 2018b)*

Subjected to high levels of two ten-cycle packets of one-way axial cyclic loading, the offshore pile has also experienced severe decreasing in its stiffness, especially in the second packet of ten cycles where the loading ratio has increased (Buckley et al. 2020). The second packet had led to stiffness degradation of about 25-35%.

These reported negative effects of axial cyclic loading, in terms of accumulated displacement and degradation of bearing capacity, are generally controlled by its level and its characteristics. Hence, under certain combinations of $Q_{mean}$ and $Q_{cyc}$, axial cyclic loading may be beneficial for the post cyclic pile response. Results of post cyclic tension tests performed on a number of tested piles by Buckley et al. (2018b) are summarised in table 1.9. Comparing to the static resistances, variation in pile capacity is related to its cyclic history. Although the cyclic failure generates very marked losses in the pile capacity (up to 43%), the un-failed tests exhibited slight variation in capacity with an increase of 5% in the case of stable test.

*Table 1.9 : Post cyclic results, (Buckley et al. 2018b)*

| Test code | One way axial cyclic loading | | Post cyclic axial tension loading | |
|---|---|---|---|---|
| | $Q_{max}$ kN | Class | $Q_{pc}$ kN | Capacity change % |
| DP1-CY1 | 103 | MS/S | - | - |
| DP1-CY2 | 164 | US | 117.6 | - 43 |
| DP4-CY1 | 145 | MS/S | 216.8 | + 5 |
| DP4-CY2 | 146 | S | - | - |
| DP5-CY1 | 99 | MS/S | - | - |
| DP5-CY2 | 146 | US | 158.4 | - 24 |
| DP7-CY1 | 120 | MS/S | 177.9 | - 14 |

Concerning the effect of axial cyclic loading on the base resistance of the pile, available data are limited. Generally, as the amplitude of cyclic loading at the base is very small, degradation of base resistance occurs at very high displacements and higher than admissible displacements. Thereby, one can neglect the negative effect of axial cycling loadings on base resistance of the pile.

## 1.4 Laboratory tests used to model axially loaded pile behaviour

Full-scale experimental tests of piles subjected to axial loading are considered relevant and give an efficient and reliable approach for assessing the ultimate bearing capacity of piles. Unfortunately, the cost of such experiments makes it rare and difficult to perform a sufficient number of tests. Therefore, laboratory experiments are considered an alternative method for imitating the behaviour of chalk-pile interface under axial loading in addition to the behaviour of surrounding chalk. Specific laboratory testing may then be introduced in order to replicate the state of the chalk-pile interface, whether considering remoulded chalk or intact chalk. Figure 1.29 presents how laboratory tests, simple shear and triaxial tests, can be used to simulate the behaviour of an axially loaded pile (Coyne et al. 2015).

These tests are necessary in order to obtain appropriate friction parameters for chalk-pile interface at relatively reliable normal stress levels capturing the levels encountered in the case of onshore and offshore applications, which are considered as low stress levels. Section 1.2.2.3 explains different responses of intact chalk under triaxial tests. It shows the strong dependence of confining pressure.

For intact chalk, Lord et al. ( 2002) marked that the effective cohesion c’ can range from 100 kPa to > 2 MPa with an effective friction angle φ’ varying between 36° and 42°. Turning to

remoulded chalk, c' ranges between 0 and 10 kPa with 29° < φ' < 42°. Undrained triaxial tests on "puttified" Wikinger chalk indicate c'= 0 and φ'≈ 31° (Buckley et al. 2020). Recent interface shear tests on remoulded chalk, under constant normal stress condition with different values of normal stress, indicated a chalk-steel interface friction angle equal to 25.6° and an apparent cohesion of 13 kPa (Kopf 2019).

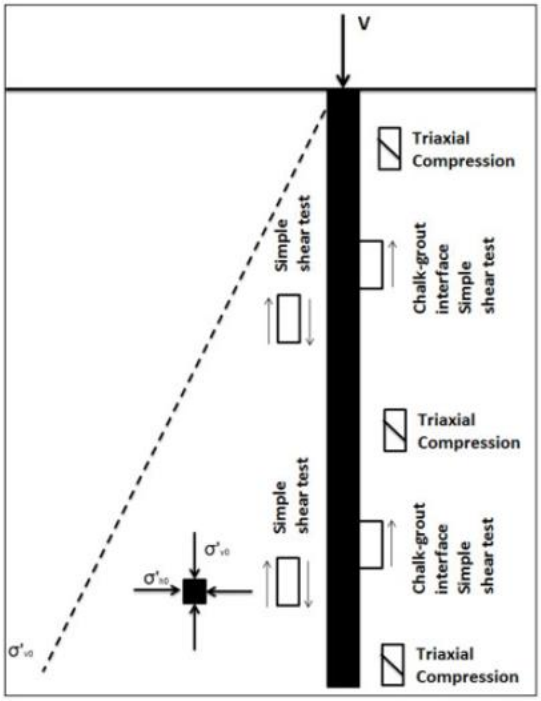


*Figure 1.29 : Illustration of how laboratory tests can model the behaviour of an axially loaded pile, (Coyne et al. 2015)*

It should be noted that, under cyclic loading, the soil behaves in a manner different from its behaviour under static loading. A decrease in the interstitial pressure in the soil, an accumulation of permanent displacements and a degradation of soil rigidity are the principal and important differences derived from cyclic loading (O'Reilly and Brown 1991).

## 1.4.1 Triaxial tests

In order to evaluate the behaviour of a weathered chalk, a series of monotonic triaxial tests under different confining pressures, representing the in-situ conditions, have been performed (Muhammed et al. 2018). Figure 1.30 presents these tests results in terms of the evolution of normalised deviator stress and excess pore pressure in function of external axial strain. Chalk specimens clearly show an initial contracting phase followed by a dilatant phase which is more or less pronounced depending on the sample type. The dilating behaviour of chalk leads, in some cases, to high deviator stress values since the shear resistance continues to increase with

the decrease in interstitial overpressure, traditionally observed in dilatant soils. In some cases, progressive stabilisation of the interstitial overpressure is observed at large deformations.

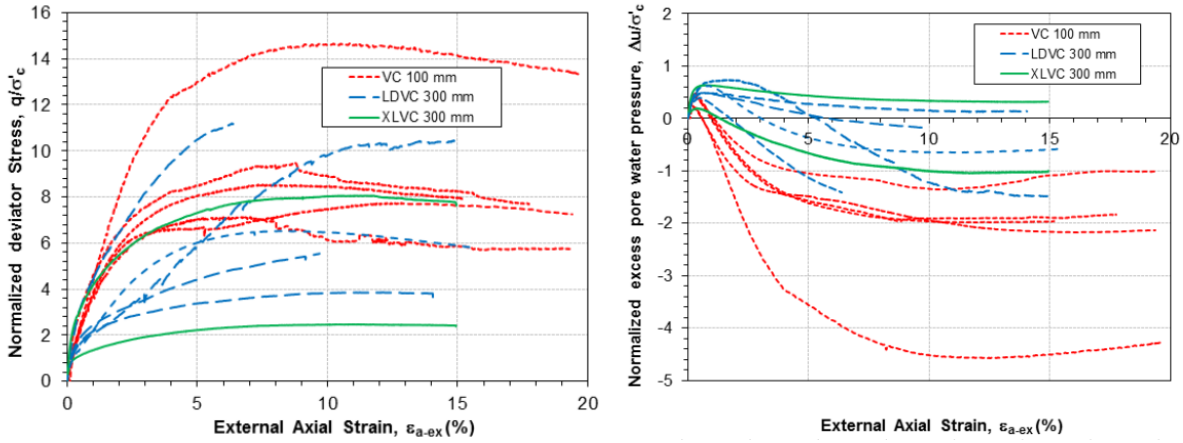


*Figure 1.30 : Results of triaxial tests on weathered chalk samples, (Muhammed et al. 2018)*

Consolidated undrained triaxial tests have been undertaken for assessing the role of chalk putty in the ageing process (Doughty et al. 2018). For this reason, chalk samples have been prepared according to a specific procedure to simulate the remoulded chalk found in the context of driven piles. A comparison has been made between test results considering un-aged sample and aged samples of different ageing time (7 and 14 days) and confining pressure. Figure 1.31 illustrates the deviator stress as a function of axial strain. It has been noticed that the aged tests exhibit a higher initial stiffness than the un-aged test, due to possible re-cementation occurred at the grain contacts. All aged samples present a dilation phase, depending on ageing time and confining pressure, after some initial contraction.

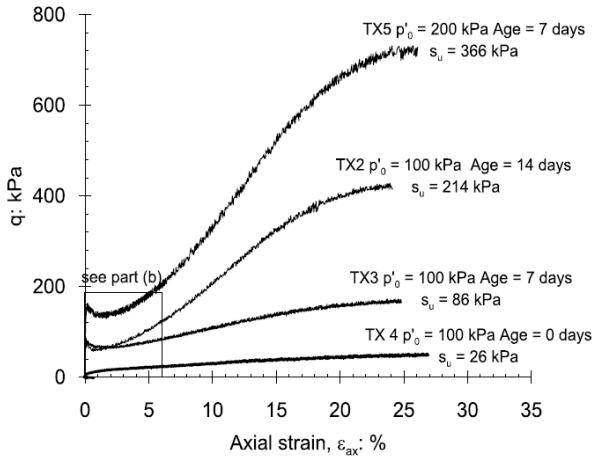


*Figure 1.31 : Stress-strain behaviour of aged and un-aged chalk samples, (Doughty et al. 2018)*

A laboratory programme, using non-destructive wave velocity propagation measurements, has been done to study the mechanical behaviour of reconstituted samples from crushed chalk (Bialowas et al. 2018). Time-dependent behaviour of fully saturated reconstituted chalk samples subjected to ageing periods up to 72, under different isotropic sustained stresses, has been investigated. Corresponding results have shown an increase in the shear stiffness with time. This increase appeared to be governed by secondary creep deformations.

Considering cyclic loading, Siwak (1994) listed the conditions under which chalk will undergo quick rupture under this type of loading:

- Low confining pressure;
- Low minimum cyclic stress;
- High amplitude of cyclic loading and maximum cyclic stress is close to its rupture value, i.e., static resistance.

In this case, rupture is a result of intense compaction. Accumulation of permanent displacements is accelerated during cycles. One phase can be observed with an exponential variation of irreversible axial and volumetric deformations in function of cycles until rupture figure 1.32a.

In all other cases, i.e., where rapid rupture cannot occur, behaviour of chalk under low confining pressure, in function of the number of cycles, is decomposed in 3 zones, similarly to the case of creep (figure 1.32b). In the first zone, permanent deformations rapidly reach 10 to 50% of the total irreversible deformation depending on the values of the confining pressure and applied stress. The volume variations are very small or even negligible compared to the total volume variation. There is probably a break in the intergranular connections that are the weakest energetically. In the second zone, the plastic deformations evolve at a constant rate. Chalk undergo hardening and contracting volumetric variations evolve slowly. Siwak (1994) stated that this phase appears as a transformation phase where the dissolution-recrystallization phenomena must play an important role. As for the third phase, reached after 1000 cycles for the Lezennes chalk, a variation in chalk behaviour is noticed: irreversible deformations and volume variations increase strongly, resulting in an intense compaction of the material.

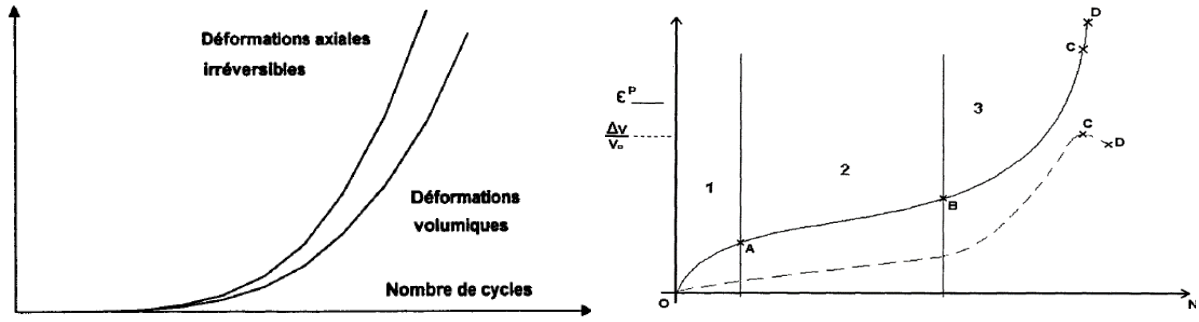


*Figure 1.32 : Variations of axial and volumetric plastic deformations in function of the number of cycles N: a) quick rupture, b) all other cases, (Siwak, 1994)*

Coyne et al. (2015) examined the cyclic behaviour of chalk strata encountered in the North Sea by a series of cyclic triaxial tests. During cyclic loading applied to chalk, a degradation of the intact strength can be noted. This degradation is highly dependent on the ratio of the cyclic loading to the static strength and the number of cycles. Under this type of loading, cementation between chalk particles may break down which results in a sudden decrease in resistance and stiffness. Hence, this breakdown leads to remoulding chalk with a lower permeability than intact chalk. Yet, excess pore water pressures may accumulate during cycling and therefore the effective strength will decrease. Low to medium density chalk tends to exhibit contraction behaviour under shear stresses (Lord et al. 2002). Therefore, Coyne et al. (2015) related reduction in effective strength of chalk, during cyclic loading, to its expected contraction under shearing. The principal observation during these tests conducted by Coyne et al. (2015) was the existence of a "Threshold limit" presenting a particular level of applied cyclic stress. When the applied cyclic loading is below this limit, chalk specimen does not undergo significant degradation or deterioration within the range of number of cycles considered, and therefore presents relatively stable response. Equation 1.18 presents the stability criterion suggested by Coyne et al. (2015), illustrating the "threshold limit", in function of the characteristics of the applied cyclic loading on chalk, i.e. the amplitude of cyclic loading $\tau_{cyc}$, the average cyclic loading $\tau_{avg}$, and the static shear resistance $\tau_{max\ static}$.

$$\tau_{cyc}/\tau_{max\,static} < 0.17 - \tau_{avg}/\tau_{max\,static} \quad (1.18)$$

Figure 1.33 illustrates the cyclic stability diagram issued from results of cyclic loading on chalk. Assuming that failure under axial loading of grouted pile in chalk will occur in the chalk mass, Coyne et al. (2015) assumed that this cyclic diagram of chalk to be generally representative of grouted pile response in chalk under cyclic axial loading. The "Threshold limit' of chalk seems

to be conservative and lower than thresholds limit of other materials, such as sand (Jardine et al. 2012) and clay (Poulos 1988), also presented in figure 1.33.

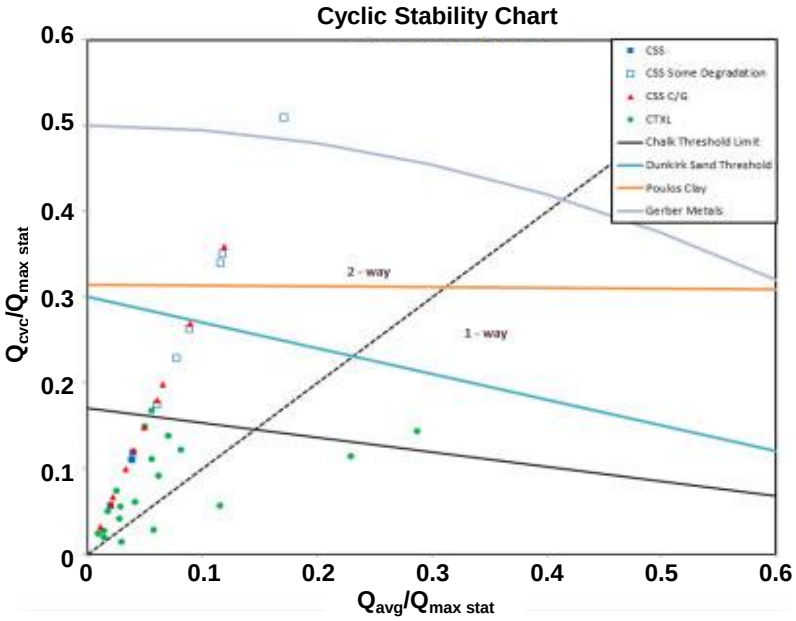


*Figure 1.33 : Cyclic stability diagram for chalk, (Coyne et al. 2015)*

Studying the cyclic hydromechanical behaviour of an altered marine chalk, Muhammed et al. (2018) have found, during a series of un-drained triaxial tests, that chalk progressively generates significant positive interstitial overpressures. However, under these undrained cyclic loadings, developed axial strains were relatively low except for high to very high values of cyclic deviator stress where important accumulation of axial strains may be developed (greater than 5 to 6%), without any observation of liquefaction phenomenon. Under same test conditions, the fact of ensuring dissipation of interstitial overpressure, by the mean of drainage between two cyclic sequences, resulted in less important increase in the rate of pore water pressure accumulation despite the increase in the applied cyclic stress (figure 1.34a). Hence, drainage may lead to chalk densification and amelioration of its resistance to cyclic loading. During two-way cyclic loadings, it was noticed that the increase in axial strain was more pronounced than in the case of one-way cyclic loadings.

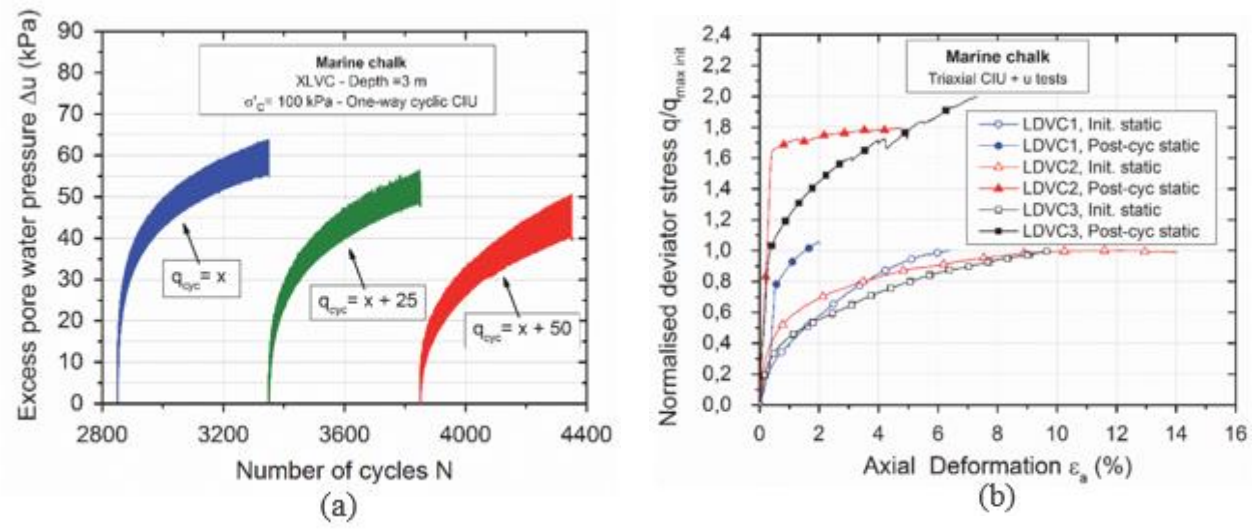


*Figure 1.34 : Results of cyclic and post-cyclic triaxial tests on weathered chalk: a) Evolution of excess pore water pressure during axial cyclic loading, b) Evolution of normalised deviatoric post-cyclic stress in function of axial deformations, (Muhammed et al. 2018)*

Considering the post-cyclic behaviour of the marine chalk, a series of post-cyclic static tests have also been conducted by Muhammed et al. (2018) on chalk specimens with final accumulated cyclic axial strains less than 7.5%. The complete dissipation of excess pore water pressure during cycles led to densification of the material. Hence, this densification resulted in an increase of the static undrained post-cyclic shear strength of chalk due to a dilatancy response of chalk. Thus, it may be concluded that the post-cyclic static response of chalk is more dilative and stiffer than the initial static response before cyclic loading (figure 1.34b). It should be noted that these observations of post-cyclic chalk response are strongly dependent on the characteristics of applied cyclic loading and number of cycles.

## 1.4.2 Shear tests

Motivated by the development of offshore and onshore windfarms, recent researches have been arisen in order to reproduce the behaviour of the chalk-pile interface, especially for the case of driven piles where annulus of remoulded chalk has been reported to appear around. For this aim, conventional shear tests have been widely performed to evaluate the behaviour of the interface. Considering that the intact chalk around the remoulded chalk zone has the possibility to relax in direction of the latter zone, a constant normal stiffness condition (CNS) is seen as most appropriate (Randolph and Gourvenec 2011). Nevertheless, intact chalk may represent a very high stiffness. Therefore, the relaxation of radial stresses around the remoulded zone may

be very significant. In this case, constant volume conditions (CV) are more suitable, as proposed by (Carrington et al. 2011).

Published data regarding monotonic and cyclic shear tests on chalk samples are considered very limited. A series of CNS direct shear tests on remoulded chalk has been done in order to calibrate a computer program named "RATZ" used to predict pile behaviour (Dührkop et al. 2015).

An investigation concerning the interface shearing behaviour of remoulded "puttified" chalk under constant normal stress conditions has been recently done (Chan et al. 2019). Direct shear and ring shear tests have been performed on low-to-medium density chalk samples, from the St. Nicholas-at-Wade research test site in Kent, UK, considering chalk-steel interfaces. A special attention has been made regarding the ageing process. These experiments showed that the interface shear strength of chalk tends to increase with time. Figure 1.35 shows the variation of sample height in function of shear displacement for an aged and an un-aged sample. It is clear that both tests presented dilation before contracting to ultimate conditions. Though, the aged interface established way less contraction under large tangential displacement.

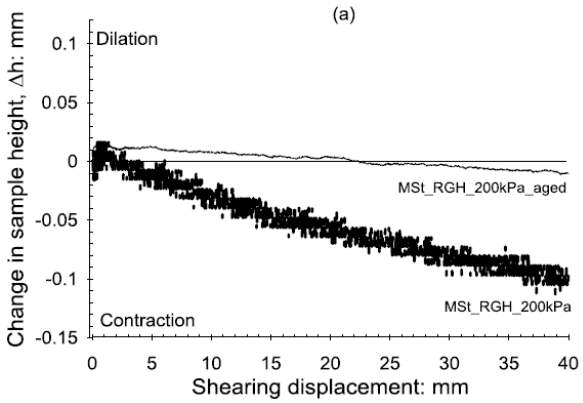


*Figure 1.35 : Comparison of change in sample height between aged and un-aged interface ring shear tests, (Chan et al. 2019)*

Similarly, the behaviour of remoulded chalk samples from British Channel, has been investigated on the basis of remoulded chalk-steel interface (Kopf 2019). A series of direct shear tests under constant normal stress (CNL) and constant normal stiffness of 200 kPa/mm (CNS) have been done. Without considering the effect of ageing, remoulded chalk samples showed a pure contractive behaviour until the ultimate state, which is more or less pronounced depending on initial normal stress. Figure 1.36 illustrates some of these test results presenting the effect of ageing on shearing mechanism for unsaturated samples. This figure shows that the aged sample tended to present a dilative behaviour, increasing with time, unlike the un-aged

sample which presented a pure contractive behaviour. Consequently, the interface shear strength showed an increasing tendency with ageing time. This reflects the importance of considering the ageing process while designing piles in chalk. Driven piles in chalk tend to develop higher bearing capacity with time.

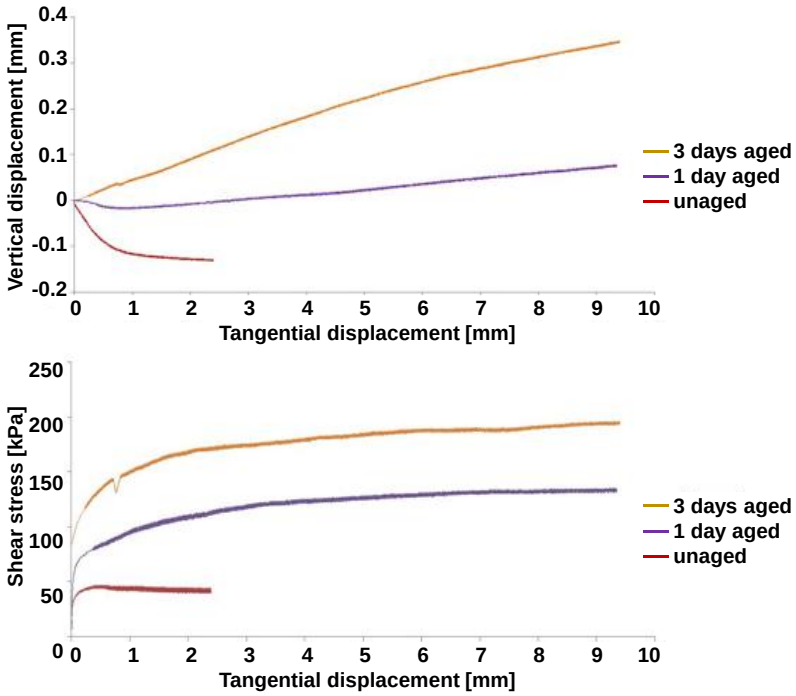


*Figure 1.36 : Results of direct shear tests under CNS conditions, $k_n$=200 kPa/mm, considering unaged and aged samples of remoulded chalk from British Channel: a) vertical displacement against tangential displacement, b) shear stress against tangential displacement, (Kopf 2019)*

Considering cyclic shear tests, performed experiments are extremely limited. In this field, a series of cyclic direct simple shear tests under constant volume conditions (CV) have been conducted (Carrington et al. 2011). The aim was to evaluate the effects of driven pile installation on the static shear strength of low to medium density chalk samples. Cyclic loading, in this case, has been employed in order to simulate the effects of pile driving. Figures 1.37a and 1.37b present an example of these tests results. It illustrates the variation of shear stress according to the number of cycles as well as the shear path. This test showed a strong degradation of shear stress and normal stress with cycles number. The mobilised shear stress rapidly decreases to a residual value and the minimum vertical effective stress tends toward zero. These cyclic tests have been followed by subsequent static shear tests to failure after 48 hours rest period. After losing approximately all the initial consolidation stress, one of the samples named (CS-1), has been reconsolidated to recover the vertical effective stress, prior the post-cyclic test. Figure 1.38 demonstrates the shear paths of different post-cyclic tests of chalk

samples that have not been reconsolidated along with the sample (CS-1), as well as the shear path of an initial static test. The reconsolidation process of the sample (CS-1) allowed it to fully dissipate the excess pore pressures generated during cyclic loading and re-alignment of the soil matrix. Therefore, as shown in figure 1.38, this sample behaved in a similar manner of the sample (DSS-1) only subjected to static shear test. An initial phase of contraction is followed by a dilation phase to a peak value. The non-reconsolidated samples showed a pure dilative behaviour after the 48 hours rest period.

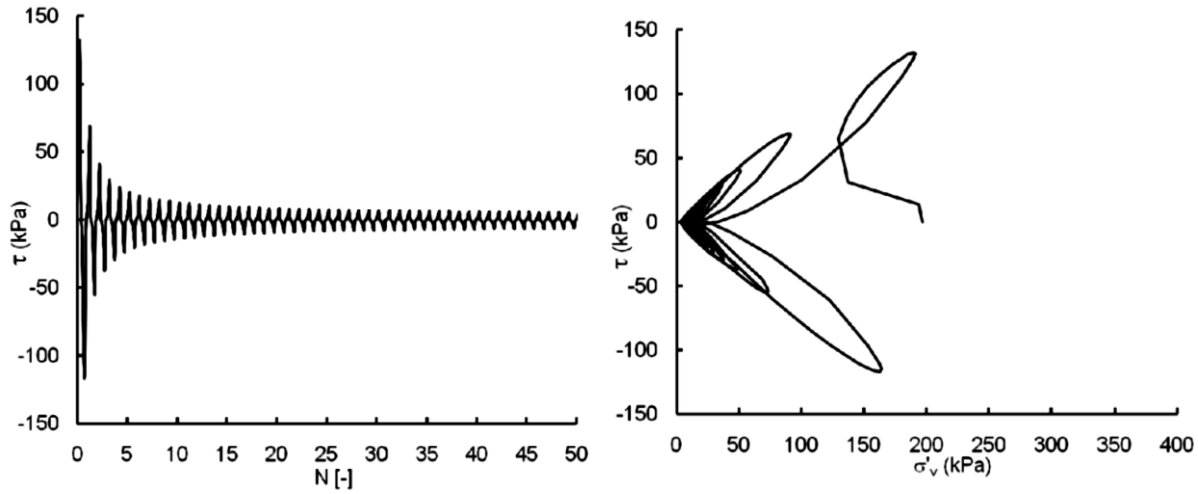


*Figure 1.37 : Results of cyclic direct shear test under constant volume condition: a) shear stress against number of cycles, b) stress path, (Carrington et al. 2011)*

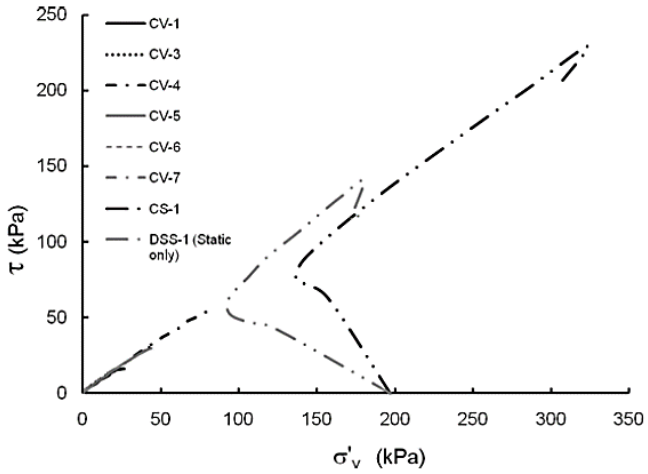


*Figure 1.38 : Comparison between stress paths of post-cyclic tests and a static test, (Carrington et al. 2011)*

The investigation of cyclic behaviour of chalk done by Coyne et al. (2015) included, in addition to cyclic triaxial tests, a series of simple shear tests on chalk-chalk and chalk-grout interfaces. The evaluation of cyclic shear strength degradation was demonstrated by an increase in shear

strain. Figures 1.39a and 1.39b present two different behaviours of the interface, degradation and no degradation in the cyclic strength, concluded by either the increase or the stabilisation in the shear strain. The appearance of one or other behaviour is related to the applied cylic loading which results in a stable or unstable response. The simple shear test results contributed also in the drawing of the stability diagram of chalk (see figure 1.33), and in the formulation of the "threshold limit" (equation 1.18).

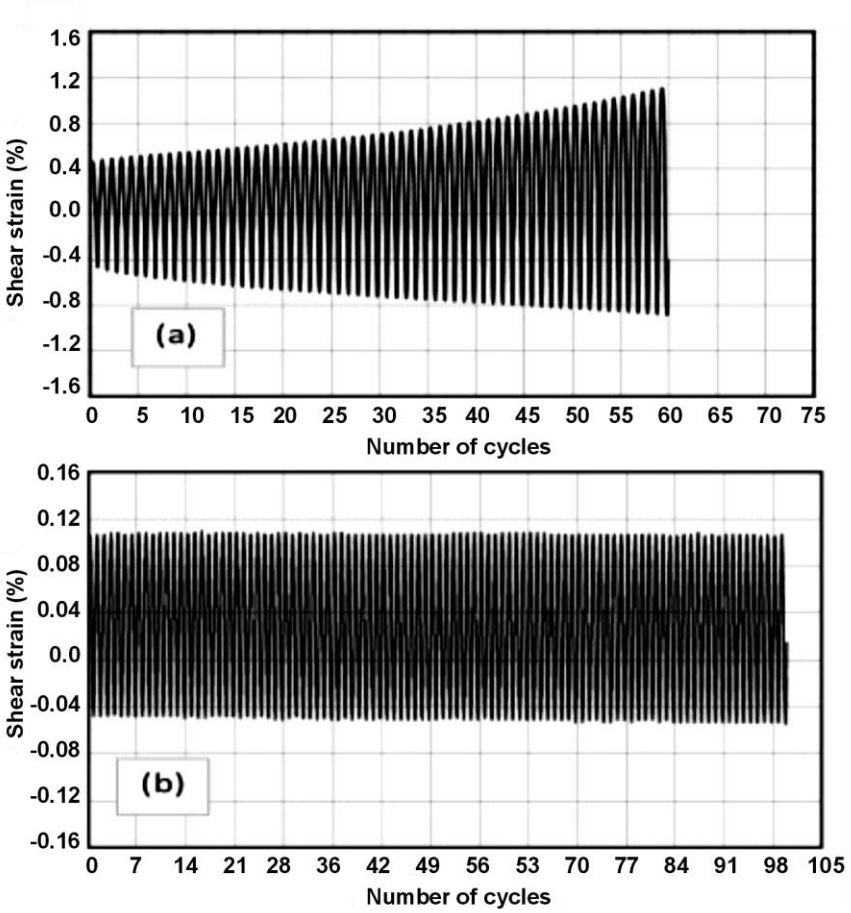


*Figure 1.39 : Results of cyclic simple shear tests: (a) strength degradation, (b) no strength degradation (Coyne et al. 2015)*

## 1.5 Conclusion

Chalk can be found under great parts of Northern Europe, and it is often encountered in geotechnical works operated in these areas. Recent development of onshore and offshore wind energy projects and other foundation projects in chalk rises the importance of a better knowledge and understanding of how foundations behave in this material. Known as a variable and unpredictable material, it has brought new challenges to the civil engineering industry.

The first part of this chapter allows to describe the **behaviour of chalk** under several solicitations. The influence of chalk porosity and water content on its mechanical behaviour is also investigated. Chalk can exhibit three different types of plastic yields depending on the mean stresses value to which it is exposed. A detailed description of how chalk would behave in each case is done. In addition to time independent behaviour, the deformations in chalk may also occur only because of time-dependent mechanisms that should be considered.

The second part of this chapter focuses on the study of **the behaviour of piles in chalk**. From an engineering point of view, we can find under the term chalk different materials. CIRIA C574 (Lord et al. 2002) summarises the properties of British chalks, and gives a detailed description of chalk and a classification for engineering purposes based on intact dry density and fabric grade. In general, chalks are defined as structureless class D chalk or structured chalks. Structured chalks are characterised by their density (low, medium, high, very high) and their grade (A, B, C) according to their fracturing state. French standard NF P94-262 (AFNOR 2012) classifies chalk into three categories, soft, weathered and sound, based only on results from Pressuremeter Test (PMT) or Cone Penetration Test (CPT). This variability of chalk results in a wide range of pile responses in this material. Hence, the second part of this chapter firstly allows to describe the response of piles subjected to monotonic axial loading and to present different methods adopted in the French national standard for the application of EUROCODE 7 (NF P 94-262) for the calculation of pile capacity in chalk.

**Effects of pile installation** techniques and time on the mobilised pile resistance is also investigated. Particularly, process of pile driving in chalk results in crushing and deterioration of chalk structures and produces low-strength, viscous material, identified as “putty chalk”, that spreads along the pile. This remoulded material severely causes a decrease in pile shaft resistance in the short-term after installation. Field evidence of ageing has been reported in the literature and results in pile shaft capacity increasing over time. However, this possible increase has not been considered in pile design recommendations in chalk. While large open-ended driven piles are used more frequently in offshore works, highly significant benefits may be taken if ageing trends are investigated and considered in chalk. For this purpose, recent onshore and offshore industrial-academic research projects have been developed (Jardine et al. 2018, Jardine, et al. 2019, Buckley et al. 2020, 2018a, 2018b).

Furthermore, this chapter gives a detailed description of **pile behaviour in chalk under axial cyclic loading**. Designing of piles under this type of solicitation requires an estimation of cyclic bearing capacity and accumulated displacements at the pile head. Considering the very limited database regarding the axial cyclic loading on piles in chalk, experiments conducted by Buckley

et al. (2018b) constitute the base for the description of different mechanisms encountered during one-way axial cyclic loading on piles in chalk. The paucity of experience that model the chalk behaviour at the scale of structure, especially the case of piles under cyclic loading, is considered a key issue in designing offshore wind turbine foundations.

Finally, the last part gives an overview of **laboratory tests** conducted on chalk samples, in order to recapitulate the possible response of chalk-pile interface under axial loading, and the response of the surrounding chalk as well. These laboratory experiments are considered as an alternative method to overcome the high cost of full-scale experimental tests. Triaxial and simple shear tests are the compatible experimental laboratory tests.

In the coming chapter, a comparison between the French and the English perspectives regarding pile design in chalk is presented. Results of this comparison are preceded by an overview of the English practice.

# Chapter 2
# Review of pile design approaches in chalk used in France and the UK: case studies from French sites

*This chapter was the subject of a journal article (Doghman et al. 2020)*

## 2.1 Introduction

Deep foundation projects developed in Northern Europe where chalk is found widespread (figure 2.1) raise some major issues for geotechnical engineering design. In particular, chalk covers most of the regions of the Paris Basin and the London Basin, where different philosophies are faced. Indeed, the assessment of pile capacity has been done according to different approaches, related to different ground investigation techniques.

Known as a complex and unconventional material, chalk presents important geotechnical challenges to engineers seeking to find the most accurate and efficient pile design. Specifically, the upcoming Offshore Windfarm projects that will take place on both the French and English sides of the English Channel and along the south-east coast of England rise the importance of assessing the reliability of common practices. Yet, there are almost no studies corresponding to the comparison of different methods used for pile design in chalk developed in France and the UK. Despite the publication of these diverse rules, a little practical guidance is available for driven piles design in chalk. The effect of pile driving on the pile capacity and the progressive evolution in time can certainly impact the foundation design of civil engineering projects.

The first chapter of this thesis gave an overview of the practices adopted in France for pile design in chalk according to the specifications of the French national standard NF P 94-262 (AFNOR 2012). Thereby, the UK perspective is reviewed in the beginning of this chapter where the recommendations of CIRIA C574 (Lord et al. 2002) are presented.

This chapter aims to compare the French and the English perspectives regarding pile design in chalk. The comparison is then based on the analysis of static pile load tests performed by the Laboratoire Central des Ponts et Chaussées (LCPC, now called IFSTTAR) at four sites located in the Paris Basin. Therefore, a detailed geotechnical description of each site is presented, followed by a comparison between measured and calculated values. It should be noted that these case histories have been part of the database used to derive the NF P 94-262 (AFNOR 2012) recommendations. Furthermore, a special attention is also paid to the ageing effect usually encountered in the case of driven piles in chalk. Capacity-ageing trends of driven piles found in the LCPC database are investigated.

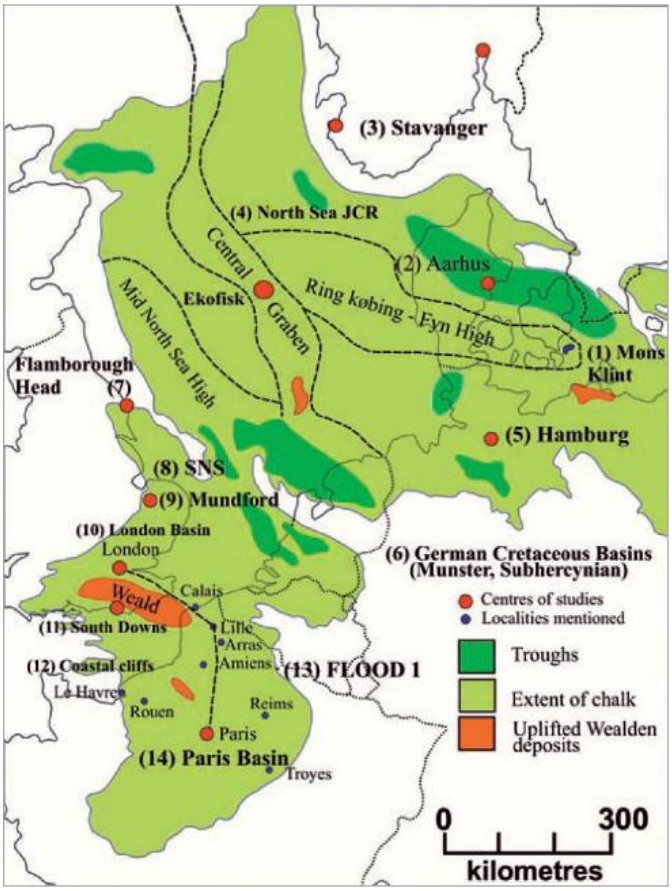


*Figure 2.1 : Presence of chalk in Northern Europe (Mortimore, 2012)*

## 2.2 UK perspective for pile design in chalk

CIRIA C574 (Lord et al. 2002) is considered as the official guide for pile design in chalk. Based on several case histories empirical relationships have been adopted for estimating the shaft resistance and base resistance of different pile types.

### 2.2.1 Shaft resistance

CIRIA C574 (Lord et al. 2002) recommendations give a distinction when the concrete is cast against chalk and when it is not, for shaft resistance assessment.

- In the first case (bored piles, continuous flight auger piles (CFA) and driven cast-in-place piles with concrete cast against chalk), calculation of shaft resistance in low to medium density chalk is done using a conventional earth pressure approach presented in equation 2.1.

$$\bar{\tau}_{sf} = k.\tan\delta' .\bar{\sigma}'_v = \beta.\bar{\sigma}'_v \quad (2.1)$$

Where, k is the coefficient of earth pressure, $\bar{\sigma}'_v$ the average vertical effective stress and $\delta'$ the effective angle of interface friction. Hence, the β effective stress approach is used for predicting

pile shaft resistance. The contribution from made ground and fill (engineered or not) should be omitted in determining $\overline{\sigma}'_v$, unless the pile capacity was proved otherwise by a pile test. The CIRIA C574 guidelines recommend a β value of 0.8 for conventional bored and driven cast in place piles, and 0.45 for CFA piles. These values of β are used with limitations regarding the value of the vertical effective stress: for bored piles $\overline{\sigma}'_v$ should be less than 400 kPa, for CFA piles it should be less than 200 kPa and for driven cast-in-place it should be less than 100 kPa. Otherwise, the ultimate shaft resistance for bored piles is limited to 320 kPa, for CFA piles to 100 kPa and for driven cast-in-place to 80 kPa.

After collaboration between CIRIA and the FPS (Federation of Piling specialists), β value for CFA piles has been updated. FPS (2013) recommends a new procedure for assessing β value, as follows:

- Where medium density chalk is present over the whole shaft, i.e., $N_{SPT} > 10$ or $q_c > 4$ MN/m$^2$, β value of 0.80 is allowed to be taken in the design.
- Where chalk cannot be demonstrated as a medium density chalk over all the pile shaft, i.e., $N_{SPT} < 10$ or $q_c \leq 4$ MN/m$^2$, the effective stress pile friction coefficient β in the case of poor-quality chalk should be taken as 0.45 throughout.

$N_{SPT}$ is the number of SPT blow counts and $q_c$ the cone resistance.

In high-density grade A chalk, pile should be treated as a rock socketed pile.

- In the second case (mainly driven performed piles where concrete is not cast against chalk) two types of piles are considered: small displacement piles such as H-piles, open-ended steel and box piles, and large displacement piles such as precast concrete piles, closed-ended steel tubes and boxes.

Recommendations of CIRIA C574 (Lord et al. 2002) regarding these types of piles are based on a limited database (figure 2.2). There is no apparent relationship in the dataset between average shaft resistance and average vertical effective stress. Hence, the average effective stress method is replaced with fixed shaft resistance values, varying only with chalk density. In the case of small displacement piles, the CIRIA C574 (Lord et al. 2002) guidelines recommend taking ultimate shaft resistance of 120 kPa for high density chalk and 20 kPa in all other densities and grades. The latter value is reduced to 10 kPa when the pile may experience whipping during driving, for example, flexible H-pile. For large displacement piles, these limits range from 30 to 50 kPa.

The limited database related to the recommendations of CIRIA C574 (Lord et al. 2002) for the case of driven piles and their possible economic impact on engineering projects have led to the

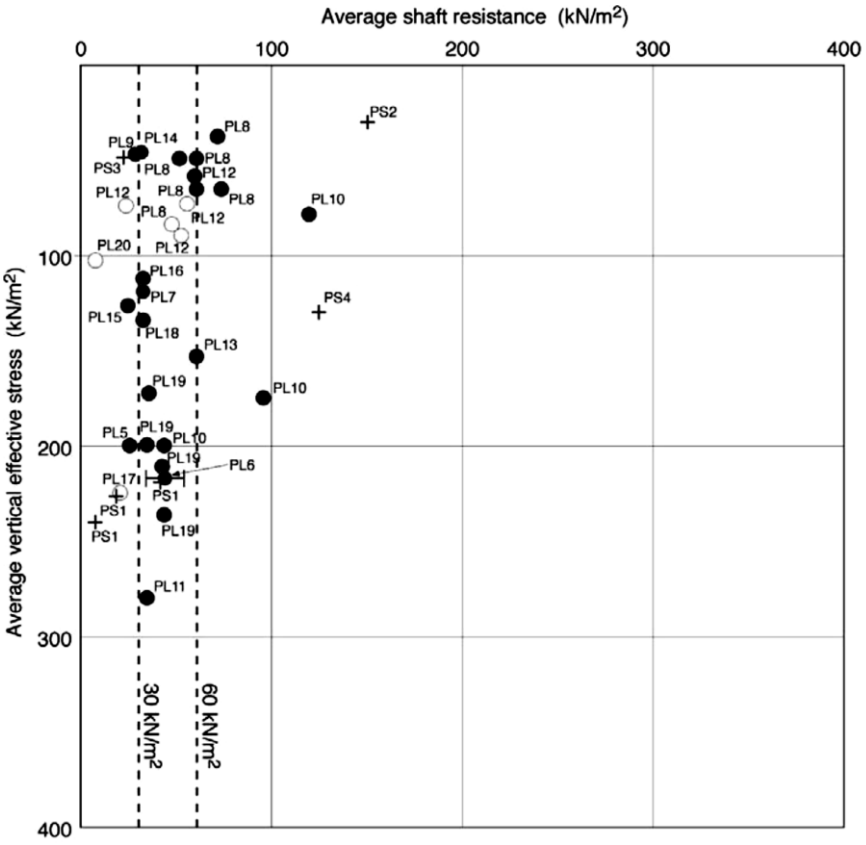


*Figure 2.2 : Average shaft resistance versus average vertical effective stress in chalk for driven pre-formed piles (Lord et al. 2002)*

development of "Chalk ICP-18", a new predictive method (Jardine et al. 2018, Buckley et al. 2020). This effective stress-based approach was developed for the assessment of driven pile resistance in low to medium density chalk following the ICP-05 approach (Jardine et al. 2005) for driven piles in sands and clays. Long-term limit shaft resistance of driven piles in chalk is expressed according to the equation 2.2 following the Coulomb criterion:

$$\tau_f = \sigma'_{rf}\, tan(\delta') \tag{2.2}$$

Where, $\sigma'_{rf}$ is the shaft radial effective stress at failure which is the sum of the local radial effective stress developed after installation, $\sigma'_{rc}$, and the dilatant increase that may appear during loading, $\Delta\sigma'_{rd}$, as it is shown in equation 2.3. $\delta'$is the interface shear angle.

$$\sigma'_{rf} = \sigma'_{rc} + \Delta\sigma'_{rd} \tag{2.3}$$

The initial radial effective stress $\sigma'_{rc}$ is calculated according to equation 2.4. It depends on total CPT cone resistance, $q_t$, and relative tip depth h/R$^*$ where $R^* = (R^2_{outer} - R^2_{inner})^{0.5}$ which is the pile equivalent solid radius and $R_{outer}$ and $R_{inner}$ are the pile's outer and inner radii.

$$\sigma'_{rc} = 0.081 q_t \left(\frac{h}{R^*}\right)^{-0.52} \quad (2.4)$$

The dilatant component of the effective radial stress is determined according to equation 2.5 where G is the shear modulus, Δr is the average radial movement caused by dilation at the interface and D is the pile diameter. A value of 0.5 μm is recommended in the "Chalk ICP-18" for the Δr term (Buckley et al. 2018a).

$$\Delta\sigma'_{rd} = \frac{4G\Delta r}{D} \quad (2.5)$$

The development of the "Chalk ICP-18" method was done to simulate the field behaviour in Wikinger and St Nicholas-at-Wade sites where predictive results gave a good representation of the shaft resistance of driven piles experimented in these sites (Jardine et al. 2018, Buckley et al. 2020). Corresponding researchers imply the necessity to consider this approach as a preliminary proposal which may need further updating.

### 2.2.2 Base resistance

Regarding the ultimate base resistance, its assessment is related to the number of SPT blow counts. CIRIA C574 (Lord et al. 2002) recommends the followings ultimate base resistances to be adopted for different pile types:

- Bored piles: $q_u = 200 * N_{SPT}$ (kN/m²)
- CFA piles: $q_u = 200 * N_{SPT}$ (kN/m²)
- Driven cast-in-place piles: $q_u = 250 * N_{SPT}$ (kN/m²)
- Driven pre-formed piles: $q_u = 300 * N_{SPT}$ (kN/m²)

## 2.3 Case studies

### 2.3.1 Locations

The case studies of our back-analysis are based on full-scale pile load tests which were performed over the last fifty years on chalk from the Paris Basin by the LCPC. Four sites were chosen from the French database that are compatible with the objective of the comparison. Geological contexts are characterised by the presence of chalk as bearing layer for deep foundations. Fleury-sur-Andelle, Cambrai, Viaduct of Scardon and Montereau-Fault-Yonne are the corresponding sites. Locations are given in figure 2.3.


*Figure 2.3 : Location of case studies*

These sites were the subject of several geotechnical site investigations (Bustamante et al. 1980, Bustamante and Gianeselli 1995, LCPC 2004, IFSTTAR 2015). In-situ tests -PMTs and CPTs -were performed in all the four sites. SPT test results were available for Fleury-sur-Andelle, Scardon and Cambrai sites, but not for Montereau-Fault-Yonne site. In the following, a detailed geological and geotechnical description of different study sites is presented. Chalk categories mentioned in the following description of ground conditions for each case, i.e., soft, weathered and sound are taken from the corresponding classification indicated in each reference.

## 2.3.2 Geological context and geotechnical characteristics

### *2.3.2.1 Fleury-sur-Andelle*

Ground conditions comprise clay and gravel over soft chalk encountered at depths between 3 m and 9.5 m underlain by weathered chalk (Bustamante et al. 1980). Despite the difficulty in obtaining intact chalk specimen for laboratory testing, core sampling has been done in order to determine some mechanical properties of chalk. Figure 2.4 presents the variations of total and dry density with depth. According to CIRIA C574 (Lord et al. 2002) chalk classification, the encountered soft chalk corresponds to structureless chalk (assumed Grade $D_m/D_c$). The weathered chalk, with an average dry density value of about 14 kN/m$^3$, corresponds to low density structured chalk of unknown grade.

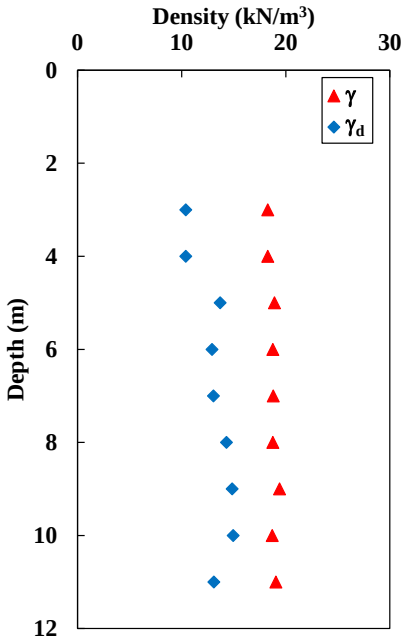


*Figure 2.4 : Variation of total density, γ, and dry density, $\gamma_d$, according to depth, Fleury-sur-Andelle*

The test area was the subject of a specific ground investigation, including Pressuremeter, Penetrometer and Standard Penetration tests. Results, in terms of net limit pressure, cone resistance and SPT N blow counts, are illustrated in figure 2.5.

The average net limit pressure of the soft chalk is about 0.7 MPa. Its average cone resistance value is 4.1 MPa. The weathered chalk has an average net limit pressure of about 1.23 MPa, and an average cone resistance value of 10.5 MPa. These values are compatible with the chalk classification according to French practices (AFNOR 2012) that define the following ranges: $p_l^* < 0.7$ MPa for soft chalk and $0.7 < p_l^* < 3$ MPa for weathered chalk and $q_c < 5$ MPa for soft chalk and $5 < q_c < 15$ for weathered chalk. The average value of SPT N blow counts in chalk layers is of about 14.

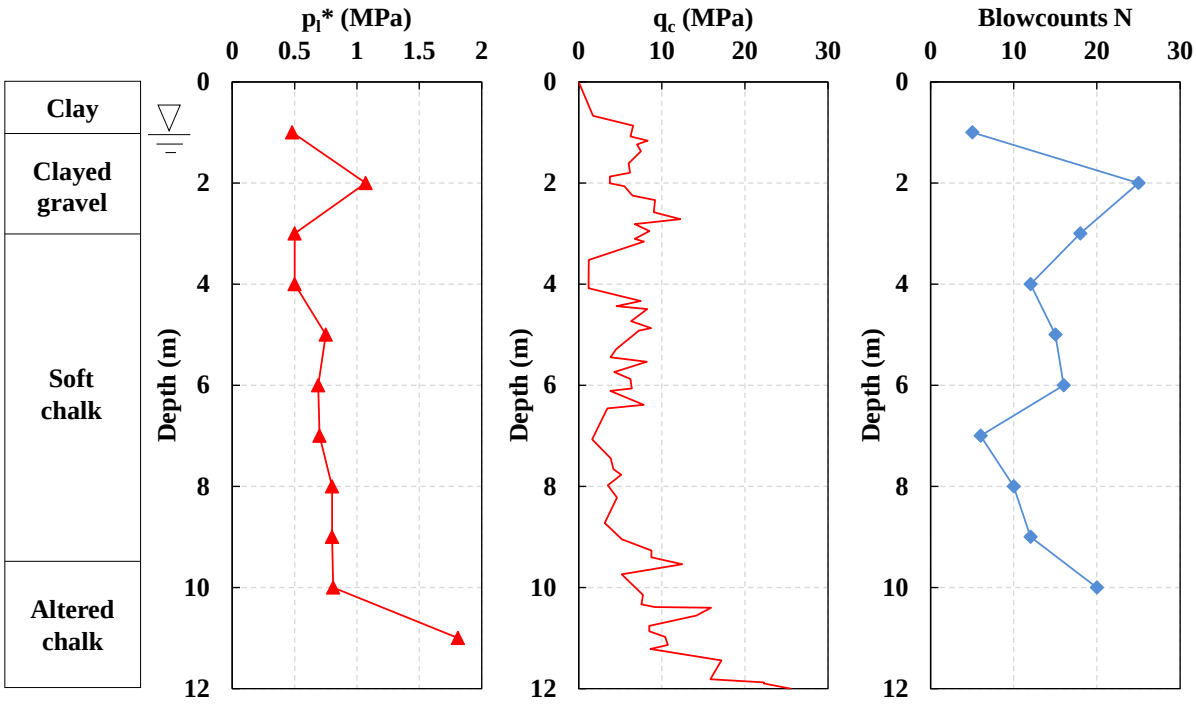


*Figure 2.5 : Profiles of net limit pressure, cone resistance and SPT N blowcounts at the site of Fleury-sur-Andelle, after (Bustamante et al. 1980)*

### *2.3.2.2 Viaduct of Scardon*

As a part of the work on the Scardon viaduct near Abbeville, Somme, LCPC has carried out a series of full-scale pile load tests in weathered chalk. At the bottom of the valley, ground conditions comprise peaty silt over soft chalk encountered at depths between 6.5 m and 11 m underlain by weathered chalk (Bustamante and Gianeselli 1995). Table 2.1 presents average values of total and dry density of different ground type. Soft chalk (in French classification) corresponds to structureless chalk according to CIRIA C574 (Lord et al. 2002). Regarding the average value of dry density, weathered chalk can be classified as low-density structured chalk of unknown grade.

*Table 2.1 : Values of total density and dry density for different ground types at the site of Scardon*

| **Ground type** | **Total density (γ) (kN/m³)** | **Dry density ($\gamma_d$) (kN/m³)** |
|---|---|---|
| **Peaty silt** | 13.80 | 10.40 |
| **Chalk** | 18.88 | 14.75 |

Soils along the road of the viaduct have been the subject of a series of ground investigations. They include Pressuremeter, Penetrometer and Standard Penetration tests. The PMT, CPT and

SPT profiles are shown in figure 2.6. The chalk formation, from 6.5 m and below, is characterised by net limit pressure values that increase from 0.3 to 4 MPa with an average value of about 2 MPa. The soft chalk has an average net limit pressure of about 0.66 MPa, while the weathered chalk is characterised by an average value of 2.5 MPa. These values lie in the range of net limit pressure for soft and weathered chalks according to NF P 94-262 (AFNOR 2012). Analysing the CPT profile shows that the soft chalk has an average cone resistance value of 4.35 MPa and the weathered chalk a value of 4.42 MPa. This latter value is slightly below the lower bound of NF P 94-262 (AFNOR 2012) classification that indicates a lower bound of 5 MPa for weathered chalk. The CPT test at Fleury-sur-Andelle site presents higher values of the cone resistance with a maximum value of about 26 MPa, while the CPT test at Scardon site does not present values higher than 10 MPa. However, the net limit pressure values and the SPT blow counts reached in Fleury-sur-Andelle are lower than those reached in Scardon. Indeed, this shows that chalk encountered at Fleury-sur-Andelle is weaker than the one at Scardon site. These observations show the sensibility of Cone Penetration test in chalk. Profiles of the cone resistance obtained in chalk present sharp and numerous peaks which clearly reflect the heterogeneity of the material (presence of flint) (Bustamante et al. 1980).

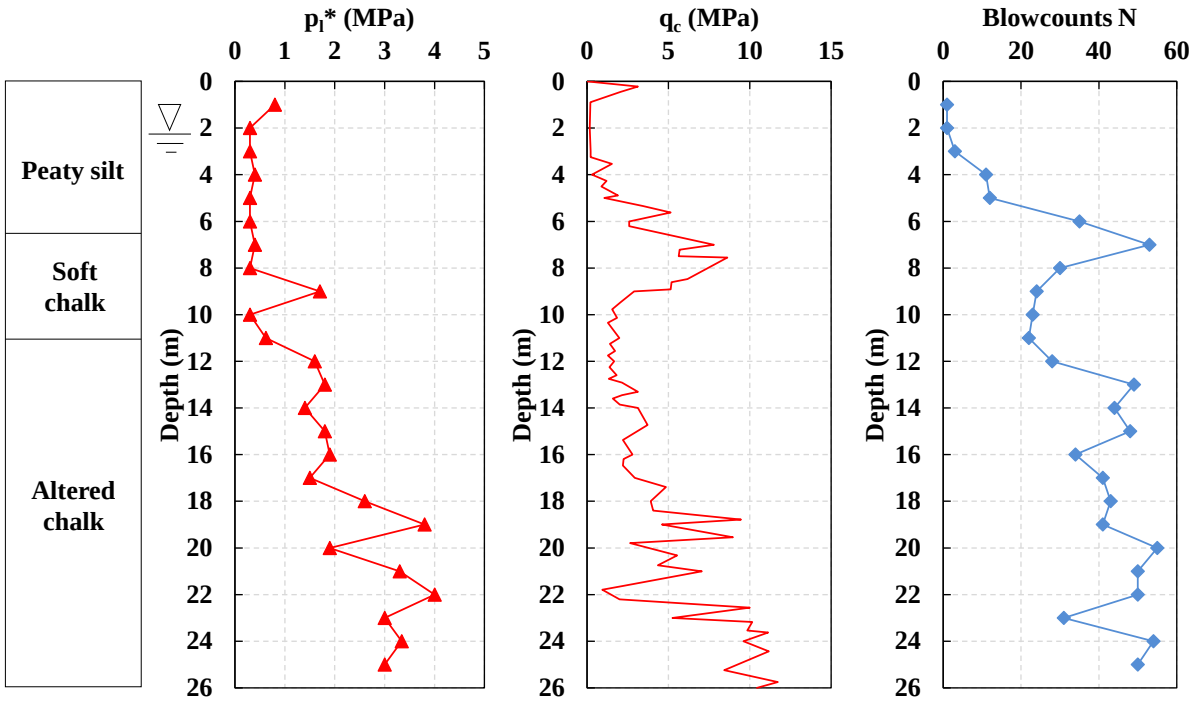


*Figure 2.6 : Profiles of net limit pressure, cone resistance and SPT N blowcounts at the site of Scardon, after (Bustamante and Gianeselli 1995)*

### *2.3.2.3 Cambrai*

This site corresponds to the construction project of the Cambrai wastewater treatment plant. It offers the possibility to study the behaviour of piles placed in Senonian Chalk. The geological profile shows the following sequence of layers (LCPC 2004):

- 0 to 5 m: silt;
- 5 to 9.5 m: flint clay, sand and gravel;
- over 9.5 m: weathered chalk.

Unfortunately, there were no site density data available for Cambrai. Considering the chalk as low-density chalk, and reading through values defined in previous cases, total density and dry density of 19 kN/m$^3$ and 14 kN/m$^3$ have been assumed.

PMT, CPT and SPT tests in the test area show the trends summarised in figure 2.7. Chalk layer presents an average net limit pressure of about 2.3 MPa, with $0.6 < p_l^* < 4.09$ MPa range. These values fall approximately in the same range as that of Scardon site. The maximum cone resistance value is around 65 MPa, while the minimum value is 2 MPa, recording an average of approximately 19 MPa. According to the French standard (AFNOR 2012), these values locate the encountered chalk in the group of weathered chalk, regarding the average value of net limit pressure, but in the range of sound chalk, regarding the average cone resistance value. In chalk layer, the Cone Penetration test refusal is systematically obtained. It can be associated with the presence of flint bands in chalk, which result in sharp local peak in CPT profile. This may explain the respectively high values of the cone resistance in the chalk formation comparing to other case studies. The average SPT N blow counts value is equal to approximately 19, where values fall between 11 and 27. The SPT N blow count values have the same range as those of Fleury-sur-Andelle site.

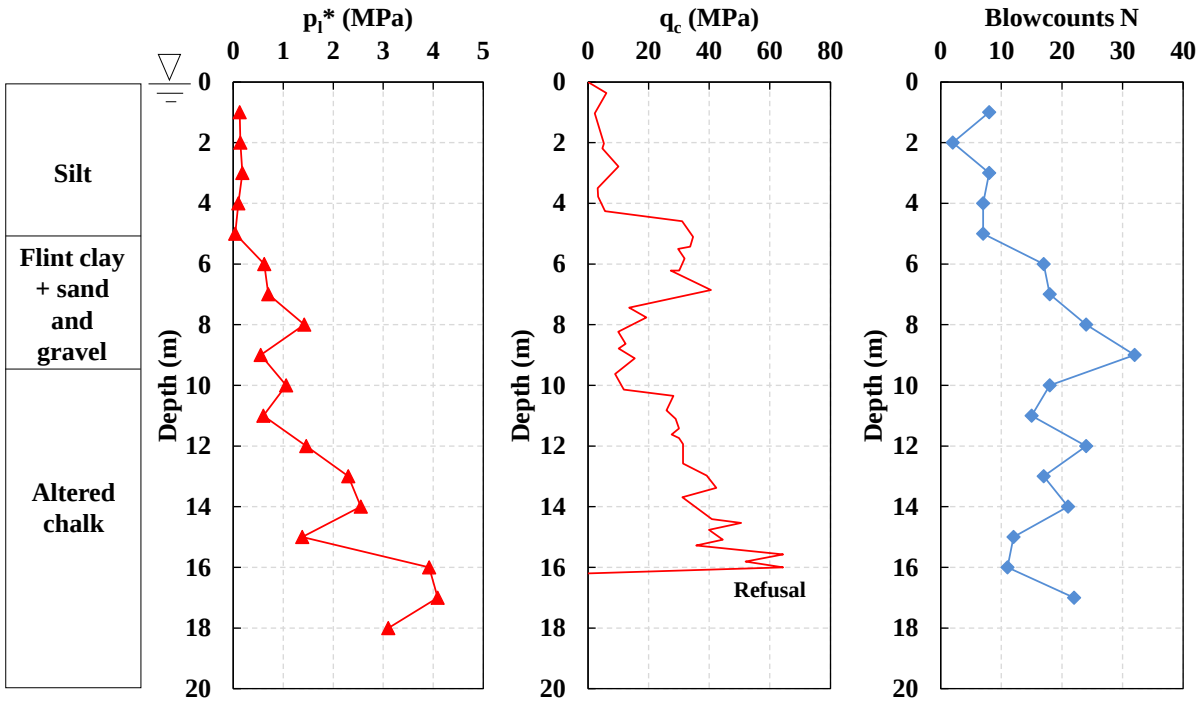


*Figure 2.7 : Profiles of net limit pressure, cone resistance and SPT N blowcounts at the site of Cambrai, after (LCPC 2004)*

### *2.3.2.4 Montereau-Fault-Yonne*

The site used for pile load tests is located on the right bank of the Yonne just before the confluence with the Seine. A thickness of 7 to 8 m of alluvium made up of clayey and sandy passages covers a thick layer of chalk that is first weathered and then more compact in depth. Geological profile consists of the following succession of layers:

- 0 to 1 m: Sand alluvium at the surface;
- 1 to 3.5 m: Clay alluvium;
- 3.5 to 7.5 m: Sand and gravel;
- 7.5 to 15 m: weathered chalk;
- Over 15 m: sound more compact chalk.

Total density and dry density of 19 kN/m$^3$ and 14 kN/m$^3$ have been assumed, regarding the lack of measurements related to these parameters.

Results of PMT and CPT tests are presented in figure 2.8. The net limit pressure of weathered chalk is about 1.16 MPa on average, with values ranging from 0.59 to 2.05 MPa. Whereas the sound chalk layer is characterised by an average net limit pressure of 3.65 MPa with a maximum value of 5 MPa. CPT test results present an average cone resistance value of about 2 MPa for weathered chalk and 9.4 for sound chalk. The maximum value reached by the cone resistance is around 26 MPa. Values of cone resistance are relatively low regarding the limits defined by

NF P 94-262 (AFNOR 2012) for chalk classification. Sound chalk means that it is not weathered, this is related to its dry density which is rarely determined in France due to the lack of samples, therefore it is not surprising to have such discrepancies even in previous sites.

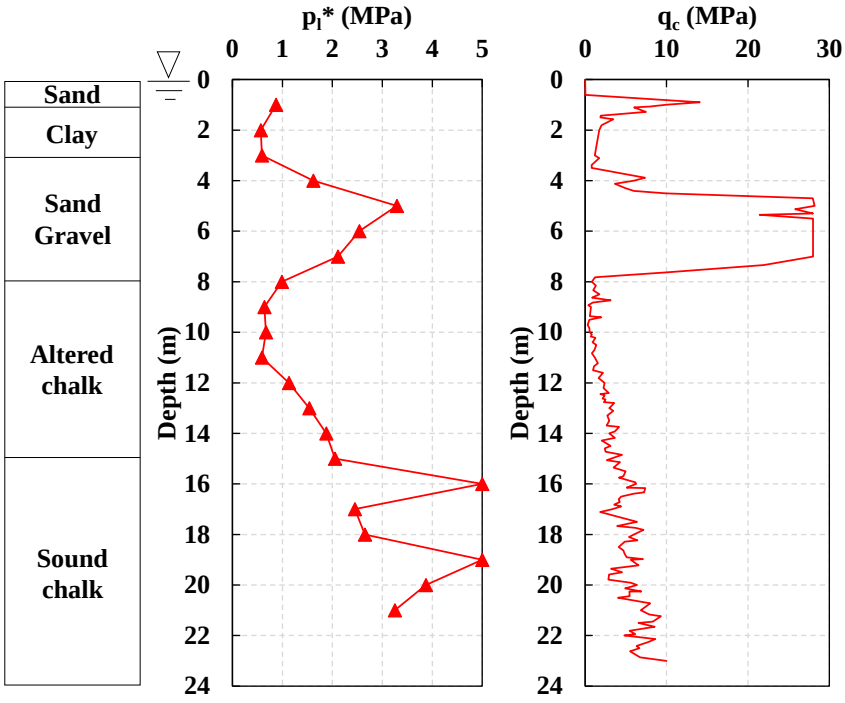


*Figure 2.8 : Profiles of net limit pressure and cone resistance at the site of Montereau-Fault-Yonne, after (IFSTTAR 2015)*

## 2.3.3 Presentation of Piles

### *2.3.3.1 Pile characteristics*

The full-scale load tests performed at different study sites by the LCPC are compressive-incremental load tests, the load being maintained for a duration of one hour at each load level. They were carried out at different times during the past fifty years. Experimental piles are of different types, but most are driven piles in chalk bearing layer. Table 2.2 summarizes the different types of piles and their corresponding geometry parameters.

Tests carried out on piles at Fleury-sur-Andelle site have been performed in the years of 1976 and 1977. Six full scale pile load tests were conducted on square pre-cast concrete pile between March 1976 and January 1977. These compressive loading tests were performed at different periods ranging from 86 days to approximately one year after driving. Similarly, a closed-ended cylindrical steel pile was subjected to three compressive loading tests between March 1976 and November 1977, at periods ranging from 86 days to 693 days after driving. A driven H-pile was also subjected to four compressive loading tests between March 1976 and June 1977 at

different periods ranging from 86 days to 546 days after driving. These aspects, related to ageing effect, are discussed in detail in the last part of this chapter.

The experimental closed-ended cylindrical steel pile of Scardon viaduct site, was tested on September 1995, i.e. 12-days after driving. Likewise, after 12-day rest period, H pile was tested on October 1995.

The screw pile used in Cambrai site, was tested on May 2004, after it was placed on February 2004.

The screw pile experimented in Montereau site was tested on 2015.

*Table 2.2 : Piles characteristics*

| Site | Pile | Section dimensions (cm) | Total length (m) | Penetration in chalk (m) |
|---|---|---|---|---|
| **Fleury-sur-Andelle** | Closed-ended square pre-cast concrete pile | 40 × 40 | 10.2 | 7.2 |
| | Closed-ended cylindrical steel pile | ϕ 44.5 | 10.2 | 7.2 |
| | Driven H-pile | h=33<br>b=36 | 10.2 | 7.2 |
| **Scardon** | Closed-ended cylindrical steel pile | ϕ 50.8 | 21 | 15 |
| | Driven grouted H-pile 310×79 | h=29.9<br>b=30.6<br>Base frame 40×40×3 | 21 | 15 |
| **Cambrai** | Screw pile | ϕ 36 | 14 | 4.5 |
| **Montereau-Fault-Yonne** | Screw pile | ϕ 62 | 16.6 | 9.1 |

### *2.3.3.2 Calculation parameters*

Empirical parameters defined in section 1.3.2.2 in addition to the net limit pressure, $p_l^*$ , and cone resistance, $q_c$, values extracted from in-situ test profiles presented in section 2.3.2 are used for the calculation according to the French approaches. Parameters needed for pile resistance assessment according to UK approach are presented in figure 2.9 and tables 2.3 to 2.6. Figure 2.9 illustrates the variation of the vertical effective stress, according to depth, needed for shaft resistance calculation for different sites. Considering the UK approach, calculations related to ground conditions other than chalk are done according to the recommendations of British Standard BS 8004:2015 (BSI 2015). “Chalk ICP-18” approach mentioned in section 2.2.1 will

not be examined in the present chapter because of the lack parameters needed for the calculation. No site-specific data regarding the shear modulus G, or the interface shear angle δ' were available for all the case studies used for comparison. However, it was important to list this recent design approach as one of the chapter objectives is to review the practices adopted in France and the UK for pile design in chalk.

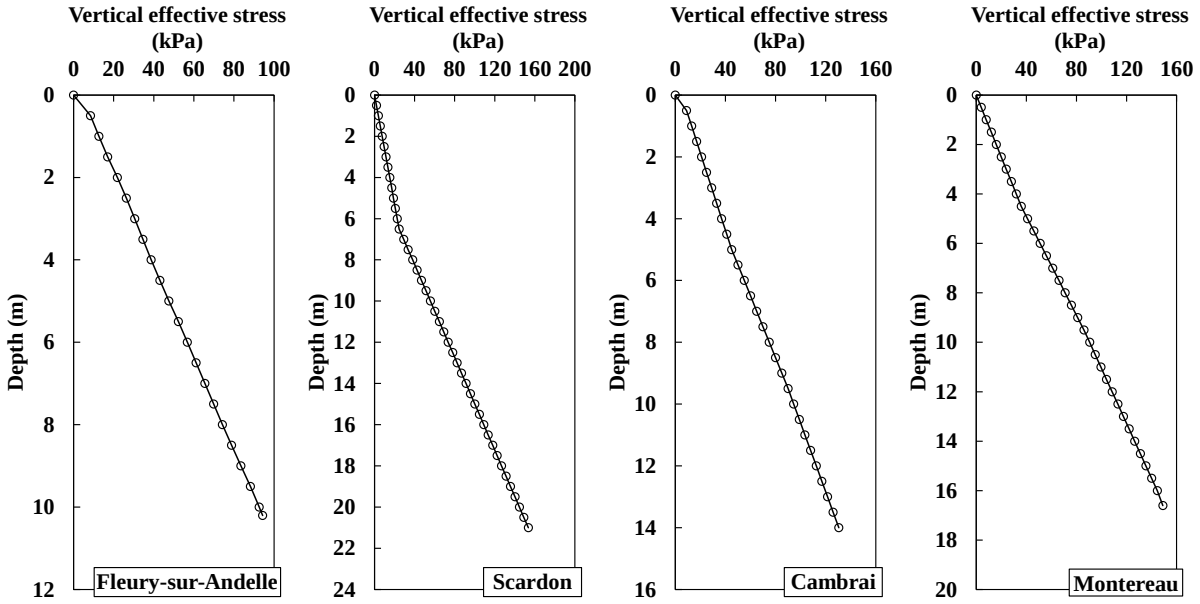


*Figure 2.9 : Evolution of in-situ vertical effective stress according to depth*

The majority of experimental piles described in section 2.3.3.1 are driven piles, except those placed in Cambrai and Montereau sites that are screw piles. Three of the five driven piles are defined as large displacement piles (the pre-cast concrete pile and the closed-ended cylindrical steel pile in Fleury-sur-Andelle and the closed-ended cylindrical steel pile in Scardon), while the driven H-pile in Fleury and the driven grouted H-pile in Scardon are considered as small displacement piles, according to CIRIA C574 (Lord et al. 2002). This classification limited the shaft resistance in chalk to 30 kPa for large displacement piles, and to 20 kPa for small displacement pile for the encountered type of chalk. For the driven H-pile the 20 kPa limit is reduced to 10 kPa according to CIRIA C574 (Lord et al. 2002) recommendations. No reference is indicated for the case of driven grouted H-pile in CIRIA C574 (Lord et al. 2002), hence the limit value for the shaft resistance for this pile is considered equal to 20 kPa instead of 10 kPa given that the grouting improves the pile capacity. For screw piles in Cambrai and Montereau, the value of β used for the calculation of shaft resistance is equal to the corresponding value of bored piles (i.e., 0.8).

*Table 2.3 : Calculation parameters for piles in Fleury-sur-Andelle*

| **Fleury-sur-Andelle** *(All piles)* | | | |
|---|---|---|---|
| **Ground** | $\delta'$ | $k$ | $\beta = k*\tan\delta'$ |
| **Clay** | 20° | 0.66 | 0.24 |
| **Clayed gravel** | 30° | 1 | 0.6 |
| **Chalk** | - | - | - |
| **Chalk base 10.2 m** | $N_{SPT}$ | - Closed-ended square pre-cast concrete and cylindrical steel piles: $q_b=300*N_{SPT}$<br>- H-pile: $q_b=250*N_{SPT}$ | |
| | 22 | | |

*Table 2.4 : Calculation parameters for piles in Scardon*

| **Scardon** *(All piles)* | | | |
|---|---|---|---|
| **Ground** | $\delta'$ | $k$ | $\beta=k*\tan\delta'$ |
| **Peaty silt** | 20° | 0.66 | 0.24 |
| **chalk** | - | - | - |
| **Chalk base 21 m** | $N_{SPT}$ | - Cylindrical steel pile: $q_b=300*N_{SPT}$<br>- Grouted H-pile: $q_b=250*N_{SPT}$ | |
| | 50 | | |

*Table 2.5 : Calculation parameters for pile in Cambrai*

| **Cambrai** *(screw pile)* | | | |
|---|---|---|---|
| **Ground** | $\delta'$ | $k$ | $\beta=k*\tan\delta'$ |
| **Silt** | 20° | 0.66 | 0.24 |
| **Clay, sand and gravel** | 30° | 0.7 | 0.4 |
| **chalk** | - | - | 0.8 |
| **Chalk base 14 m** | $N_{SPT}$ | $q_b=200*N_{SPT}$ | |
| | 21 | | |

*Table 2.6 : Calculation parameters for pile in Montereau*

| **Montereau** *(screw pile)* | | | |
|---|---|---|---|
| **Ground** | $\delta'$ | $k$ | $\beta=k*\tan\delta'$ |
| **Sandy-silty Alluvium** | 20° | 0.66 | 0.24 |
| **Clay complex with peaty passages** | 20° | 0.66 | 0.24 |
| **Sandy-gravelly complex with Clayey passages** | 30° | 0.7 | 0.4 |
| **chalk** | - | - | 0.8 |

## 2.4 Results

The study carried out makes it possible to compare ultimate measured to ultimate calculated pile capacity for different experimental pile types and different sites. Each pile was instrumented with removable extensometers, which made it possible to measure the mobilisation of the shaft friction along the pile length and the base resistance during loading stages. Experimental results have been analysed to obtain the ultimate pile capacity. Obtained values are presented in table 2.7. For sake of simplicity, each pile will be defined by a nomenclature code referring to the first letter of its corresponding site, after that its type will be defined. For example, the precast concrete pile in Fleury-sur-Andelle site will be named by F-Precast concrete. Total ultimate pile capacity, $R_c$, given in table 2.7, is decomposed into shaft resistance, $R_s$, and base resistance, $R_b$.

*Table 2.7 : Pile load tests results*

| **Pile** | **Total resistance** | | |
|---|---|---|---|
| | **$R_s$ (kN)** | **$R_b$ (kN)** | **$R_c$ (kN)** |
| **F-Precast concrete** | 825 | 285 | 1110 |
| **F-Closed ended steel** | 379 | 321 | 700 |
| **F-H** | 500 | 360 | 860 |
| **S-Closed ended steel** | 675 | 1525 | 2200 |
| **S-Grouted H** | 3365 | 2023 | 5388 |
| **C-Screw** | 1551 | 1571 | 3122 |
| **M-Screw** | 4500 | 1000 | 5500 |

Table 2.8 summarises all calculation values, in terms of shaft, base and total pile capacity, according to French and UK approaches. As one of the main goals of our work is to assess pile capacity in chalk, estimated amount of shaft resistance, received from soils other than chalk, will be deducted from total values. In the following, shaft and base resistance will be analysed separately. SPT test had not been conducted at Montereau site. It will be excluded from the comparison of the base resistance.

*Table 2.8 : Calculation results*

| Pile | French standard | | | | | | English standard | | |
|---|---|---|---|---|---|---|---|---|---|
| | PMT | | | CPT | | | CIRIA | | |
| | $R_s$ kN) | $R_b$ (kN) | $R_c$ (kN) | $R_s$ (kN) | $R_b$ (kN) | $R_c$ (kN) | $R_s$ (kN) | $R_b$ (kN) | $R_c$ (kN) |
| **F-Precast concrete** | 761 | 553 | 1314 | 631 | 552 | 1183 | 397 | 1056 | 1453 |
| **F-Closed ended steel** | 356 | 537 | 894 | 346 | 537 | 882 | 347 | 1026 | 1374 |
| **F-H** | 331 | 303 | 634 | 308 | 359 | 667 | 144 | 653 | 797 |
| **S-Closed ended steel** | 854 | 1632 | 2486 | 415 | 273 | 687 | 727 | 3040 | 3768 |
| **S-Grouted H** | 4427 | 952 | 5379 | 1927 | 188 | 2140 | 497 | 2000 | 2497 |
| **C-Screw** | 1128 | 504 | 1632 | 999 | 980 | 1979 | 639 | 428 | 1066 |
| **M-Screw** | 3586 | 2226 | 5812 | 2032 | 613 | 2645 | 1742 | - | - |

## 2.4.1 Shaft resistance

### *2.4.1.1 Statistical analysis of results*

Experimental and calculated values of ultimate shaft resistance in chalk, are presented in table 2.9. In order to estimate the uncertainty related to calculation approaches in chalk, the ratio $R_{s,c}/R_{s,m}$ is calculated for each pile and presented in table 2.10 and in figure 2.10.Three sets of results are shown, related to French (PMT and CPT) and UK (CIRIA C574) approaches for all the piles adopted for the study.

It can be noticed that the majority of ratios are less than 1. This indicates that most of the calculations underestimate the shaft capacity available to the experimental piles.

*Table 2.9 : Values of shaft resistance in chalk*

| Pile | Shaft resistance of chalk layer, $R_{schalk}$ (kN) | | | |
|---|---|---|---|---|
| | PMT | CPT | CIRIA | In-situ |
| **F-Precast concrete** | 530 | 343 | 346 | 428 |
| **F-Closed ended steel** | 185 | 133 | 302 | 321 |
| **F-H** | 183 | 131 | 99 | 490 |
| **S-Closed ended steel** | 609 | 280 | 694 | 571 |
| **S-Grouted H** | 3 664 | 1 543 | 464 | 3 115 |
| **C-Screw** | 576 | 353 | 458 | 769 |
| **M-Screw** | 1 947 | 581 | 1 574 | 1 296 |

*Table 2.10 : $R_{s,c}/R_{s,m}$ ratios*

| Pile | $R_{s,c}/R_{s,m}$ | | |
|---|---|---|---|
| | PMT | CPT | CIRIA |
| **F-Precast concrete** | 1.24 | 0.80 | 0.81 |
| **F-Closed ended steel** | 0.58 | 0.42 | 0.94 |
| **F-H** | 0.37 | 0.27 | 0.20 |
| **S-Closed ended steel** | 1.07 | 0.49 | 1.22 |
| **S-Grouted H** | 1.18 | 0.50 | 0.15 |
| **C-Screw** | 0.75 | 0.46 | 0.60 |
| **M-Screw** | 1.50 | 0.45 | 1.21 |

Figure 2.10 shows the following results: the PMT method tends to overpredict the pile shaft capacity in chalk with a maximum ratio equal to 1.5. The CPT method tends to underestimate the measured values with a maxim ratio of 0.8, while other ratios fall between 0.27 and 0.5. The CIRIA method tends to underestimate the pile shaft capacity with a maximum ratio of 1.22 and a minimum ratio equal to 0.15 showing a large scatter.

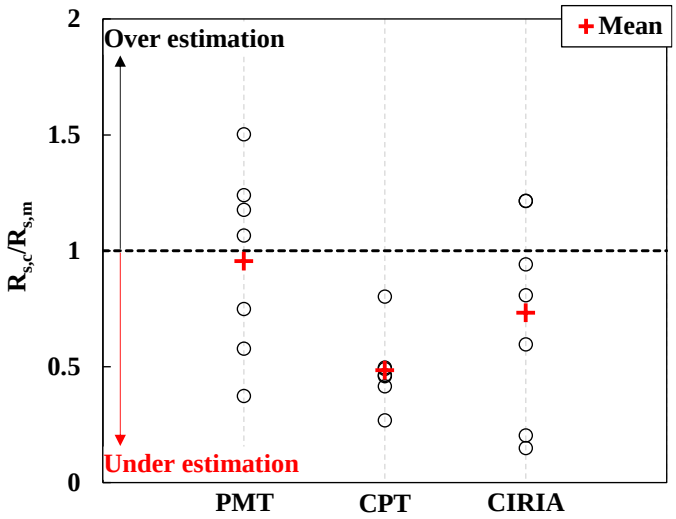


*Figure 2.10 : Graphical representation of $R_{s,c}/R_{s,m}$ ratios*

Table 2.11 presents the statistical data of the ratio $R_{s,c}/R_{s,m}$ for all piles and according to different approaches.

The mean value of the PMT method series is equal to 0.95 and the value of the standard deviation is 0.37 which shows that this method gives the best representation of measured values with low scatter. In a way, these results should be expected as already mentioned in the introduction the calibration of the PMT method rules is partially based on the dataset extracted from French case histories presented in this work. The CPT method series has the lowest

standard deviation value equal to 0.15 presenting the lowest scatter amongst the three methods. However, its mean value equal to 0.48 is very low which shows that the CPT method could not estimate with a minimum of certainty the shaft capacity in chalk. The mean value of The CIRIA method series is equal to 0.73 and the standard deviation value is equal to 0.41 which shows that this method gives a better estimation than the CPT method with relatively higher scatter.

*Table 2.11 : Statistical analysis of piles shaft resistance according to calculation approaches*

| | **PMT** | **CPT** | **CIRIA** |
|---|---|---|---|
| **Mean** | 0.95 | 0.48 | 0.73 |
| **Standard deviation** | 0.37 | 0.15 | 0.41 |
| **Median** | 1.07 | 0.46 | 0.81 |

### *2.4.1.2 Profiles of unit shaft friction*

Figures 2.11, 2.12, 2.13 and 2.14 present the variation of unit shaft friction, $q_s$, along the pile length. These profiles show the trends of different assessments done according to the three calculation methods.

Experimental values, at Fleury-sur-Andelle, present a variability, especially when the driven pile penetrates the weathered chalk layer (figure 2.11). The lower part of the shaft develops a higher resistance below 9.5 m (i.e., in structured chalk layer) for all piles. Calculations for the square precast concrete pile show that the CPT and CIRIA methods produce good estimates above the depth z = 9.5 m that presents the limit between the soft and weathered chalk layers, while the PMT method gives slightly higher values. All three design methods significantly underestimate the unit shaft friction in weathered chalk, where chalk is more resistant. Figure 2.11 shows that for the closed-ended cylindrical steel pile all the design methods present a good estimation of the unit shaft friction in soft chalk (above the depth 9.5 m), but below this depth the calculation results are overconservative similarly to the case of square precast concrete pile. However, the three calculation methods underestimate the unit shaft friction in chalk formation regarding the driven H-pile especially in the weathered chalk layer where the pile develops a high shaft resistance.

These observations can be related to the phenomenon of friction fatigue. The successive loading-unloading cycles regarding pile driving led to a decrease in limit shaft resistance. In general, the increase of limit shaft resistance with increasing the depth towards the pile base, for all driven piles tested at Fleury-sur-Andelle, reflect the effect of friction fatigue phenomenon

which reduces the limit shaft resistance mobilised at a given depth as the distance to the pile base increased.

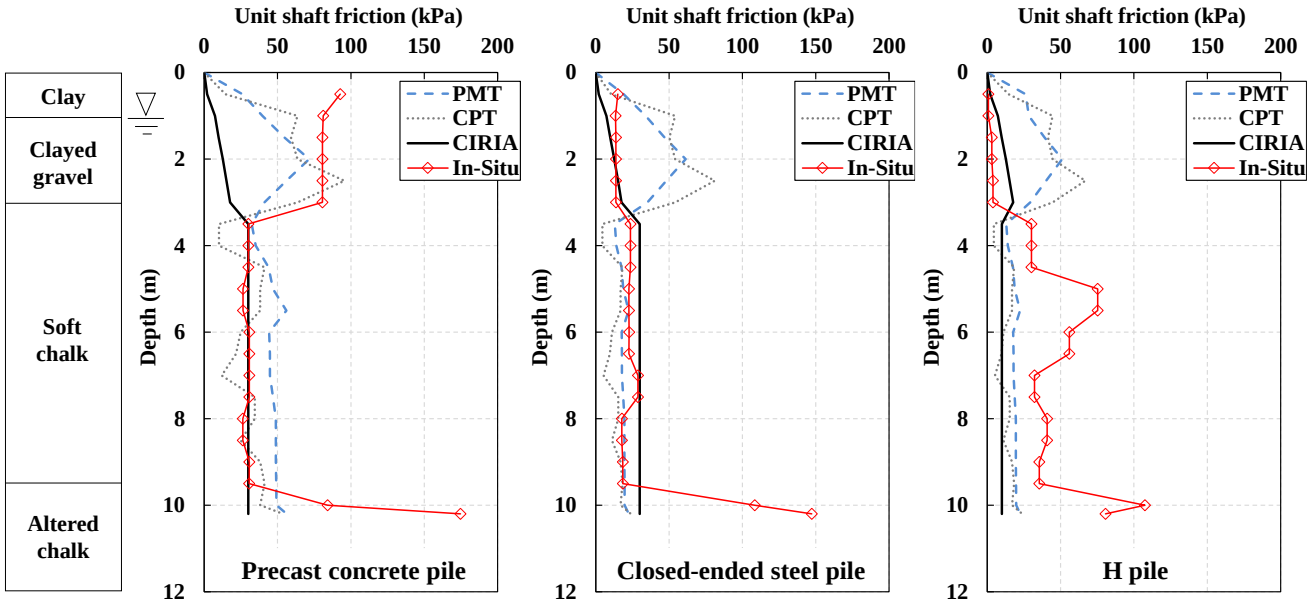


*Figure 2.11 : Unit shaft friction profiles for piles at Fleury-sur-Andelle site*

Figure 2.12 compares the unit limit shaft friction profiles obtained from the pile load test performed at Scardon and the different design methods. Calculation results of the closed-ended cylindrical steel pile indicate that in the soft chalk layer, between 6.5 and 11 m, the PMT and CPT methods give a good estimation of the unit shaft friction while the CIRIA method presents relatively higher values. In the weathered chalk layer, the PMT method shows a good agreement with the CIRIA method while the CPT method presents relatively smaller values due to the low values of the cone resistance provided by the CPT test. It can be also observed that all the design methods could not produce a good assessment of the measured values in the weathered chalk layer especially at depths below 19 m where the pile shaft develops largely higher values comparing to calculated values.

Considering the grouted H-pile, figure 2.12 shows that in the soft chalk layer, between 6.5 m and 11 m, the PMT and the CPT methods are in good agreement, and they slightly overestimate the unit shaft friction while the CIRIA method with a fixed average unit shaft friction of 20 kPa produces a good estimate. In the weathered chalk layer, same as for the pile no design methods show a good assessment of the measured values. In particular, the CIRIA method presents a significantly large underestimation of the available unit shaft friction.

The increasing trend of limit shaft resistance with depth reflects also the implications of friction fatigue in the case of driven piles at Scardon. The limit shaft resistance is greatest near the pile base and reduces with increasing the distance to the pile base.

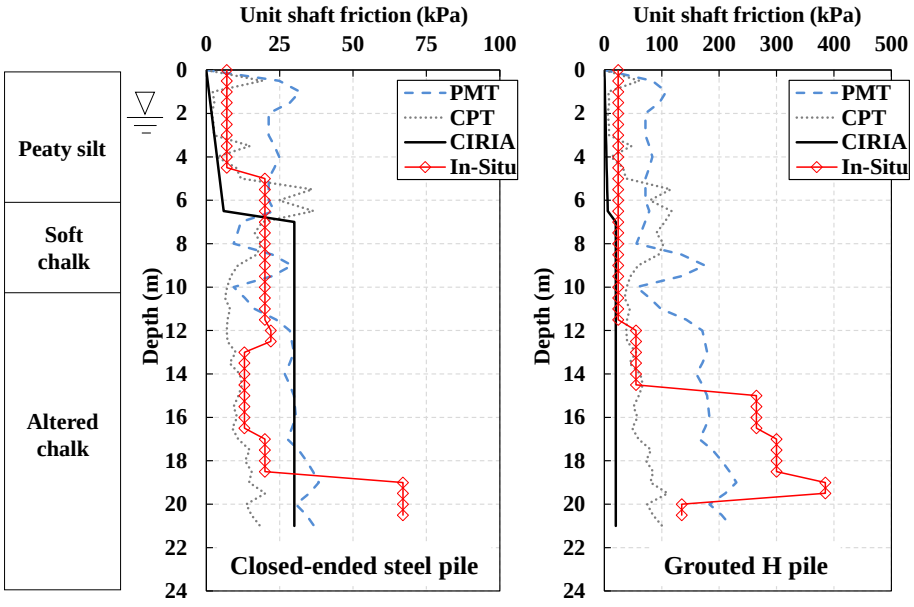


*Figure 2.12 : Unit shaft friction profiles for piles at Scardon site*

Figure 2.13 presents different profiles of unit shaft friction for the screw pile at Cambrai. Calculation results indicate that the PMT method produces a good estimation of the experimental values in chalk. The CPT method gives the lowest values amongst the design methods. Differences between different methods is less pronounced in this case.

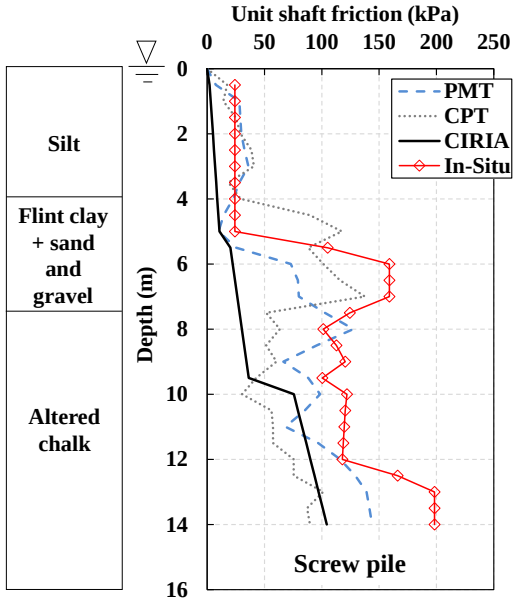


*Figure 2.13 : Unit shaft friction profile for pile at Cambrai site*

Experimental and calculation results of the screw pile of Montereau are presented in figure 2.14. The unit shaft frictions developed along the pile length in sound chalk are low regarding the high values of net limit pressure from the PMT test. Figure 2.14 shows a good agreement between the PMT and the CIRIA methods in chalk. The CPT method gives relatively the lowest values. It can be noticed that none of the calculation methods could sufficiently represent the variation of the unit shaft friction along the chalk formation. The heterogeneity and the variability of chalk may explain such observations.

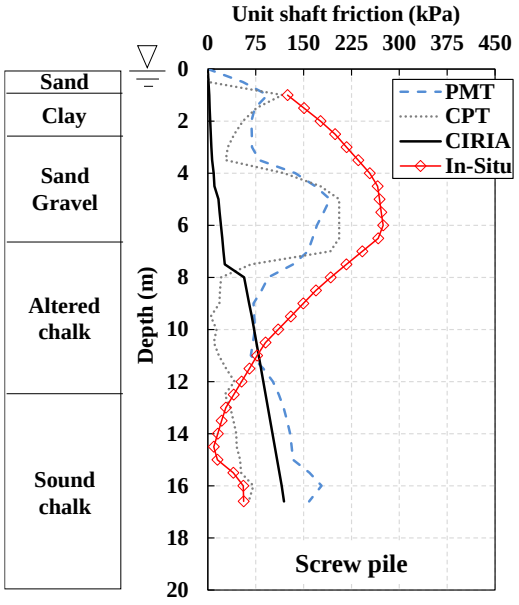


*Figure 2.14 : Unit shaft friction profile for pile at Montereau site*

Figure 2.15 plots the measured average shaft resistance plotted against the average vertical effective stress for the driven piles tested at Fleury-sur-Andelle and Scardon. This figure shows also the fixed limits of the average shaft resistance mobilisation, according to CIRIA C574 (Lord et al. 2002), for large displacement and small displacement driven piles in chalk. These limits clearly present an underestimation of measured data, especially in the case of the grouted H-pile at Scardon. All design methods, based on limited dataset, do not take into account the possible long-term increase in pile-chalk interface shaft resistance with time (Jardine et al. 2018, Buckley et al. 2018b). It should be noted that the driven piles in Scardon were tested after driving by only 12 days, hence further increase in shaft may be expected with time due to the possible ageing effect.

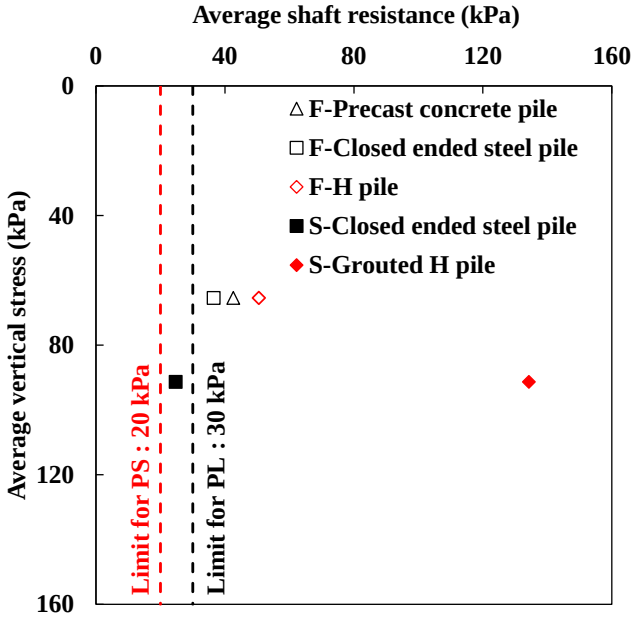


*Figure 2.15 : Average shaft resistance for tests on driven piles*

## 2.4.2 Base resistance

Calculation and experimental results, in term of pile base resistance in chalk, are presented in table 2.12. Calculated to measured base resistance ratios $R_{b,c}/R_{b,m}$ are presented in table 2.13 and figure 2.16. Three sets of results are shown, related to French (PMT and CPT) and UK (CIRIA C574) approaches. It should be noted that the comparison of different base resistance values will be held only for piles in Fleury-sur-Andelle, Scardon and Cambrai, due to the lack of information related to the SPT profile in Montereau site.

*Table 2.12 : Values of base resistance*

| Pile | Base resistance: $R_b$ (kN) | | | |
|---|---|---|---|---|
| | PMT | CPT | CIRIA | In-situ |
| **F-Precast concrete** | 553 | 552 | 1056 | 285 |
| **F-Closed ended steel** | 537 | 537 | 1026 | 321 |
| **F-H** | 303 | 359 | 653 | 360 |
| **S-Closed ended steel** | 1632 | 273 | 3040 | 1525 |
| **S-Grouted H** | 952 | 188 | 2000 | 2023 |
| **C-Screw** | 504 | 980 | 428 | 1571 |

*Table 2.13 : $R_{b,c}$ / $R_{b,m}$ ratios*

| Pile | $R_{b,c}$/ $R_{b,m}$ | | |
|---|---|---|---|
| | **PMT** | **CPT** | **CIRIA** |
| **F-Precast concrete** | 1.94 | 1.93 | 3.70 |
| **F-Closed ended steel** | 1.68 | 1.67 | 3.20 |
| **F-H** | 0.84 | 1.00 | 1.82 |
| **S-Closed ended steel** | 1.07 | 0.18 | 1.99 |
| **S-Grouted H** | 0.47 | 0.09 | 0.99 |
| **C-Screw** | 0.32 | 0.62 | 0.27 |

Calculated ratios present large scatter, especially in the case of the CIRIA method. Approximately 50% of the calculations largely overestimate the measured base resistance.

Figure 2.16 shows that the PMT method is likely to overestimate the pile base resistance in chalk with a maximum ratio of 1.94. It is noticed that the PMT method gives a good estimation in the case of closed-ended cylindrical steel piles at Fleury-sur-Andelle and Scardon. The CPT method tends to underestimate the measured base resistance with a minimum ratio of 0.09 and a maximum ratio of approximately 2 corresponding to the square precast concrete pile at Fleury-sur-Andelle where the two French methods present the same ratio. This method presents a good representation of the measured base resistance corresponding to the driven H-pile at Fleurty-sur-Andelle. The CIRIA method presents very high ratios with a maximum value that exceeds 3 corresponding to the pre-cast concrete pile and the closed-ended cylindrical steel pile at Fleury-sur-Andelle. However, the CIRIA method gives good estimates of the base resistance of the grouted H-pile in Scardon but significantly underestimates the base resistance of the screw pile in Cambrai. According to Lord et. (2002), the estimates of SPT blow counts from case histories were very uncertain due to the significant scatter of results. This would explain the large scatter encountered in the calculation results of CIRIA method.

Analysing results in a statistical way leads to table 2.14. It presents the mean, standard deviation and median values of each approach series.

Table 2.14 shows that the PMT method, with a mean value of 1.05, provides the best estimation of available static tests results. However, the standard deviation value of 0.59 shows that the calculated results present a large scatter. The CPT method underestimates experimental values in most cases with large scatter. The CIRIA method presents a clear overestimation, with a standard deviation value of 1.18 that shows the larger scatter. In fact, Lord et. (2002) have mentioned that the SPT N values are operator-dependent and exhibit considerable scatter, but they are a measure of the compressive strength of the chalk. Nevertheless, this trend to overestimate base resistance is quite common for many calculation methods as reported by

Burlon et al. (2014a). Since the years 1970, analysis of pile calculation methods has shown a continuous increase of the calculated shaft resistance which balances the calculated base resistance.

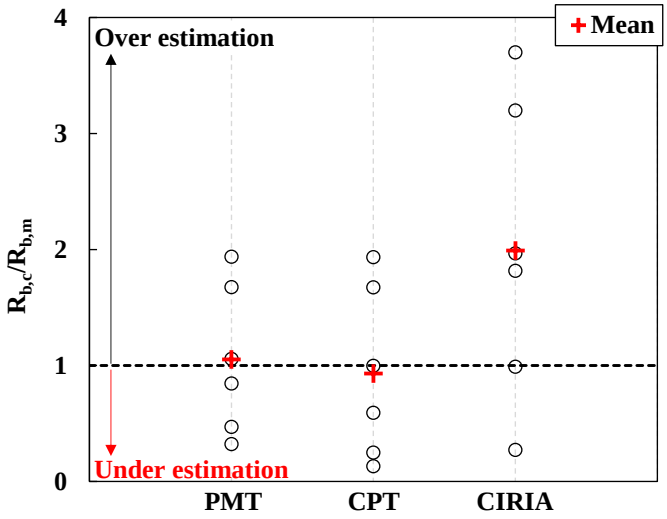


*Figure 2.16 : Graphical representation of $R_{b,c}$ / $R_{b,m}$ ratios*

*Table 2.14 : Statistical analysis of piles base resistance according to calculation approaches*

| | PMT | CPT | CIRIA |
|---|---|---|---|
| **Mean** | 1.05 | 0.92 | 1.99 |
| **Standard deviation** | 0.59 | 0.70 | 1.18 |
| **Median** | 0.96 | 0.81 | 1.91 |

## 2.5 Ageing effects

Beneficial time effects have been widely reported in sands and clays (Jardine et al. 2006, Gavin et al. 2015). Similarly, several researchers have studied the effect of time after pile driving in chalk. An increase in the pile capacity over time has been reported (Pasturel 1968, Bustamante et al. 1980, Buckley et al. 2018b) and is related to the evolution of shaft resistance over time. The base resistance seems to not evolve according to time. This phenomenon is also called "set-up" of piles and is more predominantly observed in driven piles.

Piles driving results in crushing and deterioration of calcium carbonate particles in chalk. Therefore, driving of piles in chalk produces a low-strength putty along the pile length which limits the effective normal stresses and shear resistances acting on the pile shaft (Florentin et al. 1961, Lake 1975, Lord et al. 2002). Long-term pore pressure dissipation and re-cementing of the putty annulus around the pile allow the mobilization of shaft friction and the increase in

pile capacity with time. Redox chemical reactions may also contribute in pile capacity increase with time (Buckley et al. 2018b).

Several empirical relationships have been proposed in the literature to represent such evolution in clays and sands (Bogard and Matlock 1990, Mesri et al. 1990, Tan et al. 2004). Buckley et al. (2018b) suggest that the hyperbolic relationship (equation 2.6), proposed by Tan et al. (2004) for sand, seems to be convenient to represent the observed evolution during pile testing in chalk.

$$Q(t) = Q_u \left\{ m + (1-m) \left[ \frac{t/T_{50}}{1 + \left(t/T_{50}\right)} \right] \right\} \quad (2.6)$$

Where, $Q_u$ is the ultimate capacity, $T_{50}$ the time required to achieve 50% of $Q_u$ and m an empirical coefficient (around 0.2) applied to improve the fit at the early age.

Table 2.15 presents results of pile load tests performed at Fleury-sur-Andelle. The aim of this part is to study the ability of the mentioned relationship (equation 2.6) to account for the evolution of the resistance of driven piles at Fleury-sur-Andelle subjected to several pile load tests over years. Additional experimental results of other driven piles are presented in table 2.15. They correspond to compressive pile load tests performed on driven piles in chalk at Oissel by the LCPC (Pasturel 1968). The corresponding driven piles are a precast concrete cylindrical pile and a Box pile which is fabricated from hot rolled sheet piles. The latter was loaded for two different depths: 17.35 m and 22.5 m. Table 2.15 includes values of pile resistance at the end of driving (EoD) as well as values of pile resistance corresponding to each pile load test performed after a specific time from driving.

Figure 2.17 plots the ratio of pile capacity at time t to the EoD pile resistance against time. The hyperbolic relationship plotted presents equation 2.6 that has been determined on the basis of experimental results extracted from tests conducted by Buckley et al. (2018b) on open-ended steel cylindrical piles driven in chalk. Experimental pile capacity had reached an ultimate value of 225 kN after 246 days, while its resistance at the end of driving was 39.3 kN. Hence, the $T_{50}$ parameter in equation 2.6 had given a value of 27 days. Evolution of pile capacity of tested piles from the LCPC database as well as experimental piles from Buckley et al. (2018b) tests are both presented in figure 2.17.

*Table 2.15 : Summary of test histories for ageing investigation*

| Site | Pile | Pile resistance at the EOD (kN) | Time after driving (days) | Pile resistance (kN) |
|---|---|---|---|---|
| **Fleury-sur-Andelle** | Closed-ended square pre-cast concrete pile | 205 | 86 | 780 |
| | | | 104 | 904 |
| | | | 118 | 979 |
| | | | 130 | 1010 |
| | | | 149 | 1044 |
| | | | 387 | 1110 |
| | Closed-ended cylindrical steel pile | 126 | 92 | 590 |
| | | | 693 | 700 |
| | H-pile | 156 | 86 | 550 |
| | | | 394 | 800 |
| | | | 461 | 850 |
| | | | 546 | 860 |
| **Oissel** | Closed-ended cylindrical pre-cast concrete pile | 122 | 10 | 265 |
| | Box pile | 44 | 3 | 75 |
| | | 101 | 1 | 140 |

It should be mentioned that no information had been provided regarding the pile capacity at the end of driving for driven piles at the site of Fleury-sur-Andelle. Considering the assumption that the ratio of the final resistance to the EoD resistance of driven piles of Fleury-sur-Andelle is on the hyperbolic curve determined by Buckley et al. (2018b), the EoD pile resistance was determined. The corresponding values are summarised in table 2.15. The EoD resistances for piles at Oissel have been already determined by the authors (Pasturel 1968).

At Fleury-sur-Andelle, the final four tests performed on the precast concrete pile appear to follow a similar trend as the proposed hyperbolic relationship. Figure 2.17 indicates a set-up factor of 5.4 after 387 days for this pile, showing approximately 441% of gain in capacity over time. The closed-ended steel pile shares broadly the same hyperbolic evolution with a set-up factor of 5.5, presenting 456% of gain in capacity after 693 days. The H pile shows some discrepancies for the first two tests. It indicates a set-up factor of 5.5 after 546 days with 451% of gain in capacity.

Likewise, these observations can be noticed for driven piles at Oissel, showing approximately the same beneficial ageing over time. The precast concrete pile presents a set-up factor of 2.2

after 10 days from driving, while the box pile shows a set-up factor of 1.7 for the first driving depth, 17.35 m, after 3 days and 1.4 for the second one, 22.5 m, after only one day from driving.

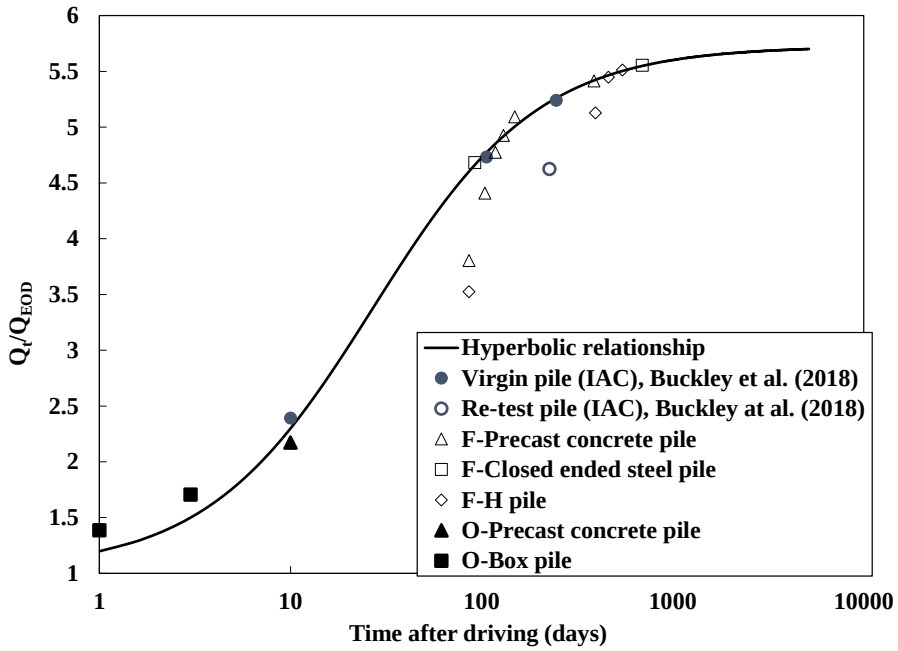


*Figure 2.17 : Evolution of shaft capacity with time*

## 2.6 Conclusion

This chapter presents a comparison between different pile design approaches in chalk adopted in France and the UK. Different ground investigation techniques can be performed and used into various calculation methods. In France, design of piles in different ground types is done according to the specifications of the French national standard NF P 94-262 (AFNOR 2012) used for the application of the Eurocode 7 to the design of deep foundations. It includes two methods based on in-situ tests results which are the Pressuremeter (PMT) and the Cone Penetration (CPT) tests. In the UK, CIRIA C574 (Lord et al. 2002) is the official document for the assessment of pile capacity in chalk. The shaft and base resistances calculated by these methods are compared to resistances measured in place for seven piles tested at four different sites in the Paris Basin. For these seven full-scale pile load tests, the ratio of shaft and base calculated resistances to the measured resistances is analysed. Statistical parameters of these ratios are given. In addition, profiles of unit shaft resistance assessed by the different methods are plotted for all piles. It can be noticed that the comparisons show significant differences for both shaft resistance and base resistance. It is difficult to conclude about the reliability of the different calculation methods due to the limitations of the number of piles in the database as well as the variability in the quality of the in-situ data. It is of great importance to perform

further comparative researches relative to results from new pile load tests in heterogeneous chalk in order to compare both approaches more in details.

Furthermore, the case of driven piles in chalk is analysed. As they remould the chalk and create a "puttified" zone along the pile shaft, the calculation methods are more difficult to calibrate. Anyhow, due to ageing effects, the shaft capacity increases with time. It is shown that resistance of driven piles in chalk from the LCPC database present a hyperbolic increasing trend with time that is similar to the hyperbolic relationship suggested in the literature for driven piles.

According to this preliminary work, it has been shown that the current methods have a significant dispersion and do not allow to take into account, in a reliable way, what is happening at the interface between the pile and the complex material such as chalk. For this reason, we intended to deepen our fundamental knowledge which is the objective of the second axis of this thesis. Hence, in the following chapter, we proposed a numerical approach, based on experimental results from direct shear tests, for assessing the influence of the variation of radial stress around the pile shaft on the mobilisation of shaft friction and therefore of pile capacity.

# Chapter 3
# Modelling the soil-pile interface with a simplified flow rule

## 3.1 Introduction

The prediction of the bearing capacity and the assessment of the stability of geotechnical applications, such as deep foundations for Onshore and Offshore wind turbine industry, tunnels and retaining structures, depend on the skin friction that develops between the soil and the structure. The behaviour of such applications is therefore governed by the soil-structure interaction. The analysis of the complex mechanisms and frictional characteristics of soil-structure interface, that evolve through a thin layer of soil in contact with the structure, is of great importance for a relevant understanding and an economical and reliable design of several geotechnical structures where the problem of soil-structure interaction often arises. This topic has been the subject of an extensive series of studies and researches considering various categories such as laboratory and in-situ experimental investigations and constitutive modelling taking into account different boundary conditions (Wernick 1978, Boulon and Foray 1986, Boulon 1988, 1989, Lehane et al. 1993, Shahrour and Rezaie 1997, Fakharian and Evgin 1997, Porcino et al. 2003, Mortara et al. 2007, Coyne et al. 2015, Pra-ai and Boulon 2016, Ziogos et al. 2017). Despite the soil type, a fundamental feature related to interface shearing is the variation of normal stress acting on the interface that may tend to increase or to decrease depending on several factors such as shearing level, soil density and interface roughness. This aspect causes a proportional variation of the ultimate shear resistance of the interface that has implications on the structure capacity. A special attention should be paid for the case of cyclic loading. The pile capacity degradation during cycles is related to the progressive decreasing in lateral stress along the pile shaft which leads to a decrease in the interface shear resistance (Puech 1982, Poulos 1984b, 1989, Boulon and Foray 1986, Buckley et al. 2018b).

This chapter begins by reviewing the principles and boundary conditions of experimental investigations used for the soil-structure interface testing, in addition to constitutive laws developed for modelling the interface behaviour. Afterwards, an alternative method for the simulation of the interface response is presented. A constitutive law used to account for the effect of normal stress variation on the interface shear behaviour is developed.

The developed model is based on the principles of elastoplasticity with a single yield mechanism, which acts upon Mohr-Coulomb criterion. Its corresponding flow rule is characterised by its capacity to enable typical volume behaviour of the interface under shear loading, to be developed. It is based on experimental curves illustrating the variation of normal displacement, according to shear displacement in the case of monotonic loading, and according to the number of cycles in the case of cyclic loading. In order to quantify this variation by the

mean of numerical expressions, a large number of direct shear tests under CNL and CNS conditions, with several combinations of either monotonic characteristics or cyclic characteristics, is needed. Hence, the proposed model is once calibrated and tested on experimental results of monotonic direct shear tests considering a very well-known material with plenty experimental data in the literature, the sand, and on recently available experimental results considering chalk samples. Considering cyclic loading, a corresponding numerical expression is proposed and calibrated on simulation results of cyclic direct shear tests from a validated approach named SOLCYP based on experimental results of sand interfaces.

## 3.2 Soil-structure interface

### 3.2.1 Definition

Soil-structure interface is the thin zone around the structure which undergoes large deformations due to the localised shear caused by the transmission of tangential force of axially loaded structure to the soil. Mainly constituted by a part of the soil in contact with the structure, and secondarily by a few particles torn from the structure (Boulon 1988), the interface zone therefore has mechanical properties largely different from the surrounding soil.

Considering the soil-structure friction, principal findings on the interface behaviour show that the variation of the shear resistance fit the Mohr-Coulomb criterion according to the general relationship:

$$\tau_{ult} = \sigma_n \tan \delta \tag{3.1}$$

Where, $\tau_{ult}$ is the ultimate shear resistance, $\sigma_n$ is the normal stress applied by the surrounding soil on the structure, $\delta$ is the friction angle of the interface between soil. Hence, the variation of the interface shear resistance is proportionally related to the variation of the interface normal stress. The latter is controlled by the expansion or contraction of the soil resulting from shear loading.

### 3.2.2 Experimental characterisation of the interface

To date, the investigation of mechanical response of soil-structure interfaces has been considered in numerous laboratory and field tests to understand and capture the interface behaviour in a reliable way. Considering laboratory tests, several devices have been developed and used to study the interface behaviour with different boundary conditions under cyclic and monotonic loading. The conventional direct shear box (figure 3.1) has been broadly used in

order to assess the interface behaviour (Desai et al. 1985, Boulon 1989, Al-Douri and Poulos 1992, Shahrour and Rezaie 1997, Porcino et al. 2003, Mortara et al. 2007) regarding the simplicity of the device and experimental procedure. Simple shear apparatus has also been widely used (Uesugi et al. 1989, Fakharian and Evgin 1997, Coyne et al. 2015) and it is characterised by its simplicity and its ability to overcome the drawbacks of direct shear test manifested by the distinction between interface sliding and shear deformation of soil (figure 3.2). The ring shear apparatus presented efficient manner to capture the interface behaviour (Yoshimi and Kishida 1981, Ziogos et al. 2017). However, like all shearing devices it shows some disadvantages particularly technical ones.

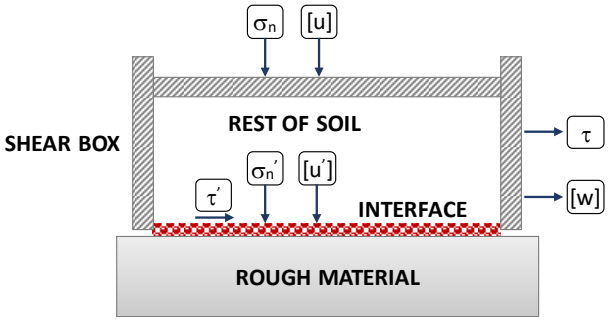


*Figure 3.1 : Direct shear test interpretation, after (Boulon 1989)*

The existence of a thin shear zone, close to an axially loaded pile, has been shown by previous model testing (Robinsky and Morrison 1964, White and Bolton 2004). They have shown that the distant soil around the shaft presents approximately no deformations. Many other researchers have studied the soil-pile interface behaviour by the mean of model piles axially tested both in compression and in tension (Boulon and Foray 1986, Boulon 1988, Lehane et al. 1993, Lehane and White 2005). Among field tests, we can also cite pull-out tests performed on metal strips and bars (Schlosser and Guilloux 1981).

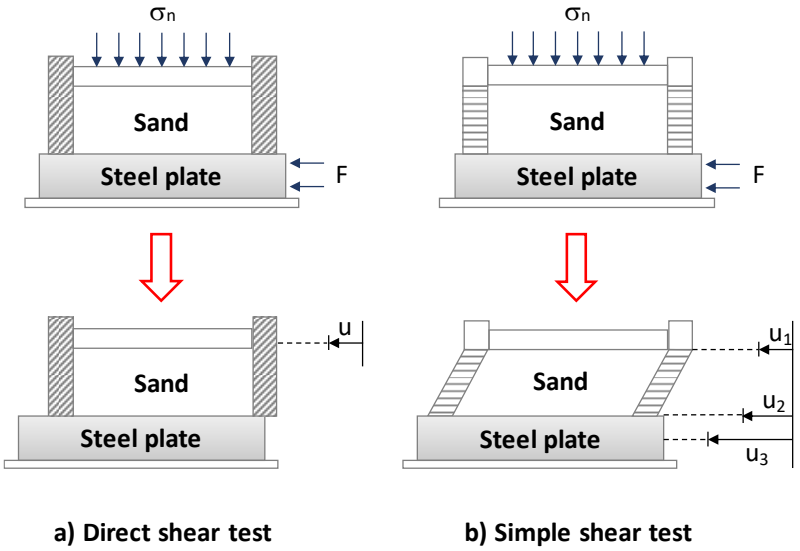


*Figure 3.2 : Difference between direct shear test and simple shear test, after (Uesugi et al. 1989)*

### 3.2.3 Boundary conditions and experimental observations

The behaviour of interfaces is not only controlled by the applied shearing force but also by the boundary conditions exerted by the surrounding soil. The response of an underground opening or deep foundation constrained by the neighbouring soil differs from the behaviour of a slope or a retaining wall. The Boundary conditions considered in interface shear experiments can be classified into three categories as shown in figure 3.3: Constant normal load (CNL), constant normal volume (CV), and constant normal stiffness (CNS).

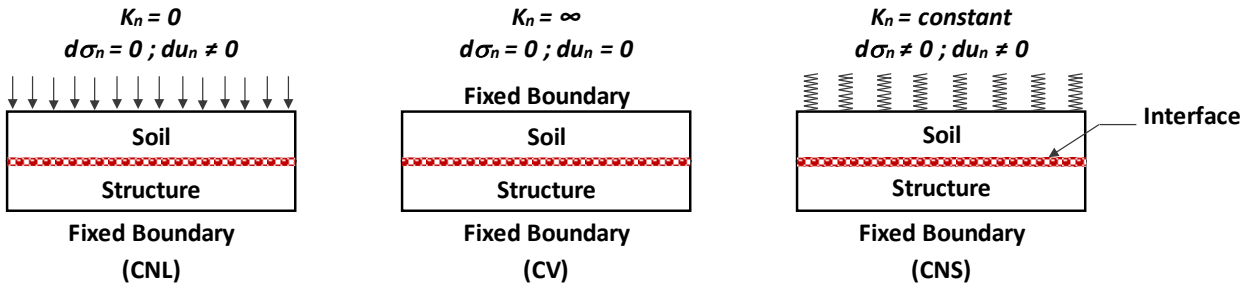


*Figure 3.3 : Boundary conditions in the normal direction of the interface, after (Fakharian and Evgin 1997)*

A conventional interface experiment with constant normal load acting on the interface plane (CNL) would be relevant for stability problems such as slope stability and retaining walls. However, some geotechnical applications experience a variation of normal stress acting on the interface during shear loading. Considering the interface between a pile shaft and the surrounding soil, the latter exhibits an elastic restraint to any possible change in the interface

volume induced by shearing. In other terms, changes in normal stresses acting on the pile shaft derive from changes in volume of the interface zone. Thus, normal stress may increase or decrease depending on whether the interface has tendency to dilate with increasing of confinement levels provided by the surrounding soil, or to contract. These features are equivalent to those seen in interface shear tests under constant normal stiffness (CNS) (Boulon and Foray 1986, Boulon 1988, 1989, Fakharian and Evgin 1997). This boundary condition is considered the intermediate between the two other extreme conditions defined in figure 3.3, the CNL and the CV conditions. In order to capture the local mobilisation of shaft friction at the pile-soil interface, Boulon and Foray (1986) suggested the CNS condition for direct shear tests where the stiffness of surrounding soil has been expressed by a Pressuremeter modulus. Figure 3.4 presents the analogy between the behaviour of the pile shaft subjected to shearing and a direct shear test with imposed normal stiffness.

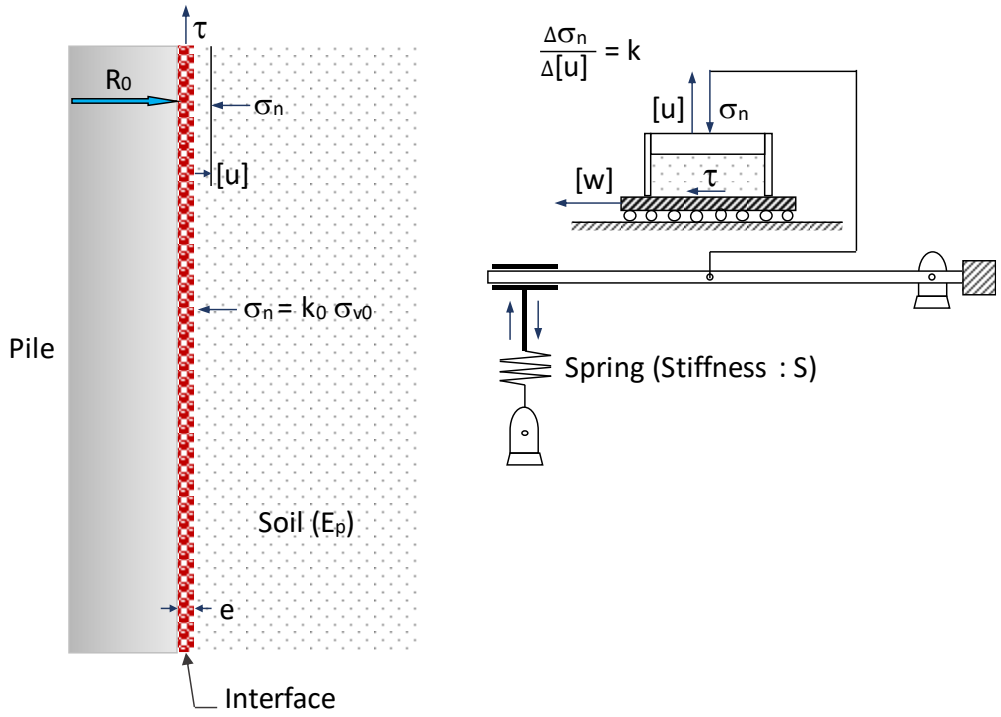


*Figure 3.4 : Analogy between the localised shear along a pile and a direct shear test with constant normal stiffness boundary condition, after (Boulon and Foray 1986)*

According to the spring model suggested by Wernick (1978), the variation of normal stress, $\Delta\sigma_n$, is proportional to the variation of normal displacement of the interface, $\Delta u_n$, according to the following relationship:

$$\Delta\sigma_n = -k_n \, \Delta u_n \tag{3.2}$$

Where, $k_n$ represents the imposed normal stiffness. Constant normal stiffness condition (CNS) is reached in direct shear tests by regulating the applied normal stress during shearing to satisfy the relationship mentioned in equation 3.2.

Under monotonic loading, the interface may show a contractive or a dilatant behaviour depending on whether the soil is loose or dense and the surface is smooth or rough. Generally, under cyclic loading an interface presents a tendency to experience a contractive response at the end of each cycle (Al-Douri and Poulos 1992, Shahrour and Rezaie 1997, Fakharian and Evgin 1997) and therefore a cumulative shear resistance degradation. The degradation of shear resistance along the pile shaft results in pile capacity degradation with the number of cycles. The degradation in shaft resistance due to cyclic loading is assigned to the compressibility of the soil (Poulos 1989), which leads to a reduction in soil volume close to the pile shaft and therefore to a decrease in the normal stress. In this regard, high-porosity chalk may experience rapid degradation when subjected to cyclic loading.

Several studies concerning the response of soil-structure interfaces using the CNS boundary condition in direct and simple shear tests have been conducted. They have considered different constant normal stiffness in both monotonic and cyclic loading conditions in addition to different interface roughness in order to capture the whole variety of soil-structure interfaces.

CNS direct shear tests under monotonic loading have been performed by a number of researchers (Hoteit 1990, Tabucanon et al. 1995, Mortara 2001, Pra-ai 2013). Pra-ai (2013) studied the influence of normal stiffness on different type of interfaces for loose and dense sand. Figure 3.5 shows that dense samples exhibited a contractive behaviour at the beginning of loading resulting in a slight decrease in normal stress and afterward a dilative phase occurred causing an increase in both normal and shear stresses. The higher values of normal stiffness (k) induced an important increase in peak normal and shear stresses. On the other hand, loose samples showed contractive behaviour all over the shearing phase with significant compression magnitude at the beginning. The contractive response of the interface resulted in a continuous degradation of both normal and shear stresses.

Effects of CNS direct and simple shear tests on the interface behaviour considering cyclic loading have been the subject of several researches (Hoteit 1990, Airey et al. 1992, Tabucanon et al. 1995, Fakharian and Evgin 1997, Mortara et al. 2002, 2007, Zhang and Zhang 2006, Pra-ai 2013). These effects are more critical than those associated to monotonic loading. As mentioned before, the main aspect related to cyclic shear loading is the possible degradation of normal stress along with the degradation of shear stress caused by the progressive densification. Fakharian and Evgin (1997) have considered a dense/rough interface in order to study the effect

of normal stiffness using a two-way cyclic tangential-displacement-controlled test with simple shear apparatus. Starting with the same initial normal stress, figure 3.6 shows that the shear stress decreased rapidly, and its maximum value was lower after the same number of cycles (N) as the normal stiffness (K) increased. Similarly, the normal stress degradation occurred faster at higher normal stiffness values.

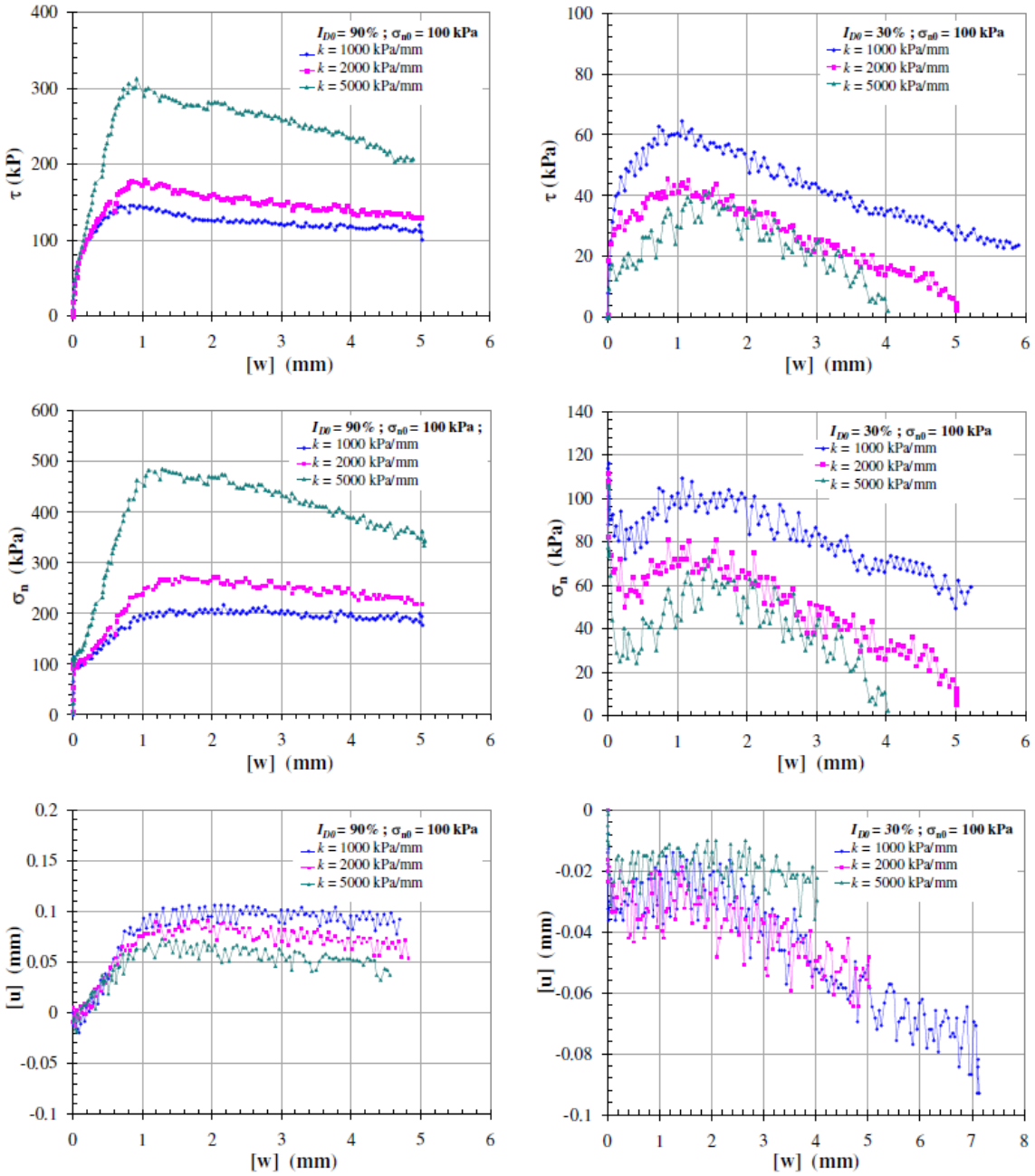


*Figure 3.5 : Results of monotonic CNS interface tests with three different value of normal stiffness (k), for a rough interface, on dense and loose sand, (Pra-ai 2013)*

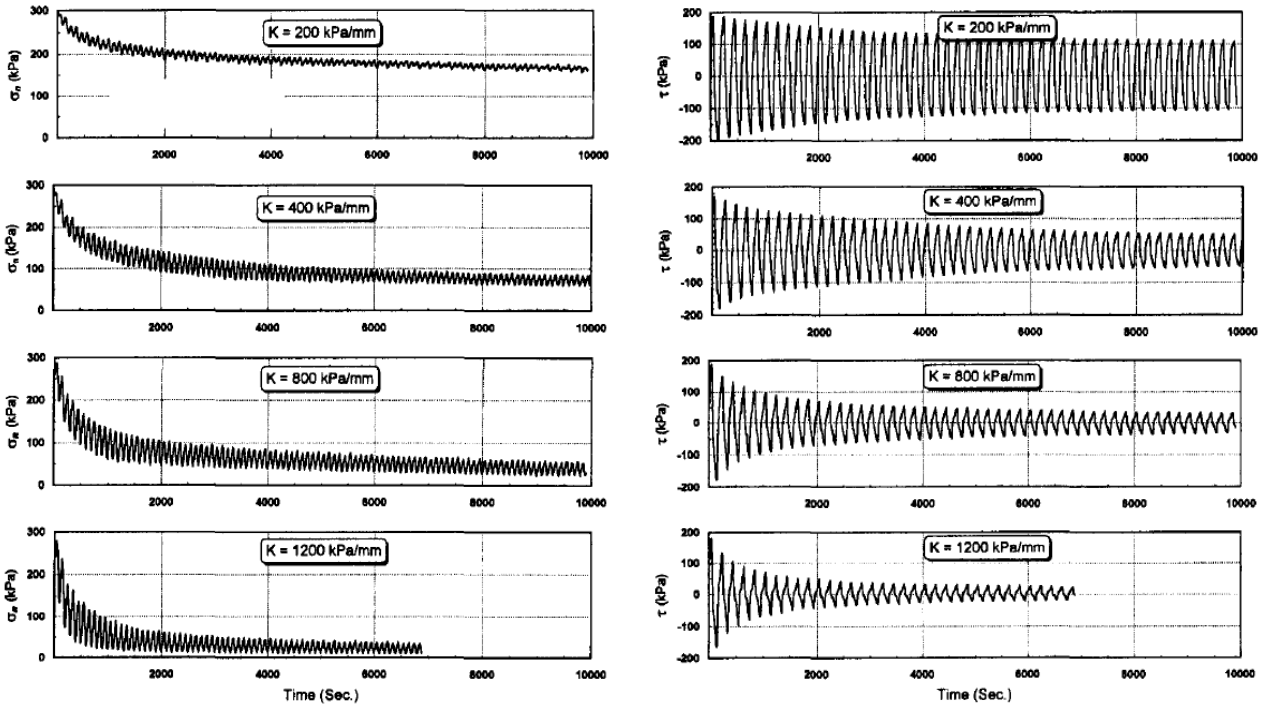


Figure 3.6 : Variation of interface normal and shear stresses during cyclic CNS shear tests with different values of normal stiffness on dense sand/ rough surface, (Fakharian and Evgin 1997)

Mortara et al. (2007) have also reported the effect of constant normal stiffness (k) on different interface roughness under cyclic loading using a direct shear apparatus in addition to the post cyclic response of different interface. Figure 3.7 shows the results obtained for two types of interface, rough and smooth, with the same normal stiffness and initial normal stress. The overall cyclic behaviour of the two interfaces showed a contractive response and therefore normal and shear stresses decreased as the number of cycles increased. Rough interface presented alternating phases of compression and dilation, while smooth interface exhibited only compression phases with no dilative phase. Consequently, no recovery of stresses occurred for the smooth interface in the post cyclic phase contrary to the case of rough interface where the dilative behaviour allowed the post cyclic recovery of normal and shear stresses.

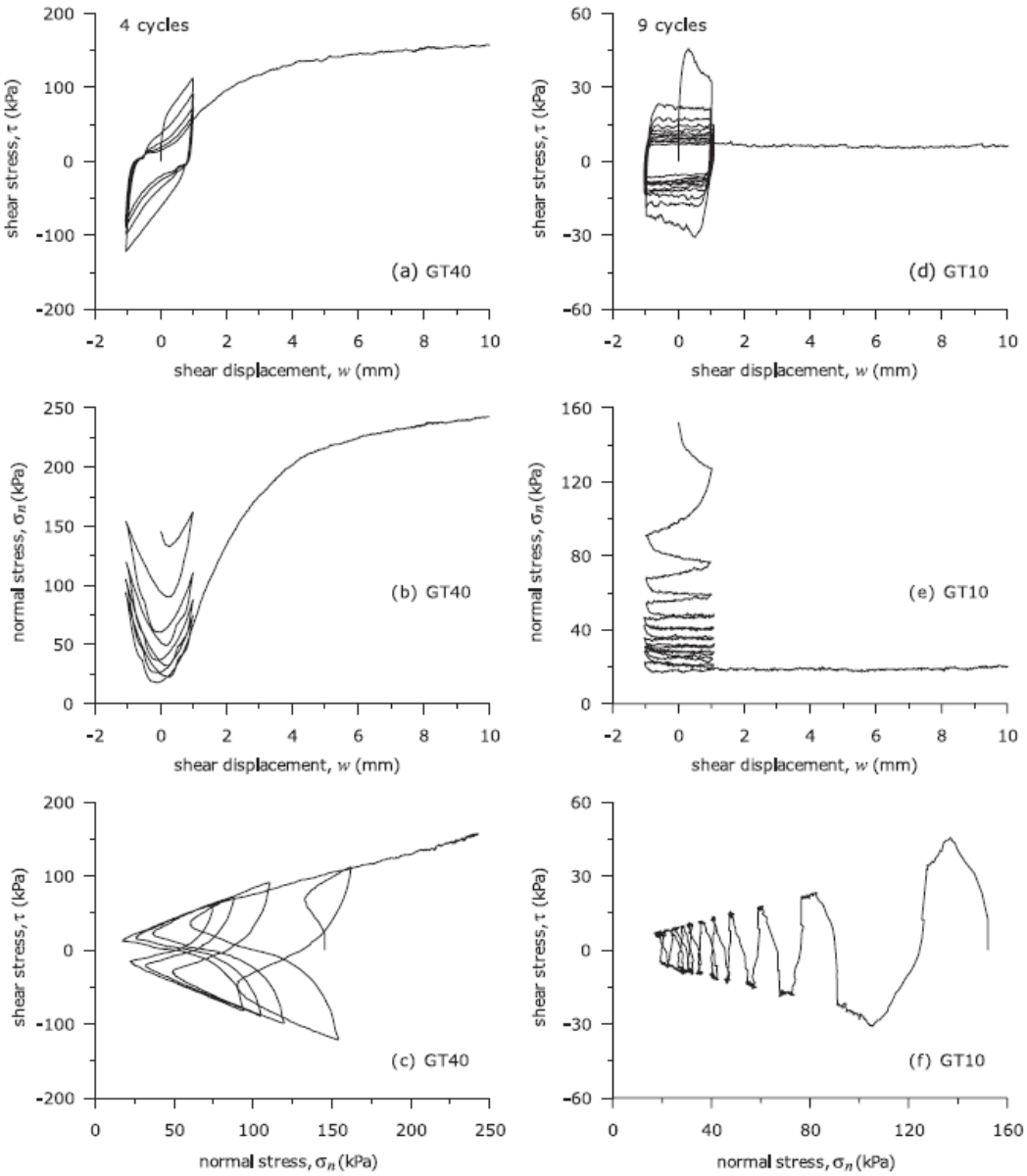


Figure 3.7 : Comparison between cyclic shear displacement controlled CNS tests with different values of roughness on sand-steel interface, (Mortara et al. 2007)

## 3.2.4 Constitutive models

### *3.2.4.1 Implicit models*

Subjected to either monotonic or cyclic loading, the interface may experience hardening or softening as mentioned in previous section. Depending on several elements such as stress level and surface roughness, interfaces undergo either localised dilation or contraction. The interface behaviour has been described by various types of constitutive law that have been proposed in the literature. These models have been up to date formulated for describing the mechanical response of interfaces which is so important for achieving a reliable solution of the

corresponding boundary problems. Constitutive laws determining the mechanical response of interfaces include several phenomena which can be classified conforming to Coulomb friction, interface elastoplasticity, finite friction, strain hardening and softening interface, and time dependent attributed to creep and viscoplasticity.

Based on the theory of elastoplasticity, some authors have considered linear elastic perfectly plastic models using the Mohr-Coulomb shear failure criterion as yield surface incorporating either associated or no associated flow rule (Day and Potts 1994). These models consider shear displacements but lack the probability of considering plastic deformations before failure. Perfect elastoplastic models do not adequately reproduce the typical mechanical responses of the interface observed experimentally, in particular: progressive strain-hardening and phase change (contractancy-dilatancy) defined as characteristic state. This reason justifies the need for developing more sophisticated models.

More complex models have also been proposed to describe the behaviour of the interface. These models incorporate one or more of the following phenomena: strain hardening, softening, contractancy, dilatancy and damage (De Gennaro and Frank 2005, D'Aguiar et al. 2011, Lashkari and Kadivar 2016, Stutz and Mašín 2016, Saberi et al. 2019). Considering the framework of classical elastoplasticity, De Gennaro and Frank (2005) have proposed a Mohr-Coulomb criterion type model taking into account a positive deviatoric hardening and softening, modelling the characteristic state (contractancy-dilatancy passage) and the critical state at large displacements. On the basis of this model, a three-dimensional interface model, formulated in invariants, has been developed by Said (2006) in order to capture the effect of the three-dimensional confinement stresses applied to the interface.

Another type of these complex models would be the incremental models whose principle is to obtain the incremental response to any incremental loading by rheological interpolation from a set of experimentally defined stresses formulated analytically through interpolation functions (Boulon 1988, 1989, 1991, Rouainia et al. 1992, Garnica-Anguas 1993, Pra-ai 2013).

In the case of cyclic loadings, the aforementioned approaches are not suitable because previous loading history cannot be stored in a single plastic domain. In this regard, several approaches have been proposed to account for the response of interfaces under cyclic loading where stress reversals occur frequently (ratchet, adaptation, relaxation, etc…). The theory of multi-surface plasticity and the theory of bounding surface, in other terms theory of two surfaces, have been broadly used for assessing the phenomena that may occur in the case of cyclic loading. Multi-surface approach has been originally proposed by (Mróz 1967) and it consists in multiplying the plasticity mechanisms which amounts to presenting the yield surfaces one inside the other.

These models have the disadvantage of requiring a very large number of parameters and present a certain complexity, particularly in the management of the different yield surfaces and in the calculation of each of the plastic multipliers. Shahrour and Rezaie (1997) and Mortara et al. (2002) have proposed constitutive laws that are two-surfaces Mróz models with a continuous evolution of hardening modulus. These models with non-linear kinematic hardening are characterised by the presence of a yield surface that delimits the elastic domain and a limit surface to which an isotropic hardening mechanism can be added.

The Modjoin law developed by Shahrour and Rezaie (1997) belongs to zero-thickness interface elements and it allows to account for the elastic behaviour of the interface and also its contractive-dilative behaviour for each stress reversal. These phenomena are considered by the presence of two families of surface: a bounding surface with isotropic hardening defining the limit resistance of the interface and a cyclic surface with kinematic hardening enclosing the yielding domain (figure 3.8). Both surfaces are closed on the axis of normal stresses $\sigma_n$, and the flow rule is not associated. The main model equations are presented below:

$$\text{Bounding surface: } f_m = |\tau| + \sigma_n R_{max} \qquad R_{max} = tan(\varphi) + DR\left(1 - e^{ADR\gamma_t^p}\right) \tag{3.3}$$

$$\text{Cyclic yield surface: } f_c = |\tau - \sigma_n R_c| + \sigma_n R_0 \quad dR_c = \lambda H_c \quad H_c = \gamma_c |R_{max} - R_c|^{\beta_c} \tag{3.4}$$

$$\text{Flow rule: } \frac{\partial g}{\partial \sigma_n} = \left(M_g - \frac{|\tau - \sigma_n R_c|}{\sigma_n}\right) e^{-a_c u_{tc}^p} \qquad \frac{\partial g}{\partial \tau} = \frac{\tau}{|\tau|} \tag{3.5}$$

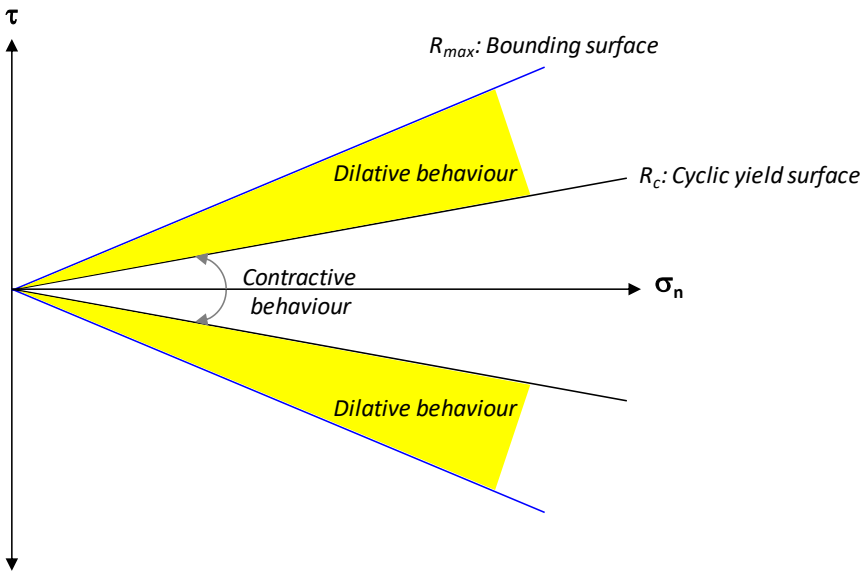


*Figure 3.8 : Illustration of Modjoin model principles (Shahrour and Rezaie 1997)*

Cao (2010) has tested potentialities of Modjoin law in different loading path and has suggested different scenarios for improvement. He has also treated the case of a pile subjected to axial cyclic loading. Using the Modjoin law, Cao (2010) has analysed the effects of cyclic loading on the pile capacity and its displacement.

### *3.2.4.2 Explicit models*

Cyclic solicitations of a foundation may be induced by various actions. The characteristics of cyclic loading are of a large variety, both in terms of frequency and significant number of cycles as classified in figure 3.9. According to this classification, offshore wind turbines may be subjected to a very large number of cycles which can exceed 10000 cycles. For this type of structures, the understanding of the mechanism of soil-pile interaction at large numbers of cycles is fundamental in order to achieve a safe and economical dimensioning of the foundation and correctly apprehending the behaviour of the superstructure.

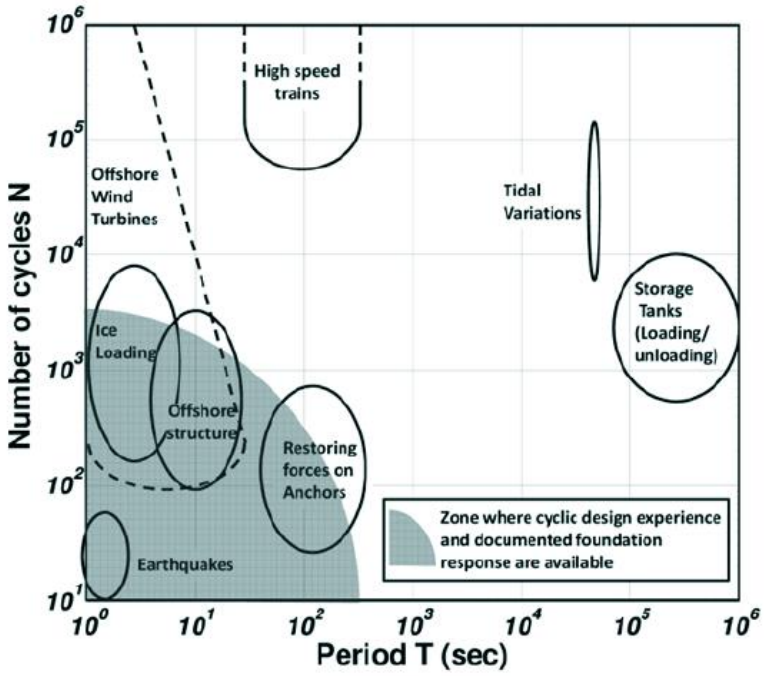


*Figure 3.9 : Periods and number of cycles of typical cyclic phenomena, (SOLCYP project)*

Considering the scale of a structure, incremental calculations, performed cycle by cycle, with even simple elastoplastic constitutive laws prove to be not applicable taking into consideration computation time. Thus, the complex models, so-called implicit models (Wichtmann 2005), presented above seem to be useful only to understand the mechanisms of deformation at the scale of either the sample or the structure only for a few cycles which does not exceed 100

cycles. The reason behind this restriction is the accumulation of numerical errors and massif calculation effort. In order to overcome these numerical drawbacks, alternative computational strategies must therefore be developed to acquire tools that are useful in engineering practice.

Wichtmann (2005) has distinguished classical models, implicit models, which describe each cycle using multiple increments, from those analogous to viscoplastic models in terms of equivalence between time and number of cycles. According to this classification, Papon (2010) has synthesised the numerical strategies developed in the literature in order to account for the cyclic response. He defined three categories: methods that use models that predict an average behaviour, pseudo-creep, and methods that use classical models, and finally mixed methods that use both beforementioned types of models.

The methods that show an equivalence between time and number of cycles, called pseudo-creep, are based on the qualitative and quantitative analogy that can be made between a creep test and a cyclic test. Hence, the evolution of the permanent deformation of a material under cyclic loading is to be reflected by the evolution of the deformation of the same material under constant loading in the case where it has a certain viscosity. It is then possible to replace a cyclic loading with a monotonic or even constant loading. The only problem lies in the choice of an elastoviscoplastic behaviour law and in the calibration of its parameters which cannot be obvious with conventional soil mechanical tests.

The methods that use classical models include several types. These methods are all based on the same principle (figure 3.10): between two cycles i and j for example, the load F undergoes by the structure is globally constant because the cyclic loading varies between the two cycles to return to its initial value (at the ending of cycle i) again. Between these two cycles, plastic deformations accumulated. These methods are based on a prediction of these plastic deformations and their consideration in the calculation as a nodal force vector. The difference between these methods corresponds to the forecasting of these plastic deformations.

The method of “skipped cycles” is one of these methods. They propose the simulation step-by-step of one (or several) cycle(s), using constitutive laws accounting for cyclic effects. Then, depending on the results, the value of one (or more) variable(s) is extrapolated over a number of cycles fixed beforehand or determined at each extrapolation. The extrapolation of variables is done linearly or via more complex functions. Sai (1993) developed a “skipped cycles” method, in a viscoplastic frame, for metal alloys imposed to high temperature. It has been based on the extrapolation of internal variables from a Taylor expansion. Inspired by this method, Cao (2010) and Burlon et al. (2014b) proposed a ‘skipped cycles” method, in a plastic frame only, for soil-structure interfaces subjected to cyclic loading.

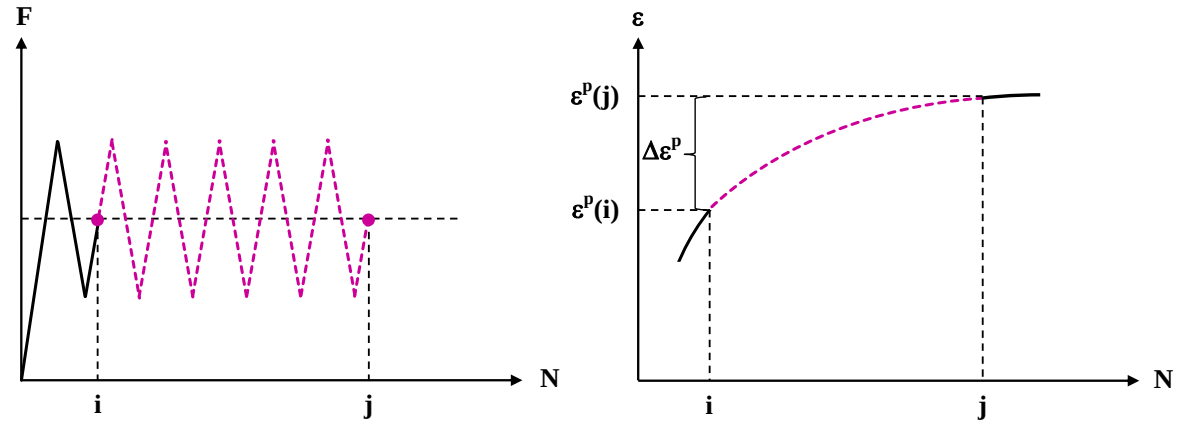


*Figure 3.10 : Principle of methods that use explicit models*

Considering the homogenisation of the loading history in the framework of finite element method, Shahrour and Meimon (1995) have estimated the evolution of plastic strains at each integration point of the mesh by taking into consideration the stress range of the previous loading cycles. Papon (2010) has also used a homogenisation method for simulating repeated undrained triaxial and cyclic Pressuremeter tests for normally consolidated clay. His aim was to evaluate the effectiveness of the time homogenisation method comparing to the step-by-step resolution.

Considering the third category, Niemunis et al. (2005), Wichtmann (2005), Wichtmann et al.(2005) and Wichtmann et al. (2010) have developed a numerical strategy which implements two models of behaviour: a so-called classic model and a model that describes an average behaviour of the soil (figure 3.11). They have proposed a high cycle accumulation model to capture the strain variations during the loading cycles without estimating the variation of cyclic stress. This model used a great number of parameters determined from a considerable number of cyclic drained triaxial tests. It has been developed for non-cohesive materials. Based on this explicit model, Pra-ai (2013) has proposed an analytical model , in the domain of soil-structure interface, to accurately and simply simulate the mean cyclic displacements in the case of loose and dense sand for a large number of cycles (N=10000). This model has been based and calibrated on an extensive amount of CNL direct shear tests performed on loose and dense samples considering rough interface. Using a special formulation, the model has been extended in order to apprehend the case of CNS condition.

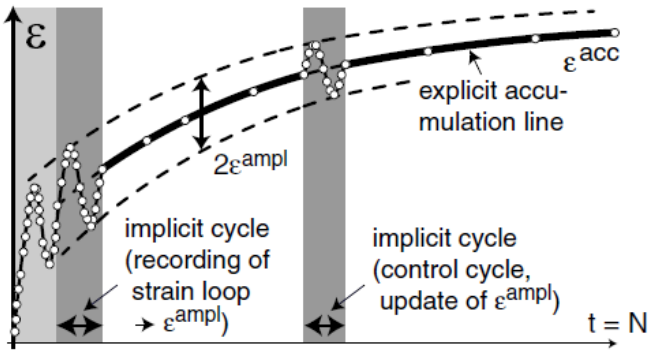


*Figure 3.11 : Calculation procedure using two types of behaviour models,* (Wichtmann 2005)

## 3.3 Proposition of a model for the soil-pile interface: an experimental flow rule

The determination of the real evolution of normal stress at the soil-pile interface is of a great interest to describe the evolution of the skin friction during shear loading. The overall behaviour of the soil-pile interface has been captured using different constitutive models as mentioned in paragraph 3.2.4.1. These constitutive laws with different hardening rules have become more and more sophisticated in order to simulate all the complex phenomena occurring at the interface during shearing. Predictions of these models have been compared with a large number of experimental results extracted from CNL and CNS interface tests and have presented their reliability in modelling the interaction between the soil and the pile. However, the large number of parameters needed and used in these constitutive laws makes their use complicated for engineering practices.

Based on the hypothesis that the plastic regime mainly manages the normal displacements of the interface along the pile shaft, which therefore results in the increase or the decrease of normal stress, this section proposes a model of elastoplastic behaviour, with linear isotropic elasticity, and a single plastic mechanism. The plastic mechanism involves a non-associated flow rule and a potential function based on experimental data that depends on the plastic normal displacements.

The frictional interaction between the soil and the pile develops through a thin layer of soil. Under the circumstances of such limited thickness, the interface exhibits a large strain localisation when subjected to shear loading. Hence, the behaviour of the interface is generally investigated in terms of relative displacements rather than interface strains. The following presentation of the model defines its two parts: the elastic and the plastic part.

Our model is framed in the classical elastoplastic theory supposing the increment of relative displacement as the sum of an elastic part $du^e$ and a plastic part $du^p$. Thus, increments of relative shear displacement, $du_t$, and relative normal displacement $du_n$ are decomposed into an elastic part and a plastic part:

$$du_t = du_t^e + du_t^p \tag{3.6}$$

$$du_n = du_n^e + du_n^p \tag{3.7}$$

### 3.3.1 Elastic part

The increments of normal stress, $d\sigma_n$, and shear stress, $d\tau$, are connected to those of elastic relative displacements by a linear and isotropic relationships, with constant coefficients:

$$d\sigma_n = k_n du_n^e \tag{3.8}$$

$$d\tau = k_t du_t^e \tag{3.9}$$

Where $du_n^e$ and $du_t^e$ are the increments of the elastic relative normal and shear displacement. $k_n$ and $k_t$ are the normal and shear stiffness of the interface. The increment of elastic normal displacement, $du_n^e$, is extracted from experimental curves presenting the evolution of relative normal displacement on the basis of direct shear tests. Therefore, the evolution of the normal stress is governed by equation 3.8.

### 3.3.2 Plastic part

The plastic part of the model is defined by a single mechanism, where the plasticity criterion is a function of normal and shear stresses and acts upon a Mohr-Coulomb criterion. Equation 3.10 presents the yield surface:

$$f(\tau, \sigma_n) = |\tau| - \sigma_n tan\varphi \tag{3.10}$$

Where, $\varphi$ is the interface friction angle. The plastic theory is based on the consistency relationship (equation 3.11) which allows the respect of rupture criterion at each increment of loading.

$$f\left(\sigma_n^f - d\sigma_n, \tau^f - d\tau\right) = 0 \rightarrow f\left(\sigma_n^f, \tau^f\right) - \frac{\partial f}{\partial \sigma_n} d\sigma_n - \frac{\partial f}{\partial \tau} d\tau = 0 \tag{3.11}$$

Where, $d\sigma_n$ and $d\tau$ are respectively the plastic normal and shear stress correction, and $\sigma_n^f$ and $\tau^f$ are the trial normal and shear stress (i.e., stress which surpasses the yield stress). Based on the theory of plasticity, these parameters are defined according to the following equations:

$$d\sigma_n = k_n \lambda \frac{\partial g}{\partial \sigma_n} \tag{3.12}$$

$$d\tau = k_t \lambda \frac{\partial g}{\partial \tau} \tag{3.13}$$

Where, $\lambda$ is the plastic multiplier, and g is the potential function defined by equation 3.14:

$$g(\tau, \sigma_n) = |\tau| + \sigma_n \frac{\partial g}{\partial \sigma_n} \tag{3.14}$$

Usually, according to equations 3.11, 3.12 and 3.13, the plastic multiplier, $\lambda$, is determined according to the following equation:

$$\lambda = \frac{f\left(\sigma_n^f, \tau^f\right)}{\frac{\partial f}{\partial \tau} k_t \frac{\partial g}{\partial \tau} + \frac{\partial f}{\partial \sigma_n} k_n \frac{\partial g}{\partial \sigma_n}} \tag{3.15}$$

In our proposed model, the flow rule is given by equation 3.16:

$$du_n^p = \lambda \frac{\partial g}{\partial \sigma_n} \rightarrow \frac{\partial g}{\partial \sigma_n} = \frac{du_n}{\lambda} \tag{3.16}$$

Hence, if the variation $du_n^p$ is extracted from experimental curves, then the quantity $\frac{\partial g}{\partial \sigma_n}$ can be substituted in equation 3.12. Therefore, the new formulation of the plastic multiplier can be calculated according to the following equation:

$$\lambda = \frac{f\left(\sigma_n^f, \tau^f\right) - \frac{\partial f}{\partial \sigma_n} k_n du_n^p}{\frac{\partial f}{\partial \tau} k_t \frac{\partial g}{\partial \tau}} \tag{3.17}$$

Depending on the obtained values of the plastic multipliers, plastic corrections are applied for the trial stresses. The variation of normal displacement derived from experimental curves, will be considered as a disturbed relative normal displacement at the interface nodes. The correction of normal and shear stresses will be done according to equation 3.11. Therefore, the corrected values of normal and shear stresses are calculated depending on the following equations:

$$\tau^c = \tau^f - k_t \lambda \frac{\partial g}{\partial \tau} \tag{3.18}$$

$$\sigma^c = \sigma^f - k_n du_n^p \tag{3.19}$$

The proposed flow rule intends to obtain the volumetric behaviour of a material when modelling the interface and therefore to avoid the need to use a complex behaviour law. Indeed, assessing the problem considering this analysis will capture the real evolution of the interface normal stress where the degradation, the contracting and dilatant behaviour are explicitly presented by the experimental curves. Hence, the main aspect of the model proposed in this section is the determination of experimental curves presenting the evolution of the normal relative displacement which can describe the general direct shear paths that can govern the different possible responses of the interface in both cases, under monotonic and cyclic shear loading.

In this study, the experimental curves in terms of normal displacement, in the case of monotonic loading, are determined as a function of shear displacement, $u_n = f(u_t)$. According to the classification of constitutive models defined in section 3.2.4, we can say that our developed model is a combination between an elastoplastic constitutive model and an incremental model. Although the normal stress, which varies proportionally to normal displacement in CNS conditions, is defined according to an analytical approach based on a series of shear tests, the shear stress is determined according to an elastoplastic correction procedure.

Considering the case of cyclic loading, it should be noted that in this work, we are more interested in the reduction of the calculation time related to the dimensioning of a soil-pile interface subjected to cyclic solicitation, than in the quality of the representation of reality by the behaviour model. According to Wichtmann (2005) and Wichtmann et al. (2005), the mean cyclic path during cycles is more important than the detail of each cycle. Hence, according to the explicit model proposed by Wichtmann (2005), Niemunis et al. (2005) and Wichtmann et al. (2010), the number of cycles is considered rather than time scale in a pseudo-creep approach. Thus, experimental data in terms of normal displacement, are in the form of: $u_n = f(N)$.

In the following sections, several forms of interpolation function are described for constructing the experimental curves that present an approximate illustration of the interface behaviour. A formulation based on phenomenological approach is proposed, which considers different parameters that may have an effect on the behaviour of the interface under monotonic and cyclic loading.

## 3.4 Proposition of a numerical equation for experimental curves: monotonic loading

This study focuses on representing the different physical phenomena that may alternate during monotonic shear loading under constant normal stiffness condition (CNS), i.e., the contracting phase, the dilating phase, the stabilisation, etc. These different phases are more or less pronounced depending on the skeleton of the material, the initial soil density, its different mechanical characteristics and the interface rigidity as well.

Generally, a dense soil exhibits a slight initial contracting phase at the very beginning of loading, where the normal stress slightly decreases. This phase is followed by an important phase of dilation resulting in an increase of the normal stress. In the case of sand, a following small contraction may occur related to grain breakage where the normal stress associated with shear stress decreases to the critical state. However, the level of shear loading may be not high enough to allow the grain crushing, thus in this case the dilation phase will be followed by stabilisation where no variations of normal stress will occur. On the other hand, a loose soil exhibits a more pronounced contracting behaviour at the beginning of shear loading due to densification followed by a slight dilation phase after which it continues to contract. Depending on the load level and the soil mechanical characteristics, a loose soil may present only a contracting behaviour throughout shear loading.

Indeed, the behaviour of the soil-pile interface can result in a high or low shaft resistance and consequently high or low pile capacity. For example, considering a small-displacement piles driven into chalk layer (for example closed-ended steel piles), the resulting remoulded high-density chalk is shown to be dilatant when shearing, whereas the resulting remoulded low to medium density chalk is shown to be contractant (Lord et al. 2002). The former will exhibit high shaft resistance while the latter will generate low shaft resistance.

These possible responses captured at the interface level can be mathematically presented by the mean of a specific numerical equation that will be explained and calibrated in the following sections.

### 3.4.1 Numerical equation

The description of the path of normal displacement according to shear displacement can be done using a relatively simple expressions that make it possible to visualize and calibrate the equations according to the results of shear tests.

The expression of the hyperbolic secant equation modified according to a statistical distribution function (equation 3.20) is retained to mathematically represent different phenomena occurred during shear loading.

$$u_n = f(u_t) = A\,sech\left(\frac{u_t - B}{2C}\right) + D \tag{3.20}$$

Figure 3.12 presents the shape of the curve described by the equation 3.20 where it clearly explains our choice of the secant hyperbolic function. This figure presents two curves where the difference comes mainly from the sign of different parameters. The considered expression can simulate two different behaviours of the interface, dilatant and purely contractant behaviour.

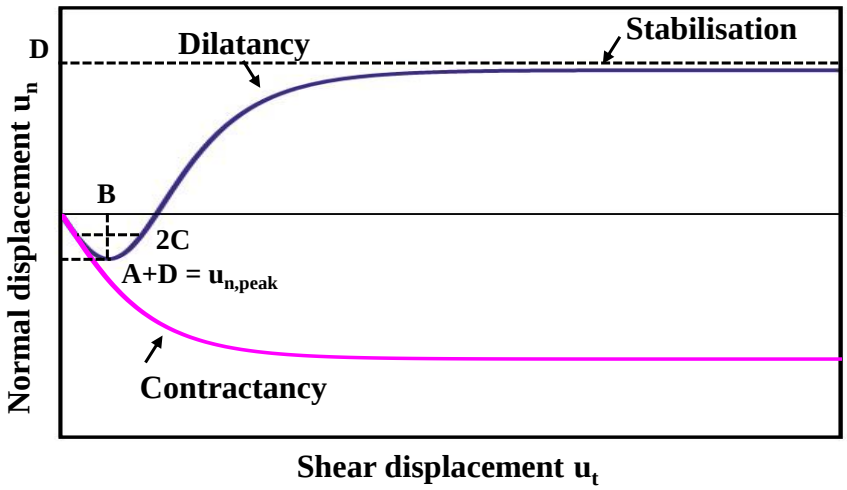


*Figure 3.12 : Graphical representation of the numerical equation, $u_n = f(u_t)$*

According to figure 3.12, physical significations of each parameter of the function are as follows:

B: a parameter equivalent to an average value, it allows to define and place the peak of the curve and therefore the entire curve.

C: a parameter equivalent to a standard deviation, it gives the curve opening and finally it is indicative of the rate of change of the displacement.

D: the value of the global vertical shift of the curve, it positions the asymptote.

A+D: the maximum value, corresponding to the peak of the curve defined as $u_{n,peak}$.

This function can clearly present an initial contractive behaviour followed by a dilation phase after the peak and a final phase of stabilisation. In addition, it can present a globally contractive behaviour.

The procedure of the calibration of each parameter on the basis of shear tests will be discussed later. The determination of the parameter C was done on the basis of a mathematical resolution to ensure that the curve starts with the origin point (x = 0, y = 0). The expression of the parameter C is presented in the equation 3.21.

$$C = \frac{-B}{2\,ln\left(\frac{A}{D} + \sqrt{\left(\frac{A}{D}\right)^2 - 1}\right)} \tag{3.21}$$

The expression presented by equation 3.20 is modified in order to consider the possible contracting phase that may occur after the dilating phase. For this purpose, a new parameter is added, and the new formula is as follows:

$$u_n = f(u_t) = A\,sech\left(\frac{u_t - B}{2C}\right) + D + A_d u_t^2 \tag{3.22}$$

The additional part that was added to the initial equation allows the decrease in normal displacement after the dilation phase where it has reached a maximum value equal to the parameter D. Hence, parameter $A_d$ reflects the level of degradation taking place. Figure 3.13 presents the three different behaviours that can be simulated by the proposed expression.

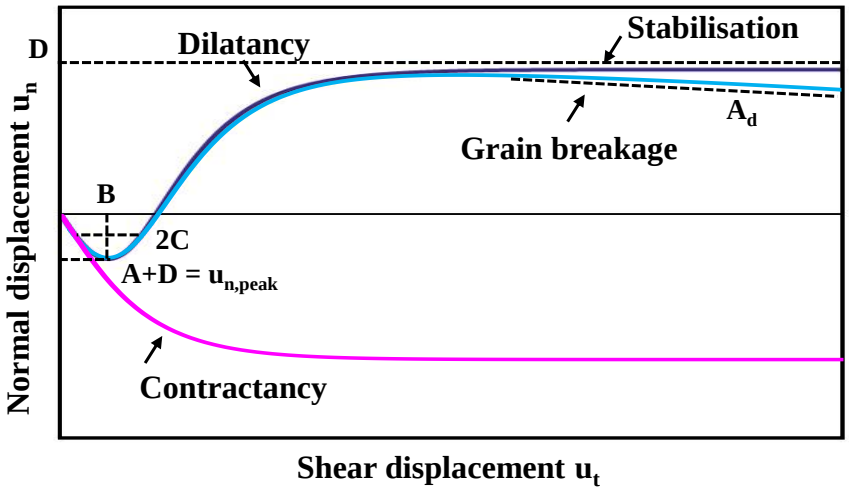


*Figure 3.13 : Graphical representation of the numerical equation, $u_n = f(u_t)$, with possible grain breakage*

## 3.4.2 Parametric study

This section presents a parametric study that illustrates the effect of each parameter of the numerical expression presented in equation 3.22.

Figures 3.14 and 3.15 illustrate the effect of each parameter on the global shape of the curve presenting the normal displacement as a function of shear displacement. They also illustrate an example of the estimated evolution of shear stress as a function of shear displacement, in the case of shear test under CNS condition, for each simulation and how each parameter may affect this evolution. Figures 3.14 consider the existence of a dilation phase while figures 3.15 consider only contraction phase.

A higher value of the parameter B expands the elastic domain of the interface (figure 3.14a). Thus, as B increases, the shear stress mobilisation curve at the interface (figure 3.14b) is more flexible. The shear displacement required to mobilise the maximum shear stress increases. By increasing the value of the parameter D (figure 3.14c), the maximum value reached at the very end of the dilation phase increased which reflects a higher value of normal displacement and therefore a higher value of normal stress at large tangential displacements. As a consequence, the maximum shear stress value increases as D increases (figure 3.14d). In addition, a higher value of the sum A+D, i.e. a higher value of the peak, $u_{n,peak}$, illustrates a more pronounced contracting behaviour at the beginning of loading (figure 3.14e). However, figure 3.14f shows that the sum A+D has approximately no effect on the mobilisation of the shear stress. As for the parameter $A_d$, it has a negative value, or it may be considered equal to zero. Figure 3.14g shows that the more $A_d$ increases the more the normal displacement decreases which presents a higher reduction rate. Therefore, as $A_d$ increases, the final value reached by the shear stress at the critical state decreases (figure 3.14h). When $A_d$ is set equal to zero, the curve presents no degradation after the dilation phase. Therefore, no grain breakage is considered. Indeed, a zero value of $A_d$ eventually cancels out the variations of the plastic displacements, dilating or contracting, where the value of shear stress is therefore constant.

Considering an entirely contracting behaviour, presented in figure 3.15, the parameter $A_d$ is set in all cases equal to zero, where a final stabilisation phase may be presented after contraction. In this case, the parameter B is a negative number. Figures 3.15a and 3.15b show the effect of the parameter B. It affects the slope of the contracting phase, and its value has a direct effect on the parameter C that illustrates the opening of the curve. An increase of B decreases the contractancy for small tangential displacements, the normal displacement decreases and similarly the normal stress. This parameter has no effect on the normal displacements at large tangential displacements. An increase in D delays the stabilisation of contraction for large tangential displacements, which corresponds to a more contracting behaviour of the interface (figure 3.15c). A decrease in the mobilised shear stress is therefore a direct consequence of the variation of the normal stress which is proportional to the variation of normal displacement

(figure 3.15d). On the other hand, the sum A+D, therefore parameter A, has a slight influence on the variation of normal displacement and the mobilisation of the shear stress (figures 3.15e and 3.15f).

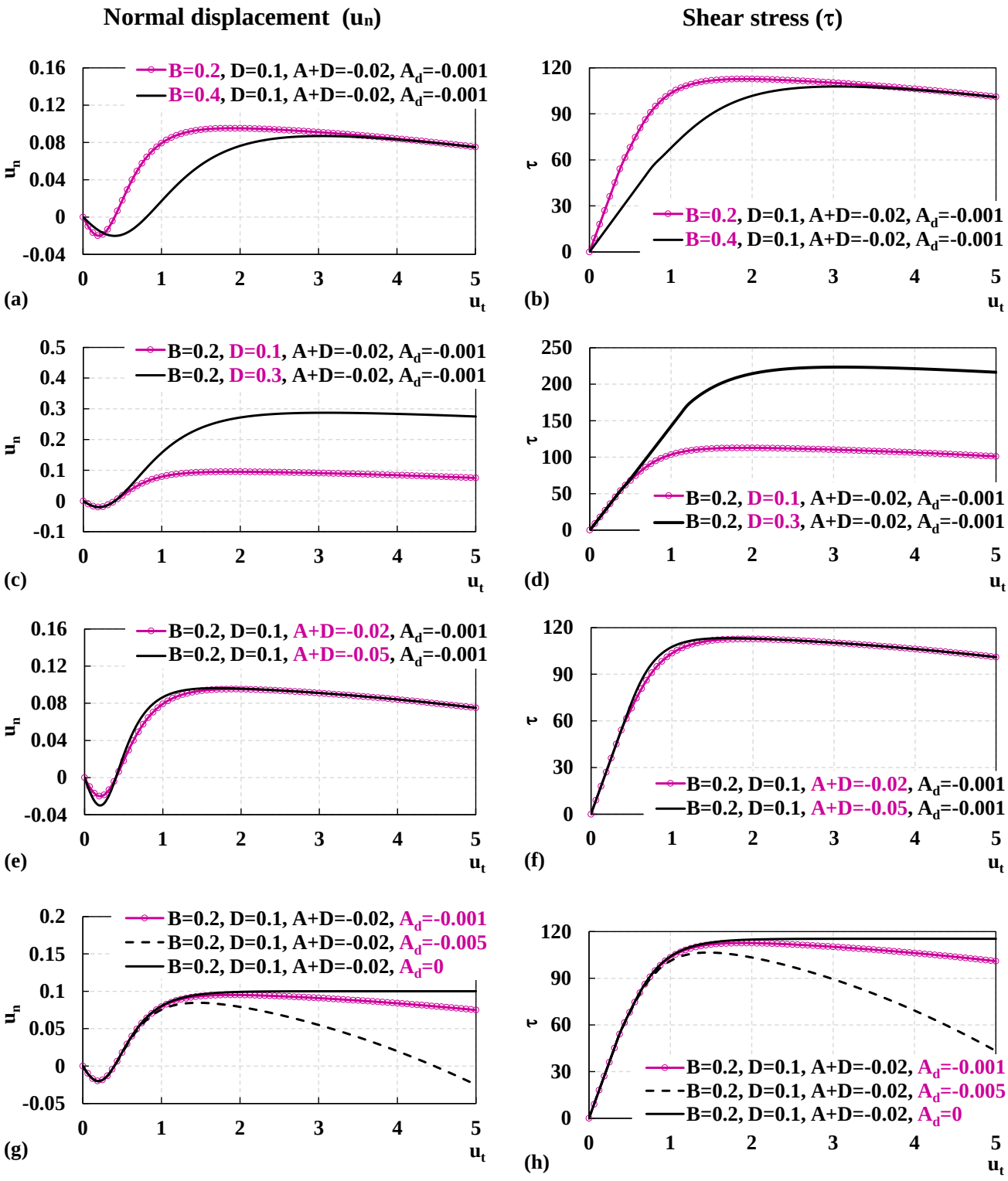


*Figure 3.14 : Influence of the numerical expression parameters on the results of a shear test under CNS condition: existence of a dilation phase*

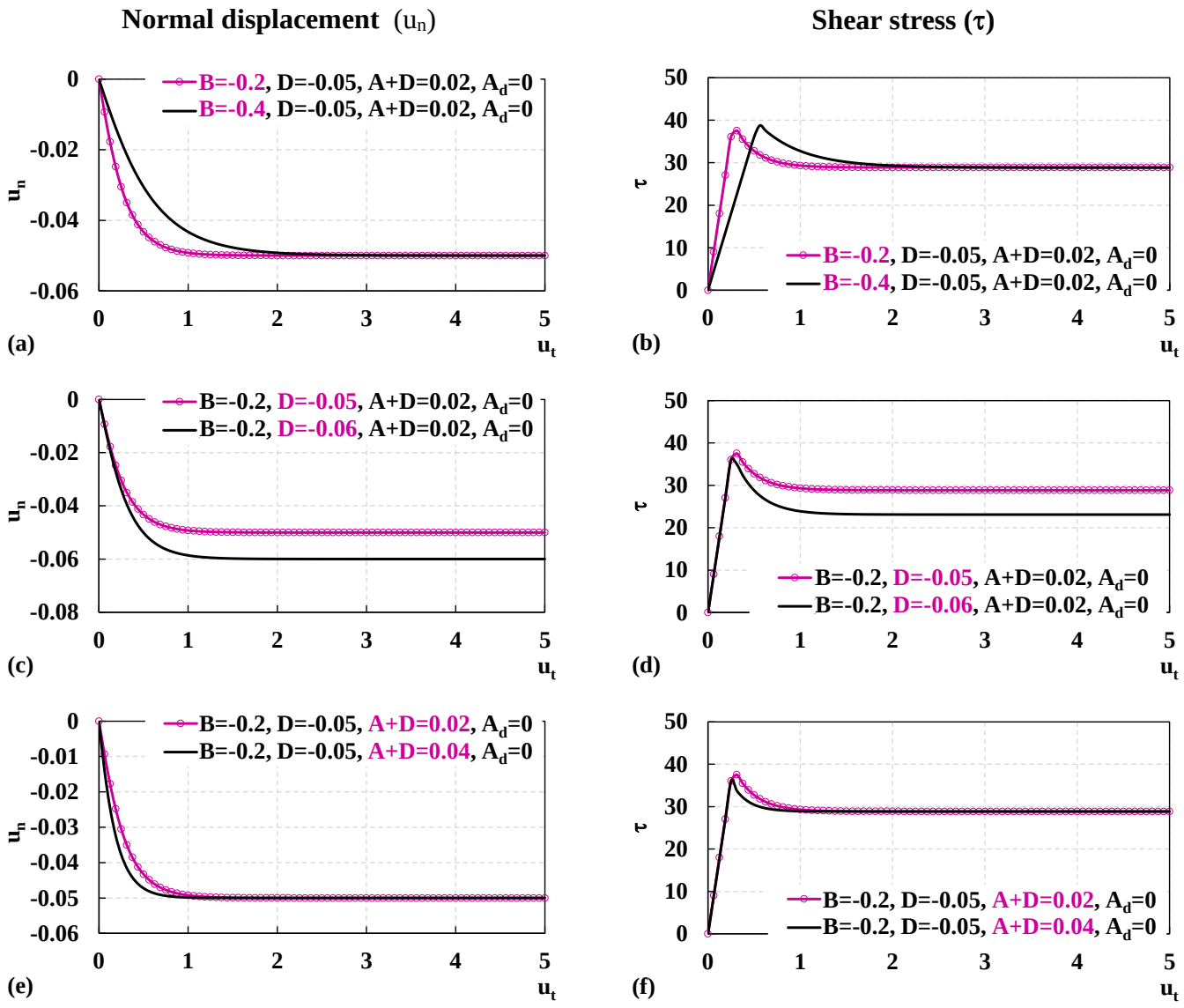


*Figure 3.15 : Influence of the numerical expression parameters on the results of a shear test under CNS condition: contraction phase only*

### 3.4.3 Procedure of parameters identification

The identification of the equation parameters must be based on data from a series of typical direct shear tests under constant normal stiffness and constant normal stress: different types of direct shear tests differ only in the value of the normal stiffness applied to the interface, hence a CNL test is considered as a particular case of CNS tests with zero normal stiffness. The main idea is to extract the value of each parameter from experimental curves considering different characteristics that define the direct shear test. Hence, results of several direct shear tests under a wide range of normal stiffness values ($k_n$) and initial normal stress values ($\sigma_{n0}$) allow to define the variation of each of the parameters according to these characteristics. These basic key parameters are then formulated as a function of $k_n$ and $\sigma_{n0}$.

The principle of parameters determination is relatively simple to implement. The aforementioned process can be done using MATLAB fitting application "Curve fitting". Having a total number of nine shear tests, with three different values of normal stiffness ($k_n$) and initial normal stress ($\sigma_{n0}$), is relatively sufficient for the calibration. The corresponding experimental curves describing the variation of normal displacement as a function of shear displacement are fitted using MATLAB fitting application "Curve fitting". Then, values of $u_{n,peak}$, B, D and $A_d$ are extracted from each experimental curves, which helps to formulate a general relation for each parameter in function of $k_n$ and $\sigma_{n0}$. Finally, we obtain a general expression of type $u_n = f(u_t)$ calibrated for each series of tests and each combination of values $k_n$ and $\sigma_{n0}$.

In order to simulate the mobilisation of shear stress during a shear test, the calibration of the corresponding value of shear stiffness $k_t$, in the case where dilation is considered, is done as follows. The parameter B of equation 3.22 determines the limit between the contracting domain and the dilating domain. This limit defines the characteristic state of the interface (figure 3.16). It is considered equal to the half of the shear displacement corresponding to the limit between the elastic part and the plastic part ($u_t^e$). Since our model follows the criterion of Mohr-Coulomb, then $u_t^e$ can be determined and subsequently the value of shear stiffness:

$$\tau = k_t u_t^e = \sigma_{n0} \tan \varphi \tag{3.23}$$

$$B = \frac{u_t^e}{2} = \frac{\sigma_{n0} \tan \varphi}{2k_t} \rightarrow k_t = \frac{\sigma_{n0} \tan \varphi}{2B} \tag{3.24}$$

Where, φ is the interface friction angle.

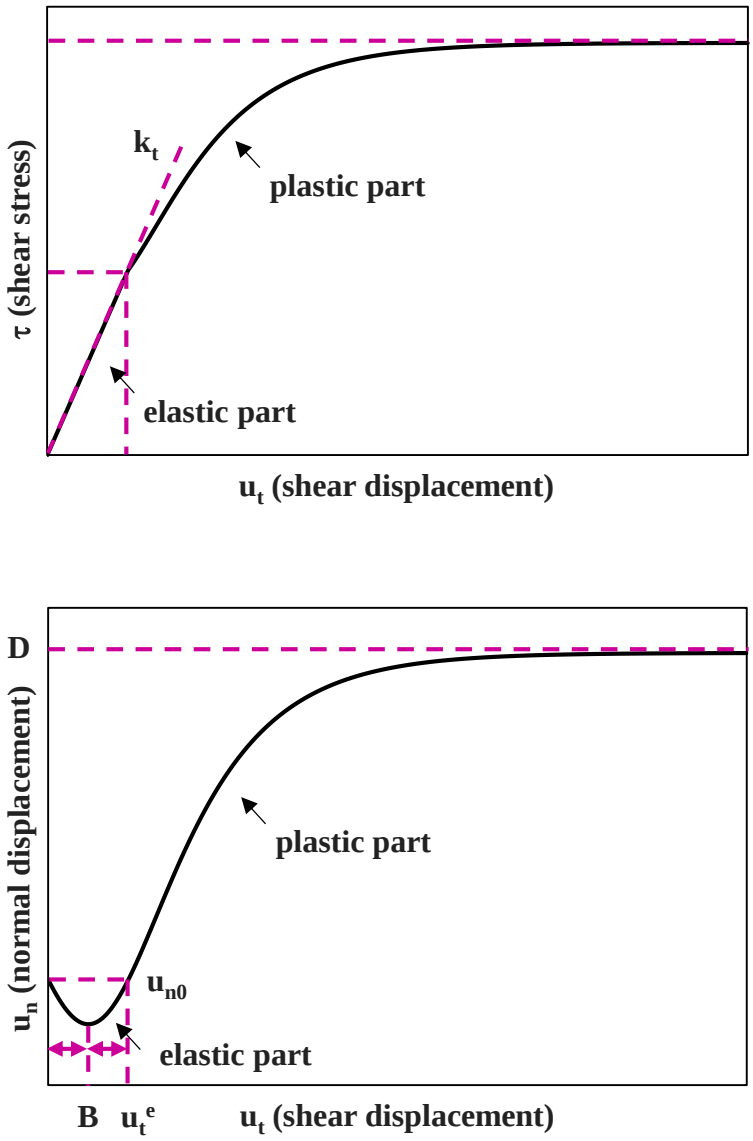


*Figure 3.16 : Determination of interface shear stiffness*

### 3.4.4 Calibration on direct shear tests results: example of sand samples

At first, in order to evaluate the reliability of our model as well as of our proposed function, this part will rely on experimental results presented in the thesis of Pra-ai (2013) under the National SOLCYP Project (2008-2013).

A series of monotonic shear tests has been carried out by Pra-ai (2013) on dense and loose sand samples from the Fontainebleau using a rough or smooth plate to represent the pile. In the following, we will consider the results of shear tests carried out on the dense samples using rough plates in order to calibrate our parameters. Some examples of these tests results are shown in section 3.2.3 (see figure 3.5). Dense sand samples clearly showed dilative behaviour followed

by a degradation phase. The following table summarises the conditions of monotonic interface shear tests realised by Pra-ai (2013) and adopted in the calibration.

*Table 3.1: Conditions of monotonic direct shear tests, dense sand and rough plate, (Pra-ai 2013)*

| Type of plate | Normal stiffness $k_n$ (kPa/mm) | Initial normal stress $\sigma_{n0}$ (kPa/mm) |
|---|---|---|
| Rough | 0 (CNL) | 60, 120, 310 |
| Rough | 1000 (CNS) | 60, 100, 310 |
| Rough | 2000 (CNS) | 100 |
| Rough | 5000 (CNS) | 60, 100, 310 |

The mobilised critical friction angle determined from different shear tests is equal to 30°. This value of friction angle will be used in the simulations.

Using MATLAB fitting application "Curve fitting", all of the parameters defined for the equation 3.22 are extracted from the experimental curves under study. Figure 3.17 presents values of $u_{n,peak}$, B, D and $A_d$ derived from monotonic CNL tests and CNS tests with $k_n$ = 1000 and 5000 kPa/mm on dense sand.

The parameter $u_{n,peak}$ clearly increases as a function of normal stress but decreases as a function of normal stiffness (figure 3.17a). It seems like the normal stiffness have more influence on $u_{n,peak}$ at high initial normal stress than low initial normal stress. The parameter B also shows the same trends as a function of $k_n$ and $\sigma_{n0}$ (figure 3.17b). Unlike $u_{n,peak}$, $k_n$ has more effect on B at low $\sigma_{n0}$ than at high $\sigma_{n0}$. An increase of normal stiffness and normal stress totally or partially inhibits the change in volume, and as consequence it causes the reduction rate of D (figure 3.17c). The influence of normal stiffness on D is the same at all levels of initial normal stress. Considering $A_d$, this parameter decreases as a function of $k_n$ but increases as a function of $\sigma_{n0}$ (figure 3.17d). The variation of has approximately no influence on the evolution of $A_d$ at low initial normal stress.

After the determination of the corresponding values of each parameter, the next step is to define the equation of their evolution as a function of $k_n$ and $\sigma_{n0}$. For this purpose, MATLAB application "curve fitting" is also used for the calibration of functions, Parameter = f ($k_n$,$\sigma_{n0}$). This calibration work showed that the key parameters can be written as a second-degree polynomial equation in function of $k_n$ as shown in the following equations:

$$u_{n,peak} = a_1 {k_n}^2 + b_1 k_n + c_1 \tag{3.25}$$

$$B = a_2 {k_n}^2 + b_2 k_n + c_2 \tag{3.26}$$

$$D = a_3 {k_n}^2 + b_3 k_n + c_3 \tag{3.27}$$

$$A_d = a_4 {k_n}^2 + b_4 k_n + c_4 \tag{3.28}$$

Where each parameter $a_i$ and $b_i$ is defined as a linear equation in function of $\sigma_{n0}$. Table 3.2 summarises the expressions of these parameters.

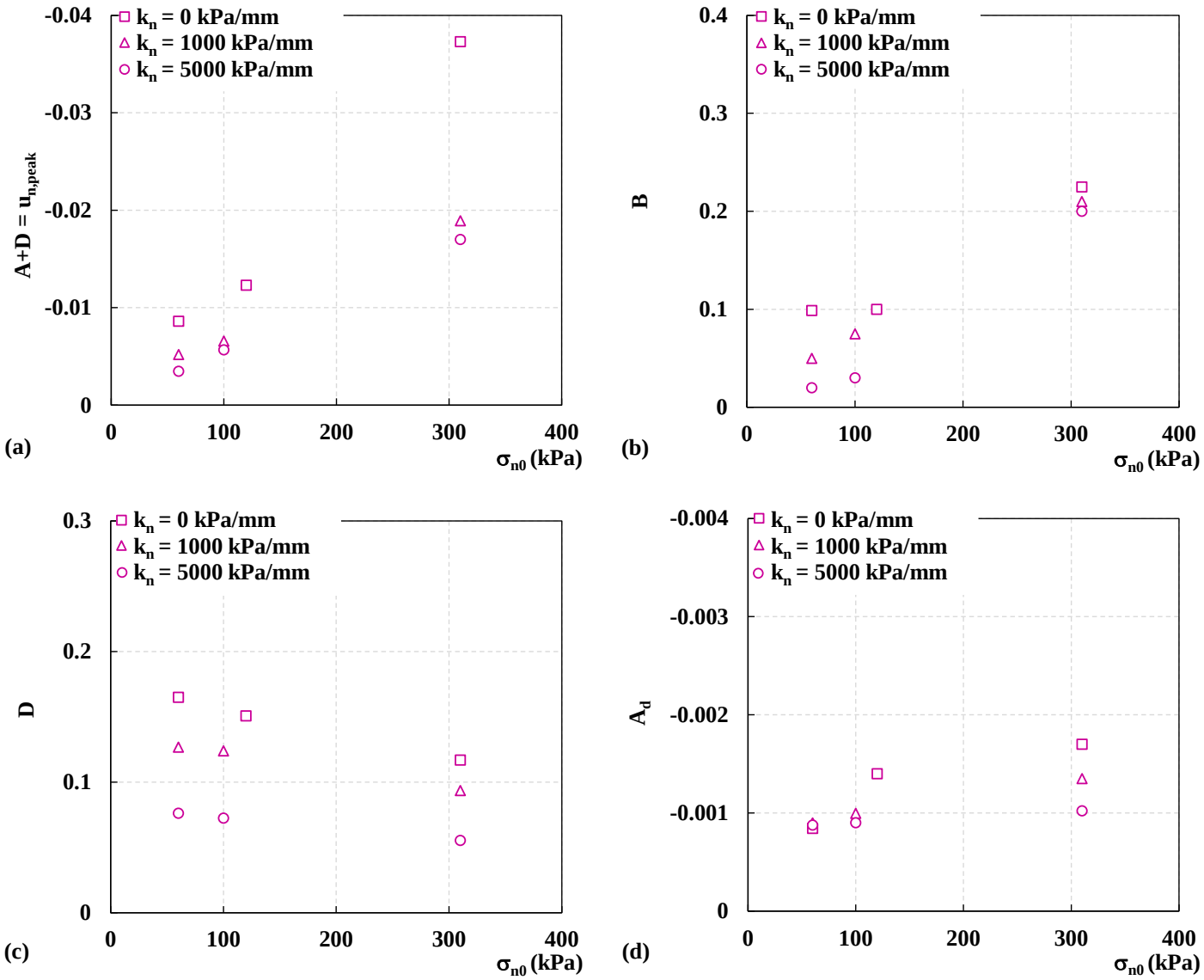


*Figure 3.17 : Calibrated values of key parameters of the numerical equation with different values of $k_n$ and $\sigma_{n0}$, dense sand and rough plate*

*Table 3.2 : Summary of key parameters in function of $\sigma_{n0}$ (kPa), dense sand and rough plate*

| $a_1$ | $b_1$ | $c_1$ |
|---|---|---|
| $-1.2e^{-11} * \sigma_{n0} + 1.4e^{-10}$ | $7.2e^{-8} * \sigma_{n0} - 5.4e^{-7}$ | $-1.2e^{-4} * \sigma_{n0} - 1.0e^{-3}$ |
| $a_2$ | $b_2$ | $c_2$ |
| $2.0e^{-11} * \sigma_{n0} + 1.1e^{-9}$ | $-9.6e^{-8} * \sigma_{n0} - 1.8e^{-5}$ | $7.2e^{-4} * \sigma_{n0} + 3.0e^{-2}$ |
| $a_3$ | $b_3$ | $c_3$ |
| $-6.4e^{-12} * \sigma_{n0} + 4.6e^{-9}$ | $5.2e^{-8} * \sigma_{n0} - 4.1e^{-5}$ | $-2.0e^{-4} * \sigma_{n0} + 1.7e^{-1}$ |
| $a_4$ | $b_4$ | $c_4$ |
| $-1.3e^{-13} * \sigma_{n0} - 1.2e^{-11}$ | $1.1e^{-9} * \sigma_{n0} + 6.6e^{-8}$ | $-2.7e^{-6} * \sigma_{n0} - 8.6e^{-4}$ |

The parameter A is then determined according to the following equation:

$$A = u_{n,peak} - D \tag{3.29}$$

### *3.4.4.1 Comparison with experimental results*

In order to analyse the potentialities of the constitutive law based on a shear test under CNS conditions, the model equations presented in section 3.3.1 as well as the calibrated equation presented in section 3.4.1 are implemented in EXCEL using the VBA language.

Figures 3.18a, 3.18b, 3.18c and 3.18d show the comparison between the experimental results and model predictions of monotonic CNS tests with $\sigma_{n0}$=100 kPa, $k_n$=1000, 2000 and 5000 kPa/mm on dense sand (Pra-ai 2013). Results of CNS tests with $k_n$=2000 kPa/mm, were not used initially to calibrate our numerical equation.

The capability of the proposed model to simulate the experimental observations is satisfactory. Indeed, the proposed model can well simulate the interface behaviour, especially at large tangential displacement where the degradation phase is clearly well represented (figure 3.18). It can clearly reproduce the critical phase of the interface. However, it should be noted that the proposed model lacks the ability to reproduce the peak shear stress. It only shows the contracting behaviour after the dilation phase without presenting a clear peak of the shear stress. This observation is probably related to the choice of the perfect plasticity considered in our model. Figure 3.18d clearly shows this behaviour where the calculated stress paths do not meet experimental stress paths, except at the plasticity where the variation of the two stresses is related to the rupture criterion with a friction angle equal to 30°. Comparisons with experimental results considering other values of $k_n$ and $\sigma_{n0}$ can be found in the Appendix A.

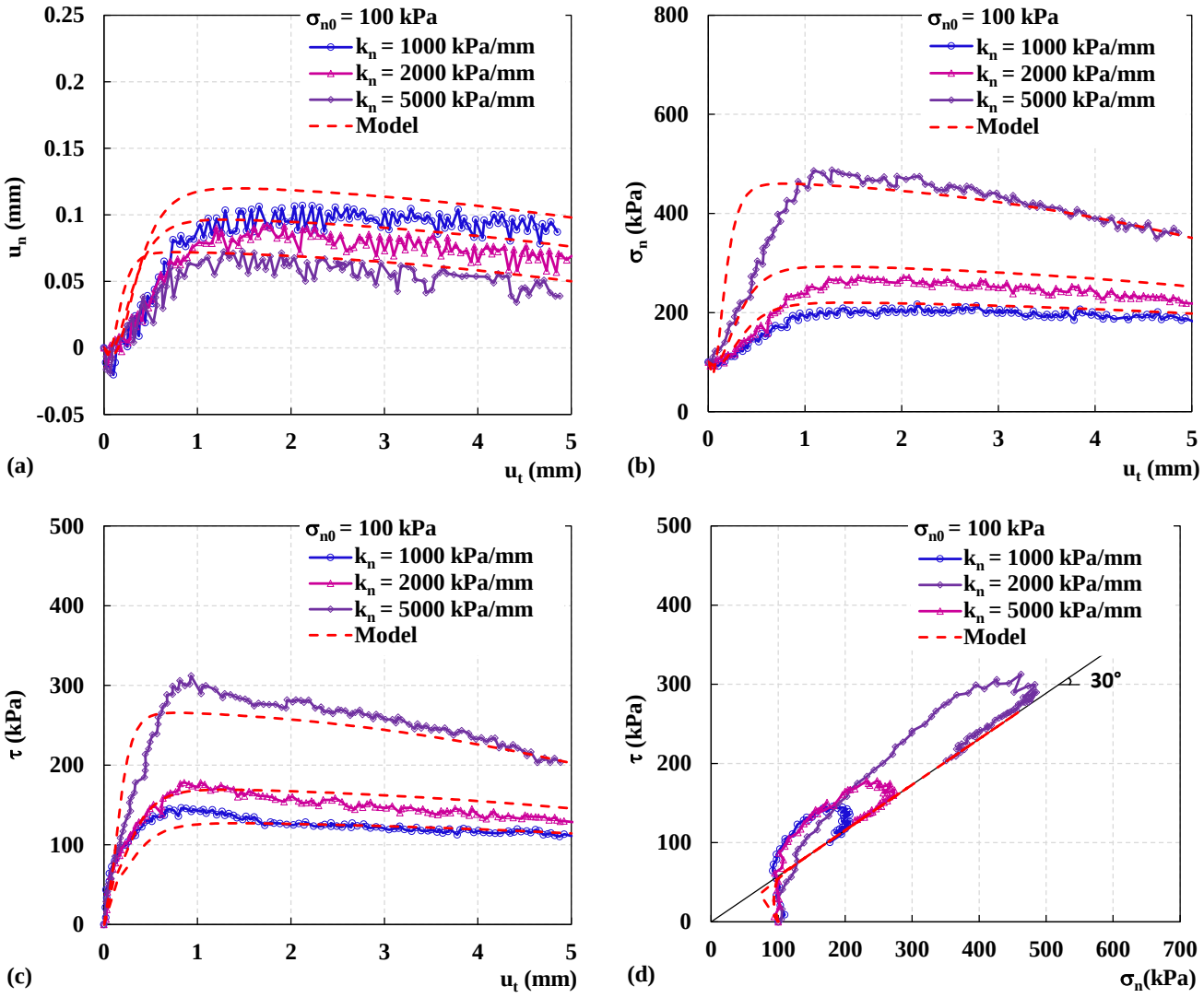


*Figure 3.18 : Comparison between experimental results and model predictions, $\sigma_{n0}$=100 kPa, $k_n$=1000,2000 and 5000 kPa/mm with rough plate and dense sand*

### *3.4.4.2 Comparison with classical Mohr-Coulomb criterion results*

In this section, additional simulations of a shear test under CNS conditions are be carried out using the proposed model. The aim is to compare our developed model results with simulation results obtained while using another model combining linear elasticity and a classical Mohr-Coulomb failure criterion (MC model) considering different values of dilatancy angle, $\psi$. The elastic parameters of the interface, $k_t$ and $k_n$, as well as the strength characteristic $\varphi$ are the same for both models. In this calculation example, $\sigma_{n0}$ is set equal to 100 kPa and $k_n$ equal to 1000 kPa/mm. Considering our proposed model, calculations will be held one time using the numerical equation 3.20 where no additional degradation will be considered after the dilation phase ($A_d$ = 0), and the other time using the numerical equation 3.22 where the parameter $A_d$ is

not equal to zero reflecting additional contractive phase. The other parameters of the numerical equation will be taken as they were calibrated previously. Similarly, regarding the MC model, three values of the dilatancy angle, $\psi$, will be considered, 0°, 1° and 2°.

Figures 3.19a, 3.19b, 3.19c and 3.19d present simulation results. The elastic domain is the same in all cases, where the shear stress evolves linearly. The interface reaches the plastic regime at the same time in all simulations.

The normal stress is constant according to the MC model while it varies according to the proposed numerical equation when using the developed model.

With the MC model, in the plastic regime, no further variation of the shear stress neither of the normal stress with $\psi$=0, no hardening is considered. While when $\psi$ increased, the normal stress associated with shear stress are continuously increasing where the rate of evolution increases as $\psi$ increases: the interface behaviour is always dilative with linear hardening.

With the proposed model, in the plastic regime, we can notice an increasing of the normal stress along with the shear stress considering the two simulations done ($A_d = 0$ and $A_d \neq 0$): the interface behaviour is firstly dilative. However, the proposed model allows the transition from an initial dilating to either contracting behaviour ($A_d \neq 0$) or stable behaviour ($A_d = 0$) where no further hardening is shown. Hence, the increase of stress state evolves with the shear displacement until reaching the maximum value and then either remains unchanged or decreased to the critical state.

These results justify the use of a constitutive model with modified flow rule different from the conventional MC criterion that is non-adapted to our purpose.

Additional simulations, using the calibrated experimental curve, with different values of normal stiffness and normal stress, always considering shear tests under CNS condition are presented in the Appendix A.

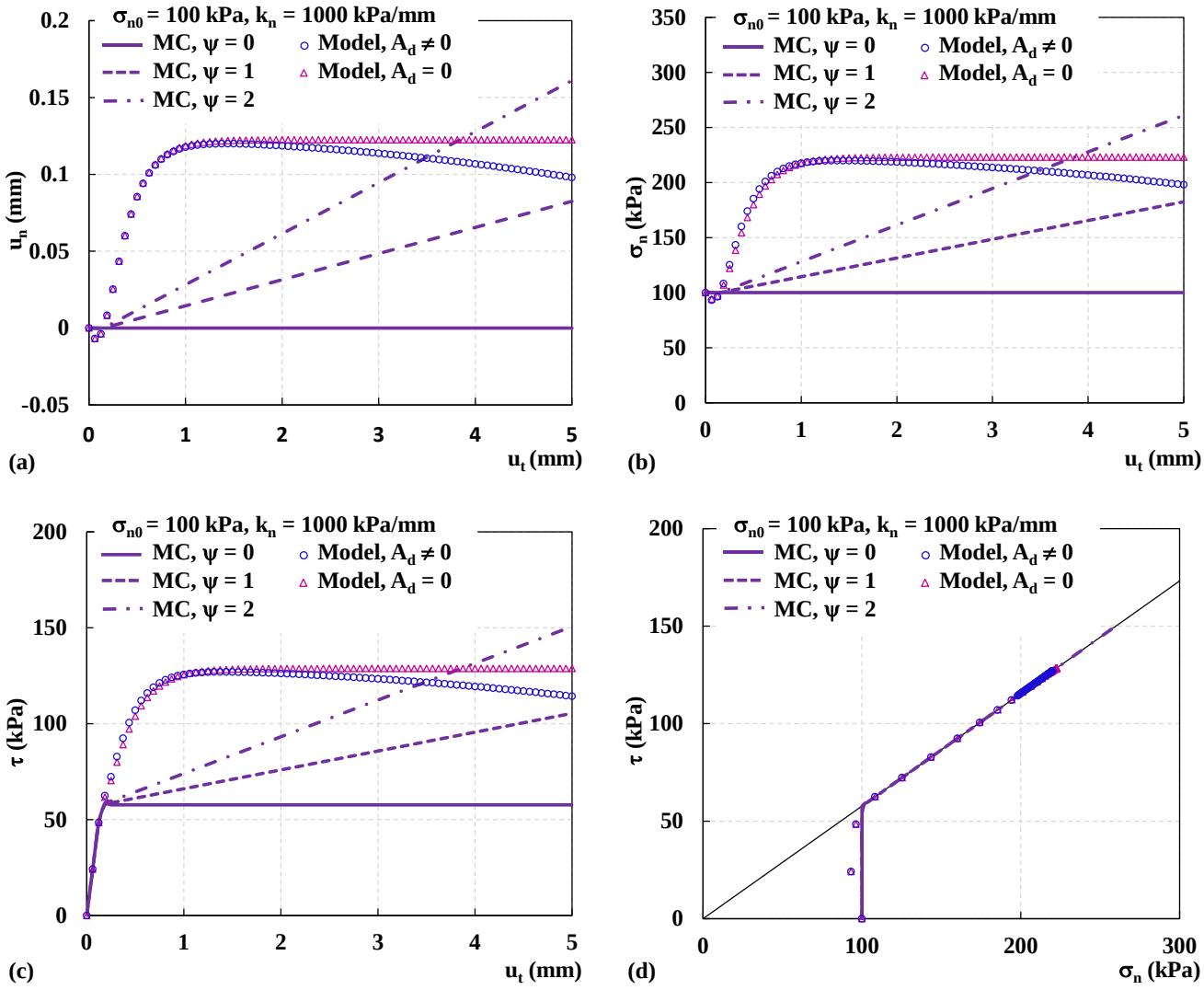


*Figure 3.19 : Comparison between calculation results with classical Mohr-Coulomb criterion and model predictions, $\sigma_{n0}$=100 kPa, $k_n$=1000 kPa/mm*

### 3.4.5 Calibration on direct shear tests results: example of chalk samples

In order to calibrate our model to a greater number of tests and considering chalk samples, results of shear tests on chalk samples have been recently provided in the frame of the French national project SOLCYP+ (continuation of SOLCYP). An experimental study has been recently held in Laboratoire 3SR, in Grenoble, in order to assess the behaviour of the interface between chalk and steel. The objective of SOLCYP+ project is to enhance the design of monopiles forming the foundations of offshore wind turbine parks in the north-west of France. For this purpose, an experimental campaign of several interface shear tests under CNS conditions has been done.

A series of monotonic shear tests has been performed considering low-density remoulded chalk and smooth interface, under constant normal stiffness (CNS) condition adopting different

combinations of normal stiffness $k_n$ and initial normal stress $\sigma_{n0}$. Table 3.3 presents the conditions of interface shear tests performed on chalk samples and used in the calibration. The mobilised friction angle determined from different shear tests was found equal to 28°. This value will be used in the following simulations.

*Table 3.3 : Conditions of monotonic direct shear tests, low-density remoulded chalk and smooth plate*

| **Type of plate** | **Normal stiffness $k_n$ (kPa/mm)** | **Initial normal stress $\sigma_{n0}$ (kPa/mm)** |
|---|---|---|
| Smooth | 500 (CNS) | 100, 200, 300 |
| Smooth | 1500 (CNS) | 100, 200, 300 |
| Smooth | 2500 (CNS) | 100, 200, 300 |

Following the same procedure in part 3.4.4, different parameters of the numerical equation were extracted from the corresponding experimental curves using MATLAB fitting application "Curve fitting". Parameter A, B and D obtained from the combinations of different shear tests under CNS conditions ($k_n$= 500, 1500 and 2500) are presented in figure 3.20.

The parameter A tends to increase with increasing initial normal stress, but it shows an opposite tendency as the normal stiffness increases (figure 3.20a). The effect of normal stiffness increases as the initial normal stress increases. The parameter B decreases with increasing both variables, initial normal stress and normal stiffness (figure 3.20b). The effect of normal stress seems to be steady with different values of initial normal stress. The parameter D obviously increases as a function of $\sigma_{n0}$ whereas it shows a decreasing tendency with increasing $k_n$ (figure 3.20c). The effect of $k_n$ has more influence on D for higher values of $\sigma_{n0}$, especially for the lowest value of $k_n$.

As in the first calibration example (sand samples), the key parameters of the numerical equation can be expressed in this example as a second-degree polynomial equation in function of $k_n$ as shown in the following equations:

$$A = a_1 {k_n}^2 + b_1 k_n + c_1 \tag{3.30}$$

$$B = a_2 {k_n}^2 + b_2 k_n + c_2 \tag{3.31}$$

$$D = a_3 {k_n}^2 + b_3 k_n + c_3 \tag{3.32}$$

Table 3.4 presents the expressions of each parameter ai and bi described as a linear equation in function of $\sigma_{n0}$.

Comparisons of calculation results to experimental results are shown in figure 3.21. It should be noted that the elastic parameter of the interface, the shear stiffness $k_t$, is taken equal to the normal stiffness $k_n$ in each simulation, in order to imitate the initial slope of different mobilised shear stress.

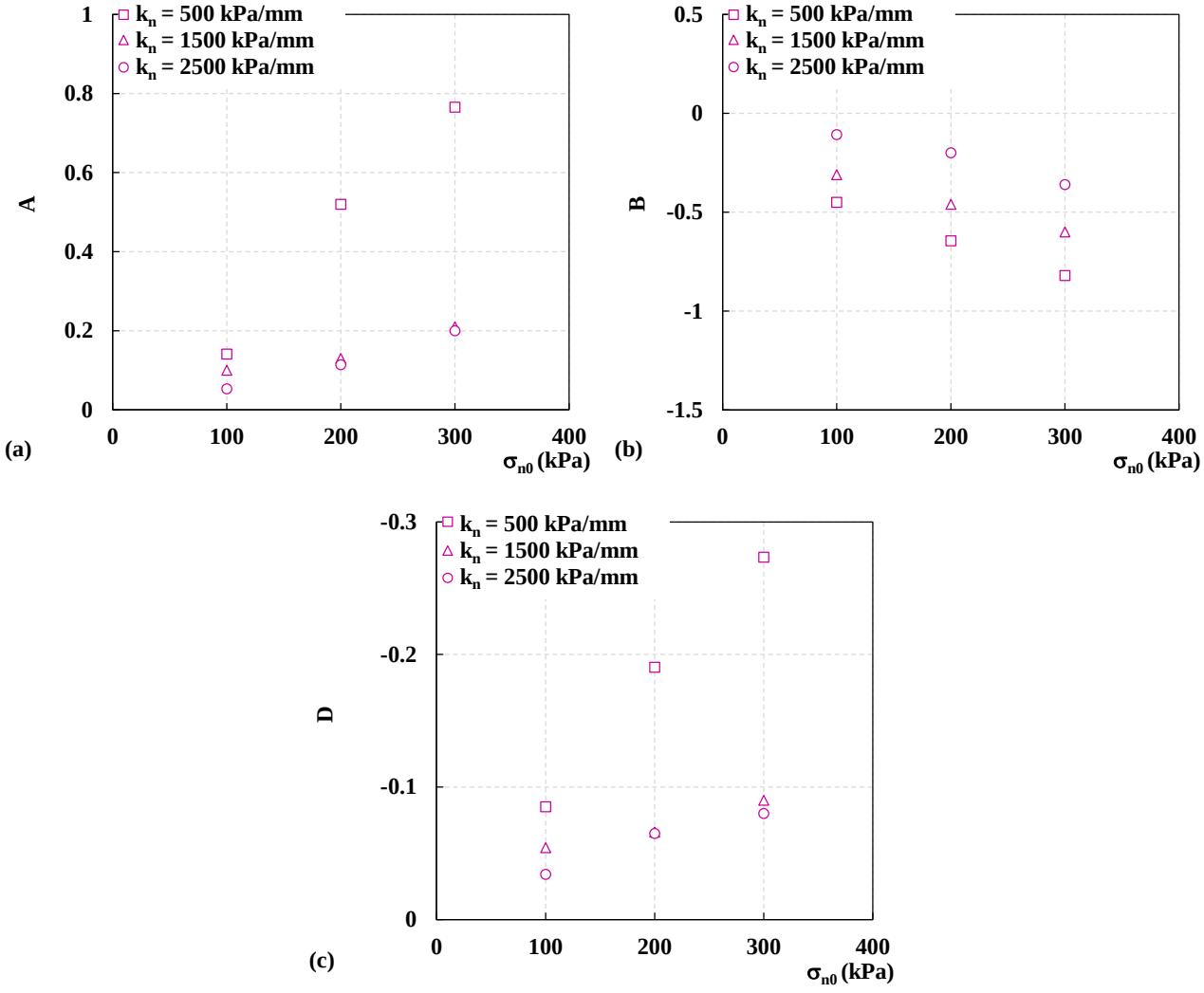


*Figure 3.20 : Calibrated values of key parameters of the numerical equation with different values of $k_n$ and $\sigma_{n0}$, low-density remoulded chalk and smooth plate*

*Table 3.4 : Summary of key parameters in function of $\sigma_{n0}$ (kPa), low-density remoulded chalk and smooth plate*

| $a_1$ | $b_1$ | $c_1$ |
|---|---|---|
| $1.4e^{-9} * \sigma_{n0} - 1.2e^{-7}$ | $-5.3e^{-6} * \sigma_{n0} + 4.3e^{-4}$ | $5.4e^{-3} * \sigma_{n0} - 3.3e^{-1}$ |
| $a_2$ | $b_2$ | $c_2$ |
| $-1.0e^{-10} * \sigma_{n0} + 4.7e^{-8}$ | $6.1e^{-7} * \sigma_{n0} + 7.5e^{-6}$ | $-2.1e^{-3} * \sigma_{n0} - 2.8e^{-1}$ |
| $a_3$ | $b_3$ | $c_3$ |
| $-5.0e^{-10} * \sigma_{n0} + 4.0e^{-8}$ | $1.7e^{-6} * \sigma_{n0} - 1.2e^{-4}$ | $-1.7e^{-3} * \sigma_{n0} + 5.5e^{-2}$ |

Comparisons presented in this part cover the shear tests performed with $\sigma_{n0}$=200 kPa for different values of $k_n$ (500, 1500, 2500 kPa/mm). The proposed numerical equation with the calibrated parameters presents well the experimental curves as shown in figure 3.21a. The variation of normal stress, presented in figure 3.21b, which is proportional to the variation of normal displacement is also well simulated. Although the proposed model can satisfactorily reproduce the evolution of the mobilised shear stress at large tangential displacement, some inconsistencies are noticed especially at small tangential displacement. The proposed model could note simulate the mobilised shear stress at small tangential displacement (figure 3.21c). Stress paths illustrated in figure 3.21d confirm these observations. Calculated stress paths are far different from experimental stress paths, except at the very end of loading. Same observations were noticed in the first example (sand samples).

Comparisons of other experimental results and the corresponding calculated results are presented in the Appendix B.

Additional calculations are presented in the Appendix B in order to determine the capacity of the calibrated equation to present the behaviour of a contractant interface for different combinations of normal stiffnesses and initial normal stresses.

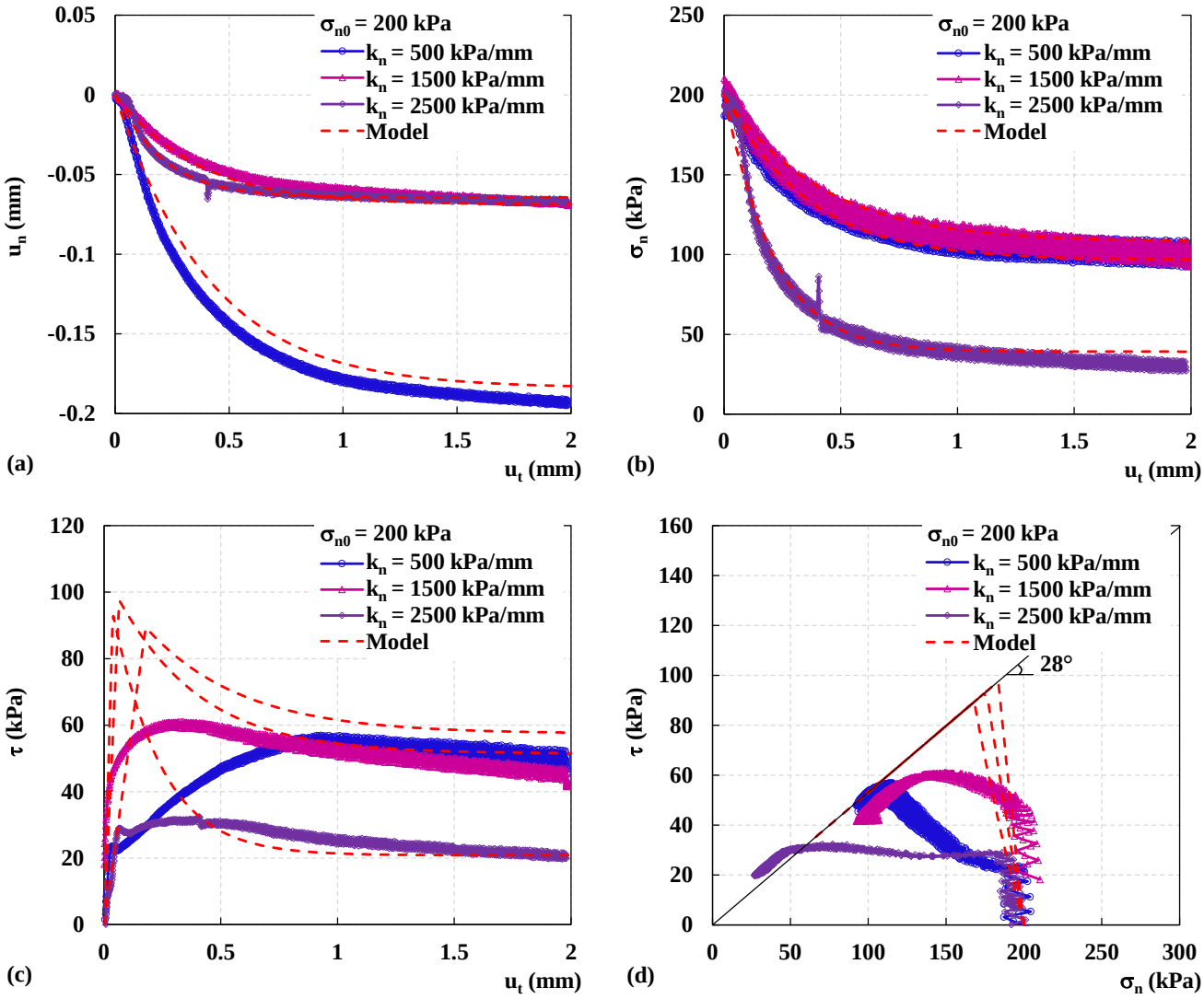


*Figure 3.21 : Comparison between experimental results and model predictions, $\sigma_{n0}$=200 kPa, $k_n$=500,1500 and 2500 kPa/mm with smooth plate and low-density remoulded chalk*

## 3.5 Proposition of a numerical equation for experimental curves: cyclic loading

One of the major issues, related to cyclic loading and addressed in the first chapter and in the review sections at the beginning of this chapter, is the degradation of the interface normal stress during cyclic shearing. This phenomenon is of great importance due to its direct consequence which is the degradation of the bearing capacity of the pile.

This study focuses on the analysis of the mechanism of shear resistance degradation along the pile shaft under cyclic loading. In the current work we will attempt to model the decrease in the cyclic normal stress at the soil-pile interface based on cyclic shear tests under CNS conditions. In this perspective, the relative normal displacements, accumulated during cycles, are described as pseudo-creep functions. Eventually, a simple analytical formulation of the variation of the

normal stress according to cyclic characteristics can be directly translated into variation of the interface shear stress. A first condition is therefore to have a quality database with a sufficient number of experimental results.

The evolution of the cyclic normal displacement depending on the number of cycles can be mathematically presented using a specific numerical equation that will be explained and calibrated in the following sections, depending on different cyclic parameters.

### 3.5.1 Numerical equation

The description of the normal displacement paths according to the number of cycles N must use a relatively simple expression that makes it possible to visualise and calibrate the equations according to the results of experimental shear tests. This numerical expression should consider the important reduction in normal stress due to the accumulation of contraction encountered in the case of CNS condition.

The expression of rational equation is considered to represent the evolution of the mean cyclic normal displacement in function of the number of cycles (equation 3.33). This equation is retained due to its capability to produce the possible rate of degradation and final value reached by the normal displacement at large number of cycles that may be encountered in the case of pile foundation for offshore structures.

$$u_n = f(N) = \frac{A_c N^2 + B_c N}{C_c + N} \tag{3.33}$$

Figure 3.22 illustrates the graphical representation of equation 3.33. This figure presents the final shape of the proposed equation which illustrates the evolution of normal displacement, considering the middle, the top or the bottom of the cycle, in function of cycles number, N. It should be noted that positive values of normal displacement considered here, reflect the contraction.

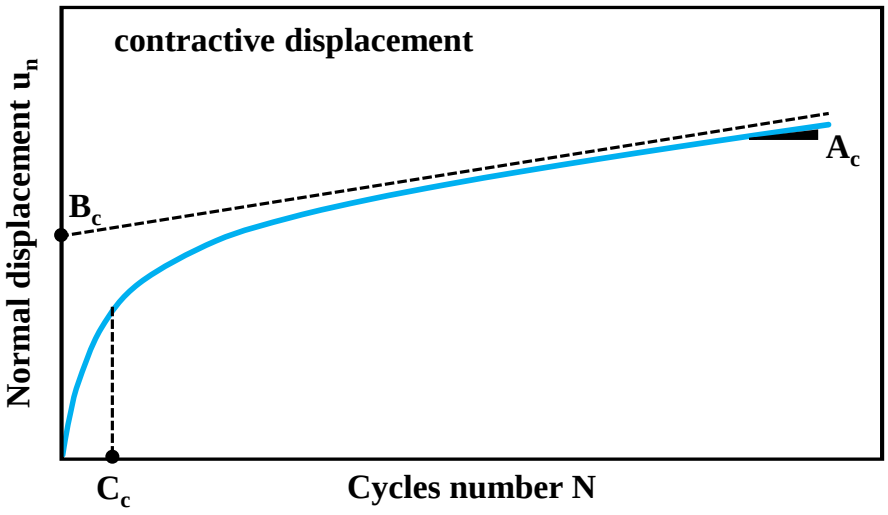


*Figure 3.22 : Graphical representation of the numerical equation, $u_n = f(N)$*

As it can be seen in figure 3.22, parameter $C_c$ presents the number of cycles which separate the two rates of the evolution of cyclic normal displacement. Before reaching this number of cycles, the evolution of displacement is fast. After that, the rate of evolution begins to decrease until reaching a certain asymptote. Parameter $B_c$ defines the y-axis intercept of the asymptote of the curve for large number of cycles. The slope of this asymptote is set by the parameter $A_c$.

The procedure of the calibration of each parameter based on shear tests will be discussed later. Each parameter should be formulated in a certain way that considers different cyclic characteristics.

### 3.5.2 Parametric study

In order to quantify the effect of different parameters on the global shape of the numerical expression given in equation 3.33, a parametric study is performed for a given set of parameters. For each parameter, two different values are considered.

Figure 3.23a illustrates the effect of $A_c$. As it was defined, this parameter influences the slope of the second part of the curve. The variation of $A_c$ has no effect on the first part of the curve, i.e., for a number of cycles smaller than $C_c$. On the other hand, for a number of cycles higher than $C_c$, increasing the value of $A_c$ generates a faster rate of evolution, and therefore a higher value of normal displacement reached for the same number of cycles (for example for 10000 cycles).

The parameter $B_c$ has an influence on the entire curve (figure 3.23b). As $B_c$ increases, the rate of evolution is not affected but the value of the normal displacement increases for any value of N.

As $C_c$ decreases, the normal displacement reaches faster its asymptotic value. In this case, the numerical equation provides steeper curves at the origin (figure 3.23c).

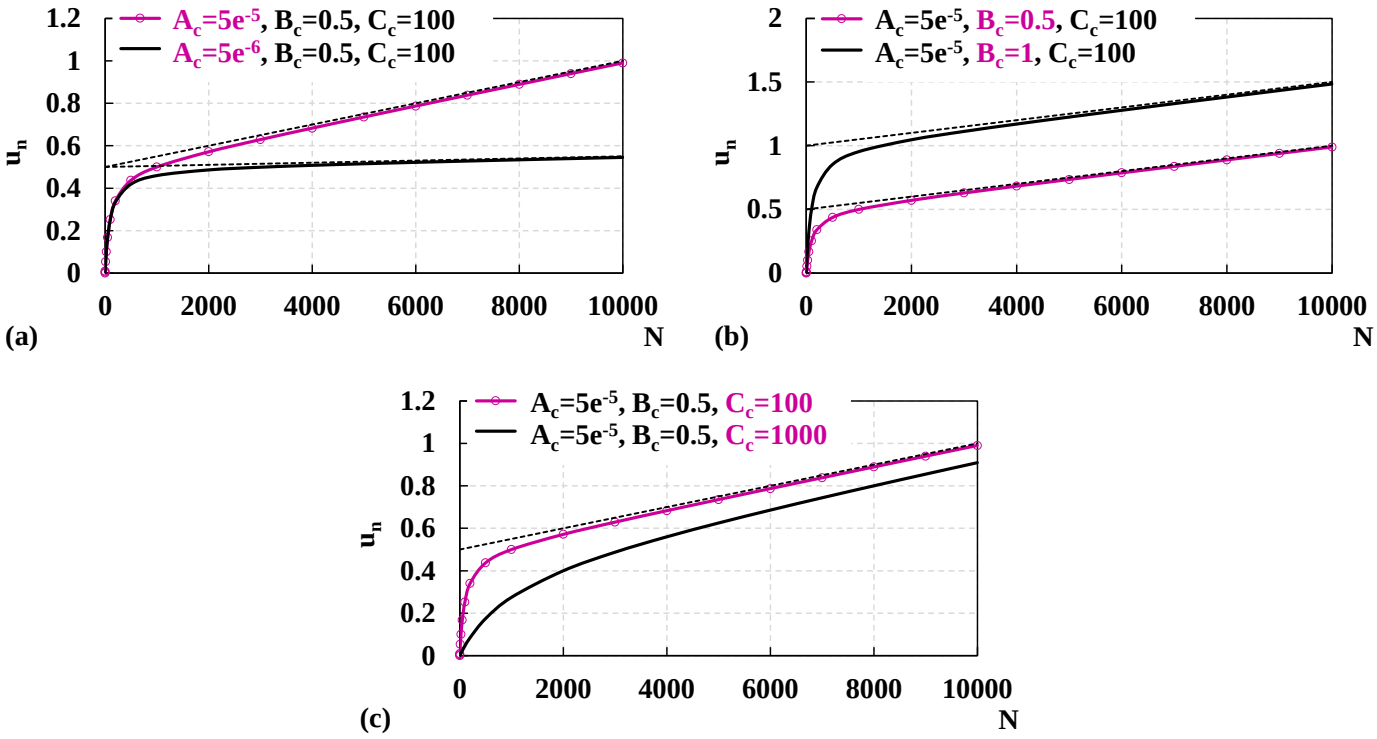


*Figure 3.23 : Influence of the numerical expression parameters on the evolution of normal displacement in function of number of cycles*

### 3.5.3 Example of calibration: chalk sample ((Carrington et al. 2011)

The methodology is essentially phenomenological. The main objective is to model the results of laboratory tests which are considered as of good quality, and which simulate conditions as close as possible to the real response of the interface. For this purpose, all the parameters mentioned in the numerical equation should be expressed as functions of different cyclic characteristics presenting the real trends inherent to the considered structures.

Although the chalk is the type of soil that we are looking forward in our study, the calibration of the parameters could not be done based on experimental tests carried out on chalk samples, meant to be performed in the frame of the French national project SOLCYP+ (continuation of SOLCYP), due to lack of time and sanitary conditions (COVID-19). In addition, it is clearly mentioned in the first chapter the lack of experimental database, devoted to chalk samples, considering shear tests under cyclic solicitations. However, the only reliable cyclic shear test performed by Carrington et al. (2011) showed the degradation trend anticipated by the normal stress and the shear stress according to the number of cycles. One can notice that the proposed numerical equation may be appropriate to simulate this degradation. The available result in this

test is the evolution of shear stress according to the number of cycles. Knowing that this evolution is directly affected by the evolution of the normal stress, the proposed numerical equation is then used to imitate the trend of shear stress evolution. Figure 3.24 presents the result of this example of simulation. It can be noticed the precise ability of the numerical equation to represent the experimental evolution of the mobilised maximum and minimum shear stress of low to medium density chalk interfaces. It is clear that the rate of degradation decreases with the number of cycles after a rapid degradation at the first cycle.

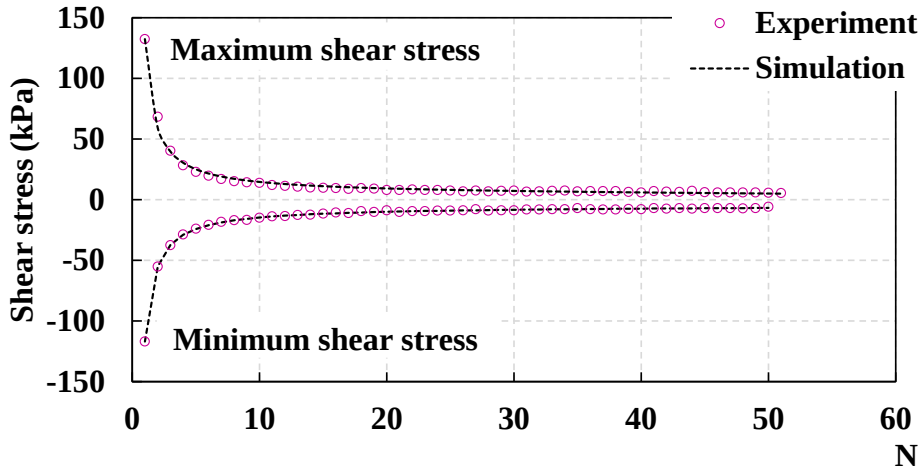


*Figure 3.24 : Simulation of shear stress degradation according to the number of cycles, chalk sample (Carrington et al. 2011)*

In order to extract a general formulation, covering all the possible combinations of cyclic characteristics and initial conditions, a large number of cyclic shear tests is needed. For this purpose, further calibrations will be held considering shear tests on sand samples.

### 3.5.4 Calibration on direct shear tests simulations: example of sand samples

It should be noted that the sand is considered as a well-known material, subjected to a large number of experimental tests available in the literature which have been used to calibrate a large number of numerical models. Based on this idea, we propose to use the results of an experimental shear tests campaign considering sand samples in the aim of calibrating our numerical expression and test its potentiality to imitate the evolution of cyclic normal displacement evolution and therefore normal stress degradation for a great number of cyclic characteristics.

Under the National SOLCYP project (2008-2013), an approach named SOLCYP has been developed to describe the evolution of the actual radial stress at the soil-pile interface. This approach was based on the interpretation of the results of normal constant stress (CNL) and

normal constant stiffness (CNS) shear box tests. The material under study was the sand of Fontainebleau. The campaign of cyclic shear tests has been performed by Pra-ai (2013) to characterise the cyclic behaviour of the sand-pile interface with a large number of cycles (typically a goal of 10000 cycles). Loose and dense samples have been considered in this study as well as rough and smooth interfaces. These tests were mainly under CNL conditions due to the ease of realising this type of tests with a large number of cycles comparing to tests under CNS conditions. Further limited tests under CNS conditions were also performed in order to validate the SOLCYP approach. The main aspect was the contractive behaviour encountered for all the CNS tests. The testing programme followed by Pra-ai (2013) is given in table 3.5. The codification of the tests presented in this table is as follows:

- $\sigma_{n\,cm0}$ is the level of initial mean cyclic normal stress;
- $\eta_{cm0}$ is the level of initial mean cyclic stress ratio: $\eta_{cm0} = \frac{\tau_{cm}}{\sigma_{n\,cm0}}$, where $\tau_{cm}$ is the level of mean cyclic shear stress;
- $\eta_p$ is the peak stress ratio determined from monotonic shear tests;
- $\Delta\tau$ is the cyclic amplitude in terms of shear stress.

*Table 3.5 : Parameters of the soil-structure cyclic shear tests programme carried out by Pra-ai (2013)*

| **Condition** | **$I_{D0}$ (%)** | **$\sigma_{n\,cm0}$ (kPa)** | **$\eta_{cm0}$** | **$\Delta\tau$ (kPa)** | **K (kPa/mm)** |
|---|---|---|---|---|---|
| CNL | 30,90 | 60 | 0; ≈ 1/2$\eta_p$; ≈ 9/10$\eta_p$ | 10 | - |
| | | 120 | 0; ≈ 1/2$\eta_p$; ≈ 9/10$\eta_p$ | 10 | - |
| | | 310 | 0; ≈ 1/2$\eta_p$; ≈ 9/10$\eta_p$ | 10,20,40 | - |
| CNS | 30,90 | 100 | ≈ 1/2$\eta_p$ | 10,20 | 1000, 2000, 5000 |

Pittos (2014) proposed an approach to modelling the degradation in normal stress from the above tests. According to Pittos (2014) work, the evolution of normal displacement, and then the degradation in normal stress, has been formulated depending on six cyclic and mechanical parameters: soil density index $I_D$, initial mean normal stress $\sigma_{n\,cm0}$, initial maximum stress ratio $\eta_{max0}$, cyclic amplitude $\Delta\tau$, imposed normal stiffness $k_n$, and finally the number of cycles N. The following equation presents the general expression developed by Pittos (2014).

$$[u]^{(kn)} = f\,(N, \sigma_{n\,cm0}, \eta_{max0}, \Delta\tau, k_n, I_D) \qquad (3.34)$$

This expression has been firstly formulated based on shear tests under CNL conditions considering the different cyclic characteristics mentioned in table 3.5. Following to that and based on the available number of shear tests under CNS condition, a special procedure has been developed in order to incorporate the effect of imposed normal stiffness. Finally, the evolution

of normal displacement can be determined for any combination of cyclic characteristics, initial normal stress, normal stiffness and soil density.

This procedure has been provided in the form of an excel file in order to benefit from its results in our work. For this purpose, several simulations were done using the provided excel tool and considering CNS condition, in order to use the resulted curves for the calibration of our numerical equation. Thus, our proposed equation will be calibrated using simulated results using SOLCYP approach already validated by Pittos (2014). Table 3.6 shows the simulation programme followed in order to obtain the calibration base. It should be noted that in our work the index "0" is not used in the codification.

Only the dense samples, $I_D$ = 0.9, with rough interfaces are considered here. For each combination of $k_n$ and $\sigma_n$, three levels of solicitation are considered: "L" for low, "M" for medium and "H" for high.

The simulations consist of different combinations of cyclic characteristics, initial normal stress and normal stiffness. According to Pittos (2014), the maximum stress ratio, $\eta_{max}$, is the parameter which its effect is the dominant on the interface behaviour. Figure 3.25 presents an illustration of the sand-structure interface responses under cyclic loading (Pra-ai 2013). These responses depend on three main parameters: the characteristic stress ratio $\eta_{car}$, the critical stress ratio $\eta_{crit}$, and the peak stress ratio $\eta_{peak}$. These parameters are extracted from monotonic shear tests. Pra-ai (2013) has found $\eta_{car}$= 0.555, $\eta_{crit}$= 0.566 and $\eta_{peak}$= 0.79, for dense sand on rough plate. The characteristic state theory indicates that the change from contracting to dilating behaviour is conditioned by the respective position of the normalised shear stress ratio $\eta_{cm0}$ with respect to the $\eta_{car}$. The various modelling attempts done by Pittos (2014) made it possible to conclude that the value of the maximum stress ratio controls the expected response of the interface. Its position with respect to $\eta_{car}$ may generate a contractive or a dilative behaviour as illustrated in figure 3.25. For this purpose, the calibration of our numerical equation will finally rely on $\eta_{max}$, $\sigma_n$, $\Delta\tau$ and $k_n$. It should be noted that $\eta_{car}$ will be considered equal to $\eta_{crit}$ = 0.566 because these two values are so close that as soon as the characteristic value is exceeded the critical value is also exceeded. Under CNS condition $\eta_{max}$ is limited to $\eta_{crit}$ , no dilative behaviour has been noticed (Pra-ai 2013).

*Table 3.6 : Parameters of the soil-structure cyclic shear tests simulation programme*

| $\sigma_n$ (kPa) | $k_n$ (kPa/mm) | $\eta_{cm}$ | $\Delta\tau$ (kPa) | $\eta_{max}$ | Level |
|---|---|---|---|---|---|
| 60 | 0, 500, 1500 | 0 | 10 | 0.083 | L |
| 60 | 0, 500, 1500 | $\approx 1/3\eta_p$ | 10 | 0.333 | M |
| 60 | 0, 500, 1500 | $\approx 1/2\eta_p$ | 10 | 0.5 | H |
| 60 | 0, 500, 1500 | 0 | 20 | 0.167 | L |
| 60 | 0, 500, 1500 | $\approx 1/3\eta_p$ | 20 | 0.417 | M |
| 60 | 0, 500, 1500 | $\approx 1/2\eta_p$ | 20 | 0.55 | H |
| 60 | 0, 500, 1500 | 0 | 30 | 0.25 | L |
| 60 | 0, 500, 1500 | $\approx 1/3\eta_p$ | 30 | 0.5 | M |
| 60 | 0, 500, 1500 | $\approx 1/2\eta_p$ | 30 | 0.566 | H |
| 120 | 0, 500, 1500 | 0 | 10 | 0.042 | L |
| 120 | 0, 500, 1500 | $\approx 1/4\eta_p$ | 10 | 0.25 | M |
| 120 | 0, 500, 1500 | $\approx 2/3\eta_p$ | 10 | 0.5 | H |
| 120 | 0, 500, 1500 | 0 | 20 | 0.083 | L |
| 120 | 0, 500, 1500 | $\approx 1/4\eta_p$ | 20 | 0.292 | M |
| 120 | 0, 500, 1500 | $\approx 2/3\eta_p$ | 20 | 0.542 | H |
| 120 | 0, 500, 1500 | 0 | 30 | 0.125 | L |
| 120 | 0, 500, 1500 | $\approx 1/4\eta_p$ | 30 | 0.333 | M |
| 120 | 0, 500, 1500 | $\approx 2/3\eta_p$ | 30 | 0.566 | H |
| 310 | 0, 500, 1500 | 0 | 10 | 0.016 | L |
| 310 | 0, 500, 1500 | $\approx 1/2\eta_p$ | 10 | 0.355 | M |
| 310 | 0, 500, 1500 | $\approx 2/3\eta_p$ | 10 | 0.516 | H |
| 310 | 0, 500, 1500 | 0 | 20 | 0.032 | L |
| 310 | 0, 500, 1500 | $\approx 1/2\eta_p$ | 20 | 0.371 | M |
| 310 | 0, 500, 1500 | $\approx 2/3\eta_p$ | 20 | 0.532 | H |
| 310 | 0, 500, 1500 | 0 | 30 | 0.048 | L |
| 310 | 0, 500, 1500 | $\approx 1/2\eta_p$ | 30 | 0.387 | M |
| 310 | 0, 500, 1500 | $\approx 2/3\eta_p$ | 30 | 0.548 | H |

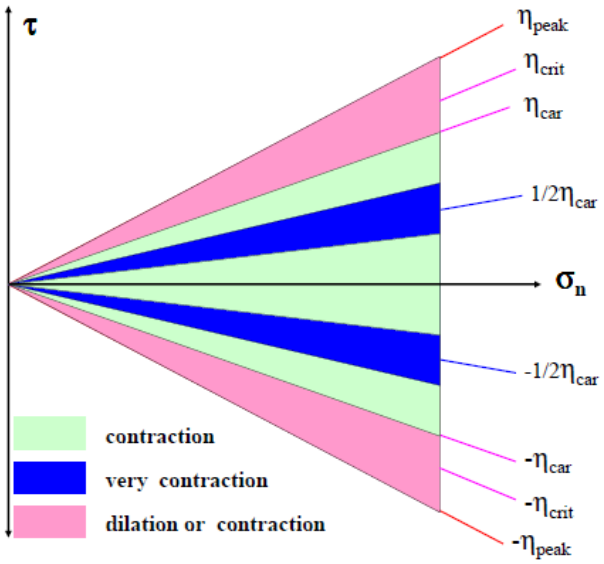


*Figure 3.25 : Behaviour of sand-structure interface under cyclic loading, (Pra-ai 2013)*

In the following section, the calibration procedure will be explained. We will begin first by formulating the equation depending on the number of cycles and values of $\eta_{max.}$ The effect of other parameters will be treated after.

### *3.5.4.1 Step 1: Effect of maximum stress ratio $\eta_{max}$*

Figures 3.26a, 3.26b, 3.26c and 3.26d allow to visualise the evolution of normal displacement obtained from different simulations according to SOLCYP approach (Pittos 2014), considering conditions listed in table 3.6. It presents the influence of the maximum stress ratio $\eta_{max}$ on the global evolution of displacement. It is clear that with increasing the level of $\eta_{max}$, the generated normal displacement increases.

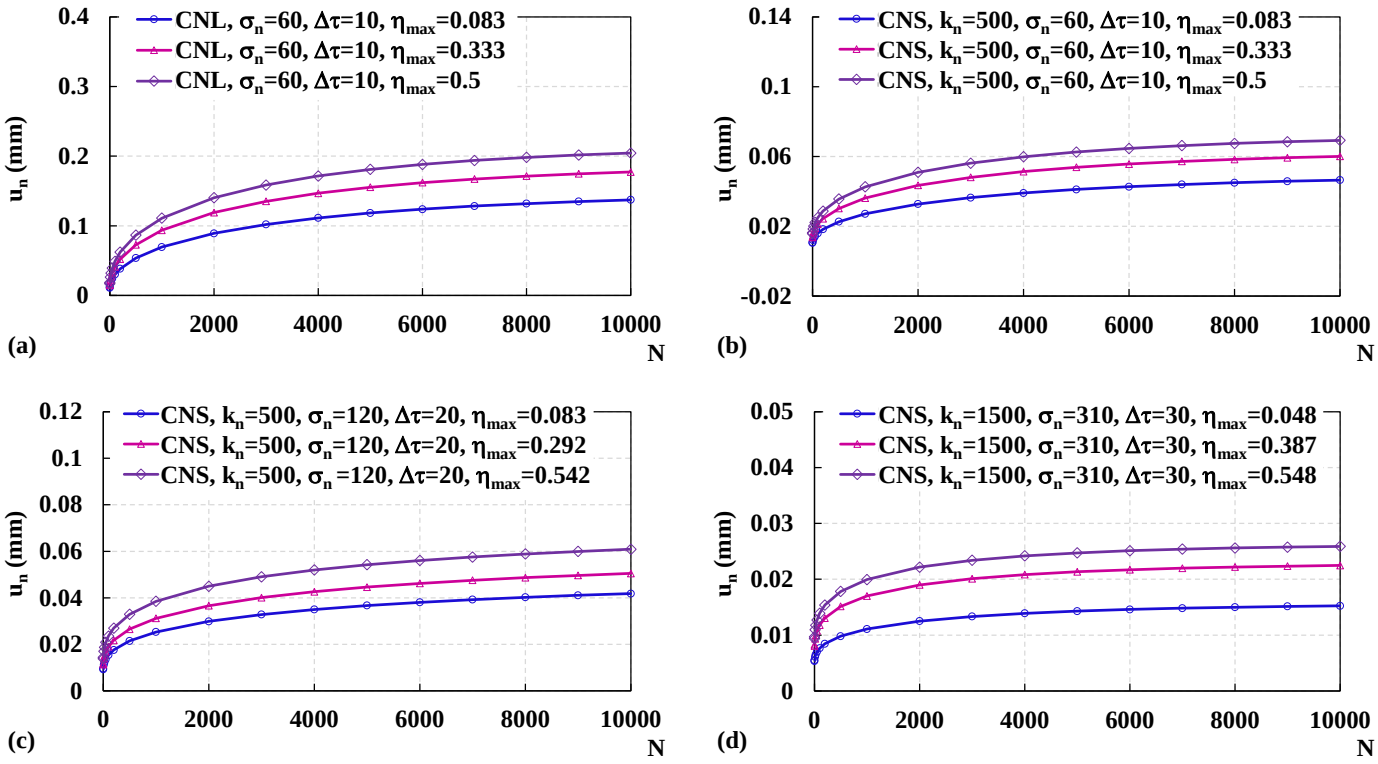


*Figure 3.26 : Effect of maximum stress ratio $\eta_{max}$ for different values of $\sigma_n$, $k_n$ and $\Delta\tau$*

The first step of formulation consists of determining the value of the numerical equation parameters for each simulation. Therefore, the aim is to achieve a global formulation in the form of: $u_n = f(N, \eta_{max})$. For this purpose, several set of three different curves, where the level of $\eta_{max}$ is variable and the other parameters are fixed (figure 3.26), are introduced in MATLAB and its fitting application "Curve fitting" is then used. The fitting is based on the hypothesis that each of the three parameters of the model, $A_c$, $B_c$, and $C_c$ can be considered as a linear function of the variable $\eta_{max}$, which initially seems to give satisfactory results. For the dependence of $k_n$, $\sigma_n$ and $\Delta\tau$ another approach is considered as described below. The reason is to minimise the complexity of calibration. Thus, the equation 3.33 can be written as following:

$$u_n = f(N, \eta_{max}) = \frac{(a_{c1} * \eta_{max} + a_{c2})N^2 + (b_{c1} * \eta_{max} + b_{c2})N}{(c_{c1} * \eta_{max} + c_{c2}) + N} \qquad (3.35)$$

Finally, this expression is introduced in MATLAB in order to calibrate each series of simulated curves. In the end, expressions of type $u_n = f(N, \eta_{max})$ calibrated for each series of simulated data and each combination of values $k_n$, $\sigma_n$ and $\Delta\tau$ are obtained. Comparisons between simulated results presented in figure 3.26 and model results are shown in figure 3.27. These figures show a good agreement between different results. The proposed numerical expression can imitate different simulations performed above.

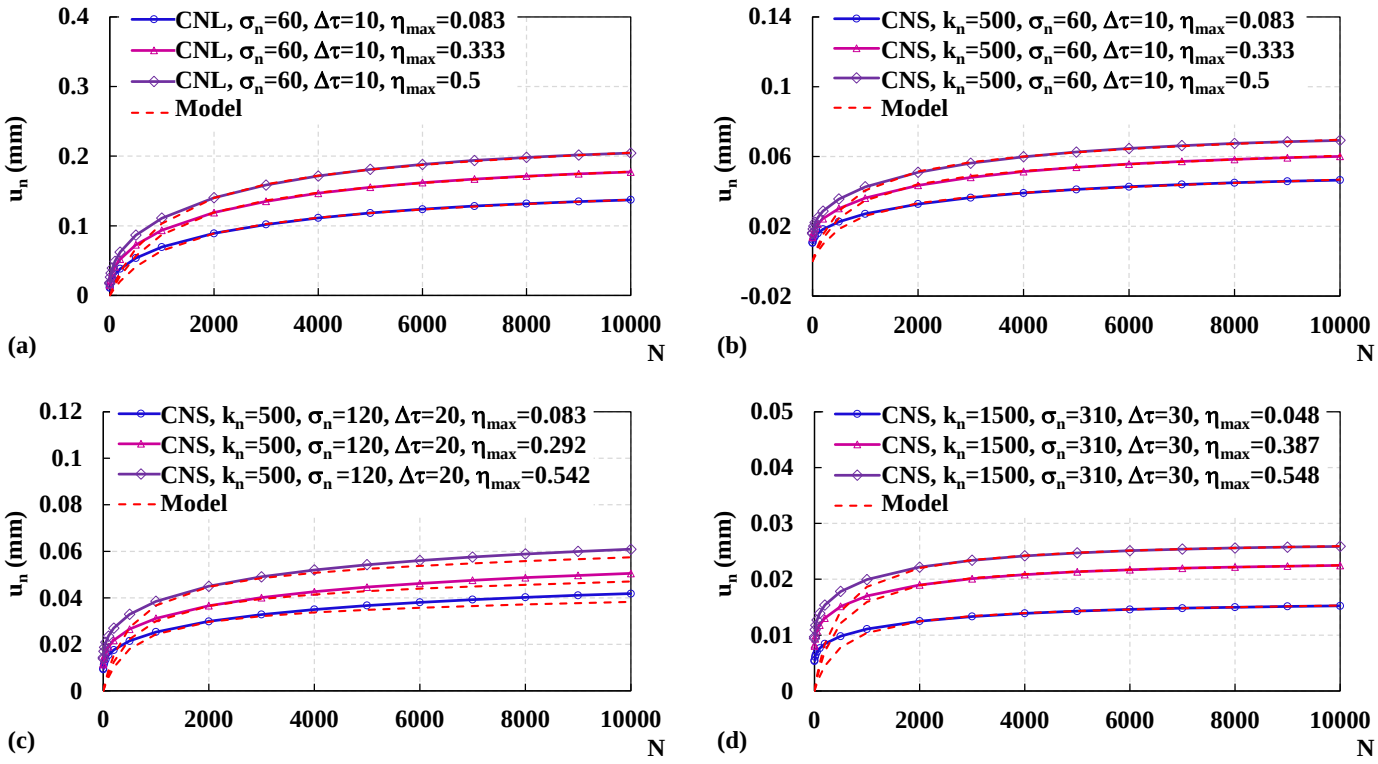


*Figure 3.27 : Comparisons between results of simulations and model results for different series of simulations*

### *3.5.4.2 Step 2: Effect of other parameters: $k_n$, $\sigma_n$, $\Delta\tau$*

In order to visualise the influence of other parameters on the evolution of normal displacement, figures 3.28, 3.29 and 3.30 present the variation trends of normal displacement in function of the normal stiffness, initial normal stress and cyclic amplitude, respectively. These trends are obtained for some performed simulations according to the programme presented in table 3.6. For fixed N values, the results presented in the ($u_n$, $k_n$), ($u_n$, $\sigma_n$) and ($u_n$, $\Delta\tau$) planes, respectively, show the linearity of the trend of each of these parameters.

It can be noticed that the increase of normal stiffness $k_n$ leads to a decrease in the normal displacement for any value of N (figure 3.28). Similarly, it is clear that the normal displacement decreases with increasing the initial normal stress $\sigma_n$ (figure 3.29). On the contrary, the effect of the cyclic amplitude $\Delta\tau$ is not the same. The increase in the value of cyclic amplitude provokes an increase in the normal displacement (figure 3.30).

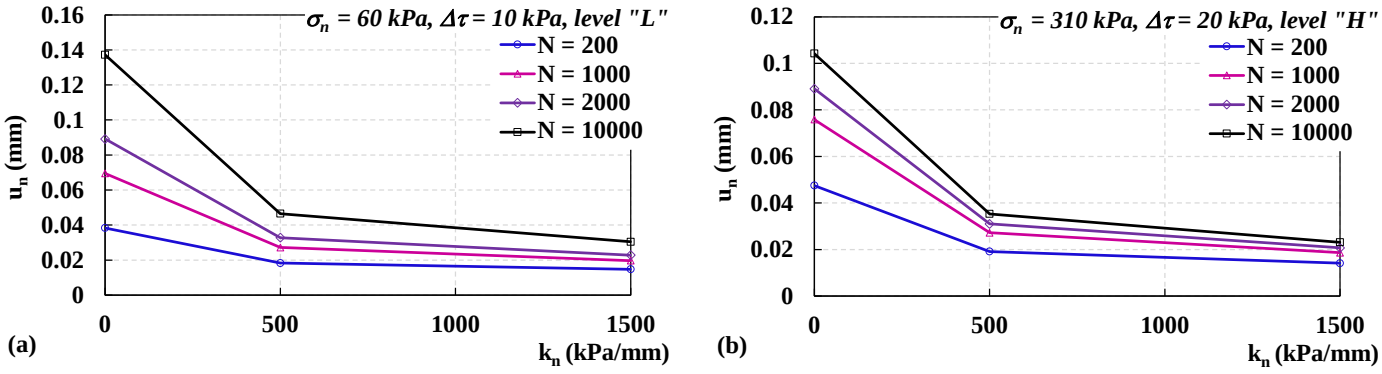


*Figure 3.28 : Effect of normal stiffness $k_n$*

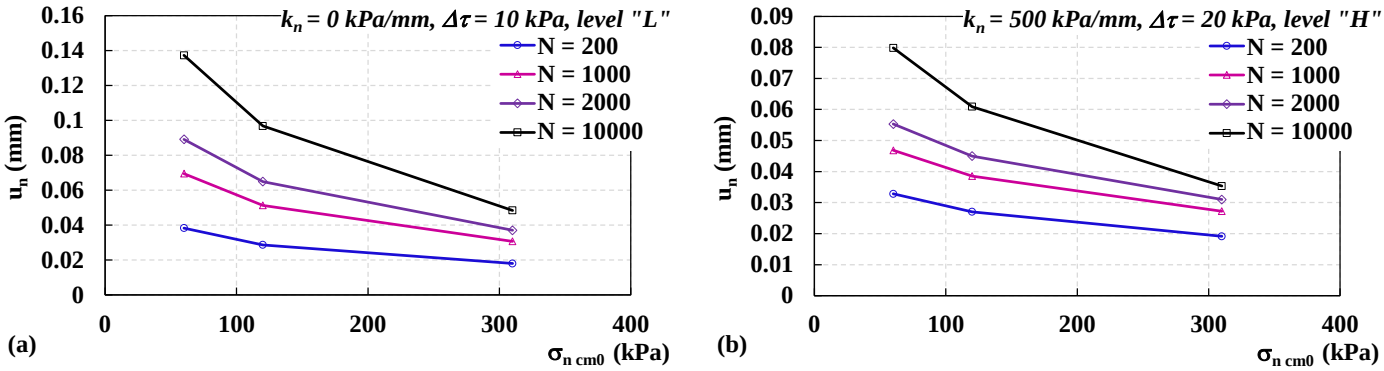


*Figure 3.29 : Effect of initial normal stress $\sigma_n$*

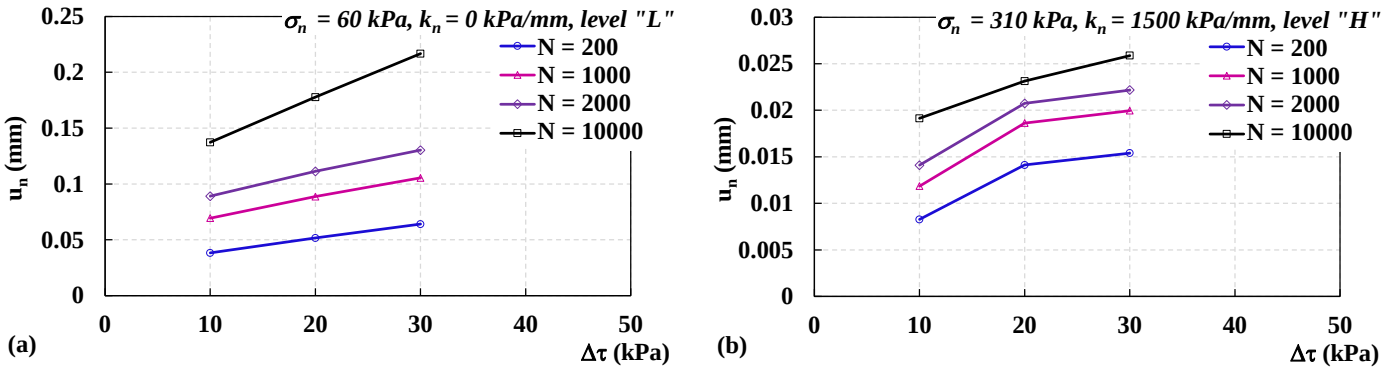


*Figure 3.30 : Effect of cyclic amplitude $\Delta\tau$*

It should be noted that from the procedure followed so far analytical expressions of normal displacement of satisfactory precision are available for each simulation performed. These expressions are in the form of surface functions of N and $\eta_{max}$, for each combination of the initial values of the other parameters ($k_n$, $\sigma_n$, $\Delta\tau$):

$u_n = f$ (N, $\eta_{max}$, $k_n$ = 0; 500; 1500 kPa/mm, $\sigma_n$ = 60; 120; 310 kPa, $\Delta\tau$ = 10; 20; 30 kPa)

In order to consider the influence of the variation of the normal stiffness, the initial normal stress and the cyclic amplitude, an interpolation or extrapolation procedure will be done consecutively.

Considering first the influence of the variation of the normal stiffness. For fixed values of N, $\eta_{max}$, $\sigma_n$ and $\Delta\tau$, we already know:

- $u_{n1}$ = f (N, $\eta_{max}$, $k_n$ = 0 kPa/mm, $\sigma_n$, $\Delta\tau$)
- $u_{n2}$ = f (N, $\eta_{max}$, $k_n$ = 500 kPa/mm, $\sigma_n$, $\Delta\tau$)
- $u_{n3}$ = f (N, $\eta_{max}$, $k_n$ = 1500 kPa/mm, $\sigma_n$, $\Delta\tau$)

The value of corresponding normal displacement for a certain value of normal stiffness $k_i$ is then determined according to the following equation:

$$u_n(N, \eta_{max}, k_i, \sigma_n, \Delta\tau) = u_{k_i} = u_{k_1} + (u_{k_2} - u_{k_1})\frac{k_i - k_1}{k_2 - k_1} \quad (3.36)$$

- if $0 < k_i < 500$ kPa/mm: $k_1 = 0$, $k_2 = 500$ kPa/mm, $u_{k1}=u_{n1}$ and $u_{k2}=u_{n2}$
- if $500 < k_i < 1500$ kPa/mm or $k_i > 1500$ kPa/mm: $k_1 = 500$, $k_2 = 1500$ kPa/mm, $u_{k1}=u_{n2}$ and $u_{k2}=u_{n3}$

Second, for the influence of the variation of the initial normal stress, the same methodology is followed. For fixed values of N, $\eta_{max}$, $k_n$ and $\Delta\tau$, we already know:

- $u_{n1}$ = f (N, $\eta_{max}$, $k_n$, $\sigma_n$ = 60 kPa, $\Delta\tau$)
- $u_{n2}$ = f (N, $\eta_{max}$, $k_n$, $\sigma_n$ = 120 kPa, $\Delta\tau$)
- $u_{n3}$ = f (N, $\eta_{max}$, $k_n$, $\sigma_n$ = 310 kPa, $\Delta\tau$)

The value of corresponding normal displacement for a certain value of initial normal stress $\sigma_i$ is then determined according to the following equation:

$$u_n(N, \eta_{max}, k_n, \sigma_i, \Delta\tau) = u_{\sigma_i} = u_{\sigma_1} + (u_{\sigma_2} - u_{\sigma_1})\frac{\sigma_i - \sigma_1}{\sigma_2 - \sigma_1} \quad (3.37)$$

- if $\sigma_i < 60$ kPa or $60 < \sigma_i < 120$ kPa: $\sigma_1 = 60$ kPa, $\sigma_2 = 120$ kPa, $u_{\sigma1}=u_{n1}$ and $u_{\sigma2}=u_{n2}$
- if $120 < \sigma_i < 310$ kPa or $\sigma_i > 310$ kPa: $\sigma_1 = 120$ kPa, $\sigma_2 = 310$ kPa, $u_{\sigma1}=u_{n2}$ and $u_{\sigma2}=u_{n3}$

Finally, the same methodology is followed in order to consider the influence of the variation of the cyclic amplitude. For fixed values of N, $\eta_{max}$, $k_n$ and $\sigma_n$, we already know:

- $u_{n1}$ = f (N, $\eta_{max}$, $k_n$, $\sigma_n$, $\Delta\tau$=10 kPa)
- $u_{n2}$ = f (N, $\eta_{max}$, $k_n$, $\sigma_n$, $\Delta\tau$=20 kPa)
- $u_{n3}$ = f (N, $\eta_{max}$, $k_n$, $\sigma_n$, $\Delta\tau$=30 kPa)

The value of corresponding normal displacement for a certain value of cyclic amplitude $\Delta\tau_i$ is then determined according to the following equation:

$$u_n(N, \eta_{max}, k_n, \sigma_n, \Delta\tau_i) = u_{\Delta\tau_i} = u_{\Delta\tau_1} + (u_{\Delta\tau_2} - u_{\Delta\tau_1})\frac{\Delta\tau_i - \Delta\tau_1}{\Delta\tau_2 - \Delta\tau_1} \quad (3.38)$$

- if $\Delta\tau_i < 10$ kPa or $10 < \Delta\tau_i < 20$ kPa: $\Delta\tau_1 = 10$ kPa, $\Delta\tau_2 = 20$ kPa, $u_{\Delta\tau1}=u_{n1}$ and $u_{\Delta\tau2}=u_{n2}$
- if $20 < \Delta\tau_i < 30$ kPa or $\Delta\tau_i > 30$ kPa: $\Delta\tau_1 = 20$ kPa, $\Delta\tau_2 = 30$ kPa, $u_{\Delta\tau1}=u_{n2}$ and $u_{\Delta\tau2}=u_{n3}$

Following this procedure of calibration, the evolution of normal displacement in function of the number of cycles can be determined for any value of cyclic parameters, normal stiffness and initial normal stress. Hence, this procedure can be used for determining the decrease in the normal stress, which is proportional to the contractive evolution of normal displacement, along the pile shaft.

Figure 3.31 illustrates the procedure followed for the determination of the variation of the normal displacement and normal stress as well.

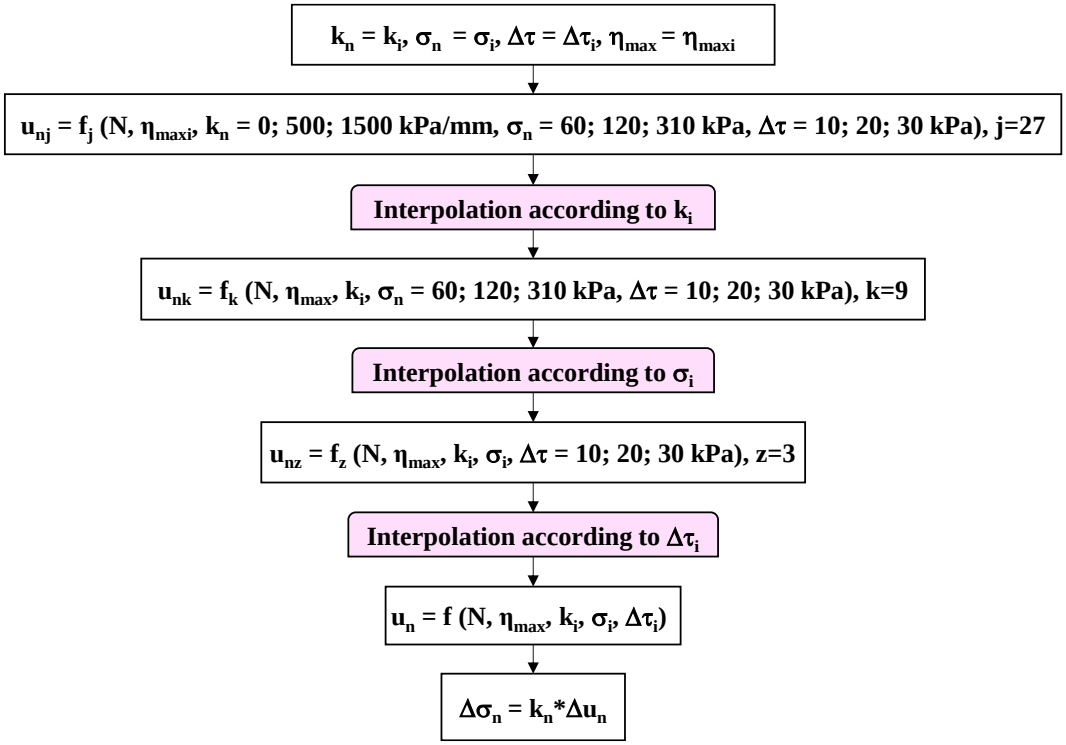


*Figure 3.31 : Procedure for estimation of the variation of normal displacement and normal stress*

## 3.6 Conclusion

This chapter presents an elastoplastic constitutive law with a single yield mechanism, acting upon Mohr-Coulomb criterion, and a non-associated flow rule. This model is characterised by a flow rule enabling typical volume behaviour of the interface to be generated, in both cases, under monotonic and cyclic loading in a typical shear test under CNS condition. It is based on experimental data in terms of evolution of normal displacement according to shear

displacement in the case of monotonic loading, and according to number of cycles in the case of cyclic loading. These expressions are capable to describe the phenomenon of contractancy-dilatancy encountered at the interface level.

Considering monotonic loading, experimental data are defined as functions of shear displacement, $u_n = f(u_t)$. A parametric study of the effect of each parameter in simple shear test is presented and the procedure for identifying the model parameters is exposed. These parameters are then calibrated on the results of experimental shear tests, some of which were carried out in the frame of the SOLCYP project on sand interfaces and others were carried out in the frame of the SOLCYP+ project on chalk interfaces.

For the case of cyclic loading, experimental data are defined as functions of number of cycles, $u_n = f(N)$. An analytical approach is proposed to identify and calibrate the model parameters on the results of numerical simulations according to SOLCYP approach, which is already validated based on available shear test results carried out under the SOLCYP project on sand interfaces.

Knowing that the evolution of normal stress is proportional to the evolution of normal displacement in case of CNS condition, the proposed functions allow to account for the variation of normal stress.

In the perspective of pile modelling, where the major interest is the assessing of the influence of the evolution of normal stress on the shear mechanism along the pile shaft, this contribution seems to be of first order.

Therefore, the aim of the following chapters consists in analysing the potentialities of the developed model at the scale of a pile.

# Chapter 4
# Calculation of axially loaded piles

## 4.1 Introduction

In-situ pile load tests are the most accurate way to assess the response of a pile subjected to axial loading. However, these tests are considered too expensive so that it is difficult to perform a sufficient number of tests. For this reason, modelling the soil-pile interface correctly makes it possible for numerical modelling to give a relevant prediction of the pile behaviour. For this purpose, two main numerical approaches are developed, one-dimensional (1D) or three-dimensional (3D) models using continuum-based methods, finite element and finite difference methods, and one-dimensional (1D) model using load-transfer method. Considered as a complex method, the first approach enables the use of any constitutive model, in order to model the whole interaction of the pile and the surrounding soil considered as a continuum. Therefore, this approach allows to take into account the rheology of the problem. It is widely explained in the previous chapter. In engineering practice, the second approach is more preferred due to its simplicity. However, this approach does not take into consideration the evolution of normal soil stresses, which is considered a limitation due the important effect of this evolution on pile shear mechanism. Thus, based on predefined t-z curves, at each level of the pile, for a certain value of displacement, we can define the corresponding shear stress which consequently prevents any rheological consideration. Nevertheless, this method gives satisfactory results for conventional piles (sufficiently slender). It can be improved by considering the evolution of normal stress, but it requires additional work to calibrate the parameters so that may not be relevant in classical cases of piles. However, for large diameter piles it becomes crucial to take into consideration the variation of normal stress and especially in the case of monopiles. Indeed, this is compatible with the demands of the national project SOLCYP+ in which the main focus is on the design of monopiles. Thus, our contribution was focused on the first approach, which seeks to develop a behaviour law for the interface in order to give a rheological sense to this behaviour. This principle was developed with the aim of being first implemented in commercial codes, notably the FLAC3D code, which is the work done in this chapter, and secondly in an original 1D approach, based on finite element analysis, which will be presented in the following chapter.

This chapter begins by reviewing different methods adopted to analyse the pile response considering monotonic and cyclic loading. Specifically, principles of the conventional t-z method, or 1D finite difference method (1D-FDM), are presented. Examples of monotonic and cyclic t-z curves developed in the literature can also be found.

Aiming to assess the behaviour of a pile subjected to tension axial loading, taking into consideration the effect of normal stress variation, this chapter presents predictions of a

theoretical pile response using the constitutive law for pile interface based on experimental results of shear tests developed in chapter 3, considering monotonic and cyclic loading. Firstly, for the case of monotonic loading, comparisons are done between a conventional t-z calculation (1D-FDM), with elastic perfectly-plastic t-z curves, and prediction of 3D analysis using the finite difference software, FLAC3D (3D-FDM), with the default interface behaviour law based on Mohr-Coulomb criterion. Afterwards, the proposed interface behaviour model is implemented in FLAC3D, and corresponding results are presented. Two initial conditions of soil normal stress are considered reflecting stress state around a bored pile on one hand and around a driven pile on the other hand.

For the case of cyclic loading, a skipped cycles procedure is developed. Combined with experimental curves describing the evolution of normal displacement in function of cycles number calibrated and presented in chapter 3, the skipped cycles procedure is used to perform tension cyclic sequences on the theoretical pile. Results of cyclic simulations are presented.

## 4.2 Methods of pile response analysis under monotonic loading

Several models have been developed to estimate the response of an axially loaded pile. The main idea is to relevantly predict the mobilisation of shear resistance along the pile shaft and the mobilisation of base resistance in function of pile displacement. Current methods can be divided into three classes: (1) elastic continuum method, (2) 1D load transfer method (1D finite difference method), and (3) 3D continuum-based methods, finite element and finite difference methods. The latter method was broadly discussed in chapter 3. The first two will be covered in this section.

### 4.2.1 Elastic continuum method

The analysis based on elasticity theory has been used by several researchers (Randolph and Wroth, 1978; Poulos and Davis, 1980). In this approach, the soil-pile interaction is modelled by dividing the pile into a series of uniformly loaded sections. The solution to the problem is to impose a compatibility between the pile displacements and the surrounding soil displacements. Pile displacements are obtained by using the compressibility of a pile subjected to axial loading. Soil displacements are obtained using Mindlin equations.

Poulos and Davis (1980) detailed the principles of this method. The soil is considered an isotropic and elastic homogeneous semi-infinite mass, having a Young's modulus $E_s$ and a constant Poisson's coefficient $\nu_s$ throughout the mass. In order to calculate the displacement of

the pile and the soil, the method considers that as long as the behaviour at the interface remains elastic, the two displacements are equal.

## 4.2.2 Method of transfer curves (t-z method)

### *4.2.2.1 Principles*

The t-z method, also known as the transfer curve method, has been first proposed by Coyle and Reese (1966). It is intended to calculate the vertical displacement of a pile subjected to axial loading. The method is based on the definition of curves linking the shear stress on the lateral surface of the pile, $\tau$, to the vertical displacement of the pile section, $u_t$, at different depths as well as curve linking the base resistance to the vertical displacement at the base in the case of compressive axial loading. The construction of these t-z curves is based on data collected during instrumented in-situ pile load tests or laboratory tests on model piles, or also from in-situ tests (CPT, PMT, etc.). The first t-z curves have been developed by Coyle and Reese (1966).

The t-z method consists of modelling the pile as a structural element supported by discrete springs that represent the resistance of the ground along the pile shaft and at the pile base. In this approach, the pile is discretised into several sections or segments. Figure 4.1 shows that the pile is discretised into 4 segments for sake of simplicity. The method is based on the resolution of the equilibrium equation 4.1 of a section of pile in compression:

$$E_p A \frac{d^2 u_t}{dz} - \pi D \tau(u_t) = 0 \tag{4.1}$$

Where, $E_p A$ is the axial rigidity of the pile and D is the pile diameter.

The main steps of a numerical resolution of the t-z method used by Poulos and Davis, 1980 can be summarised as follows:

1. The calculation process begins by imposing a small displacement, $u_b$, at the base of segment 4, and using the mobilisation law of the base resistance, the corresponding resistance is then determined.
2. At the mid-point of segment 4, a displacement $u_{m4}$ is arbitrarily considered equal to $u_b$. From the t-z curve corresponding to the depth of segment 4, the value of the shear stress along the pile section $\tau_4$ is determined. Then, the equilibrium of forces applied on element 4 allows to calculate the force at the head of the section $F_4$.
3. Assuming that the load along the small segment 4 varies linearly and considering that the pile has a Young's modulus equal to $E_p$, the displacement at the head of the segment is then determined.

4. The calculated force and displacement at the head of segment 4 are then used as imposed displacement and force at the base of segment 3. Same steps are then considered until determining the load $F_h$ at the pile head as well as the head displacement $u_h$. The calculation process is repeated for different values of imposed base displacements until a series of $F_h$ and $u_h$ values are obtained. These values are then used to plot the head load-settlement of the pile.

The t-z method has been widely used to estimate the displacement of a pile under axial loading and its results are considered satisfactory (Frank and Zhao 1982, Maleki 1995). However, Poulos and Davis (1980) mention that this method has several theoretical and practical limitations. For example, the use of transfer curves assumes that the displacement of a point at the pile length is only related to the shear stress at that point. No effect of other stresses is considered in the calculation. However, variation of normal stress along the pile shaft has a large effect on the mobilisation of shear resistance as it has been detailed in chapter 3. Moreover, the transfer curve method does not correctly consider the continuity of the soil, which makes it unsuitable for the analysis of pile group settlement problems.

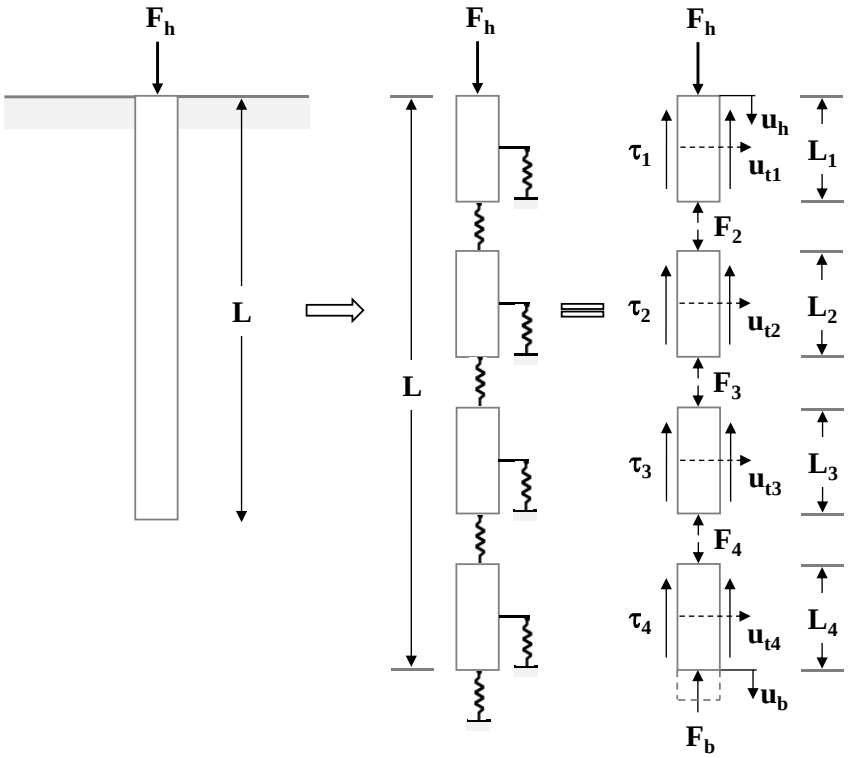


*Figure 4.1 : Principle of the transfer curve method, (Coyle and Reese 1966)*

### *4.2.2.2 Example of monotonic t-z curves*

There are several monotonic t-z curves that have been developed since 1960. The common point between these several curves is the determination of the maximum shear resistance, of the required local displacement for the mobilisation of this maximum resistance and the t-z curve profile before and after the mobilisation of the maximum shear resistance. A number of t-z curves obtained from in-situ static tests has been defined and used (Coyle and Reese 1966, Coyle and Sulaiman 1967, Reese and O'Neil 1987). Figure 4.2 presents the first t-z curve that has been developed by Coyle and Reese (1966). Other t-z curves have been investigated according to theoretical relationships with the stiffness of the soil around the pile (Randolph and Wroth 1978, Kraft et al. 1981).

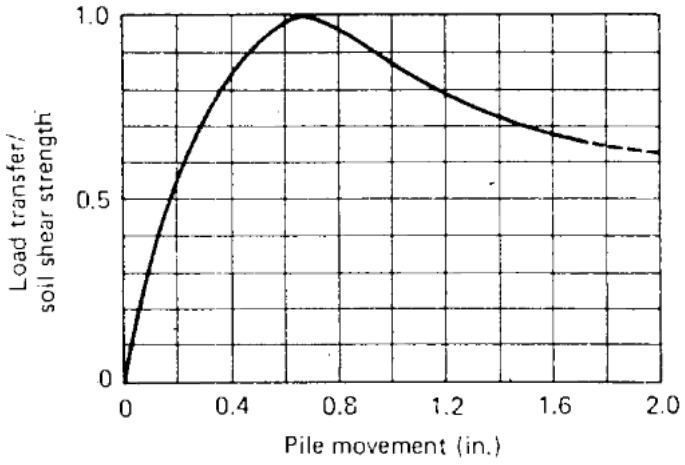


*Figure 4.2 : Example of shaft friction mobilisation curve, (Coyle and Reese 1966)*

In France, the most common used model of t-z curves is that established by Frank and Zhao (1982). It is described by the French national standard for the application of Eurocode 7 (AFNOR 2012). Frank and Zhao (1982) proposed three-linear t-z curves linking mobilised shaft friction to pile settlement. This theoretical relationship is established from Pressuremeter test results carried out along the pile length. Figures 4.3a and 4.3b illustrate, respectively, the curves of shaft friction and base resistance mobilisation as a function of the vertical displacement of the pile. Each curve consists of three segments. The first has a constant slope ($k_s$ or $k_b$) until the mobilisation of 50% of the limit value ($q_s$ or $q_b$). The second has a constant slope up to the limit value. This slope is equal to $k_s/5$ for shaft friction or $k_b/5$ for base resistance. $k_s$ and $k_b$ depend on the type of soil, the Pressuremeter modulus $E_M$ and the pile diameter D (table 4.1). The third segment corresponds to the complete mobilisation of shaft friction or base resistance. Values

of $q_s$ or $q_b$ are calculated according to the "PMT 2012" method presented in the French standard NF P 94-262 (AFNOR 2012) and detailed in chapter 1.

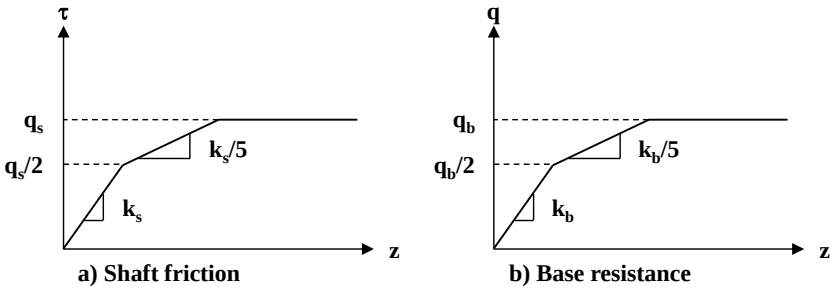


*Figure 4.3 : Curves of shaft friction mobilisation and base resistance mobilisation according to Frank and Zhao (1982)*

*Table 4.1 : Values of soil-pile stiffness, Frank and Zhao (1982)*

| Slope of the curve | Fine soils | Granular soils |
|---|---|---|
| $\mathbf{k_s}$ | $2\frac{E_M}{D}$ | $0.8\frac{E_M}{D}$ |
| $\mathbf{k_b}$ | $11\frac{E_M}{D}$ | $4.8\frac{E_M}{D}$ |

Also based on Pressuremeter test results, a nonlinear relationship for mobilised shaft friction and base resistance has been recently proposed by (Abchir et al. 2016). Figure 4.4 illustrates the curve of shaft friction mobilisation as a function of the vertical displacement of the pile according to the “AB1” model developed by Abchir et al. (2016). The limit value of shaft friction considered in this model is equal to the one developed in Frank and Zhao model (1982). The main difference between the two model is the first part of the curvature which is considered nonlinear here.

Mobilisations of shaft friction and base resistance are obtained according to the following equations:

$$\tau(w_z) = q_s\left(1 - e^{-\frac{w_z}{\lambda_s}}\right) \tag{4.2}$$

$$q(w_b) = q_b\left(1 - e^{-\frac{w_b}{\lambda_b}}\right) \tag{4.3}$$

Where $\lambda_s$ and $\lambda_b$ are two parameters depending on the soil type, the Pressuremeter modulus $E_M$ and the pile diameter D.

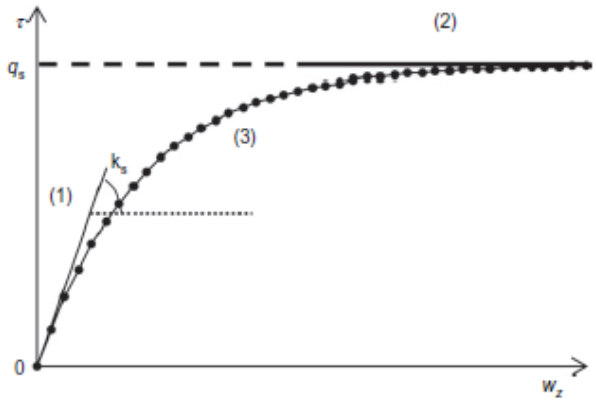


*Figure 4.4 : t-z curve developed according to "AB1" model, (Abchir et al. 2016)*

## 4.3 Methods of pile response analysis under cyclic loading

### 4.3.1 Generality

Modelling the behaviour of a pile subjected to axial cyclic loading requires consideration of the accumulation of permanent displacements and cyclic degradation of load bearing capacity. Multiple models have been developed to simulate the behaviour of piles under cyclic loading. Two categories can be considered: complex models which are intended for the complete simulation of cyclic phenomena, and simple models intended for design practical use.

Complex models have been implemented as part of 3D finite element and finite difference computing programs such as (Shahrour and Rezaie 1997, Mortara et al. 2002, Cao 2010) In such models, the response of the foundation is studied step-by-step and cycle by cycle. These models were mentioned and discussed in chapter 3. Simple models have been developed in order to globally reproduce the phenomena observed during cyclic loading. These models can be based on elastic continuum approach, like the developed numerical program named SCARP(Poulos 1989), or load transfer method. Several t-z cyclic curves can be found in the literature. Some examples will be presented in the following.

### 4.3.2 Example of cyclic t-z curves

#### *4.3.2.1 Cyclic t-z curves in RATZ*

RATZ software has been developed by Randolph (1983, 2003). The construction of corresponding t-z curve has no precise theoretical basis but permits an adequate flexibility to simulate most aspects of soil responses, such as nonlinearity and strain hardening before peak followed by strain softening after peak. Figure 4.5 illustrates the loading-unloading path according to RATZ. As it can be seen, the function includes a linear elastic stage with initial

slope ξ, a nonlinear parabolic stage with strain hardening until reaching peak shear stress $\tau_p$, followed by a strain softening stage where the current mobilised shaft friction depends on the absolute pile displacement. In this program, cyclic degradation is taken into consideration by assessing the accumulated plastic deformation (Chin and Poulos 1992).

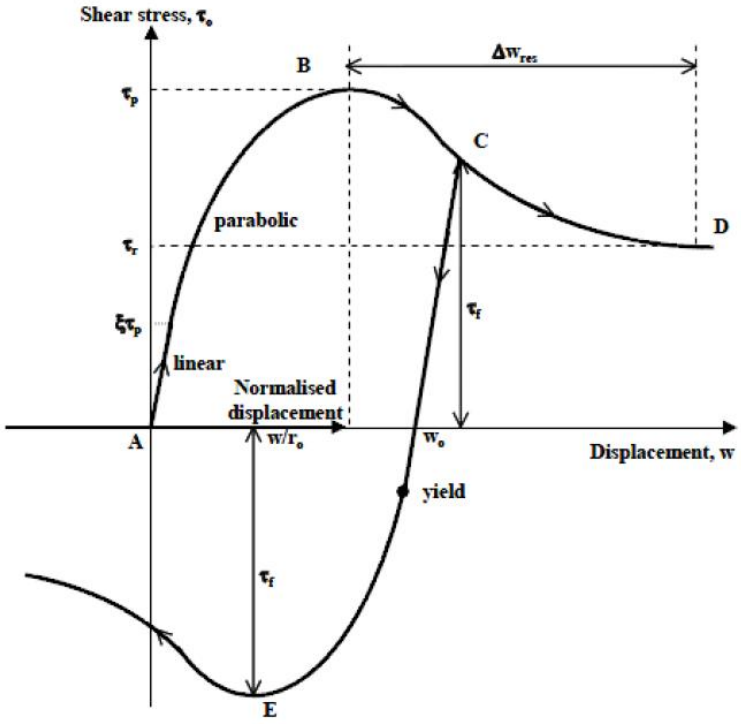


*Figure 4.5 : Illustration of cyclic t-z curve used in RATZ, (Randolph 2003)*

### *4.3.2.2 TZC model*

A more recent cyclic t-z model has been developed and tested by Burlon et al. (2013) and Abchir (2016). It is considered as an extension of the static t-z model AB1 (Abchir et al. 2016). In order to consider the cyclic nature of loading, cyclic parameters allowing to account for the degradation of the limit shaft friction, the accumulation of displacements at the pile head and the variation of the interface stiffness are introduced in AB1. The general formulation of the mobilised shaft friction according to TZC model can be expressed as following:

$$\tau(w_z) = \tau_{i-1} + A_i(-1)^{i+1}(q_s + \Delta q_{s(i)})(1 - e^{-R_i R_f \frac{|w_z - w_{zi-1}|}{\lambda_s}}) \quad (4.4)$$

Where, $w_z$ is the vertical displacement of each pile element, i the number of the half cycle considered (half-cycle of loading or half-cycle of unloading) and $\lambda_s$ a parameter which controls the initial rigidity of the soil-pile interface. $A_i$ and $R_i$ are parameters that control the rigidity of the soil during unloading and the variation of the stiffness of the curves with the number of

cycles. $R_f$ is equal to the ratio of limit shaft friction before cyclic loading $q_s$ and limit shaft friction $q_{sN}$ reached after cycle N. $\Delta q_s$ is the cyclic degradation magnitude.

In order to estimate the cyclic degradation of shaft friction, $\Delta q_s$, TZC model has been combined to two cyclic degradation approaches: ABC approach (Jardine and Standing 2000) and SOLCYP approach (Pra-ai 2013).

## 4.4 Pile calculation under monotonic loading

In order to study the behaviour of a pile under tension axial loading, it is of great importance to correctly model the soil-pile interaction. Two common methods are used for this purpose, the finite element or finite difference method in three-dimensional approach, with appropriate constitutive law combined with corresponding hardening rules, and the t-z method in one-dimensional approach. Although it is considered the most preferred method to meet the practical needs in the geotechnical analysis of piles under axial loading, one of the limitations of the t-z method is that it does not take into consideration the evolution of soil stresses in the normal direction Poulos and Davis (1980). However, the variation of the normal stress at the soil-structure interface has large implications on the pile capacity. Considering the constitutive laws developed in the literature for the soil-structure interface, they have become more complicated for practical use due to the large number of parameters needed in order to simulate the effects of shear loading on the interface behaviour and the complexity of their calibration.

This study attempts to evaluate the performance of the proposed interface model at the scale of a pile. For this purpose, the developed interface constitutive law (chapter 3) was implemented in the finite difference software FLAC3D (Itasca 2012). An application on a theoretical pile was carried out using the three-dimensional approach with FLAC3D (3D-FDM) and the one-dimensional approach with the t-z method (1D-FDM). The key issue is to study the influence of radial stresses variation on the shear mechanism along the pile shaft. Therefore, tension axial loading is considered. The aim of this section is to present the results of this application and their discussion.

### 4.4.1 Numerical model

#### *4.4.1.1 t-z method (1D - FDM)*

The modelled pile has a square section with a width of $D_p$ = 1 m and a length of L = 15 m. The Young's modulus is considered equal to 20 GPa. In order to increase the accuracy of the calculation, this pile was discretised into 30 elements, each of 0.5 m length.

The soil mass around the pile is considered homogeneous and is assimilated to dense sand in order to benefit from the developed model where the numerical equation was calibrated on the basis of shear tests conducted on dense sand samples (Pra-ai 2013). The soil density γ is considered constant throughout the mass and is taken equal to 20 kN/m$^3$. Hence, the vertical stress in the soil mass $\sigma_{v0}$ varies linearly with the depth z according to the equation 4.5.

$$\sigma_{v0} = \gamma z \tag{4.5}$$

In the case of numerical modelling, a great importance is paid to the initial radial stress state around the pile. This stress state is directly related to the method of pile installation. Considering a bored pile, a geostatic distribution is generally considered. However, regarding the effect of pile driving on the surrounding soil, another approach is considered in order to model the initial radial stress.

In our calculation, two hypotheses are therefore assumed. For the first one, the initial normal stress at the soil-pile interface $\sigma_{n0}$ is calculated from the equation 4.6. In this equation, $k_0$ refers to coefficient of earth pressure at rest. Considering that the Poisson's coefficient of the soil ν is equal to 1/3, $k_0$ is set equal to ν / (1-ν).

$$\sigma_{n0} = k_0 \sigma_{v0} \tag{4.6}$$

For the second, an initial stress state is determined according to ICP-05 method, developed for driven piles in sand and clay (Jardine et al. 2005). According to this method, the profile of initial normal stress depends on cone resistance values, $q_c$, of a CPT test. In our case, as an example, a linear profile is proposed for $q_c$ in accordance with the range of values identified for dense sand in the French standard NF P 94-262 (AFNOR 2012). Figure 4.6a illustrates the evolution of $q_c$ along the pile depth. Therefore, the initial normal stress is determined according to the following equation (Jardine et al. 2005):

$$\sigma'_{n0} = 0.029 q_c \left(\frac{\sigma_{v0}}{Pa}\right)^{0.13} \left(\frac{h}{R}\right)^{-0.38} \tag{4.7}$$

Where, $q_c$ is the cone resistance measured by a CPT test, Pa is the atmospheric pressure (Pa = 100 kPa), h is the distance according to the pile tip, and R is the pile radius. The ratio h/R is limited to a minimum value of 8. For open-ended driven piles R is substituted by an equivalent radius noted R$^*$ with $R^* = \sqrt{R_{ext}^2 - R_{int}^2}$ . For our squared shape pile, R is calculated based on equivalent solid area.

The evolution of normal stress along the pile depth, according to the two hypotheses is illustrated in figure 4.6b. These two different initial states combined with the proposed constitutive law reflect the effect of initial normal stress around the pile on the dilatancy during loading and therefore on the pile capacity.

For this application, the normal stiffness $k_n$ is determined according to the following equation:

$$k_n = \frac{2G}{R} \tag{4.8}$$

Where, G is the soil shear modulus and it is calculated according to the formula of Baldi at al. (1989), presented by the following equations:

$$G = q_c(A + B\eta - C\eta^2)^{-1} \tag{4.9}$$

$$\eta = q_c(Pa.\sigma'_{v0})^{-0.5} \tag{4.10}$$

Where, A = 0.0203, B = 0.00125 and C = 1.216e$^{-6}$. Hence, G is calculated from the profile of $q_c$. Figure 4.7 presents the evolution of $k_n$ according to the pile depth. As for the shear stiffness of the soil-pile interface, it is considered equal to $k_n/10$.

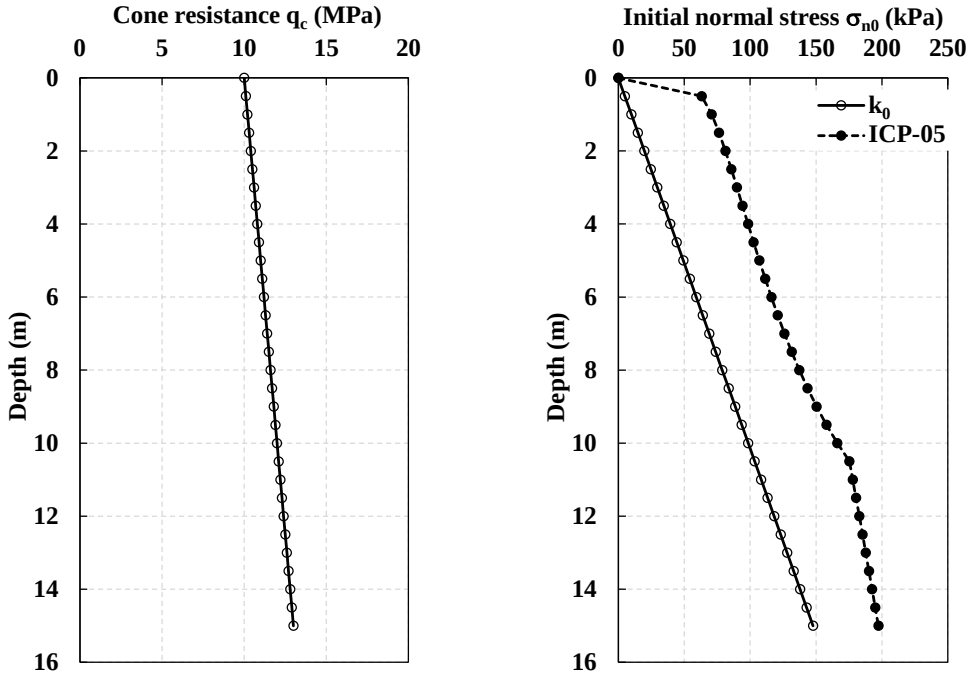


*Figure 4.6 : Evolution in function of pile depth of: a) Cone resistance $q_c$, b) initial normal stress $\sigma_{n0}$ at the soil-pile interface*

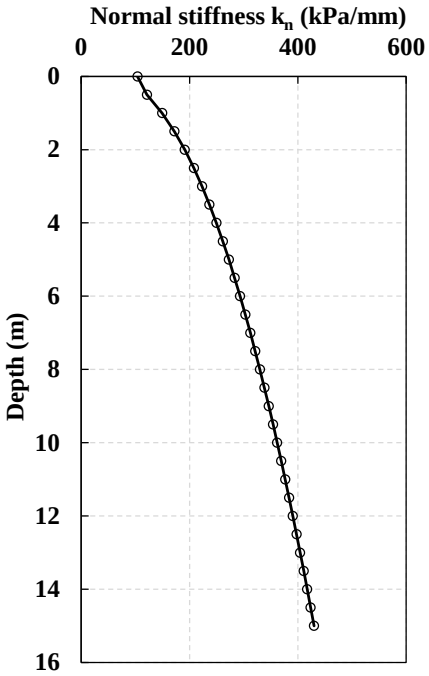


*Figure 4.7 : Evolution of interface normal stiffness in function of pile depth*

The interface friction angle is fixed at 30° (Pra-ai 2013). The limit value of the shaft friction is calculated according to the Mohr-Coulomb criterion. Thus, the limit shaft friction of each layer at a given depth z is based on the initial normal stress $\sigma_{n0}$ and the friction angle φ and it is calculated according to equation 4.11.

$$q_s = \tan\varphi \,.\, \sigma_{n0} \tag{4.11}$$

Figure 4.8 presents the elastic perfectly plastic t-z curves used in the calculation process.

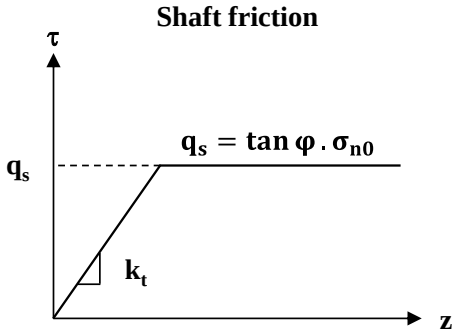


*Figure 4.8 : Elastic perfectly plastic t-z curve*

The bearing capacity of the pile under tension axial loading is calculated from the limit values of shaft friction $q_s$. The total shear resistance of the pile, $R_s$, is calculated by integrating the $q_s$ values on the entire pile length. Therefore, equation 4.12 is applied where i is the element number, P the pile perimeter and $h_i$ the element length.

$$R_s = P \sum h_i q_{si} \tag{4.12}$$

### *4.4.1.2 FLAC3D (3D - FDM)*

Taking advantage of the symmetrical nature of the model, only one quarter of the domain is modelled in FLAC3D. Figure 4.9 shows the model geometry adopted in this study. Concerning the mechanical boundaries, the model is normally fixed at its lateral sides while it is fully fixed at its bottom. The pile is also discretised into 30 elements, each of 0.5 m length. Figure 4.9 presents two configurations presenting two different model sizes and mesh densities. A comparative study between calculation results with the two different configurations is held to analyse their effect on the pile behaviour.

Both the pile and the soil are modelled in linear elastic behaviour. The contact between the soil and the pile along the pile shaft is achieved using interface elements. The interfaces are pure sliding where no detachment is allowed. An interface element in FLAC3D follows by default the Mohr-Coulomb failure criterion. Tables 4.2 and 4.3 summarise the properties of the soil, the pile and the interface. The same profile presented in figure 4.7 is considered for the interface normal stiffness in FLAC3D, and the shear stiffness is set equal to $k_n/10$.

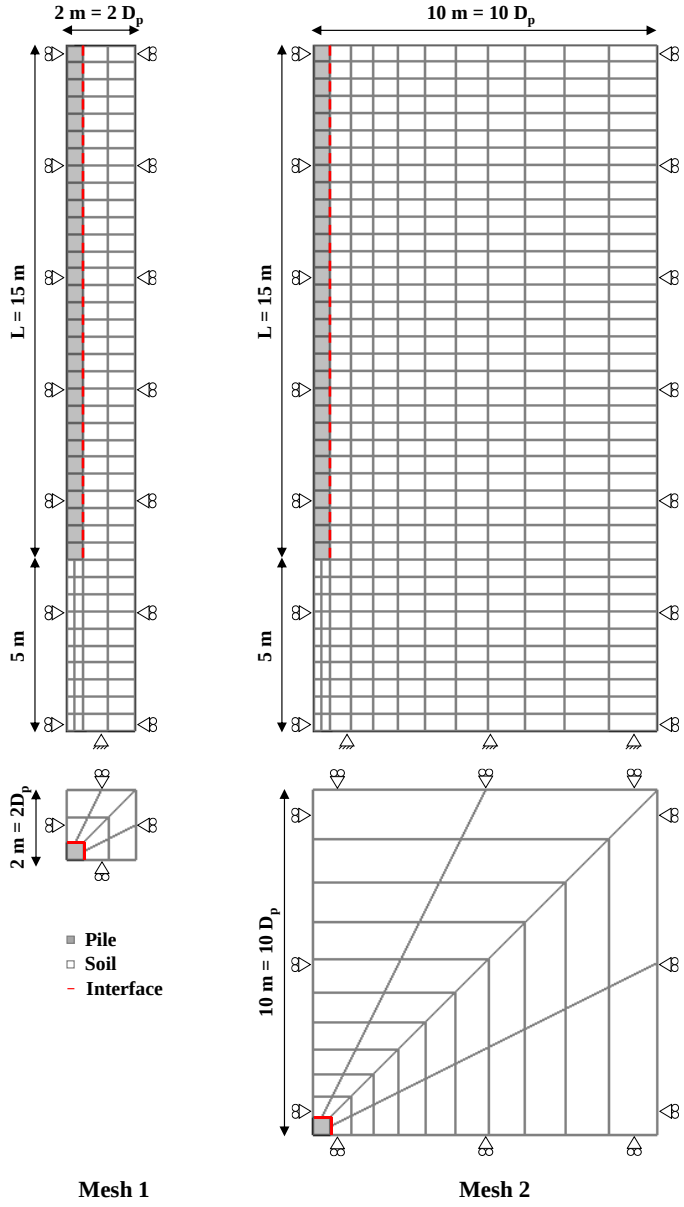


*Figure 4.9 : Geometry of the model in FLAC3D, mesh 1 and mesh 2*

*Table 4.2 : Elastic properties of materials in FLAC3D*

| Elastic material | Density (kN/m3) | Young's modulus (GPa) | Poisson's ratio |
|---|---|---|---|
| | γ | E | ν |
| **Soil** | 20 | 10 | 1/3 |
| **Pile** | 25 | 20 | 0 |

*Table 4.3 : Properties of the interface in FLAC3D*

| **Normal stiffness $k_n$ (kPa/mm)** | **Shear stiffness $k_t$ (kPa/mm)** | **Friction angle φ (°)** | **Dilation angle ψ (°)** |
|---|---|---|---|
| Figure 4.7 | $k_n/10$ | 30° | 0° |

### 4.4.2 Comparison between t-z approach and continuum approach: constant normal stress during loading ($\Delta\sigma_n = 0$)

The head load-displacement curve of the pile is determined according to numerical calculation in FLAC3D by applying an incremental monotonic vertical displacement at the top of the pile. This displacement is established by imposing a vertical velocity at the pile head with corresponding number of timesteps.

Calculation is held in order to assess the capacity of the model in FLAC3D to simulate the calculation results according to the conventional t-z method. This makes it possible to validate the modelling process. For this purpose, different comparative and parametric study regarding the mesh density and the soil Young's modulus are considered. The sensitivity study of the model according to its parameters makes it possible to determine the parameters to be preferred in the optimisation process. It should be noted that for this preliminary work, the first hypothesis of initial normal stress is considered. Afterwards, the comparison is held between the two approaches considering the two hypotheses of initial normal stress.

#### *4.4.2.1 Effect of mesh density*

It is of interest to investigate the sensitivity and the efficiency of the model mesh in terms of the computational time and results relevance. Two different meshes (Mesh 1 and Mesh 2), with different sizes and densities are presented in figure 4.9. For the mesh 1, which is less dense than the second mesh, the soil lateral extension is set at 2 m ($2D_p$) and the height of soil mass at 20 m. While the use of a higher number of elements to model the soil around the pile can achieve a greater accuracy, this also results in a denser mesh and requires a longer computational time. For this purpose, a denser mesh is considered, mesh 2. For this mesh, the soil lateral extension is set at 10 m ($10D_p$) and the height of soil mass at 20 m.

Figure 4.10 shows the distribution of the initial normal stress in the soil mass for the two meshes. With density soil $\gamma = 20$ kN/m$^3$, the mesh density and the size of the soil extension have approximately no effect on the generation of the initial normal stress in the soil and therefore at the interface.

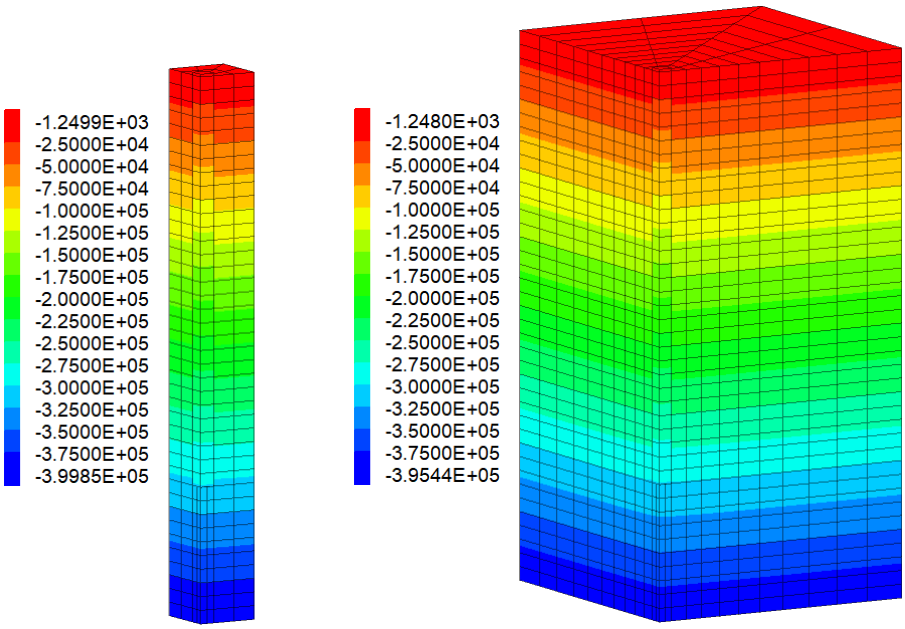


*Figure 4.10 : Initial normal stress distribution in FLAC3D for a) mesh 1 b) mesh 2*

Figures 4.11, 4.12a and 4.12b present the pile response in terms of head load-displacement curve and evolution of displacement and limit shaft friction along the pile length at the end of loading, obtained with the two meshes as well as with the t-z method. The global response of the pile according to both models, 1D-FDM and 3D-FDM, performs a very good concordance. With a geostatic linear profile of initial normal stress, the tension pile capacity is equal to 2560 kN.

Results show that the two meshes have approximately a similar degree of accuracy, no apparent difference is shown. However, the denser mesh, mesh 2 requires a longer solution time. For this reason, mesh 1 is adopted in all upcoming simulations.

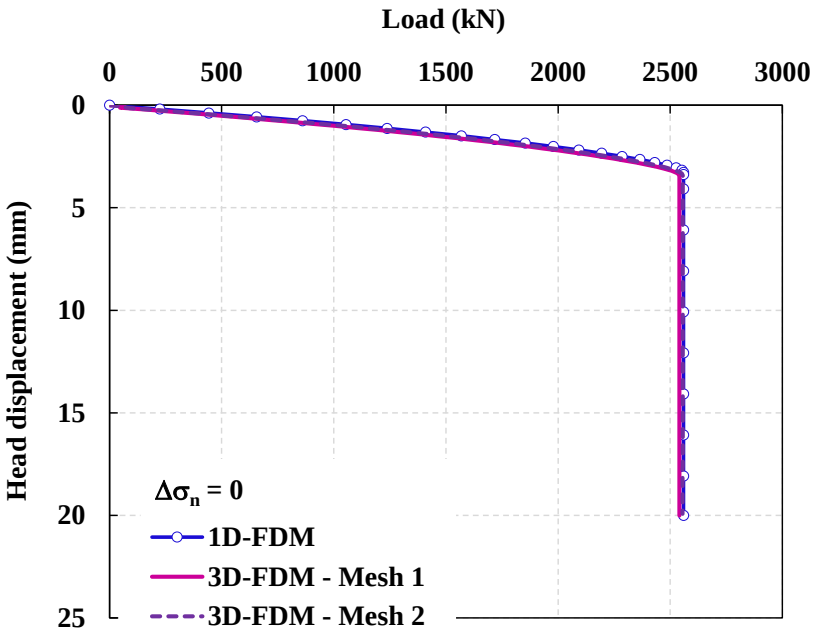


*Figure 4.11 : Head load-displacement curves, comparison between t-z (1D-FDM) results and FLAC3D (3D-FDM) results with the two meshes ($\Delta\sigma_n = 0$)*

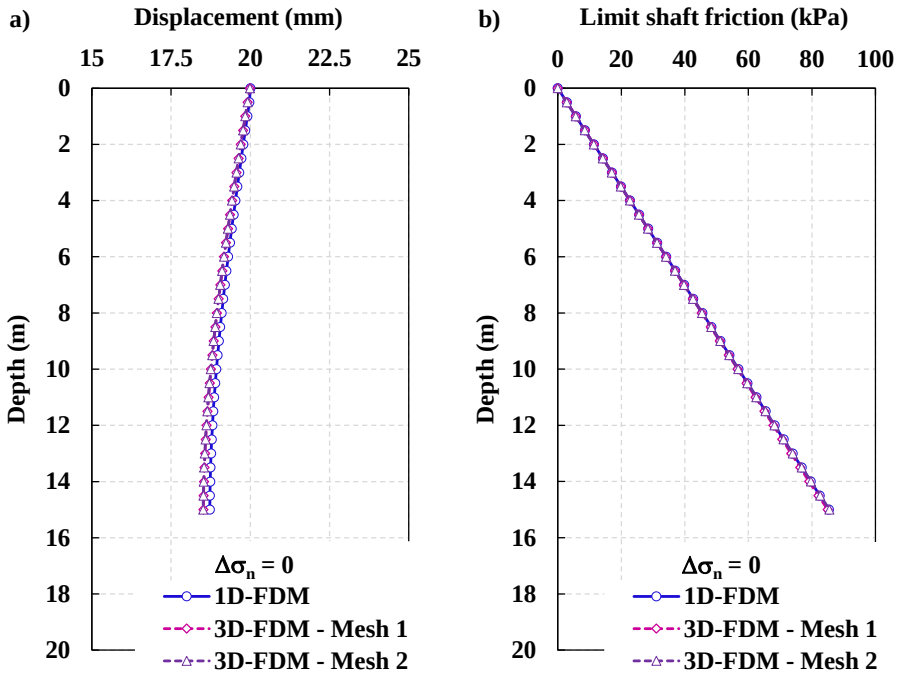


*Figure 4.12 : Comparison between t-z (1D-FDM) results and FLAC3D (3D-FDM) results with the two meshes ($\Delta\sigma_n = 0$): a) evolution of pile displacement according to depth, b) evolution of interface limit shaft friction according to depth*

### *4.4.2.2 Effect of Young's modulus*

The sensitivity of the soil Young's modulus is investigated using three values, E = 0.1, 1 and 10 GPa. The aim of this study is to assess the rigidity of the soil needed to capture the

predictions of the t-z calculation. The head load-displacement curve for each case are illustrated in figure 4.13. The evolution of pile displacement and pile limit shaft friction along its length for all three cases are presented in figures 4.14a and 4.14b respectively. It is shown that by increasing the Young's modulus, FLAC3D model predictions tend more to simulate the t-z calculation results. The soil behaviour becomes more stiffer, and the volumetric deformations decrease. Thus, the relative displacement of the interface is similar to the pile movement and the shear stress for each pile element reaches its limit value defined by the Mohr-Coulomb criterion. However, by decreasing the value of E, the soil presents a more flexible behaviour. The curve of pile head load-displacement becomes softer. Hence, the soft behaviour of the soil results in a decrease in the normal stress acting on the interface during shear loading, and therefore in a decrease in the limit shaft friction. Consequently, the tension capacity of the pile decreases.

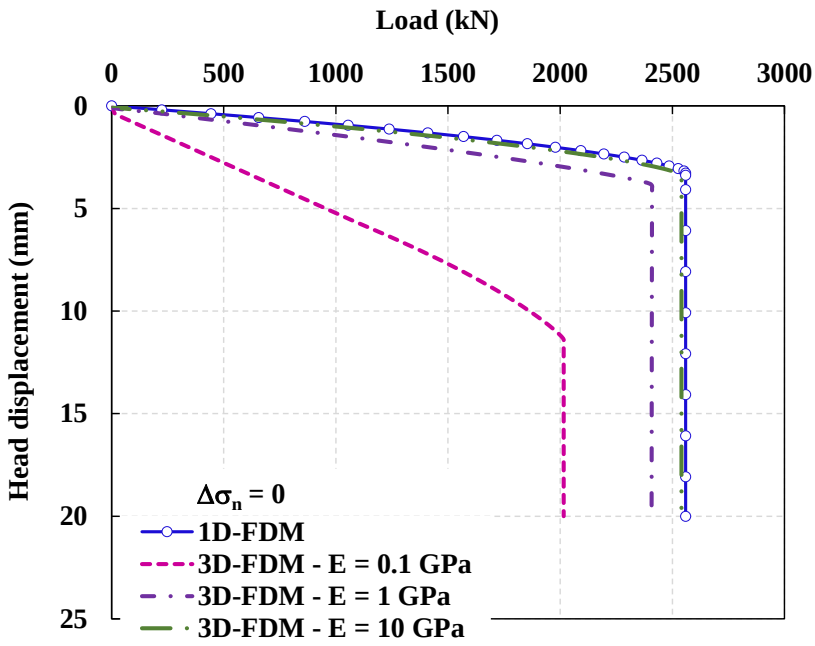


*Figure 4.13 : Effect of soil Young's modulus on the head load-displacement response of the pile*

It can be noted that the highest value of E = 10 GPa presents the nearest results to the t-z method predictions. This value ensure that the soil mass is rigid enough to localise the effect of shearing at the interface. Given this study, the following calculations are done with E = 10 GPa.

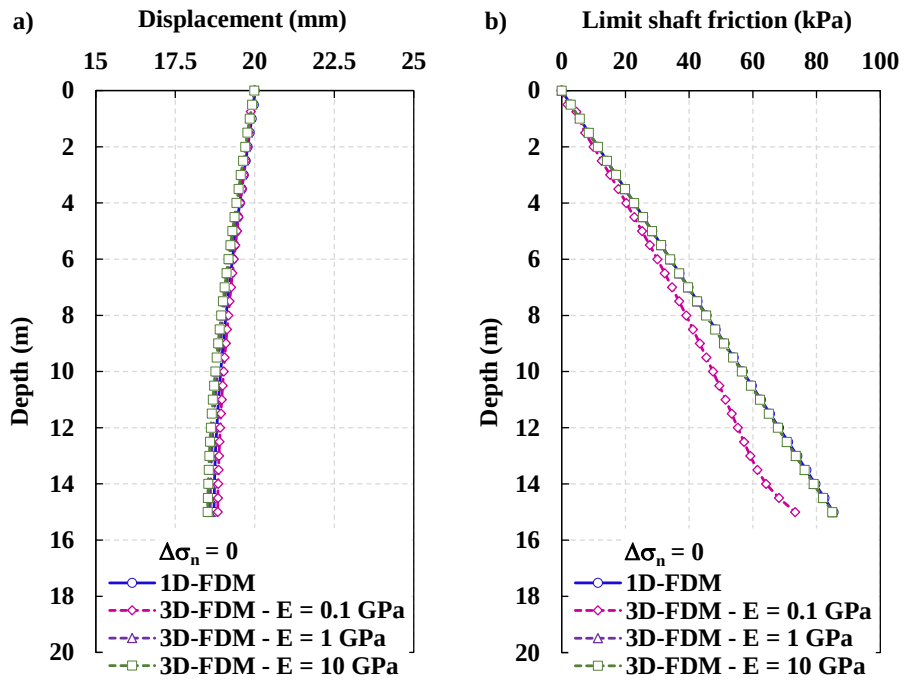


*Figure 4.14 : Effect of soil Young's modulus on: a) evolution of pile displacement according to depth, b) evolution of limit shaft friction according to depth*

### *4.4.2.3 Effect of initial normal stress*

The state of initial radial stresses around the pile is studied in this part. Indeed, the tension capacity of a pile strongly depends on the initial state of stress at the soil-pile interface. This state of stress relies on the pile installation method. Calculations presented herein are also performed according to t-z method and in FLAC3D. Comparison between results of simulations considering the coefficient of earth pressure at rest $k_0$ and the ICP-05 method is done. The initial stress state in FLAC3D is normally generated according to a $k_0$ procedure. Thus, in order to simulate the effect of pile driving, the initial normal stress calculated according to ICP-05 is imposed on the soil-pile interface using the special programming language of FLAC3D "fish language".

Figures 4.15, 4.16a and 4.16b illustrate the pile response in terms of head load-displacement curve and evolution of displacement and limit shaft friction along the pile length, at the end of loading, calculated according to t-z method and to finite-difference method of FLAC3D, considering both initial stress states. It is clear that by using either the default $k_0$ procedure for initial normal stress generation or by imposing it, calculations done in FLAC3D give a good representation of obtained results according to t-z method.

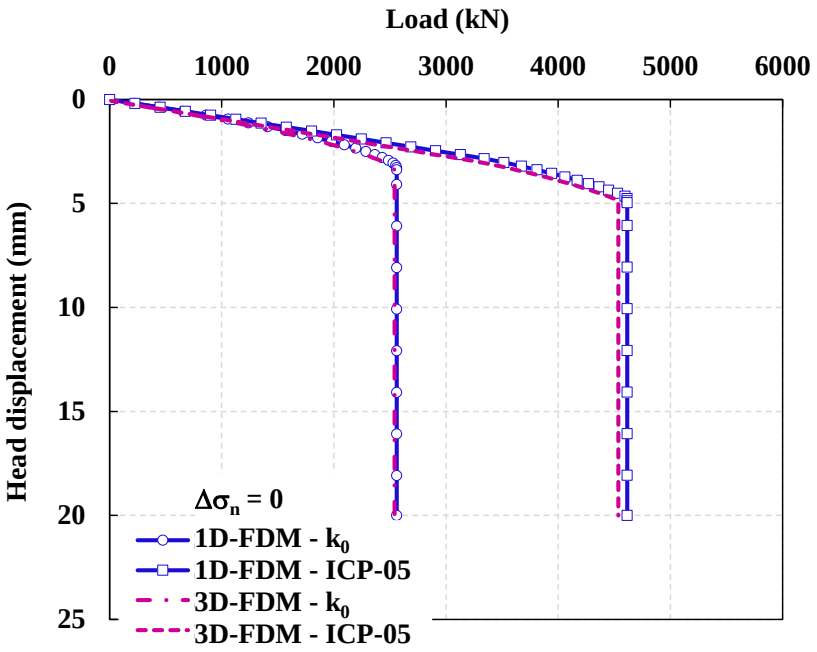


*Figure 4.15 : Head load-displacement curves, comparison between t-z (1D-FDM) results and FLAC3D (3D-FDM) results with two initial stress state, $k_0$ and ICP-05 ($\Delta\sigma_n = 0$)*

Given that the ICP-05 method leads to much higher initial stresses, corresponding calculations predict a tension capacity of approximately 4615 kN which is clearly greater than the tension capacity obtained with initial stresses determined according to $k_0$ procedure.

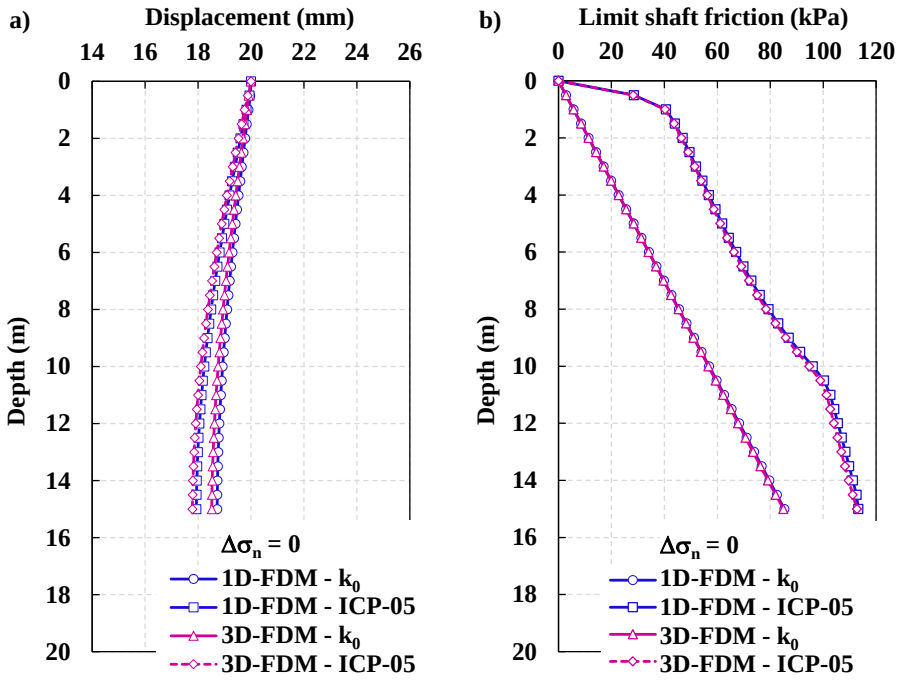


*Figure 4.16 : Comparison between t-z (1D-FDM) results and FLAC3D (3D-FDM) results with two initial stress state, $k_0$ and ICP-05 ($\Delta\sigma_n = 0$): a) evolution of pile displacement according to depth, b) evolution of interface limit shaft friction according to depth*

### 4.4.3 Comparison between t-z approach ($\Delta\sigma_n = 0$) and continuum approach ($\Delta\sigma_n \neq 0$)

In this part, simulations are done using the interface model that was developed in chapter 3. This model is implemented for the interface element in FLAC3D using the special programming language "fish language". Hence, the shear stress of the interface is described by the non-linear relationship resulted from the developed model combined with the proposed numerical equation ($u_n = f(u_t)$).

Several calculations are done considering the different initial normal stresses. For these calculations, a dilatant interface is only considered, i.e., the numerical equation 3.17 is implemented in FLAC3D with corresponding parameters calibrated on shear tests of sand samples.

Considering the simulations performed in chapter 3 on the basis of direct shear tests, the interface shear stiffness was determined from the calibrated parameter B of the numerical equation (see equation 3.21). However, the interface shear stiffness for the pile calculation is imposed and it is taken equal to $k_n/10$. Hence, in this case, the parameter B for each pile element is determined from the corresponding $k_t$ value according to equation 4.13.

$$B = \frac{\sigma_{n0} \tan\varphi}{2\, k_t} \tag{4.13}$$

The limit shaft friction of each interface node at a given depth z is based on the initial normal stress $\sigma_{n0}$, the friction angle φ and the increase in normal stress $\Delta\sigma_n$ resulted from the dilatant behaviour of the interface. $\Delta\sigma_n$ is defined based on the numerical equation proposed to assess the evolution of normal displacement along the pile shaft, as follows:

$$\Delta\sigma_n = D * k_n \tag{4.14}$$

Where, D is the parameter of the numerical equation 3.17 that defines the limit value reached by the interface normal displacement, after the phase of dilatancy.

Hence, the limit shaft friction can be determined according to the following equation:

$$q_s = \tan\varphi \,.\, (\sigma_{n0} + \Delta\sigma_n) \tag{4.15}$$

According to equation 4.15, estimated value of pile tension capacity, considering $k_0$ procedure for initial stress condition, is approximately equal to $R_s$ = 4101 kN. As for the case of ICP-05 method, the estimated value of pile tension capacity is approximately equal to $R_s$ = 6052 kN. Hence, the contribution of interface radial stresses evolution led to an increase of about 60%

and 31% in the pile capacity from its initial value obtained according to t-z calculation, considering $k_0$ and ICP-05 conditions respectively.

In the following paragraphs, we compare different results obtained with the conventional t-z method (1D-FDM) and the proposed model implemented in FLAC3D (3D-FDM) considering the two conditions of initial normal stress.

### *4.4.3.1 Head load-displacement curve*

Figures 4.17a and 4.17b illustrate the head load-displacement curves for all calculations. Black dotted line presented in each figure shows the pile capacity calculated based on equation 4.15. For each initial condition, the elastic part of the curves determined by the t-z method and by our model is the same. When reaching plasticity, dilatant behaviour arises resulting in increasing in pile tension capacity.

Overall, the head load-displacement curves obtained with the proposed model present a non-linear increasing behaviour, when the interface enters the plasticity zone, until reaching a maximum value. This increasing behaviour is strongly related to the choice of the proposed numerical equation ($u_n = f(u_t)$), which represents a dilation phase for the interface response.

As demonstrated in chapter 3, the numerical equation, developed to account for the interface normal displacement and normal stress, essentially depends on the normal stiffness $k_n$ and initial normal stress $\sigma_{n0}$. The only variable in the case of pile calculation presented here is the initial normal stress. In the case of $k_0$ initial stress, the pile capacity determined according to FLAC3D predictions reaches a value of 4039 kN, with a difference of 1.5% from its predicted value based on equation 4.15. When ICP-05 initial stress is considered, this difference is equal to 0.3%. These slight differences can be interpreted by the presence of the soil mass around the pile, which may affect more or less the interface behaviour.

The increase in ultimate tension pile capacity, due to the imposed dilatancy, is more pronounced in the case of $k_0$ initial stress state which presents lower initial values of radial stresses than the case of ICP-05. This is evident given that the level of dilatancy, obtained from the numerical equation combined with the developed interface behaviour law, is inversely proportional to the initial normal stress. These observations highlight the effect of the initial normal stress on the developed capacity of the pile.

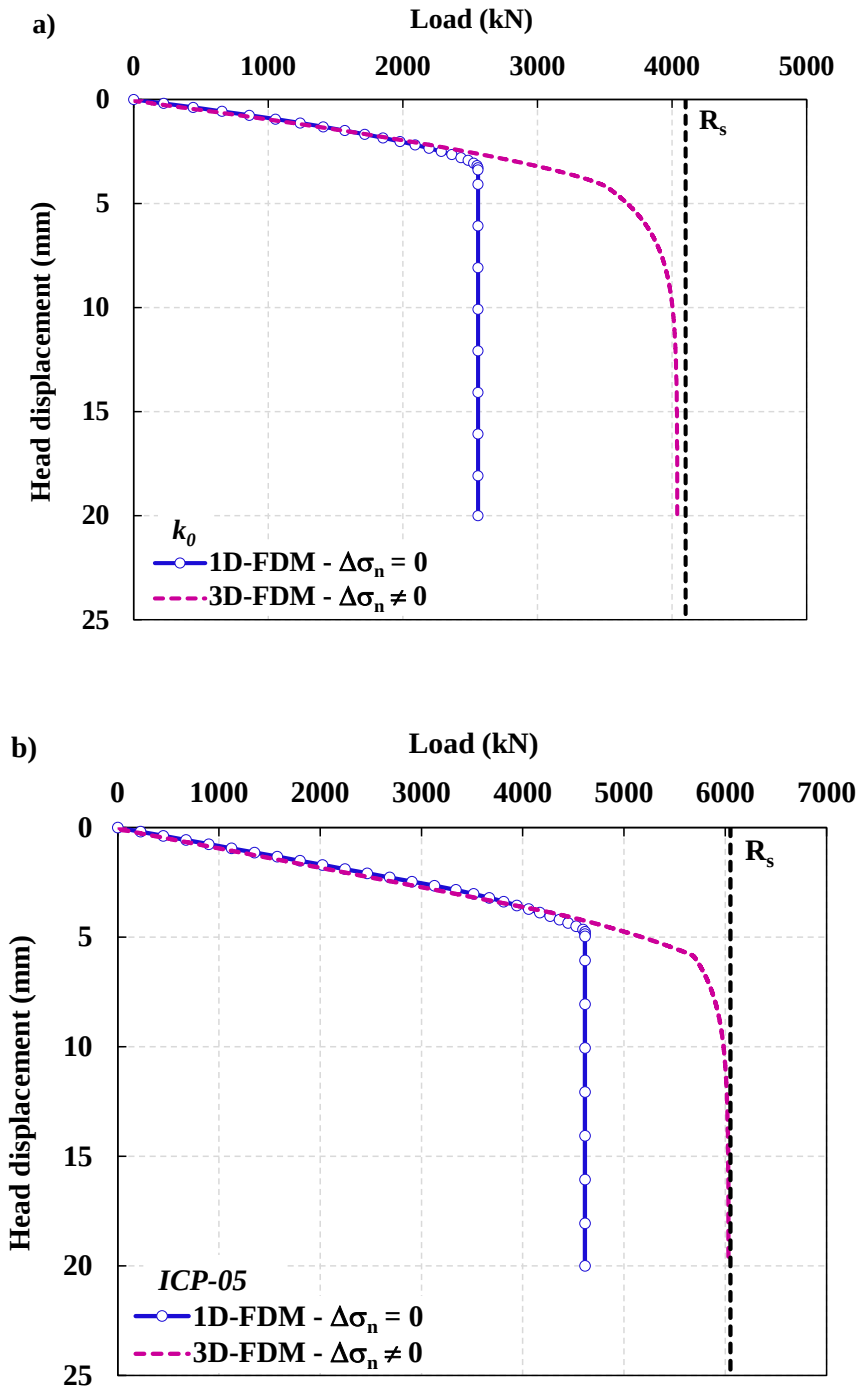


*Figure 4.17 : Head load-displacement curves, comparison between t-z (1D-FDM) results ($\Delta\sigma_n = 0$) and FLAC3D (3D-FDM) results ($\Delta\sigma_n \neq 0$) considering the proposed interface model: a) $k_0$ initial stress state, b) ICP-05 initial stress state*

### *4.4.3.2 Profile of limit shaft friction*

Figures 4.18a and 4.18b plot the profiles of the limit shaft friction as a function of depth for different simulations. For each case of initial stress state, the difference between 1D-FDM predictions ($\Delta\sigma_n = 0$) and 3D-FDM predictions ($\Delta\sigma_n \neq 0$) increases with pile depth. Indeed, as

the depth increases, values of initial normal stress and normal stiffness increase. In addition, parameters of the numerical equation that describes the variation of normal displacement and therefore the normal stress, clearly depend on values of initial normal stress and normal stiffness. Consequently, as the latter values increase, the difference between the proposed model calculations and the t-z method predictions increase. It should be noted that differences are more pronounced in the case of $k_0$ initial stress state.

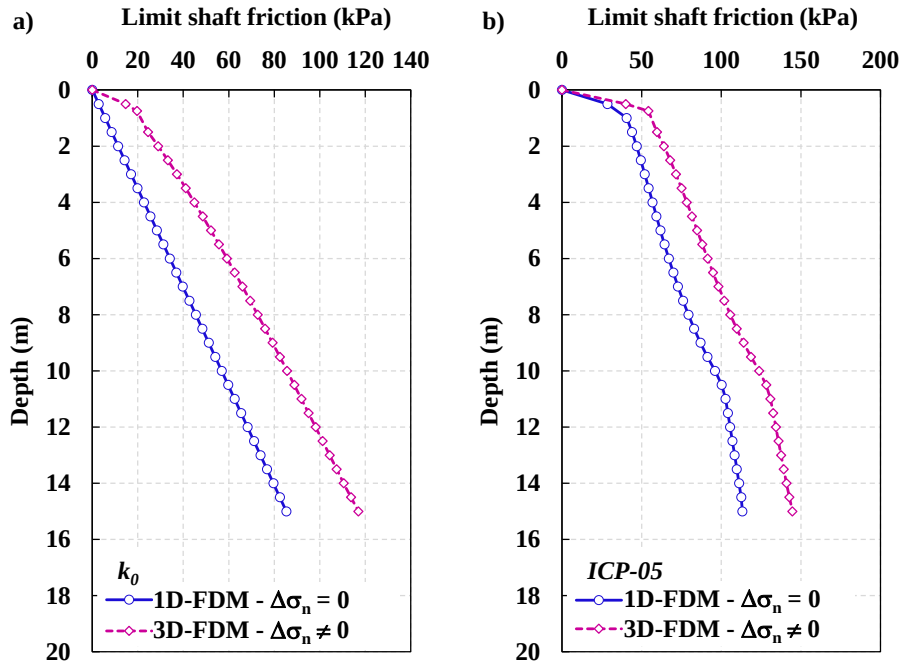


*Figure 4.18 : Evolution of limit shaft friction according to pile depth, comparison between t-z (1D-FDM) results ($\Delta\sigma_n = 0$) and FLAC3D (3D-FDM) results ($\Delta\sigma_n \neq 0$) considering the proposed interface model: a) $k_0$ initial stress state, b) ICP-05 initial stress state*

### *4.4.3.3 Shear stress and normal stress in function of shear displacement*

Figures 4.19a, 4.19b, 4.19c and 4.19d compare the mobilised shear stress as well as the normal stress of the upper, middle and lower pile elements, as a function of shear displacement for each prediction method. It is clear that the overall behaviour of the pile is confirmed by the evolution of local friction.

While the t-z method does not consider the effect of normal stress, the latter is kept constant while loading. The developed model combined with the proposed numerical equation, $u_n = f(u_t)$, manages the evolution of normal stress. With $k_0$ initial state, the ratio between the maximum normal stress reached at the end of loading and the initial normal stress is equal to 8.5 for the upper element, 1.7 for the middle element and 1.4 for the lower element. For ICP-05 initial stress, this ratio has a value of 1.6 for the upper element, 1.3 for the middle element and 1.2 for

the lower element. The evolution of mobilised shear stress is a directly governed by the variation of corresponding normal stress as it is shown in these figures.

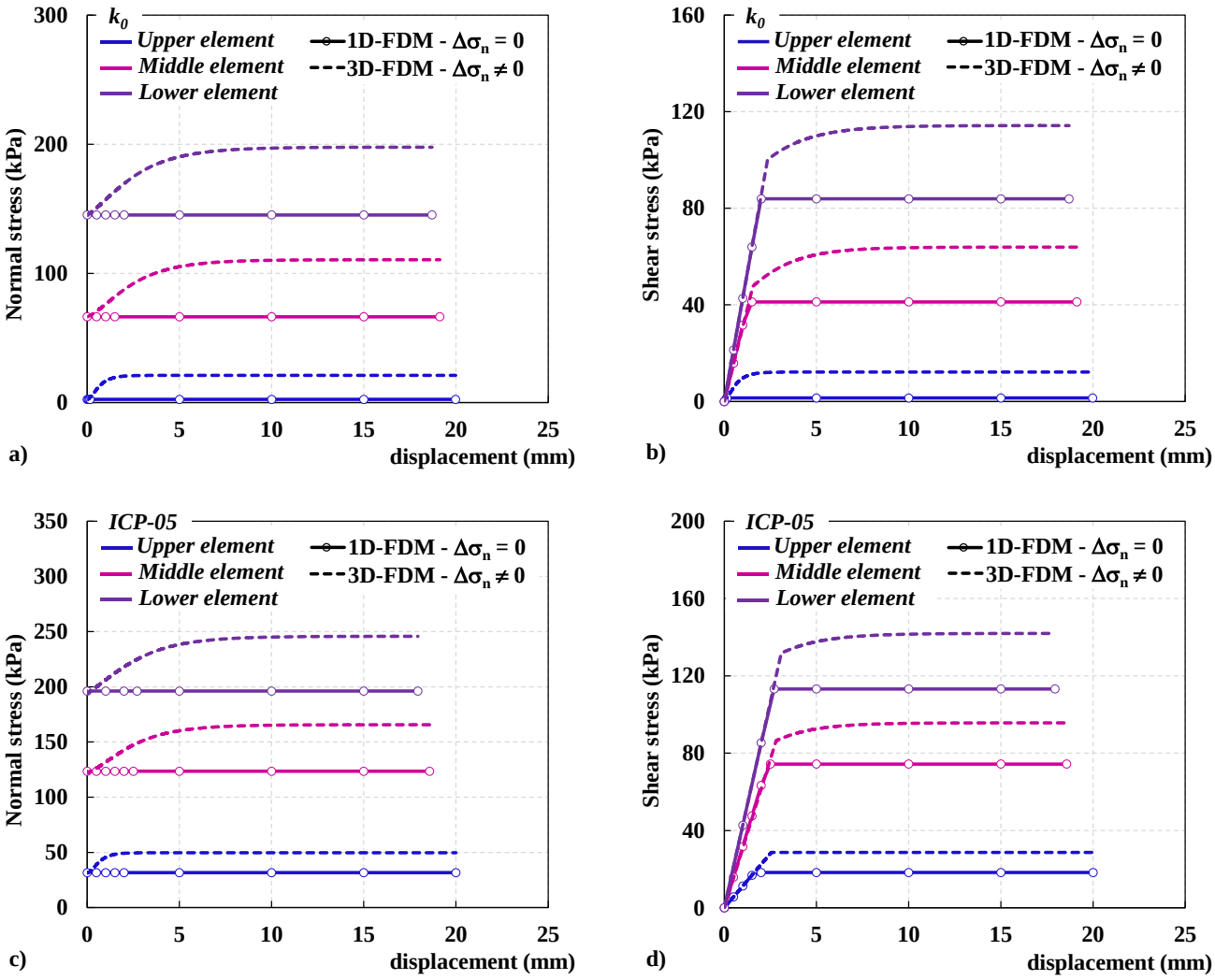


*Figure 4.19 : Normal stress and shear stress in function of shear displacement for upper, middle and lower pile elements, comparison between t-z (1D-FDM) results ($\Delta\sigma_n = 0$) and FLAC3D (3D-FDM) results ($\Delta\sigma_n \neq 0$) considering the proposed interface model: a, b) $k_0$ initial stress state, c, d) ICP-05 initial stress state*

## 4.5 Pile calculation under cyclic loading

### 4.5.1 Development of a skipped cycles method

For cyclic calculation under axial loading, a skipped cycles method is presented here. As explained in section 3.2.4.2, this method is based on the use of constitutive laws presenting cyclic effects in order to simulate step-by-step of one (or several) cycle(s). Afterwards, plastic deformations are extrapolated linearly or via more complex functions, over a number of skipped

cycles. In our study, the strategy of skipped cycles is followed. The difference presented here is the method of determining the plastic deformations. For this aim, the numerical equation detailed and calibrated in section 3.5.4 is then used. The calibration of this numerical equation is based on several parameters: normal stress $\sigma_n$, maximum stress ratio $\eta_{max}$, cyclic amplitude $\Delta\tau$, imposed normal stiffness $k_n$, and the number of cycles N. A total number of cycles, $N_{total}$, is modelled by packets of $N_{sc}$ skipped cycles. In order to take into account the effect of cycles on the behaviour of pile in terms of bearing capacity and displacement, it is necessary to update the values of cyclic parameters $\eta_{max}$ and $\Delta\tau$ during calculation. The update is done after each $N_{sc}$ skipped cycles. It worth noting that for calculations in FLAC3D $N_{sc}$ is taken equal to 10.
The procedure of cyclic calculation done in FLAC3D, using skipped cycles method combined with proposed cyclic numerical expression for normal stress degradation based on SOLCYP approach, is detailed below.

1. A first cycle is performed, step-by-step, to estimate the values of initial maximum stress ratio $\eta_{max1}$ and cyclic amplitude $\Delta\tau_1$ for each soil layer. Calculation herein follows the classical Mohr-Coulomb yield criterion with zero dilatancy. The first loading is applied up to the desired ratio of the ultimate pile capacity. The value of normal stress, $\sigma_{n1}$, is then determined. At the end of this cycle, $\eta_{max1}$ and $\Delta\tau_1$ can be calculated according to the following expressions:

$$\eta_{max1} = \frac{\tau_{max1}}{\sigma_{n1}} \tag{4.16}$$

$$\Delta\tau_1 = \tau_{max1} - \tau_{min1} \tag{4.17}$$

2. The calculation is then proceeded for the first $N_{sc}$ skipped cycles. The relative normal displacement $u_{n1}$, accumulated at the end of the first $N_{sc}$ skipped cycles, is determined from pre-defined experimental curves, describing the evolution of normal displacement according to cycles number. The variation of normal stress $\Delta\sigma_n(1)$ is estimated according to equation 4.18. This variation is then applied at each integration point along the pile length, which generates a disturbance in the soil-pile model. The evolution of the relative normal displacement $u_{n1}$ as a function of the number of cycles is plotted on the curve (1) in figure 4.20.

$$\Delta\sigma_n(1) = k_n u_{n1} \tag{4.18}$$

3. Following the Mohr-Coulomb criterion the correction of shear stresses is then done until reaching equilibrium in the model.
4. In order to model following skipped cycles, values of stress ratio and cyclic amplitude shall be updated. For this purpose, a step-by-step cycle, according to the Mohr-Coulomb criterion, is conducted. Consequently, values of $\eta_{max}$ and $\Delta\tau$ are updated. In figure 4.20, this actualisation results in the transition from curve (1) to curve (2).

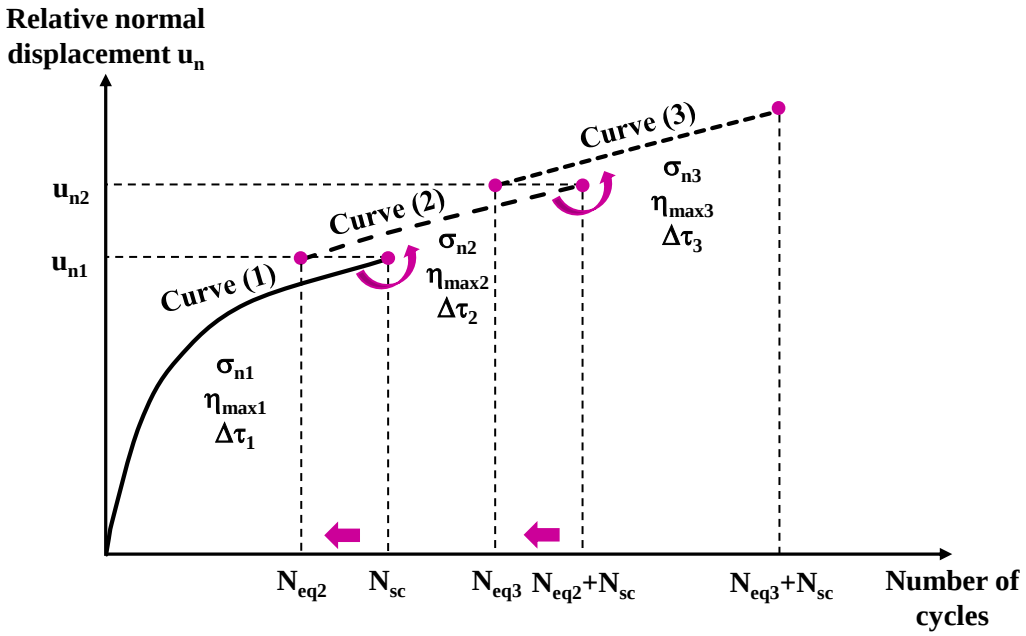


*Figure 4.20 : Evolution of relative normal displacement at soil-pile interface in function of cycles number*

5. It should be noted that it is necessary to take into consideration the effect of the first $N_{sc}$ skipped cycles on the estimation of the subsequent relative normal displacement $u_{n2}$, accumulated after the second pack of $N_{sc}$ skipped cycles. For this purpose, an equivalent number of cycles noted $N_{eq2}$ is calculated. It reflects the number of cycles required to accumulate a relative normal displacement equivalent to $u_{n1}$ by being on curve (2) in figure 4.20. It is determined using a numerical dichotomy process.
6. The calculation then continues for the second packet of $N_{sc}$ cycles starting from a number of cycles equivalent to $N_{eq2}$. The calculation stops at the end of the $N_{total}$ cycles or when a rupture occurs due to lack of equilibrium between applied loading on pile head and its resistance or due to accumulated displacement exceeding the conventional allowable displacement of $D_p/10$ ($D_p$ is the pile diameter). The lack of equilibrium can be encountered when the pile capacity at a given cycle during loading becomes smaller than the maximum loading applied at the pile head.

Figure 4.21 illustrates the evolution of the interface limit shaft friction during cycles. This figure gives a representation of the cyclic parameter, $\Delta\tau$, updated after each step-by-step cycle. It also presents the degradation in the limit shaft friction, $\Delta q_s$ (j), obtained after each j packet of $N_{sc}$ skipped cycles. This degradation is related do the degradation of the interface normal stress according to the following equation:

$$\Delta q_s(j) = \Delta\sigma_n(j) * \tan\varphi \tag{4.19}$$

The parameter $q_{s1}$ presented in figure 4.21 is the initial limit shaft friction. During cyclic loading, this parameter, $q_{sj}$, is determined after each packet of skipped cycles.

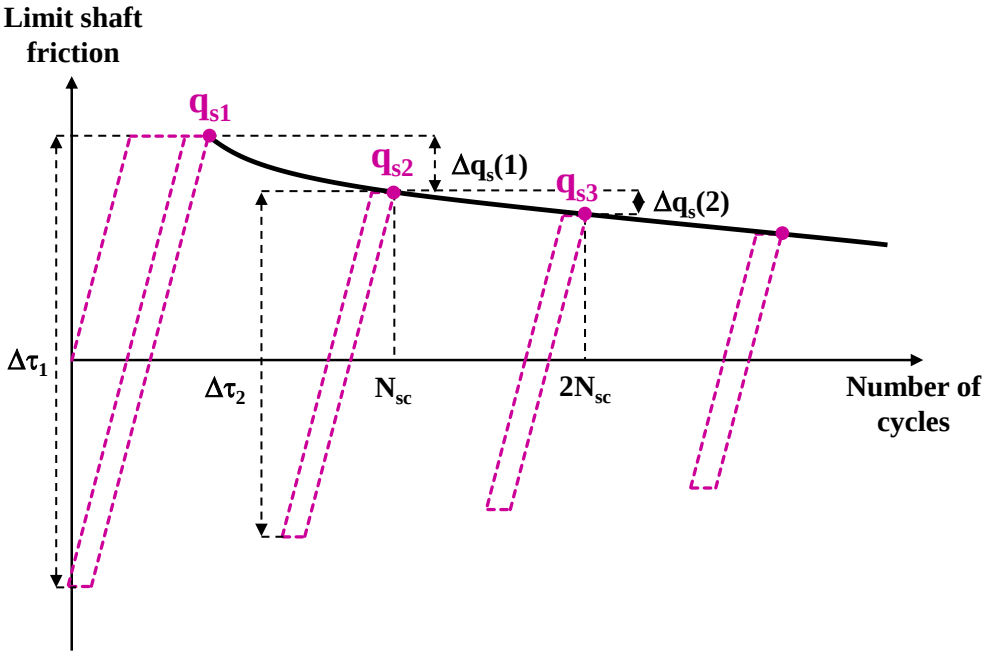


*Figure 4.21 : Evolution of the limit shaft friction at soil-pile interface in function of cycles number*

## 4.5.2 Calculation results

Aiming to test the potentialities of the developed skipped cycles method, calculations are done in FLAC3D considering the theoretical pile described in section 4.4.1 and tested under tension monotonic loading. Two maximum levels of tension cyclic loading are chosen corresponding to 30% and 70% of the pile tension capacity determined in previous monotonic calculations. For maximum level of 30%, a cyclic amplitude of 15% of the pile tension capacity is considered. For the second level, a cyclic amplitude of 35% of the pile tension capacity is considered. Table 4.4 recapitulates the details of performed cyclic sequences. Calculations are named (3D-FDM1-i) $_{i=1,2}$. In these examples, initial stress state determined according to ICP-

05 method is considered. The first step-by-step cycle is performed considering the classical Mohr-Coulomb yield criterion. The pile tension capacity is then equal to $R_s$ = 4615 kN.
The total number of cycles is fixed at 1000 cycles. These calculations allow to study the effect of cyclic characteristics, especially number of cycles and maximum applied load at the pile head.

*Table 4.4 : Characteristics of tension cyclic tests performed on pile head (3D-FDM)*

| Sequence name | $Q_{max}/R_s$ | $Q_{min}/R_s$ | $Q_{mean}/R_s$ | $Q_{cyc}/R_s$ |
|---|---|---|---|---|
| 3D-FDM1-1 | 0.3 | 0 | 0.15 | 0.15 |
| 3D-FDM1-2 | 0.7 | 0 | 0.35 | 0.35 |

Accumulated displacements at the pile head are recorded during cycles. Figure 4.22 illustrates maximum displacements accumulated at pile head in function of cycles number for each tension sequence presented in table 4.4. It should be noted that the first value for each curve (i.e., N = 0), corresponds to the initial value reached after the first step-by-step cycle. This figure shows that pile head displacements accumulate during cycles. The more the number of cycles is high the more the permanent accumulated displacement is important. It is shown that the rate of displacement accumulation increases with increasing the maximum applied load $Q_{max}$. It should be noted that the head displacement is approximately stabilised in the case of sequence 3D-FDM1-1. This can be explained by the fact that the applied $Q_{max}$ (0.3 $R_s$) is not high enough to induce plasticity in the pile after the first cycle. Therefore, following the skipped cycle method which implies zero incremental loading at the pile head, no increasing in pile head displacement is observed. In the case of cyclic sequence 3D-FDM1-2, the maximum applied load $Q_{max}$ (0.7 $R_s$) induces plasticity especially for upper elements of the pile from the first cycle. Thus, accumulation of displacement starts from the first applied cycle.
It worth noting that for the two calculation sequences, the rate of displacement accumulation is relatively very low and does not exceed 0.001mm/10 cycles. The applied cyclic sequences do not lead to exceeding the rupture criterion defined by reaching an accumulated displacement equal to $D_p/10$.
Figures 4.23a, 4.23b, 4.23c and 4.23d show respectively the evolution of normal stress and shear stress at different pile depths, i.e., for upper, middle and lower pile elements, for the two cyclic sequences. In each case, a degradation of normal stress is noticed during cycles due to the adopted behaviour law based on experimental results of direct shear tests. Considering the sequence 3D-FDM1-1 with the lower $Q_{max}$, application of the first cycle does not induce plasticity along the pile. Hence, values of shear stress are constant during cycles till reaching

330 cycles where yield criterion is reached for upper pile elements due to normal stress degradation. Therefore, the corresponding shear stresses decrease. In order to compensate this degradation, the shear stresses of soil-pile interface where no plasticity is encountered increase during loading. This is why shear stresses for middle and lower elements slightly increase after 330 cycles.

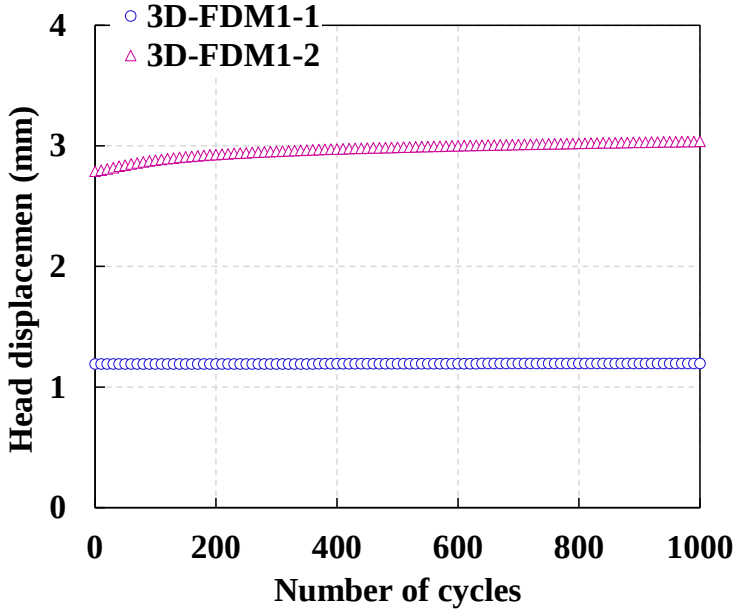


*Figure 4.22 : Evolution of pile head displacement in function of cycles number for the two tension sequences*

As for the sequence 3D-FDM1-2 with higher $Q_{max}$, plasticity is generated after the first step-by-step cycle for upper pile elements where shear stress starts directly to decrease. Consequently, shear stresses of middle and lower elements increase during cycles. After 800 cycles, the middle element reaches yield criterion, and the corresponding shear stress starts to decrease.

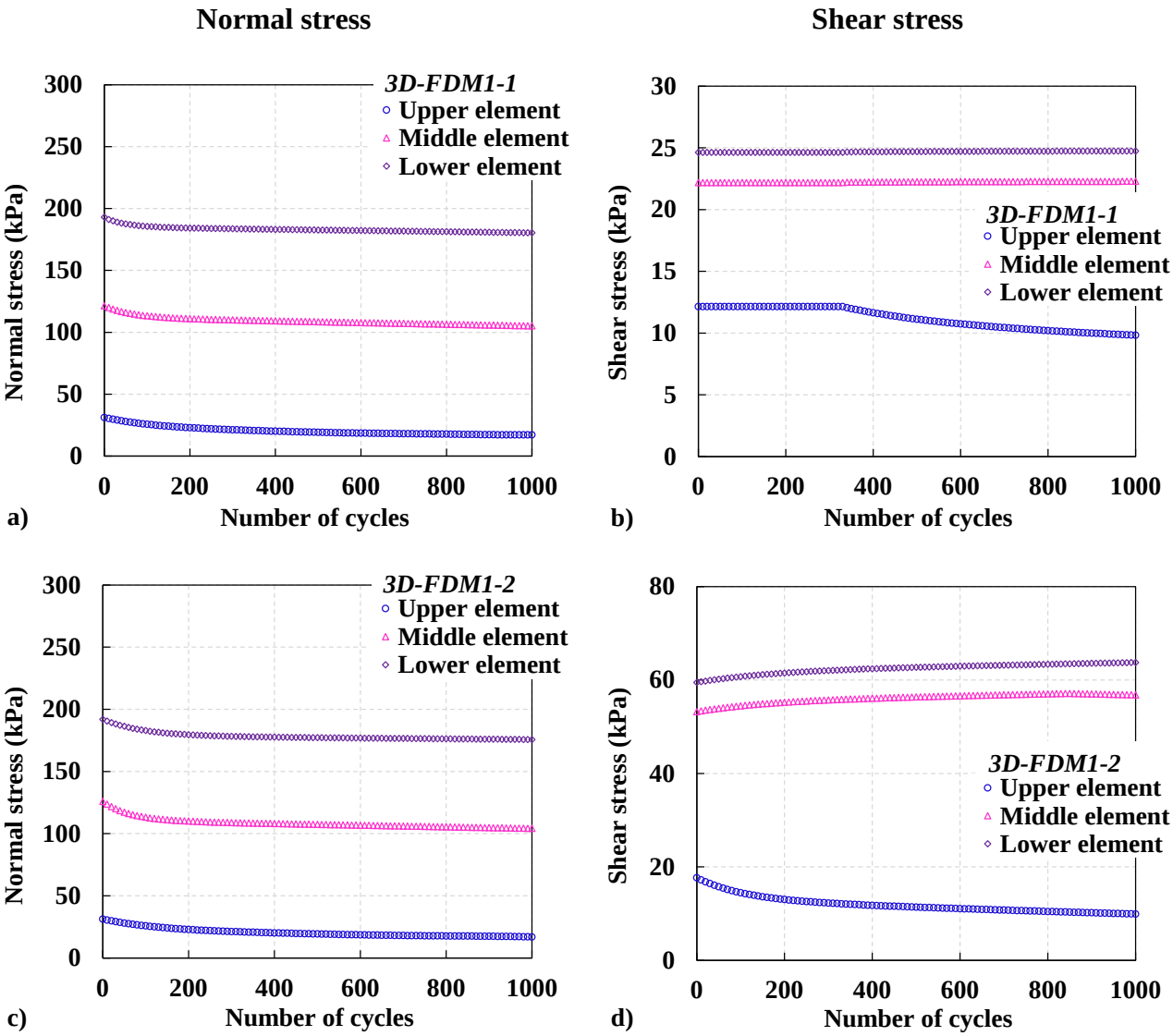


*Figure 4.23 : Evolution of normal stress and shear stress at upper, middle and lower elements of the pile for the two calculation sequences*

## 4.6 Conclusion

This chapter presents an assessment of a theoretical pile response under tension axial loading, considering monotonic loading on one hand and cyclic loading on the other hand, using the developed interface model proposed in this thesis. Radial stresses around the pile are calculated once according to the $k_0$ procedure to imitate the stress state around a bored pile, and again according to ICP-05 method to imitate the stress state around a driven pile.

At first, considering monotonic loading, calculations are done according to the conventional 1D load-transfer method (1D-FDM) combined with linear elastic perfectly plastic t-z curves with limit shaft friction related to the initial normal stress. Results of such calculations are then compared with predictions of a 3D model using the finite difference software FLAC3D (3D-

FDM), considering the default interface constitutive law with the classical Mohr-Coulomb yield criterion. This comparison is done in order to validate the modelling process. Later, the developed interface model is implemented in FLAC3D and calculation results presenting an evolution of normal stress are then compared to t-z predictions. The dilatant behaviour of the interface produces an increase in the pile tension capacity.

Secondly, the case of tension cyclic loading is treated. A skipped cycles procedure is combined with experimental cyclic results illustrating the evolution of normal displacement in function of cycles number. Different tension cyclic loading sequences are considered. The effect of cyclic characteristics, especially number of cycles and maximum loading, on the pile response in terms of pile head accumulated displacement and normal stress degradation during cycles is investigated.

Performing calculations using 3D-FDM method seems to be sufficient for a certain number of cycles. Thus, to reduce computation time, which is the object of the following chapter, a 1D finite element approach is developed in order to present an engineering tool for practical use. Several calculations will be held using the developed tool and corresponding results will be compared with 1D-FDM and 3D-FDM predictions.

# Chapter 5
# Development of a practical engineering tool for axially loaded piles calculation

## 5.1 Introduction

This chapter proposes a practical approach for modelling the behaviour of a pile subjected to axial loadings. An original 1D finite element approach is developed for practical engineering use taking into account the rheology of the problem. It allows the consideration of the normal stress variation by implementing the proposed interface model developed in chapter 3. Thus, the major contribution of this thesis is the development of this 1D approach which allows to have a reduced calculation time and to carry out a large parametric study while considering the important effect of normal stress variation.

The formulation of the finite elements and the corresponding equations used to develop this approach are firstly presented. Afterwards, the followed calculation procedure, considering monotonic loading, implemented in Fortran in a code blocks file is detailed and presented. Similarly, the followed procedure regarding cyclic loading and the developed skipped cycles method is presented.

Subsequently, the response of the theoretical pile resulting from 1D finite element analysis (1D-FEM) developed herein is compared to previous results of t-z analysis (1D-FDM) and 3D analysis (3D-FDM) considering monotonic loading. Likewise, results of cyclic simulations according to the 1D-FEM are compared to predictions of 3D-FDM simulations done using FLAC3D.

Finally, the cyclic response of such pile resulting from 1D-FEM analysis considering a large variability of cyclic characteristics, especially mean cyclic loading and cyclic amplitude, is assessed. Cyclic results in terms of accumulation of pile head displacement, normal stress degradation and pile tension capacity degradation are presented.

## 5.2 Pile analysis in 1D-FEM approach

As mentioned in chapter 4, the t-z method is considered the most appropriate way for the analysis of axially loaded pile for engineering practice. However, its limitation, regarding not considering the evolution of soil stresses in the normal direction, needs to be compensate. For this purpose, the developed numerical model was implemented and tested using a continuum-based method, the finite difference method employing the FLAC3D software. Nevertheless, this method is considered expensive in terms of computation time, especially when considering cyclic solicitations.

The main objective of this part is to propose a simple analytical method based on the one-dimensional finite element analysis and taking into consideration the effect of radial stresses on

the shear mechanism along the pile shaft. It is considered a compromise between the modesty of conventional t-z approach and the time-consuming aspect of (3D) continuum approach.

Since the geometry of the problem is simple, it is possible to model the pile by 1D *n* finite elements, more specifically bar elements, with one degree of freedom, the vertical displacement. In addition, the soil is not replaced only by surface shear springs but also by normal surface springs to capture the evolution of the radial stress along the pile shaft (figure 5.1). Hence, the change in soil volume induced by shear loading is incorporated in pile calculation.

In other terms, our work consists in conserving a simple formulation of a bar element, working in axial loading, and in considering an additional degree of freedom to take into account the variation of the volume around the pile. This variation of volume does not constitute a degree of freedom of the bar element itself, yet it forms a degree of freedom on the integration of the constitutive law.

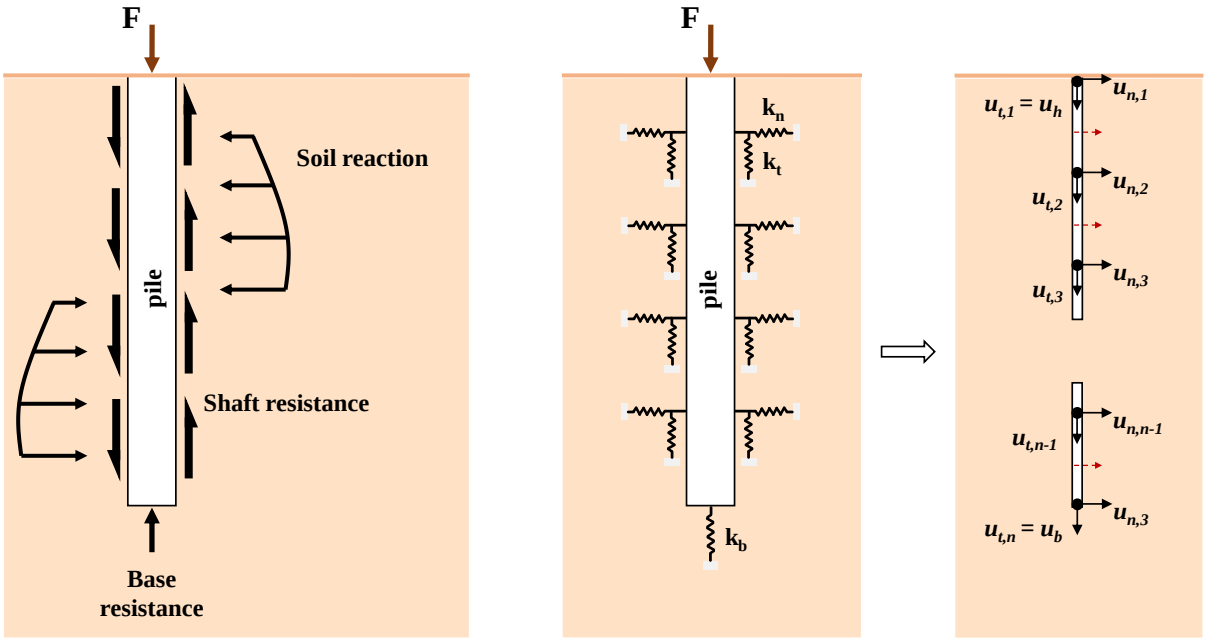


*Figure 5.1 : 1D finite element pile model*

## 5.2.1 Elemental formulation

The variational formulation of the problem leads to the following equation:

$$\left[k_p^e\right]\{u^e\} = [K^e]\begin{Bmatrix} u_{t,1}^e \\ u_{t,2}^e \end{Bmatrix} = \{F_{ext}^e\} \tag{5.1}$$

Where, $\left[k_p^e\right]$ is the stiffness matrix of the pile element, $\{u^e\}$ is the displacement vector of the pile element and $\{F_{ext}^e\}$ is the external applied loading on the pile element. $\left[k_p^e\right]$ is defined by the following expression:

$$\left[k_p^e\right] = \frac{E_{pe}S_e}{h_e}\begin{bmatrix} 1 & -1 \\ -1 & 1 \end{bmatrix} \tag{5.2}$$

In this expression, $E_{pe}$ is the Young's modulus of the pile element, $S_e$ is its surface and $h_e$ is its length.

The $\{F_{ext}^e\}$ external loading has two components: a component due to the applied loading at the pile head, $\{F_h^e\}$, and a component due to the shear and normal behaviour at the soil-pile interface and the tip reaction, $\{F_{soil}^e\}$. The latter is illustrated as following:

$$\{F_{soil}^e\}_t = -k_t^e h_e \begin{bmatrix} 1/3 & 1/6 \\ 1/6 & 1/3 \end{bmatrix}\begin{Bmatrix} u_{t,1}^e \\ u_{t,2}^e \end{Bmatrix} \text{ and } \{F_{soil}^e\}_n = -k_n^e h_e \begin{bmatrix} 1/3 & 1/6 \\ 1/6 & 1/3 \end{bmatrix}\begin{Bmatrix} u_{n,1}^e \\ u_{n,2}^e \end{Bmatrix} \tag{5.3}$$

$$\{F_{soil}^e\} = \left( -k_t^e h_e \begin{bmatrix} 1/3 & 1/6 & 0 & 0 \\ 1/6 & 1/3 & 0 & 0 \\ 0 & 0 & 0 & 0 \\ 0 & 0 & 0 & 0 \end{bmatrix} - k_n^e h_e \begin{bmatrix} 0 & 0 & 0 & 0 \\ 0 & 0 & 0 & 0 \\ 0 & 0 & 1/3 & 1/6 \\ 0 & 0 & 1/6 & 1/3 \end{bmatrix} \right) \begin{Bmatrix} u_{t,1}^e \\ u_{t,2}^e \\ u_{n,1}^e \\ u_{n,2}^e \end{Bmatrix} \tag{5.4}$$

Where, $k_t^e$ and $k_n^e$ are respectively the shear and normal stiffnesses of the interface, and $u_{n,1}^e$ and $u_{n,2}^e$ reflect the normal displacement of the interface at element nodes. We can note:

$$\{F_{soil}^e\} = [k_{soil}^e] \begin{Bmatrix} u_{t,1}^e \\ u_{t,2}^e \\ u_{n,1}^e \\ u_{n,2}^e \end{Bmatrix} \tag{5.5}$$

Matrices and vectors of each element should be assembled into a global system in order to satisfy the equilibrium condition at nodes. Finally, the global system to be resolved can be written as follows:

$$[k]\{U\} = \left[k_p + k_{soil}\right]\{U\} = \{F_h\} \tag{5.6}$$

The global displacement vector, $\{U\}$, contains then two parts, an axial part linked to the degree of freedom of the bar element, and a normal part which presents the volume variation and therefore the normal stress variation.

## 5.2.2 Calculation procedure with 1D-FEM approach

### *5.2.2.1 Non-linear iterative procedure: monotonic loading*

The problem is solved following the elastoplasticity principles. Initially, the equation of elasticity is integrated to obtain the elastic prediction of the behaviour. In a second step, the stresses are relaxed on the yield surface by correcting the plastic deformation increments by iterations. In the following paragraphs, the resolution steps are presented.

1- At first, a loading increment is applied at the pile head. The global equilibrium equation is then resolved in order to obtain the increment of shear and normal displacements for each node of the interface. From these displacements, increments of shear and normal stresses are determined at Gauss point of each element.

2- The plasticity criterion is then checked at Gauss points. If the plasticity criterion is not verified, the resolution follows an iterative process until convergence. This iterative process is performed by updating the loading vector. As the increments of plastic displacement are calculated at Gauss points, the associated loading is then determined for each element. It can be expressed by:

$$dF_p^e = [k_{soil}^e] du_p^e h_e \tag{5.7}$$

The loading vector of each element is then corrected and updated by distributing the plastic correction $dF_p^e$ over the two nodes adjacent to the element, that we noted j and j+1. Thus, for each node of each element, the corrected loadings are:

$$F^j = F^j + \frac{dF_p^e}{2} \text{ and } F^{j+1} = F^{j+1} + \frac{dF_p^e}{2} \tag{5.8}$$

It should be noted that any plasticity criterion can be implemented. For following calculations, classical Mohr-Coulomb criterion is implemented, in addition to our proposed model, developed in chapter 3.

3- This procedure is repeated for all elements. Hence, for each iteration i, we update the loading vector, and we determine the node displacements again. For the pile base, the criterion is checked at the tip node. The plastic displacement increments are also calculated on this node. The associated force is directly calculated at the node. When reaching convergence, iterations are stopped. Another loading increment is therefore applied. This iterative procedure is repeated till reaching the desired load.

The finite element formulation described here is implemented in Fortran in a code blocks file. After a phase of variables initialisation, the model input parameters are read. Figure 5.2 illustrates the flowchart of iterative programming code.

The response of the theoretical pile presented in previous chapter will be detailed in the following section. The behaviour resulting from calculations using Fortran is compared to the behaviour resulting from load transfer analysis and from 3D analysis using the developed constitutive law.

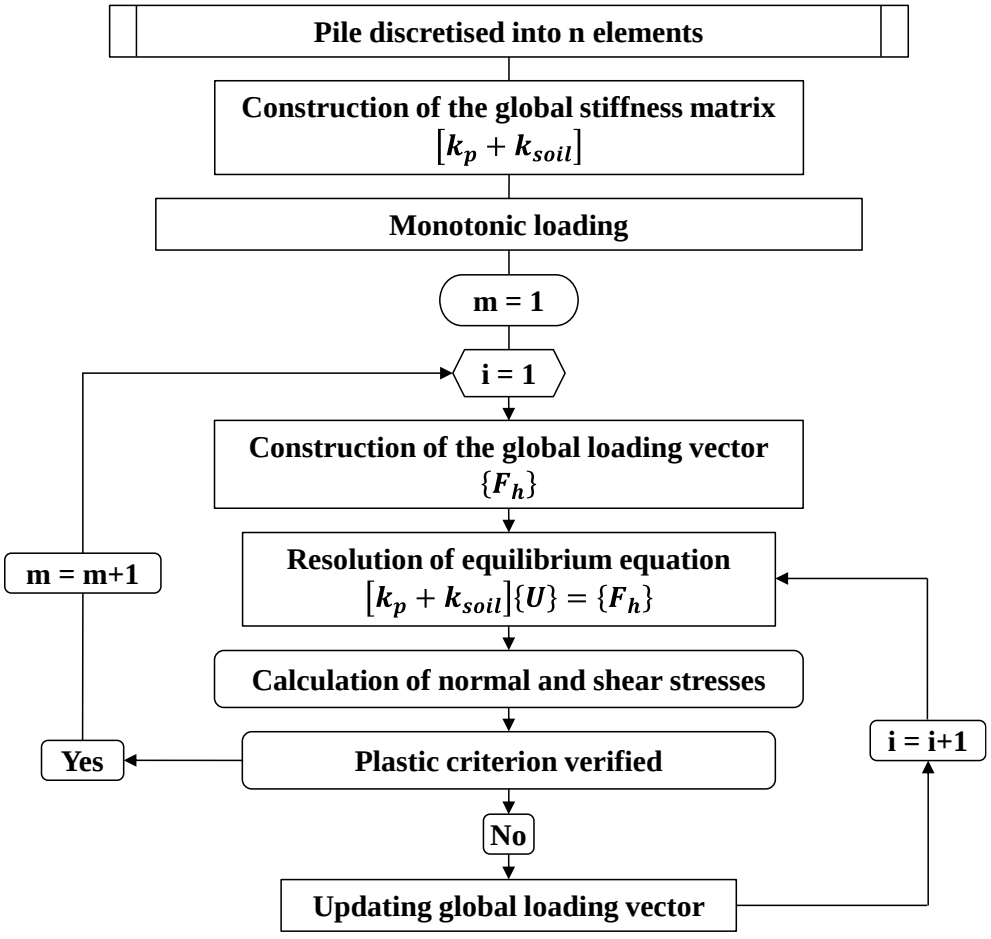


*Figure 5.2 : Flowchart of monotonic numerical programming*

### *5.2.2.2 Non-linear iterative procedure: cyclic loading*

Cyclic calculation in this chapter follows the same principles of skipped cycles method developed in chapter 4. Using global finite element formulation of the problem, non-linear iterative procedure is followed in order to determine the soil-pile interface stresses. Figure 5.3 presents the flowchart of numerical programming regarding cyclic loading. The following calculation steps are implemented in Fortran language.

1- Simulation of the first step-by-step cycle follows the incremental procedure presented in figure 5.2. Calculation steps described in section 5.2.2.1 are followed for each loading or unloading increment. The classical Mohr-Coulomb yield criterion with no dilatancy is considered.

2- After the first cycle, cyclic characteristics, $\eta_{max1}$ and $\Delta\tau_1$, and normal stresses are determined for each pile element. Using these parameters, the normal displacement $u_{n1}$ corresponding to the first packet of $N_{sc}$ skipped cycles (see figure 4.20) is calculated for each pile element. Therefore, the corresponding variation of normal stress $\Delta\sigma_n(1)$ is evaluated. It should be noted that a value of 10 cycles for $N_{sc}$ is adopted during calculations presented in this chapter. Nevertheless, higher value of $N_{sc}$ can cause some numerical disorder regarding the determination of curves $u_n = f(N)$. Calculations with $N_{sc}$=10 shows a steadier trend. In addition to that, the pile may experience cyclic rupture for a cycles number lesser than 100 cycles depending on cyclic characteristics. Hence, in order to accurately investigate the behaviour of the pile in this case a small number of skipped cycles is more suitable.

3- Afterwards, an iterative procedure is started. The global equilibrium equation is firstly solved where no increment of loading is considered, the global load vector is kept equal to the value of the maximum applied load on the pile head, $Q_{max}$. The developed increments of shear displacement for each node of the interface are obtained due to plasticity induced by the application of $\Delta\sigma_n$. Increments of shear and normal stresses are then determined.

4- The plasticity criterion is then checked at Gauss points. The global vector load is updated following the corresponding equation presented in section 5.2.2.1, and the iterative procedure continues until reaching convergence.

5- Every packet of $N_{sc}$ skipped cycles is followed by a step-by-step unloading-loading cycle in order to update cyclic characteristics, $\eta_{max}$ and $\Delta\tau$, for each pile element. This cycle obeys the classical Mohr-Coulomb yield criterion (see figure 4.21).

6- Updated cyclic parameters and normal stresses are used to determine the value of the normal displacement corresponding to the following $N_{sc}$ skipped cycles. In order to take into account the effect of previous packet of $N_{sc}$ cycles, the approach of equivalent number (see section 4.5.1) is followed.

7- The calculation stops at the end of the $N_{total}$ cycles or when a rupture occurs due to lack of equilibrium between applied loading on pile head and its resistance or due to accumulated displacement exceeding the conventional allowable displacement of $D_p/10$.

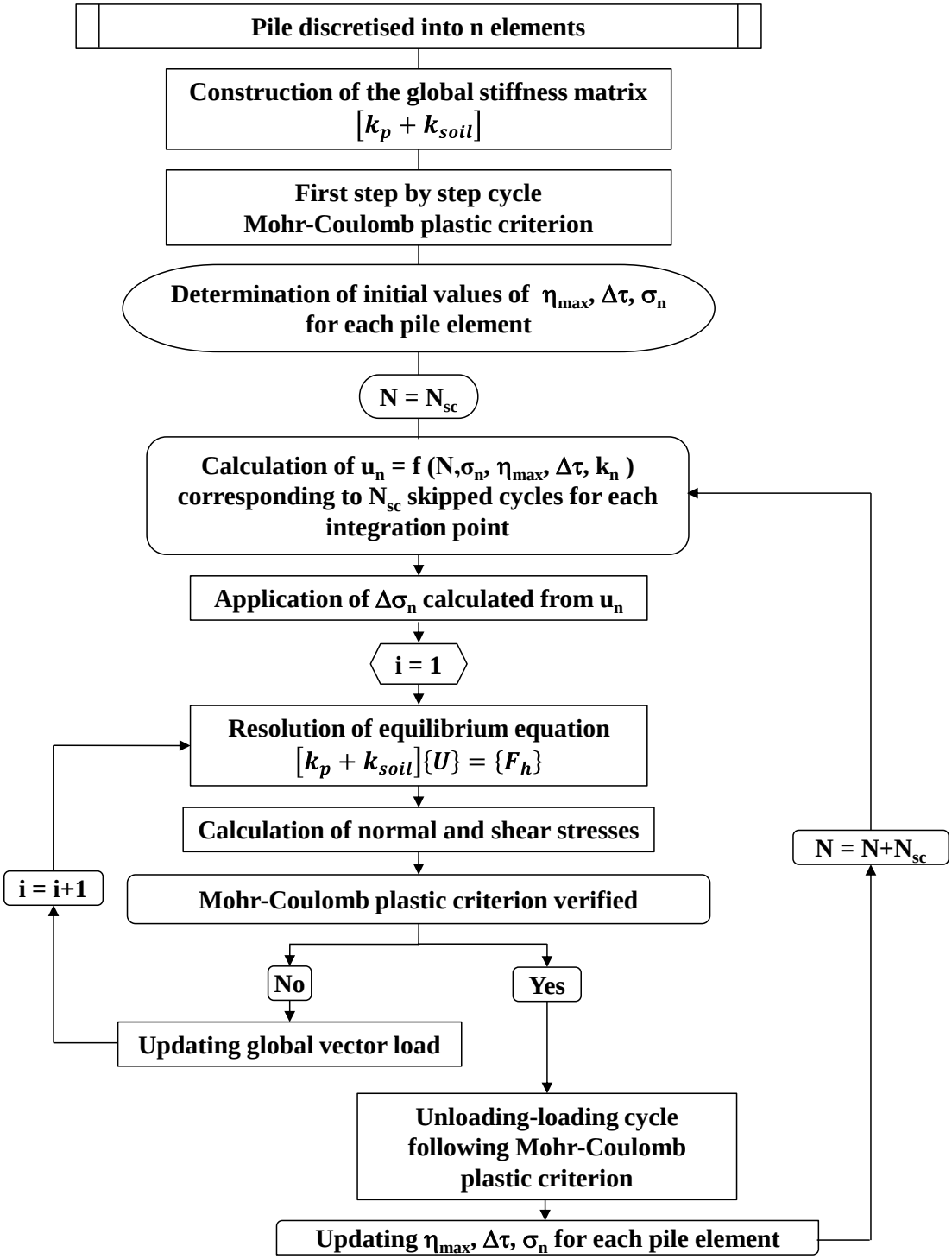


*Figure 5.3 : Flowchart of cyclic numerical programming*

## 5.3 Pile calculation under monotonic loading: Comparison with 1D-FDM (t-z) and 3D-FDM (FLAC3D) predictions

In order to evaluate the performance of the code developed in Fortran, different comparisons are proposed. Data of theoretical pile presented in chapter 4 are used as input data in the programming code. The classical Mohr-Coulomb criterion and the developed constitutive

model are implemented and tested. In addition, the two initial conditions, $k_0$ and ICP-05, are considered for the comparison. Calculations done with the t-z method and in FLAC3D with the developed constitutive law are used as reference for comparisons.

The 30 m length pile is discretised into 30 elements, each of 0.5 m length. It is subjected to incremental tension monotonic loading corresponding to 90% of the total capacity reached by the pile in different cases considered in section 4.4. This intensity of maximum loading is considered to avoid numerical divergence.

Figures 5.4a and 5.4b show curves of head load-displacement for both initial conditions and considering the two models for the pile interface. Mohr-Coulomb criterion is used in order to compare calculation results with t-z predictions (1D-FDM) where elastic perfectly plastic load transfer curves are considered (figure 5.4a). Pile response for 1D finite element model in Fortran (1D-FEM) and t-z analysis (1D-FDM) has a similar tendency, for $K_0$ initial conditions as well as for ICP-05 (figure 5.4a).

Regarding calculations done according to the proposed interface constitutive law, the response of 1D-FEM analysis is very close to the response of 3D-FDM analysis (figure 5.4b). Slight difference is occurred due to the presence of soil elements in 3D analysis. Plasticity along the pile depth in 3D analysis occurs for a pile head displacement higher than that needed in 1D-FEM analysis. This explains the disparity between different results.

Overall, predictions of the developed 1D-FEM present a good agreement with analyses results of 1D-FDM and 3D-FDM. Corresponding calculations done in Fortran allow to greatly reduce computation time. This contribution would be very beneficial in the case of cyclic loading that will be presented in following sections.

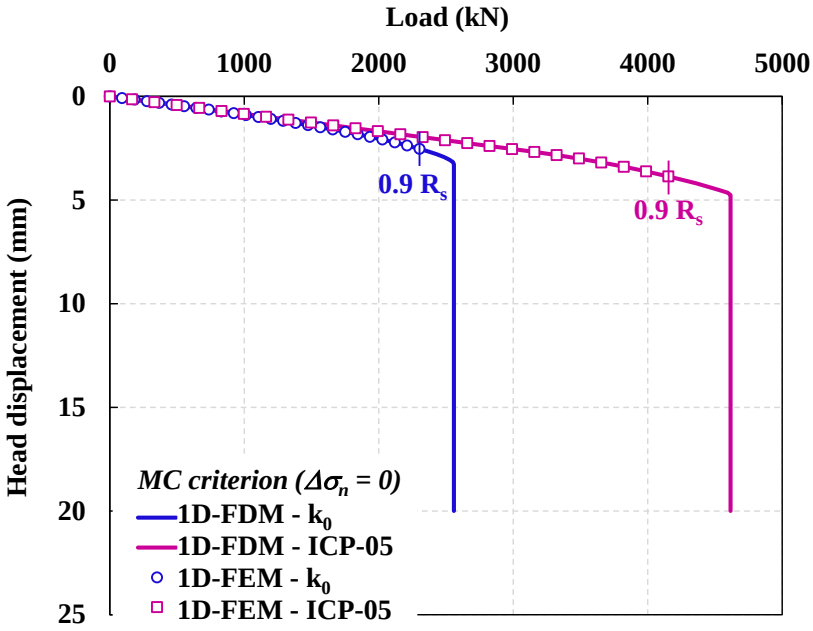


*(a) Mohr-Coulomb criterion*

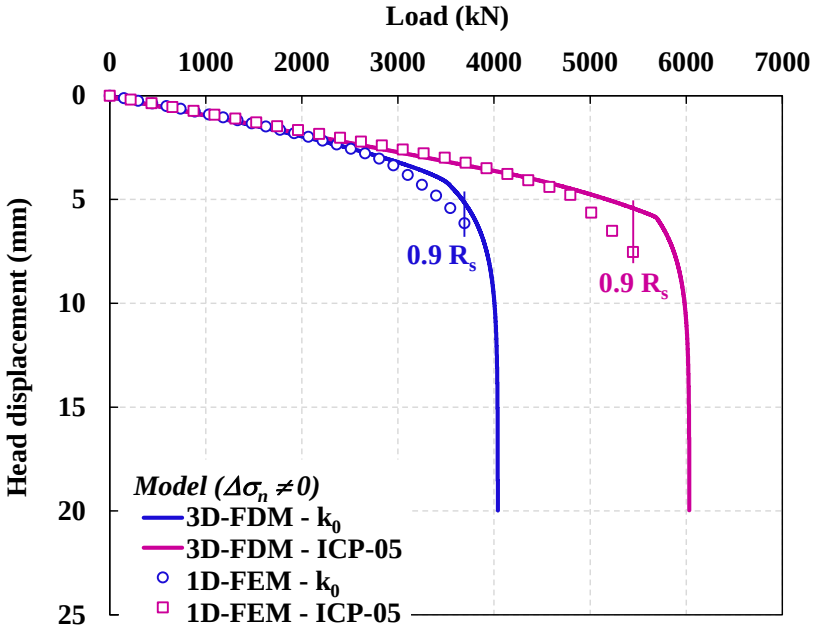


*(b) Developed Behaviour model*

*Figure 5.4 : Head load-displacement curves with $k_0$ and ICP-05 initial stress state: a) comparison between t-z (1D-FDM) results and Fortran (1D-FEM) results ($\Delta\sigma_n = 0$), b) comparison between FLAC3D (3D-FDM) results and Fortran (1D-FEM) results ($\Delta\sigma_n \neq 0$)*

## 5.4 Pile calculation under cyclic loading

### 5.4.1 Comparison with 3D-FDM (FLAC3D) predictions

In this section, predictions of 1D-FEM model are compared to results of 3D-FDM model considering cyclic loading. Table 5.1 presents details of tension cyclic sequences performed in FLAC3D in chapter 4 with their corresponding codes considering calculations done in Fortran. Same initial conditions are considered here (ICP-05). The pile tension capacity is equal to $R_s$ = 4615 kN.

*Table 5.1: Characteristics of tension cyclic tests performed on pile head (1D-FEM)*

| Sequence name | $Q_{max}/R_s$ | $Q_{min}/R_s$ | $Q_{mean}/R_s$ | $Q_{cyc}/R_s$ |
|---|---|---|---|---|
| 1D-FEM1-1 | 0.3 | 0 | 0.15 | 0.15 |
| 1D-FEM1-2 | 0.7 | 0 | 0.35 | 0.35 |

Figure 5.5 shows the evolution of pile head displacement in function of cycles number. The increase in pile head displacement for 1D-FEM and 3D-FDM analyses present similar tendency. Simulation according to 1D-FEM and 3D-FDM show approximately the same behaviours regarding displacement stabilisation and displacement evolution in function of cycles number despite the value of $Q_{max}$.

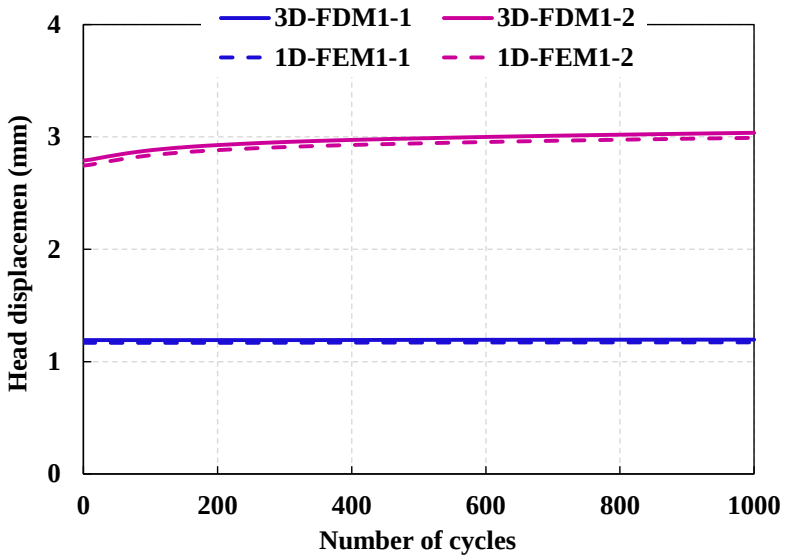


*Figure 5.5 : Evolution of pile head displacement in function of cycles number, comparison between Fortran (1D-FEM) results and FLAC3D (3D-FDM) results*

Figures 5.6a, 5.6b, 5.6c and 5.6d illustrate the variation in normal stress and mobilised shear stress along the pile during cycles for each cyclic sequence. Degradation in normal stress

resulting from 1D-FEM analysis and 3D-FDM analysis show exactly the same trend. This degradation is imposed by the mean of experimental curves defining the flow rule of the developed constitutive law.

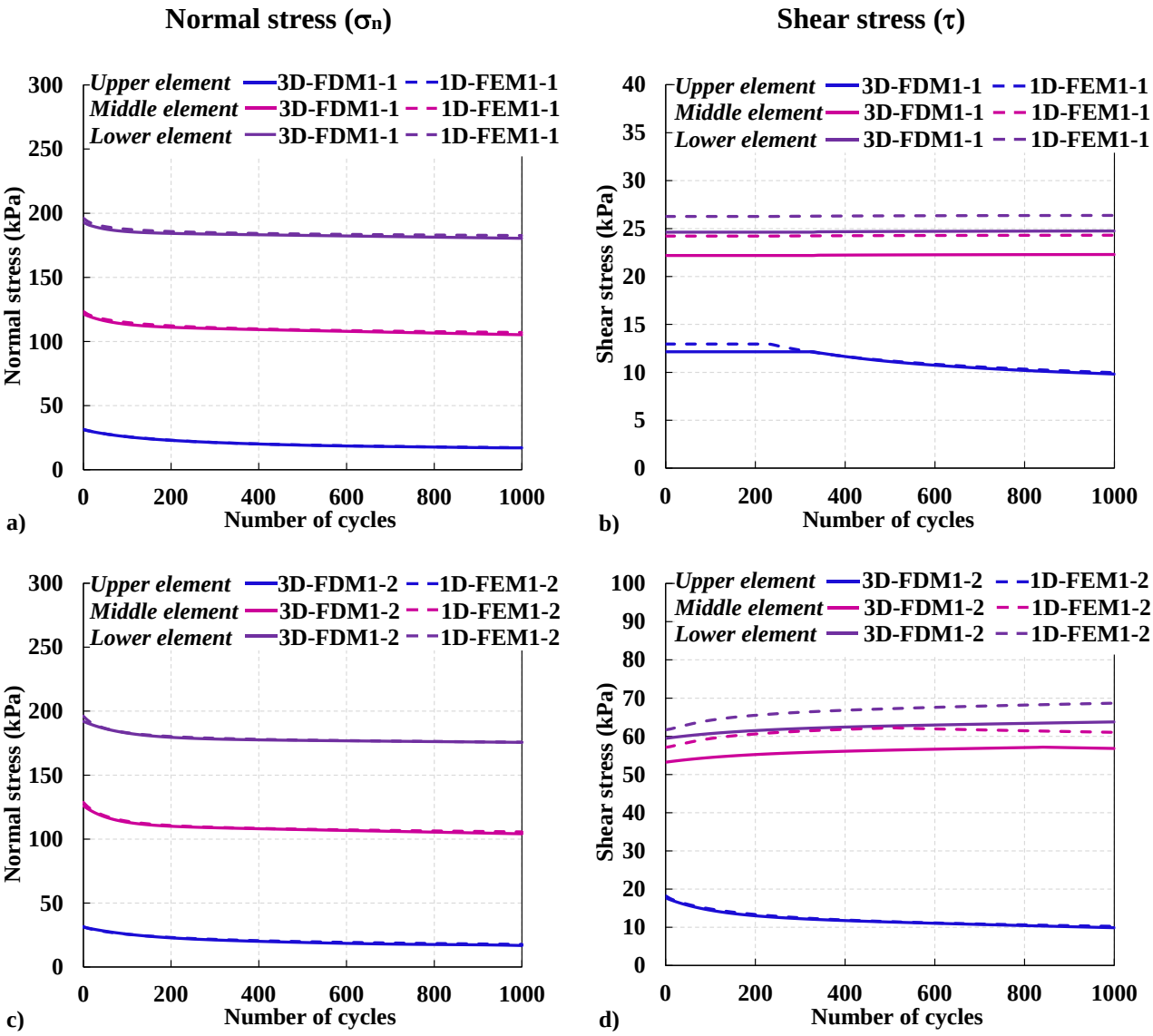


*Figure 5.6 : Evolution of normal stress and shear stress in function of cycles number for different pile depths, comparison between Fortran (1D-FEM) results and FLAC3D (3D-FDM) results*

It can be noticed that the difference between the two analyses lies in the mobilisation of shear stress especially at interface levels where plasticity is not yielded yet. When the first step-by-step cycle does not activate plasticity, a slight difference exists between values of the initial mobilised shear stress determined according to 1D-FEM and 3D-FDM analyses. Considering for example the first cyclic sequence with maximum loading equal to 30% $R_s$, it can be seen that the plasticity is developed in the upper element for a lower number of cycles according to 1D-FEM analysis comparing to 3D-FDM analysis. Thus, mobilised shear stresses at the middle

and lower elements, resulting from 1D-FEM analysis, starts to increase after 240 cycles while it needs 330 cycles according to 3D-FDM analysis.

Considering the second cyclic sequence with $Q_{max}$ equal to 70% $R_s$, the degradation of the limit shaft friction at the upper element induced by the plasticity is similar according to each analysis seeing that the first cycle results in reaching yield criterion for upper elements. Similar to what it was observed in the first sequence, according to 1D-FEM simulations, the plasticity is generated in the middle element after a number of cycles smaller than the number needed to activate plasticity according to predictions of 3D-FDM. Then, after a phase of increasing, corresponding shear stress starts to degrade according to 1D-FEM analysis before its degradation according to 3D-FDM analysis.

These observations are related to the presence of surrounding soil around the pile. The considered soil with an elastic behaviour may affect the response of the soil-pile interface. In general, predictions of 1D-FEM analysis are in very good agreement with results of 3D-FDM analysis.

Despite the development of a skipped cycles method in the aim of reducing computation time, the need of performing a certain number of, step-by-step, cycles in order to update cyclic parameters considering 3D-FDM analysis still requires a high calculation time.

From this point, the 1D-FEM method permits to greatly reduce the time consuming. Thus, performing calculations using the developed 1D-FEM would be beneficial in order to assess the pile behaviour under a large number of cycles and considering various cyclic characteristics. Results of such study are presented in following sections.

### 5.4.2 Cyclic response

Additional cyclic calculations are performed by benefitting from the great economy in computation time resulting from using the developed 1D-FEM model. Calculations done in this application concerns additional cyclic tension sequences, with different maximum loading levels and cyclic amplitudes. The aim of this study is to analyse the response of the theoretical pile regarding several possible cyclic characteristics. Due to low calculation time needed, a total number of 10000 is fixed for each case. Table 5.2 presents the details of all cyclic sequences applied to pile head. Cyclic sequences are listed in increasing order of corresponding cyclic amplitudes.

It should be noted that cyclic rupture occurred during these sequences is only generated by lack of equilibrium between applied loading on pile head and its resistance. No evidence of cyclic rupture caused by surpassing the conventional allowable displacement of $D_p/10$ is shown.

Table 5.2 also summarises the results of simulations corresponding to cyclic tension sequences. It shows the total number of cycles reached by each sequence before rupture occurred due to lack of equilibrium. Therefore, the only rupture criterion, considered herein, concerns the pile tension capacity. Indeed, the degradation of the normal stress along the soil-pile interface and therefore the resulted degradation of its shaft resistance during cyclic loading causes a degradation of the tension capacity of the pile. The latter may become less than the maximum loading applied at the pile head, $Q_{max}$, without that the displacement exceeds the conventional criterion of $D_p/10$. The pile shows then a lack of equilibrium.

Following sections present each a specific aspect of pile behaviour. Results related to the evolution of pile head displacement, tension capacity, normal stresses and shear stresses at the interface, in addition to the degradation factor of the shaft resistance in function of cycles number, are presented. It worth noting that the developed skipped cycles method combined with experimental numerical expressions predicts the degradation and changes in cyclic pile capacity better than accumulated displacements at pile head.

*Table 5.2 : Characteristics of additional tension cyclic tests performed on pile head*

| Sequence name | $Q_{max}/Rs$ | $Q_{min}/R_s$ | $Q_{mean}/R_s$ | $Q_{cyc}/R_s$ | Number of cycles |
|---|---|---|---|---|---|
| 1D-FEM2-1 | 0.05 | 0 | 0.025 | 0.025 | 10000 |
| 1D-FEM2-2 | 0.1 | 0 | 0.05 | 0.05 | 10000 |
| 1D-FEM2-3 | 0.15 | 0 | 0.075 | 0.075 | 10000 |
| 1D-FEM2-4 | 0.2 | 0 | 0.1 | 0.1 | 10000 |
| 1D-FEM2-5 | 0.3 | 0 | 0.15 | 0.15 | 10000 |
| 1D-FEM2-6 | 0.4 | 0.1 | 0.25 | 0.15 | 10000 |
| 1D-FEM2-7 | 0.8 | 0.5 | 0.65 | 0.15 | 4450 |
| 1D-FEM2-8 | 0.4 | 0 | 0.2 | 0.2 | 10000 |
| 1D-FEM2-9 | 0.7 | 0.3 | 0.5 | 0.2 | 10000 |
| 1D-FEM2-10 | 0.5 | 0 | 0.25 | 0.25 | 10000 |
| 1D-FEM2-11 | 0.6 | 0 | 0.3 | 0.3 | 10000 |
| 1D-FEM2-12 | 0.7 | 0.1 | 0.4 | 0.3 | 9040 |
| 1D-FEM2-13 | 0.7 | 0 | 0.35 | 0.35 | 8180 |
| 1D-FEM2-14 | 0.8 | 0 | 0.4 | 0.4 | 2600 |
| 1D-FEM2-15 | 0.9 | 0 | 0.45 | 0.45 | 70 |

### *5.4.2.1 Accumulation of displacements*

During cyclic calculation, accumulated displacements at pile head are registered and at each pile depth as well. In this part, two main aspects are studied: the effect of maximum loading on

one hand and of cyclic amplitude on the other hand, on pile head displacement accumulation during cycles. For this purpose, figure 5.7 illustrates maximum displacements accumulated at pile head in function of cycles number for cyclic sequences presented in table 5.2 with increasing maximum loading. Results of sequences 1D-FEM2-1, 1D-FEM2-2, 1D-FEM2-3, 1D-FEM2-4, 1D-FEM2-5, 1D-FEM2-8, 1D-FEM2-10, 1D-FEM2-11, 1D-FEM2-13, 1D-FEM2-14 and 1D-FEM2-15 are presented in figure 5.7.

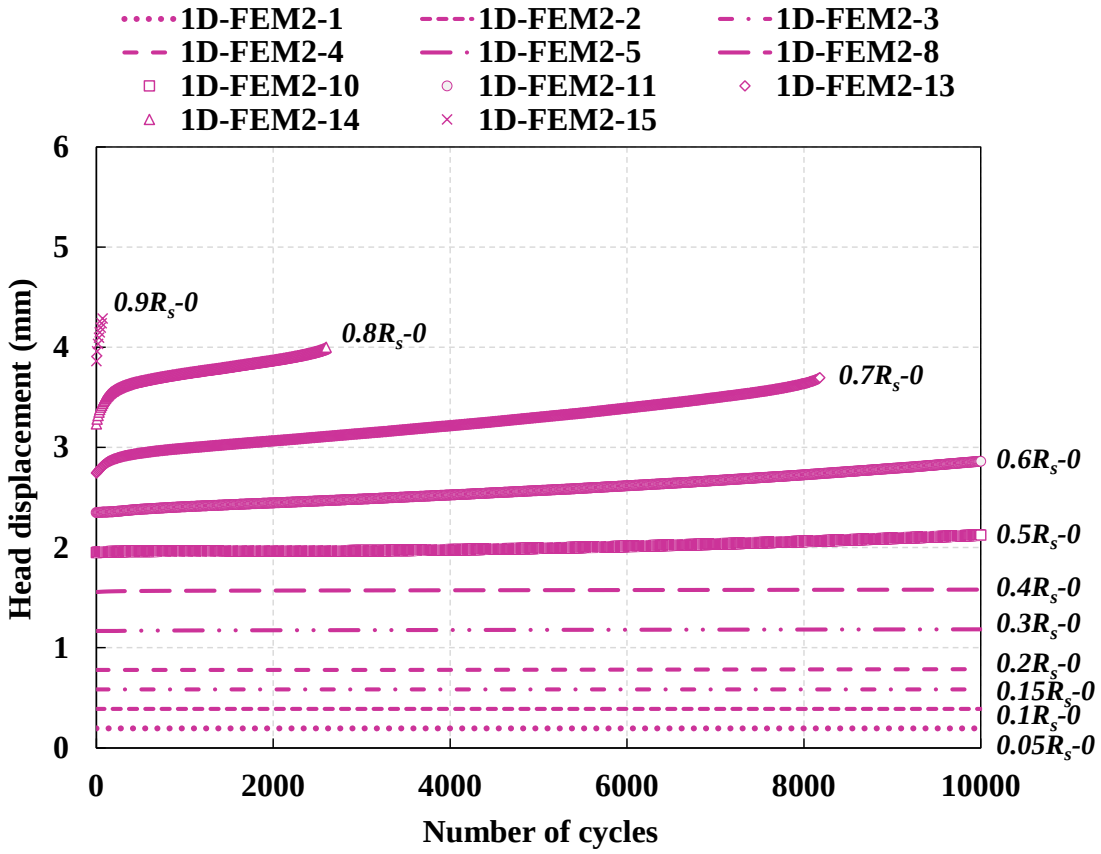


*Figure 5.7 : Evolution of pile head displacement in function of cycles number: effect of maximum loading $Q_{max}$*

It can be shown that displacements accumulate during cycles especially for high values of maximum loading $Q_{max}$. The rate of displacement accumulation and the displacement reached at the end of loading depend on cyclic characteristics, especially the maximum loading $Q_{max}$ and number of cycles. Indeed, final displacement accumulated at the pile head increases with increasing number of cycles. It should be noted that below a certain value of maximum loading (0.3 $R_s$), the displacement at the pile head is approximately the same during cycles (1D-FEM2-1, 1D-FEM2-2, 1D-FEM2-3 and 1D-FEM2-4). The stabilisation of head pile displacement can be explained by the fact that the first step-by-step cycle does not generate plasticity along pile depth, and during cyclic loading the degradation of normal stresses at each pile depth is not

sufficient to achieve plasticity and therefore to induce accumulation of displacements. The pile will not reach rupture.

From this maximum loading (0.3 $R_s$) and beyond, pile displacement is more important. Displacements gradually accumulate during cycles. The rate of accumulation is considered relatively small and does not exceed $6.10^{-3}$ mm/10 cycles. However, it can be noticed that the head pile displacement during cycles increases faster as the maximum loading $Q_{max}$ increases. This accumulation of displacements may lead to a lack of equilibrium and therefore to rupture as for sequences 1D-FEM2-13, 1D-FEM2-14 and 1D-FEM2-15.

From a practical point of view, the increase in the maximum loading $Q_{max}$ is done by increasing the cyclic amplitude of the loading $Q_{cyc}$, or the mean loading $Q_{mean}$. Figures 5.8a and 5.8b allow to clearly study the effect of these two parameters on the evolution of displacements.

Results of sequences (1D-FEM2-5, 1D-FEM2-6 and 1D-FEM2-7), sequences (1D-FEM2-8, and 1D-FEM2-9) and sequences (1D-FEM2-11 and 1D-FEM2-12) present the effect of increasing the mean loading $Q_{mean}$ (figure 5.8a), while sequences (1D-FEM2-6 and 1D-FEM2-10) and sequences (1D-FEM2-12 and 1D-FEM2-14) show the effect of increasing the cyclic amplitude $Q_{cyc}$ (figure 5.8b). These results show that the increase in these two parameters, $Q_{cyc}$ and $Q_{mean}$, produces a higher accumulation of displacements eventually leading to rupture with smaller number of cycles.

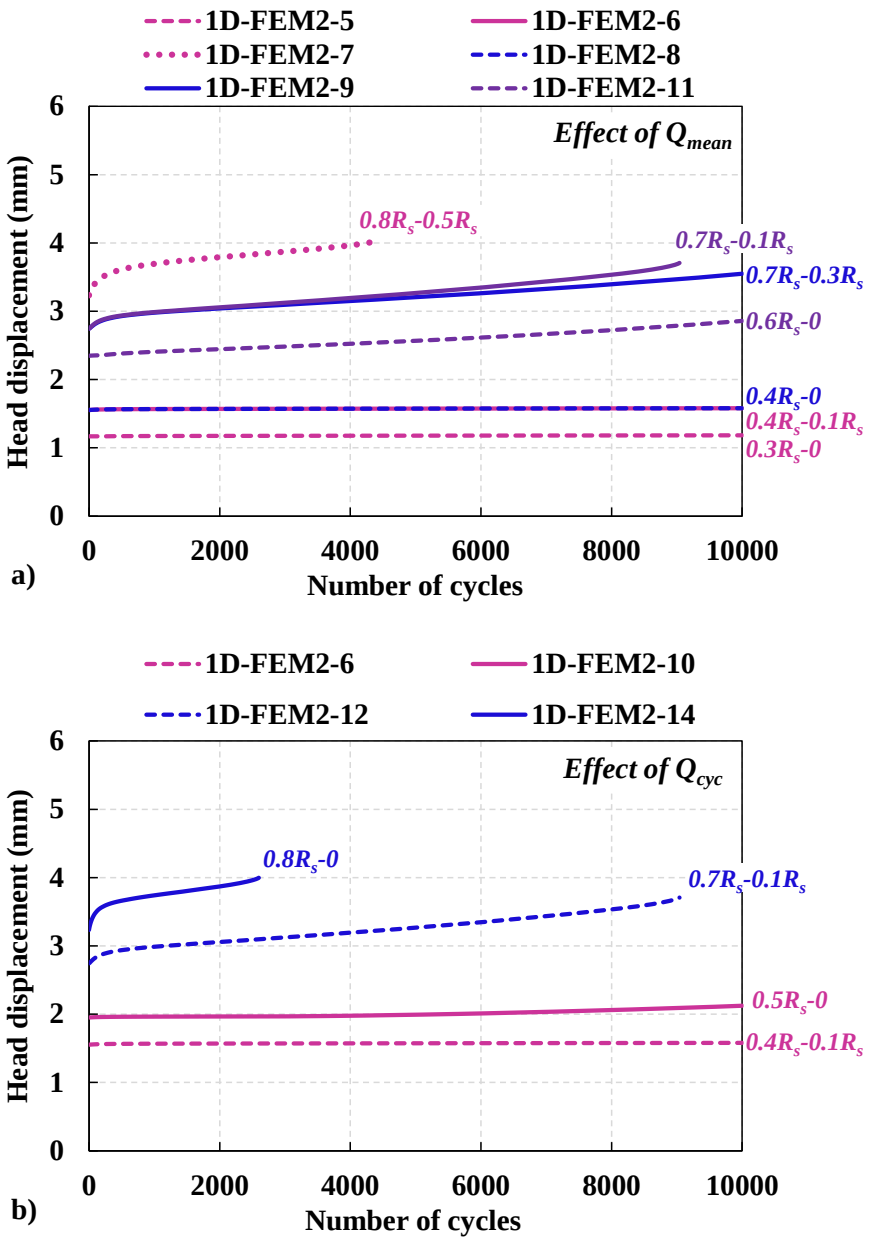


*Figure 5.8 : Evolution of pile head displacement in function of cycles number: a) effect of mean loading $Q_{mean}$, b) effect of cyclic amplitude $Q_{cyc}$*

### *5.4.2.2 Evolution of pile resistance*

The contracting behaviour of the soil-pile interface induced by experimental curves, $u_n = f(N)$, results in degradation in the pile capacity. In order to quantify this degradation, the pile resistance after each j packet of $N_{sc}$ skipped cycles is evaluated. At each pile element, the decrease in limit shaft friction can be determined according to the following equation:

$$\Delta q_s(j) = \Delta\sigma_n(j) * \tan\varphi \tag{5.9}$$

Where $\Delta\sigma_n(j)$ refers to the degradation in normal stress after each j packet of skipped cycles.

By integration the values of estimated limit shaft friction over the pile length, tension cyclic pile resistance, $R_{s,cyc}$, can be estimated after each $N_{sc}$. Figure 5.9 presents the evolution of the ratio $R_{scyc}/R_s$, where $R_s$ is the initial pile resistance to tension, in function of cycles number for all cyclic sequences presented in table 5.2. This evolution or degradation in the pile capacity is also presented in table 5.3 where the final value of pile resistance is estimated.

Figure 5.9 and table 5.3 show that for low values of maximum loading $Q_{max}$ (particularly less than 0.3 Rs), cyclic degradation undergone by the pile tension capacity remains low, even after a large number of cycles, 10000 cycles (1D-FEM2-1, 1D-FEM2-2, 1D-FEM2-3 and 1D-FEM2-4). Considering these small values of maximum loading, the degradation in pile resistance to tension does not surpass 18% of its initial value before cyclic loading.

*Table 5.3 : Summary of tension capacity degradation undergo by the pile for each sequence*

| Sequence name | Number of cycles | Percentage of degradation of $R_s$ (%) | Final resistance to tension (kN) |
|---|---|---|---|
| 1D-FEM2-1 | 10000 | 11.4 | 4088.2 |
| 1D-FEM2-2 | 10000 | 13.3 | 4002.4 |
| 1D-FEM2-3 | 10000 | 15.2 | 3915.5 |
| 1D-FEM2-4 | 10000 | 17.1 | 3825 |
| 1D-FEM2-5 | 10000 | 20.8 | 3656.7 |
| 1D-FEM2-6 | 10000 | 22.2 | 3589.8 |
| 1D-FEM2-7 | 4450 | 20 | 3692.7 |
| 1D-FEM2-8 | 10000 | 24.2 | 3496.5 |
| 1D-FEM2-9 | 10000 | 27.9 | 3327.6 |
| 1D-FEM2-10 | 10000 | 27.6 | 3340 |
| 1D-FEM2-11 | 10000 | 30.8 | 3194.2 |
| 1D-FEM2-12 | 9040 | 29.9 | 3231.4 |
| 1D-FEM2-13 | 8180 | 30 | 3231 |
| 1D-FEM2-14 | 2600 | 19.9 | 3692.6 |
| 1D-FEM2-15 | 70 | 9.6 | 4171.1 |

For higher values of maximum loading, the pile resistance degradation becomes more extensive. It can be noticed that the rate of degradation increases with increasing the maximum loading where the slope of each curve increases by increasing $Q_{max}$. This degradation may lead to cyclic rupture due to lack of equilibrium without even reaching 10000 cycles, like the case of sequences 1D-FEM2-7, 1D-FEM2-12, 1D-FEM2-14 and 1D-FEM2-15.

By analysing figure 5.9, one can say that for high values of $Q_{max}$, it is the cyclic amplitude $Q_{cyc}$ that controls cyclic degradation of the pile. In order to identify the impact of cyclic amplitude $Q_{cyc}$, sequences 1D-FEM2-9 and 1D-FEM2-12 are considered at 10000 cycles. Having a maximum loading of $0.7R_s$ and a cyclic amplitude of $0.2R_s$, the sequence 1D-FEM2-9 generates a ratio $R_{scyc}/R_s$ equivalent to 0.72 after 10000 cycles. For the sequence 1D-FEM2-12, $Q_{max}$ is equal to $0.6R_s$, $Q_{cyc}$ is equal to $0.3R_s$, and after 10000 cycles the ratio $R_{scyc}/R_s$ is equivalent to 0.69. Thus, it is obvious that the loading sequence having the highest cyclic amplitude $Q_{cyc}$ generates the highest cyclic degradation even though it has the lowest maximum loading $Q_{max}$. In general, it is clear that cyclic loading causes the tension resistance of the pile to degrade as the cycles progress. The ratio and rate of degradation depend on cyclic characteristics of loading ($Q_{max}$ and $Q_{cyc}$).

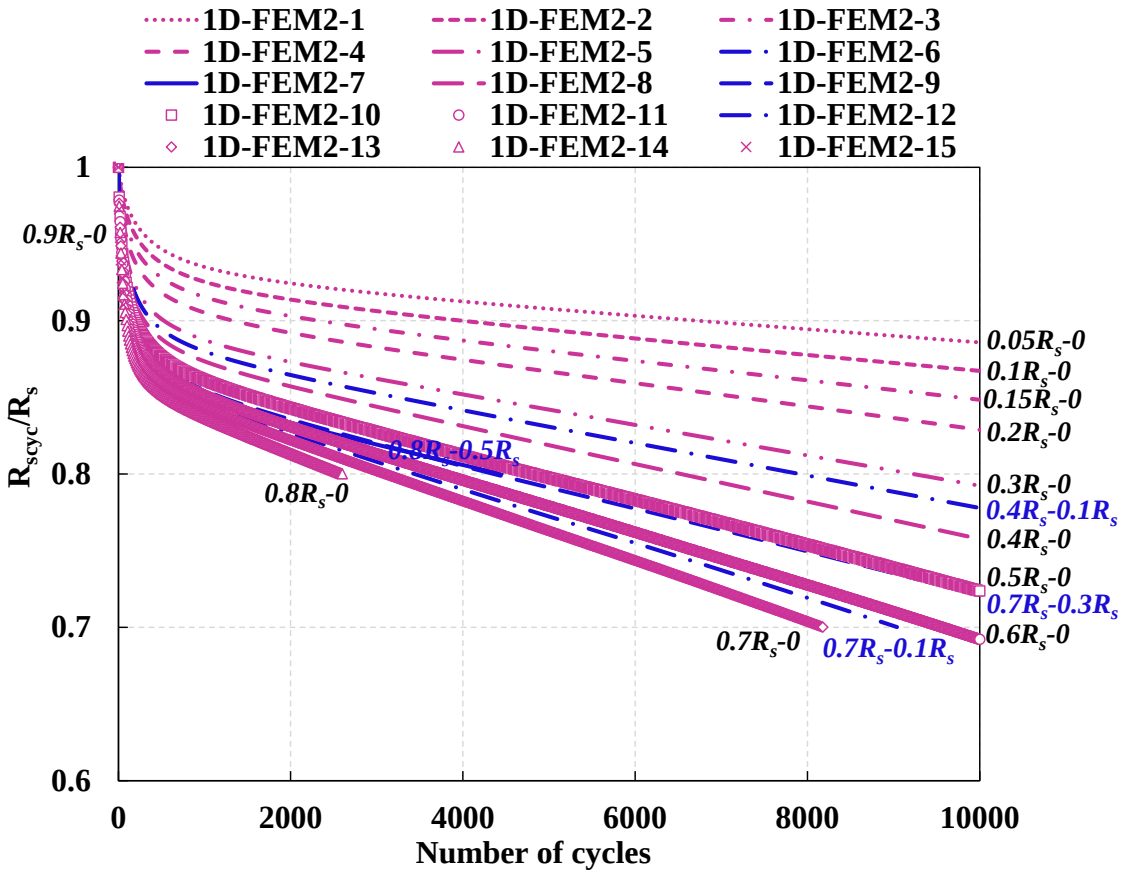


*Figure 5.9 : Evolution of pile resistance to tension in function of cycles number for all cyclic sequences*

### *5.4.2.3 Evolution of normal stress*

In this part, we will study the evolution of normal stress along the pile depth for different sequences presenting different behaviours of the interface. In the previous sections, we noticed three different aspects of the pile response. The first one is limited by the maximum loading of

$0.3R_s$ where below this value no evolution of accumulated displacement is noticed (1D-FEM2-1, 1D-FEM2-2, 1D-FEM2-3 and 1D-FEM2-4). From this value of $Q_{max}$ and above, displacements at pile head start to accumulate even though the rate of accumulation is relatively low and does not lead to conventional cyclic rupture (for example 1D-FEM2-9, 1D-FEM2-10 and 1D-FEM2-11). However, cyclic degradation may lead to lack of equilibrium of the pile and therefore to cyclic rupture (1D-FEM2-7, 1D-FEM2-12, 1D-FEM2-14 and 1D-FEM2-15). In order to assess more deeply the evolution of normal stress, results of sequences 1D-FEM2-2, 1D-FEM2-9 and 1D-FEM2-7 are considered herein.

Figures 5.10a, 5.10b and 5.10c illustrate the evolution of normal stress, $\sigma_n$, at the pile-soil interface for sequences 1D-FEM2-2, 1D-FEM2-9 and 1D-FEM2-7. Each figure includes three curves presenting the evolution of ratio $\sigma_n/\sigma_{n1}$, where $\sigma_{n1}$ is the initial normal stress, in function of cycles number. These three curves correspond to three different levels of pile depth, i.e. upper, middle and lower elements of the pile.

For the sequence 1D-FEM2-2, figure 5.10a shows that the upper element of the pile (at pile head) is subjected to a moderate degradation of normal stress reaching approximately 47% of its initial value after 10000 cycles, while other elements are subjected to a slight decreasing in normal stress despite the large number of imposed cycles.

Considering the sequence 1D-FEM2-9, degradations undergo by the three elements are higher than those seen for sequence 1D-FEM2-2 for the same number of cycles, 10000 cycles. The upper element presents an extensive degradation where the final corresponding normal stress represents approximately 18% of its initial value $\sigma_{n1}$. For middle and lower elements, normal stress degradation is moderate comparing to upper element where the final values of normal stress are approximately equivalent to 67% and 84% of the initial value respectively.

Sequence 1D-FEM2-7 presented in figure 5.10c shows an extensive degradation of normal stress. Degradation is stopped after 4450 cycles where cyclic rupture due to lack of equilibrium is occurred. The maximum applied loading $Q_{max}$ is relatively high in this sequence ($0.8R_s$).

It should be noted that as maximum loading $Q_{max}$ increases the plasticity propagates along the pile depth until approximately all the pile elements reach the yield criterion where rupture occurred. Thus, for high levels of $Q_{max}$, the parameters that manage the evolution of normal displacement ($\eta_{max}$ and $\Delta\tau$) in function of cycles number ($u_n = f(N)$) and therefore the evolution of normal stress, stabilise and remain equal for the same pile element that has reached plasticity. Consequently, considering a pile element that has already reached yield criterion the corresponding ratio of normal stress degradation $\sigma_n/\sigma_{n1}$ is approximately the same for higher

levels of maximum loading. This may explain the vicinity between results of sequence 1D-FEM2-9 and results of sequence 1D-FEM2-7. Rupture due to lack of equilibrium occurred for sequence 1D-FEM2-7 provokes the difference between the two sequences.

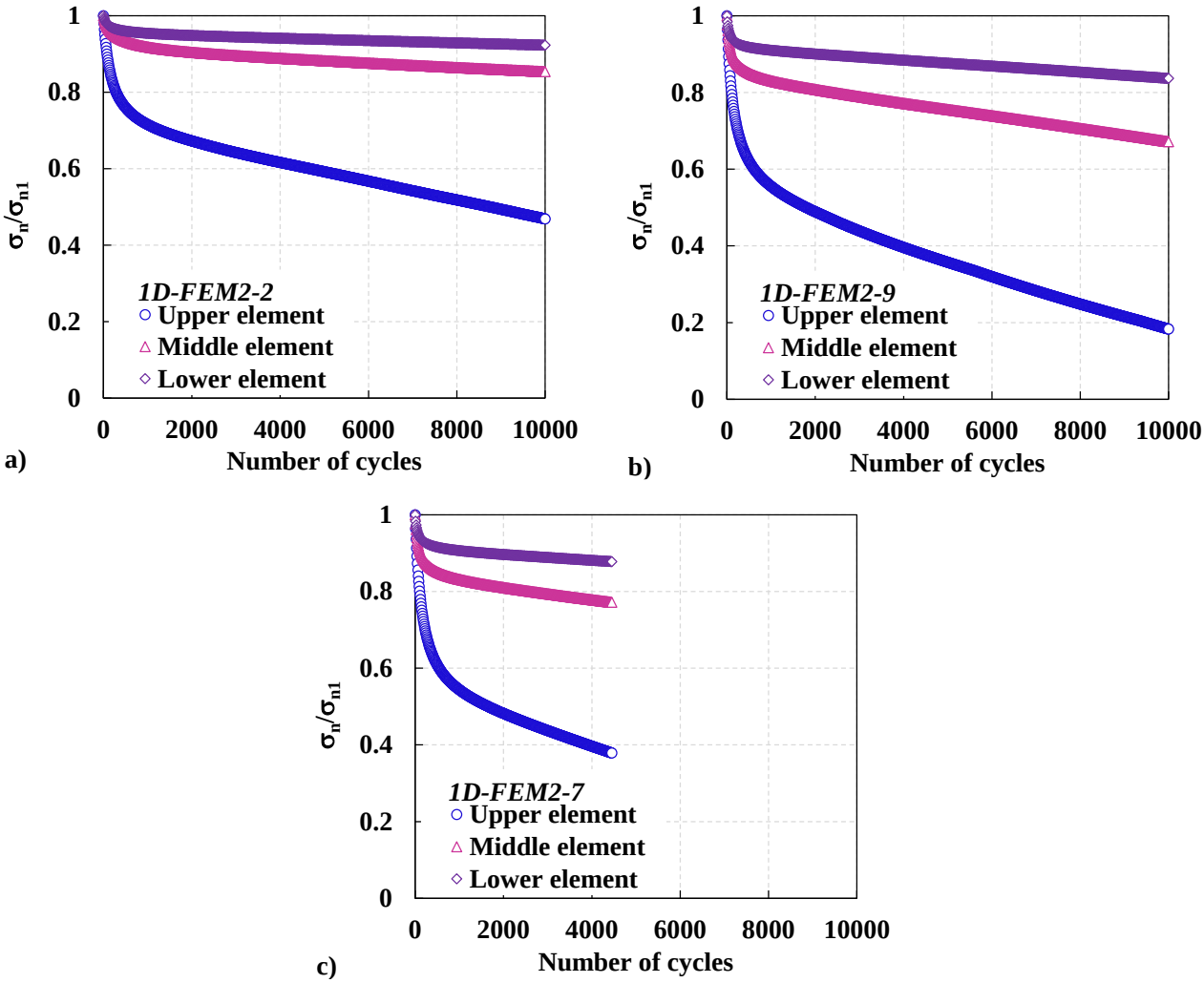


*Figure 5.10 : Evolution of normal stress at soil-pile interface in function of cycles number for: a) sequence 1D-FEM2-2, b) sequence 1D-FEM2-9 and c) sequence 1D-FEM2-7*

The degradation in normal stress directly influences the evolution of the limit shaft friction throughout the pile. The following section will hold a better visualisation of the evolution of the limit shaft friction as a function of the number of cycles with the developed skipped cycles method.

### *5.4.2.4 Evolution of shear stress*

Figure 5.11 illustrates the stress paths developed in the case of cyclic sequence 1D-FEM2-2 for different depths of the pile. The three stress paths presented in figure 5.11 move towards left generating a contracting behaviour of the interface. It can be noticed that only the normal stress

decreases during cycles for different pile elements while the shear stress remains the same. The low value of applied maximum loading $Q_{max}$ (10% $R_s$) does not generate plasticity in the pile elements even in the upper element. In addition to that, degradation of normal stresses along the pile shaft is relatively low and does not lead to reaching the yield criterion. It can be seen that the upper element is on the edge of reaching plasticity while for middle and lower elements stress paths are far from yield criterion.

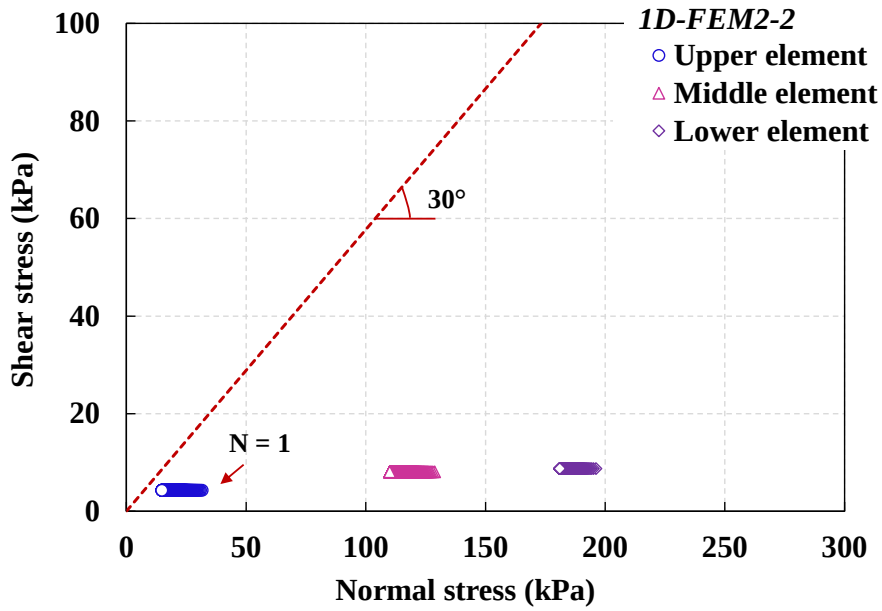


*Figure 5.11 : Stress paths for upper, middle and lower elements of the pile for cyclic sequence 1D-FEM2-2*

Figure 5.12a illustrates the evolution of degradation factor of the limit shaft friction, $D_\tau$, in function of pile depth and number of cycles for sequence 1D-FEM2-2. The degradation factor is determined according to equation 5.10. In this equation $q_{sj}$ refers to the limit shaft friction after each j packet of $N_{sc}$ skipped cycles, and $q_{s1}$ is the initial limit shaft friction. $q_{sj}$ is directly related to the normal stress and can be determined according to equation 5.11.

$$D_\tau = 1 - \frac{q_{sj}}{q_{s1}} \tag{5.10}$$

$$q_{sj} = \sigma_{nj} * \tan\varphi \tag{5.11}$$

Indeed, as the normal stress decreases, the post cyclic tension resistance of the pile decreases. Figure 5.12a shows that while the pile depth increases the degradation factor decreases. Thus, elements at the pile head undergo a more pronounced degradation of the limit shaft friction of

the interface than elements near to pile base. The evolution of this degradation factor during cycles is considered low.

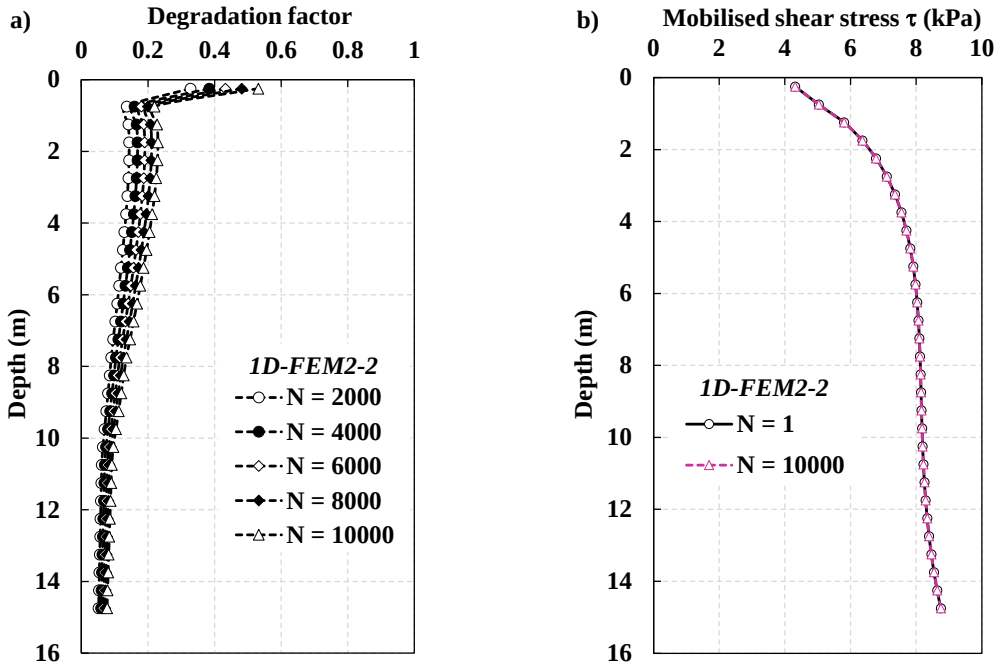


*Figure 5.12 : Sequence 1D-FEM2-2: a) evolution of degradation factor of the limit shaft friction in function of cycles number along the pile depth, b) profile of mobilised shear stress along the pile depth for first and final cycles*

Figure 5.12b presents the profile of mobilised shear stress τ along the pile depth during first and last cycles (N = 10000). These results confirm observations made in figure 5.11. Generally, sequence 1D-FEM2-2 with low maximum loading $Q_{max}$ does not affect the mobilisation of shear stress along the pile. The mobilised shear stress is always in elastic regime.

Considering the cyclic sequence 1D-FEM2-9, figure 5.13 illustrates the stress paths of three pile elements during this sequence. The pile behaviour encountered within this sequence is different from the one observed for sequence 1D-FEM2-2. The difference encountered in this case is that the applied maximum loading induces plasticity in some pile elements after the first cycle. Once plasticity is activated, the mobilised shear stress of pile elements that reached the yield criterion begins to degrade during cycles. In addition, the most severely degraded element is located at the head of the pile. This proves that the rupture propagates from the top to the bottom of the pile. Hence, in order to maintain the equilibrium in the pile, pile elements that did not reach plasticity witness an increasing in the mobilised shear stress.

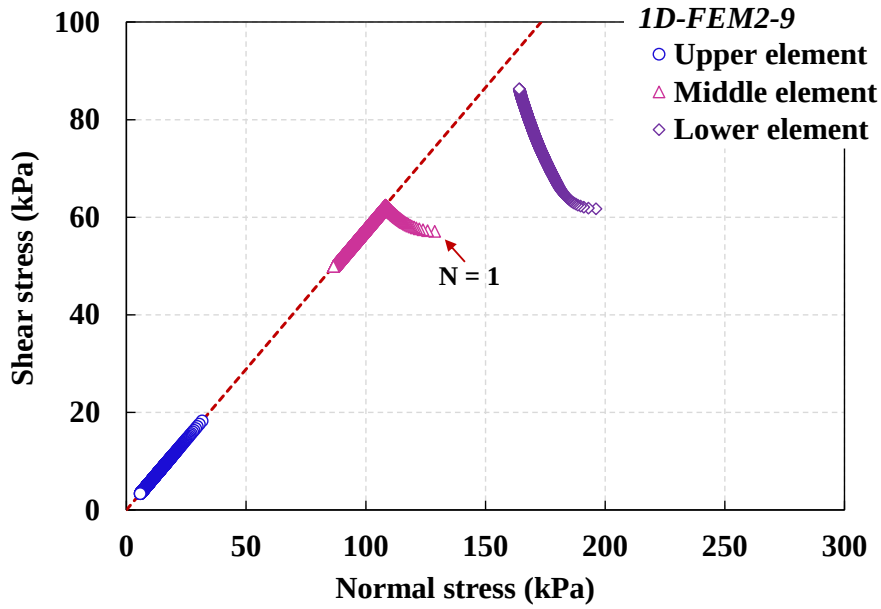


*Figure 5.13 : Stress paths for upper, middle and lower elements of the pile for cyclic sequence 1D-FEM2-9*

Figure 5.14a shows the evolution of the degradation factor of the limit shaft friction $D_\tau$ in function of pile depth and number of cycles for sequence 1D-FEM2-9. Like the sequence 1D-FEM2-2, it is clear that the degradation of the limit shaft friction decreases with depth, and it is greater at the top elements compared to the elements below. Compared to results of sequence 1D-FEM2-2, the higher value of $Q_{max}$ applied during sequence 1D-FEM2-9 imposes higher degradation of limit shaft friction and therefore higher values of $D_\tau$.

Figure 5.14b illustrates the profile of mobilised shear stress along the pile depth during the first and the final cycle of sequence 1D-FEM2-9. For this case, it is obvious that the two profiles are different. For pile elements located at pile depths less than 8 m, the yield criterion is reached due to the application of $Q_{max}$ and the degradation of normal stresses. Hence, the mobilised shear stress $\tau$ of these elements decreases during cyclic loading. In order to support the maximum applied load, pile elements located below 8m depth where the yield criterion is not reached develop an increasing behaviour of mobilised shear stress.

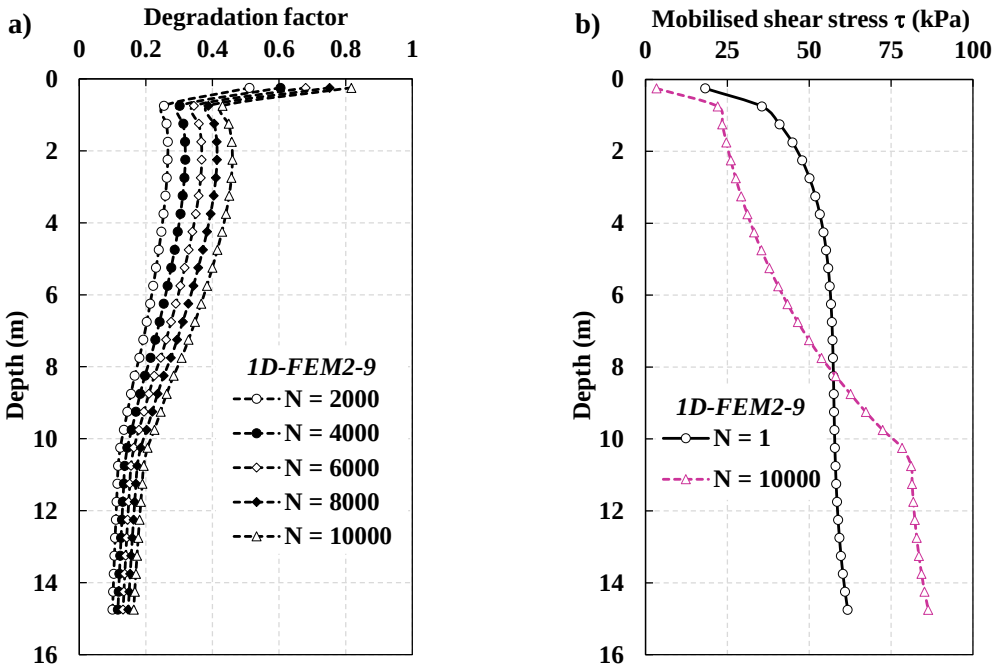


*Figure 5.14 : Sequence 1D-FEM2-9: a) evolution of degradation factor of the limit shaft friction in function of cycles number along the pile depth, b) profile of mobilised shear stress along the pile depth for first and final cycles*

Considering cyclic sequence 1D-FEM2-7, figure 5.15 illustrates the stress paths of three pile elements during this sequence. The behaviour of the pile encountered during this cyclic sequence is similar to that observed during sequence 1D-FEM2-9. The difference lies in the rupture occurred after 4450 cycles. As can be seen in figure 5.15, after a small number of cycles (40 cycles) the mobilised shear stress at the middle element begin to decrease due to the normal stress degradation and the reaching of yield criterion. After 4450 cycles, the stress path at the lower pile element reaches plasticity and therefore it will witness degradation and the pile capacity will be less than the maximum applied load. Hence calculation stops and rupture due to lack of equilibrium is encountered.

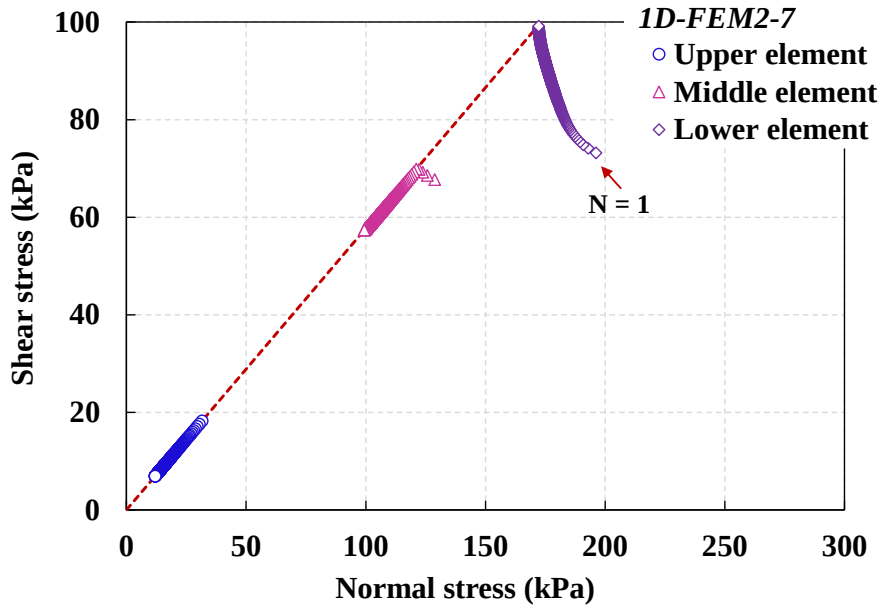


*Figure 5.15 : Stress paths for upper, middle and lower elements of the pile for cyclic sequence 1D-FEM2-7*

The evolution of the limit shaft friction degradation factor for the sequence 1D-FEM2-7 is presented in figure 5.16a. The profile of $D_\tau$ is approximately decreasing with depth and is similar to that of sequence 1D-FEM2-9. However, it has a lower degradation of the limit shaft friction for all the interface layers because the number of cycles before failure is lower than 10000 cycles (4450 cycles).

Profiles of mobilised shear stress at first and last cycles for sequence 1D-FEM2-7 are shown in figure 5.16b. For pile elements located between 1m and 6m depth, the profile of mobilised shear stress after the first cycle of sequence 1D-FEM2-7 is different from the one observed for sequence 1D-FEM2-9. The reason is that the first cycle enhances plasticity in these elements during sequence 1D-FEM2-7 with higher maximum loading $Q_{max}$ while during sequence 1D-FEM2-9 with lower $Q_{max}$ plasticity is not yielded. For pile elements above 1m, plasticity is reached during both sequences after the first cycle. Considering pile elements below 6m, the evolution of normal and shear stresses during the two sequences does not induce plasticity after the first cycle. After 4450 cycles and on the edge of rupture, profile of mobilised shear stress during sequence 1D-FEM2-7 is similar to that of sequence 1D-FEM2-9 after 10000 cycles. However, plasticity is more propagated during the former sequence reaching a depth higher than 8m.

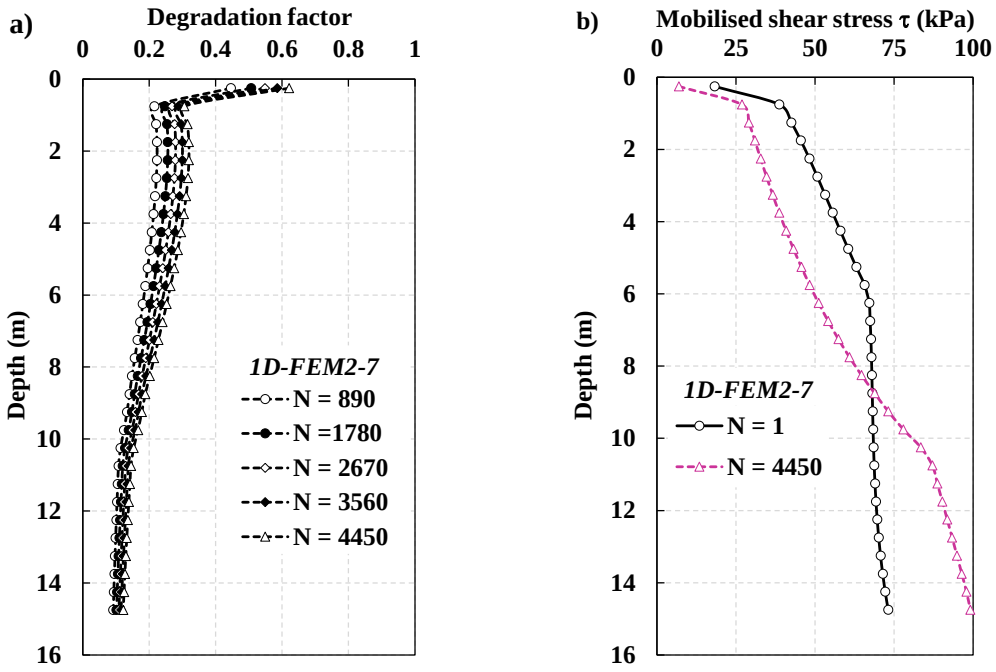


*Figure 5.16 : Sequence 1D-FEM2-7: a) evolution of degradation factor of the limit shaft friction in function of cycles number along the pile depth, b) profile of mobilised shear stress along the pile depth for first and final cycles*

### *5.4.2.5 Stability diagram*

One-way tension cyclic sequences presented in table 5.2 allowed to establish the stability diagram shown in figure 5.17. Each point on the figure is placed according to the corresponding values of mean cyclic loading $Q_{mean}$, and cyclic amplitude $Q_{cyc}$. When cyclic rupture due to lack of equilibrium is occurred, the corresponding number of cycles is marked on the figure. For all cyclic sequences, no rupture is occurred because the pile displacement exceeds the criterion of $D_p/10$.

This diagram is an application of the 1D-FEM model combined with the proposed constitutive law, and it can be practically used by engineers when designing piles. Thus, engineers having this calculation tool or prototype to build this type of diagram, will be able to evaluate for a given type of pile and soil, the behaviour of the pile under several load combinations considering one-way and two-way loadings.

Indeed, the use of this diagram allows the engineers to know the ranges of cyclic amplitude and mean loading that the pile can support. These diagrams also allow to predict more or less the number of cycles that can be supported by the pile before reaching the rupture.

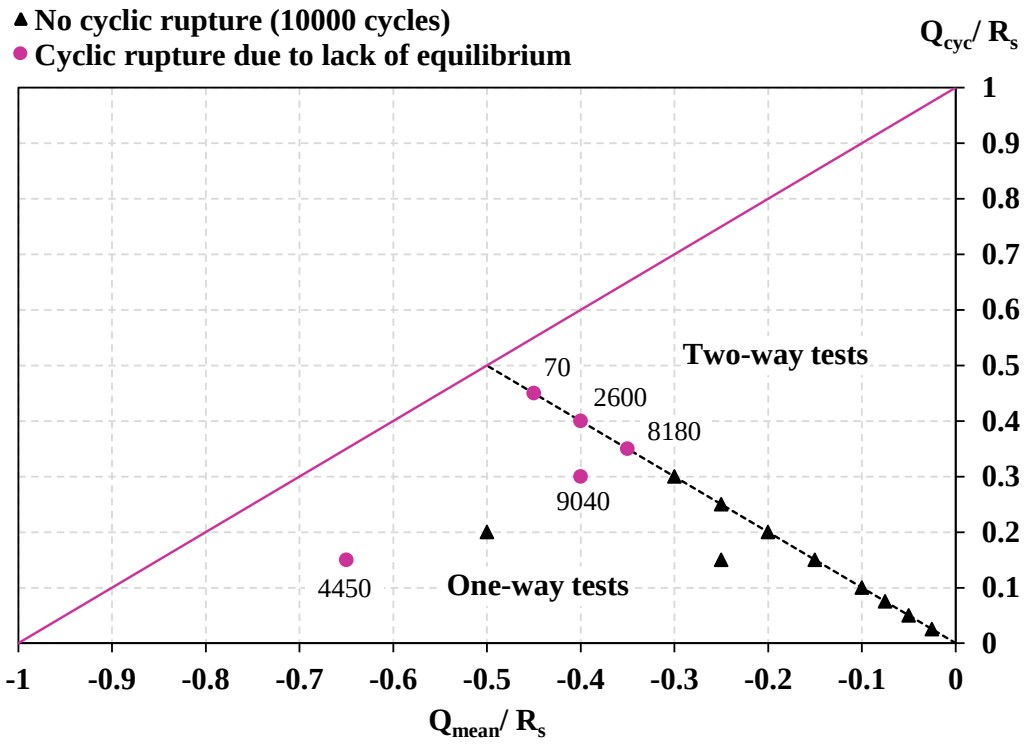


*Figure 5.17 : Cyclic diagram obtained from one-way tension cyclic sequences*

## 5.5 Conclusion

In the aim of providing an engineering tool for practical use, this chapter presents the development of a 1D approach for the analysis of an axially loaded pile. Based on the finite element method, this approach intends to discretise the pile into *n* finite elements, and the problem is treated following principles of elastoplasticity according to a non-linear iterative procedure. The proposed interface constitutive law combined with experimental expressions accounting for the variation of the interface normal stress during shear loading is implemented in this tool. Programmed in Fortran language, this practical engineering prototype permits to have a simplified and practical calculation with high time efficiency. Thus, it presents an arrangement between the conventional t-z method, which does not take into consideration the variation of normal stress along the pile shaft, and the complex 3D analysis, which needs a great numerical time consumption.

The 1D-FEM approach is employed at first to compare its predictions to those resulting from preceding 1D-FDM analysis (t-z method) and 3D-FDM analysis (FLAC3D) considering tension monotonic loading. Then, predictions of 1D-FEM approach considering tension cyclic loading are compared to predictions of 3D-FDM analysis considering the developed skipped cycles method. The global response of the axially loaded pile in different models performs a good concordance. In comparison to 1D-FEM model, the presence of the elastic soil

surrounding the pile in 3D-FDM analysis causes a slightly different local response at the soil-pile interface.

Afterwards, profiting from the great economy in computation time resulting from using the developed tool, additional tension cyclic simulations are performed in order to assess the pile cyclic response considering a large variety of cyclic characteristics and a high number of cycles. Results of such predictions in terms of accumulated displacements at pile head and pile capacity degradation are presented. It can be noted that the proposed constitutive law combined with experimental data from shear tests is capable of rendering the pile capacity degradation induced by the degradation of normal stress along the pile shaft during cycles. Indeed, the degree of degradation depends on cyclic characteristics, the more the pile is loaded the more its capacity decreases which may provoke a cyclic rupture due to lack of equilibrium. However, results of simulations in terms of accumulated displacements at the pile head point out the inability of the proposed constitutive law to accumulate high values of displacement that may cause conventional cyclic rupture. The rate of displacement accumulation remains low even with high maximum applied loading and high number of cycles reaching 10000 cycles. Despite that, the constitutive law is capable to capture qualitatively the evolutive aspect of accumulated displacement depending on cyclic characteristics.

Using results of the performed cyclic sequences, the developed 1D-FEM prototype combined with the proposed constitutive law contributes to the construction of stability diagram of the pile, which can be considered very useful for engineering practice while designing piles under cyclic axial loading.

# General Conclusion and Perspectives

This research work focused on studying the behaviour of piles under axial loading for Offshore wind turbine projects in chalk. Two objectives were conducted: an assessment of the reliability of the existing approaches of the estimation of pile capacity in chalk, and a contribution to the numerical modelling of piles under axial loading considering the evolution of the soil-pile interface normal stress.

The first part of this work presented **a comparison of different methods** adopted in France and the UK for pile design in chalk. The shaft and base resistances calculated according to different methods were compared with measured resistances of seven piles tested at four sites in the Paris Basin and recorded in the LCPC database. Ratios of shaft and base calculated resistances to the measured resistances were statistically analysed. Significant discrepancies were noticed for both shaft resistance and base resistance. It worth noting that it is difficult to give a general conclusion about the consistency of the different calculation methods due to the limitations of the number of piles in the database as well as the variability in the quality of the in-situ data. This comparison showed that the design of piles in chalk should be considered prudently. A sufficient level of reliability may be achieved by considering an increase in the partial factors for piles in chalk when it is compatible with design situations.

A further concern was addressed to the case of driven piles in chalk. Due to ageing effect, the evolution of resistance of driven piles, listed in the LCPC database, presents a hyperbolic increasing trend with time that is similar to the hyperbolic relationship suggested in the literature for driven piles.

As a consequence of this preliminary study which shows the dispersion of the current practical methods, a fundamental work needs to be done in order to take into account the real rheological behaviour at the soil pile interface, which is the goal of the second objective.

Hence, the second objective of this work focused on **the numerical modelling** of the soil-pile interface subjected to axial loading. An elastoplastic constitutive law with a single yield mechanism was proposed. It consists of a linear and isotropic elastic part. The plasticity criterion is expressed in terms of normal and shear stresses and follows the Mohr-Coulomb criterion. The principal aspect of the proposed model is related to the determination of the flow rule. The formulation of the flow rule allows to directly consider the volumetric behaviour of the interface. It is modified based on experimental data from direct shear tests. Consequently, the constitutive law was rewritten according to the new flow rule.

Regarding **monotonic shear loading**, the considered experimental results describe the variation of normal stress in function of shear displacement, which may present either a contractant or a dilatant behaviour. The numerical expression of the hyperbolic secant equation was then

selected. This expression includes essentially four parameters to be calibrated. A parametric study presenting the effect of each parameter on the evolution of normal displacement was presented. The determination of these parameters, based on direct shear tests under CNL and CNS conditions, requires a sufficient database of experimental results covering a wide range of normal stiffness values and initial normal stress values. Using the MATLAB application "curve fitting", a calibration on a set of laboratory direct shear tests, carried out in the frame of SOLCYP project considering sand samples, was firstly presented. The parameters were also calibrated based on direct shear test results considering chalk samples, recently carried out in the frame of SOLCYP+ project.

The constitutive law combined with the experimental flow rule was firstly implemented in EXCEL using the VBA language in order to imitate the results of direct shear tests. Compared to experimental results, predictions of the developed constitutive law, for both soil types, succeeded to simulate the interface response especially at high tangential displacement where the plasticity dominates. However, it was clear that the peak of shear stress was not well reproduced. This observation is probably related to the perfect plasticity considered in our model.

Compared to the classical Mohr-Coulomb criterion, with different values of dilatancy, the proposed model with modified flow rule can capture the variation of the interface normal stress encountered in direct shear tests where final phase of stabilisation is noticed.

Regarding **cyclic shear loading**, variation of normal displacement in function of cycles number is considered. The expression of rational equation was then adopted in order to illustrate the possible degradation in normal stress during cycles. This expression includes three parameters to be calibrated. A parametric study presenting the effect of each parameter on the evolution of normal displacement during cycles was done. Using the SOLCYP approach, developed in the National SOLCYP project to describe the actual evolution of normal stress for sand samples, the parameters of our cyclic numerical expression were calibrated. They were then determined, in function of normal stiffness, initial normal stress and cyclic characteristics, based on simulations done according to this approach using the MATLAB application. Comparisons with simulation results showed the ability of the proposed cyclic expression to accurately imitate the variation of normal stress in function of cycles number.

The developed interface constitutive law combined with the aforementioned numerical expressions, calibrated on results of direct shear tests of sand samples, was used and implemented first in a commercial code, FLAC3D, and second in an original 1D approach with a specific engineering tool, based on finite element analysis, in order to assess the response of

**a theoretical pile** under monotonic and cyclic loadings. More precisely, the two fundamental developments, either in 1D or 3D, are focused on takin into account the contractancy/dilatancy in a quite original way with the modification of the flow rule.

In the case of **tension monotonic loading**, predictions of FLAC3D, defined in the manuscript as **3D-FDM**, were compared with predictions of conventional load-transfer method (**1D-FDM**), combined with linear elastic perfectly plastic t-z curves. This comparison allowed to conclude that due to the dilatant behaviour of the interface induced by the developed model, the tension capacity of the pile increases. This gain of capacity is strongly dependent on the initial values of normal stress along the pile shaft.

In the case of **tension cyclic loading**, a skipped cycles method was presented. Combined with the developed constitutive law, this method succeeded in reproducing the cyclic degradation of soil resistance and therefore of the pile capacity. Considering the variation of normal stress, it was managed by an updating process during loading. It imposed the application of a step-by-step cycle after each packet of skipped cycles. Thus, even if the skipped cycles method reduces the computation time, the need to perform a certain number of, step-by-step, cycles still require large calculation time. In total 1000 cycles were carried out in this study.

The last aspect of the work, which is considered the major contribution of this thesis, concerned about the development of a **1D numerical prototype** in order to conduct a simplified and practical analysis for the design of piles under cyclic loading. This prototype is based on the finite element method, and it was designated by **1D-FEM**. Compared to previous calculations done in FLAC3D, the 1D-FEM method presented a relevant accuracy with notable decreasing in calculation time.

Additional tension cyclic calculations carried out using the developed prototype, considering a large variety of cyclic characteristics and a high number of cycles, showed that the behaviour model was able to illustrate the degradation in pile tension capacity. The magnitude of this latter is dependent on cyclic characteristics especially maximum applied load and cyclic amplitude. It should be noted that the cyclic rupture occurred was only due to lack of equilibrium. Displacements were slowly accumulated and the final value of displacement at the pile head did not exceed the conventional value of $D_p/10$ for all cyclic sequences, even for high number of cycles. However, the effect of cyclic characteristics on the evolution of pile displacement was qualitatively demonstrated.

The first direction in which it is natural to seek to extend this work is to intensely compare both approaches for pile design in chalk, based on results from new pile load tests including different types of piles and considering different categories of chalk. Consequently, combining different

techniques, when it is available for ground investigation, may be the most relevant way especially for particular geomaterial like chalk.

Another extension of this thesis work concerns the numerical modelling of the soil-pile interface. Indeed, the developed interface constitutive law has shown its limitations especially regarding the rate of displacement accumulation of the pile under axial cyclic loadings. The choice of a perfect plasticity is the reason behind these limitations. A kinematic hardening rule combined with the modified flow rule presented in this thesis would be able to overcome these shortcomings.

The numerical expression proposed to account for the degradation of normal stress during cycles, remains to be calibrated on the results of ongoing cyclic direct shear tests, provided from the “SOLCYP+” project in which this PhD research takes part.

Further cyclic sequences considering two-way cyclic loadings should be conducted in order to complete the cyclic stability diagram of the theoretical pile. This diagram is considered an application of the developed 1D prototype combined with the developed constitutive law and it can be useful for the engineer during pile design.

The developed constitutive law still requires validation by data from in-situ loading tests of full-scale piles.

The developed 1D numerical tool can be extended in the framework of the transversal cyclic loading by adjusting the elemental matrices and vectors.

# References


Abchir, Z. 2016. Contribution à l'étude du comportement des pieux isolés soumis à des sollicitations axiales monotones et cycliques dans le sable. Thèse de doctorat, Université Paris-Est, Paris.

Abchir, Z., Burlon, S., Frank, R., Habert, J., and Legrand, S. 2016. t–z curves for piles from pressuremeter test results. Géotechnique, 66(2): 137–148. doi:10.1680/jgeot.15.P.097.

AFNOR. 2012. Justification des ouvrages géotechniques-Normes d'application nationale de l'Eurocode 7-Fondations profondes, NF P94-282, Norme française. AFNOR Groupe, Saint-denis, France.

Airey, D., Al-Douri, R., and Poulos, H. 1992. Estimation of Pile Friction Degradation from Shearbox Tests. 15(4): 388–392.

Al-Douri, R.H., and Poulos, H.G. 1992. Static and Cyclic Direct Shear Tests on Carbonate Sands. Geotechnical Testing Journal, 15(2): 138–157. doi:10.1520/GTJ10236J.

Andersen, M.A. 1995. Petroleum research in North Sea chalk. Joint chalk research, phase IV, Stavanger, Norway.

Baldi, G., Bellotini, R., Ghionna, V.N., Jamiolkowsk, N.I., and Lo Presti, D.L.F. 1989. Modulus of sands from CPTs and DMTs. In Proc.12th ICSMFE. Rio de Janeiro. pp. 165–170.

Bell, F.G., Culshaw, M.G., and Cripps, J.C. 1999. A review of selected engineering geological characteristics of English Chalk. Engineering Geology, 54(3–4): 237–269. doi:10.1016/S0013-7952(99)00043-5.

Bialowas, G.A., Diambra, A., and Nash, D.F.T. 2018. Stress and time-dependent properties of crushed chalk. Proceedings of the Institution of Civil Engineers - Geotechnical Engineering, 171(6): 530–544. doi:10.1680/jgeen.17.00168.

Bogard, J.D., and Matlock, H. 1990. Application of Model Pile Tests to Axial Pile Design. In Offshore Technology Conference. Offshore Technology Conference, Houston, Texas.

Boulon, M. 1988. Contribution à la mécanique des interfaces sol-structures. Application au frottement latéral des pieux. Mémoire pour l'habilitation à diriger les recherches, Université Joseph Fourier-Grenoble I, Grenoble, France.

Boulon, M. 1989. Basic Features of of Soil-Structure Interface Behavior. Computers and Geotechnics, 7: 115–131.

Boulon, M. 1991. Le comportement d'interface sol-structure: aspects expérimentaux et numériques. REVUE FRANÇAISE DE GÉOTECHNIQUE, 54: 27–37.

Boulon, M., and Foray, P. 1986. Physical and numerical simulations of lateral shaft friction along offshore piles in sand. In The 3rd international conference on numerical methods in offshore piling. Nantes. pp. 127–147.

BSI. 2015. Code of practice for foundations, BS 8004:2015. The British Standards Institution.

Buckley, R.M., Jardine, R.J., Kontoe, S., Barbosa, P., and Schroeder, F.C. 2020. Full-scale observations of dynamic and static axial responses of offshore piles driven in chalk and tills. Géotechnique, 70(8): 657–681. doi:10.1680/jgeot.19.TI.001.

Buckley, R.M., Jardine, R.J., Kontoe, S., and Lehane, B.M. 2018a. Effective stress regime around a jacked steel pile during installation ageing and load testing in chalk. Canadian Geotechnical Journal, 55(11): 1577–1591. doi:10.1139/cgj-2017-0145.

Buckley, R.M., Jardine, R.J., Kontoe, S., Parker, D., and Schroeder, F.C. 2018b. Ageing and cyclic behaviour of axially loaded piles driven in chalk. Géotechnique, 68(2): 146–161. doi:10.1680/jgeot.17.P.012.

Burlon, S., Frank, R., Baguelin, F., Habert, J., and Legrand, S. 2014a. Model factor for the bearing capacity of piles from pressuremeter test results – Eurocode 7 approach. Géotechnique, 64(7): 513–525. doi:10.1680/geot.13.P.061.

Burlon, S., Mroueh, H., and Cao, J.P. 2014b. 'Skipped cycles' method for studying cyclic loading and soil–structure interface. Computers and Geotechnics, 61: 209–220.

Burlon, S., Thorel, L., and Mroueh, H. 2013. Proposition d'une loi t-z cyclqiue au moyen d'expérimentations en centrifugeuse. In Proceedings of the 18th International Conference on Soil Mechanics and Geotechnical Engineering. Paris.

Bustamante, M., Combarieu, O., and Gianeselli, L. 1980. Portance des pieux dans la craie altérée. Annales de L'institut technique du Batiment et des Travaux Publics, 388(SOL FOND 174): 26–56.

Bustamante, M., Gambin, M. (Mike), and Gianeselli, L. 2009. Pile Design at Failure Using the Ménard Pressuremeter: An Update. In Contemporary Topics in In Situ Testing, Analysis, and Reliability of Foundations. American Society of Civil Engineers, Orlando, Florida, United States. pp. 127–134.

Bustamante, M., and Gianeselli, L. 1981. Prévision de la capacité portante des pieux isolés sous charge verticale – Règles pressiométriques et pénétrométriques. Bulletin des Laboratoires des Ponts et Chaussées.

Bustamante, M., and Gianeselli, L. 1982. Pile bearing capacity prediction by means of static penetrometer CPT. Balkema, Rotterdam. pp. 493–500.

Bustamante, M., and Gianeselli, L. 1995. Etude expérimentale de la portance de pieux battus dans la craie altérée, Viaduc du Scardon. Internal LCPC report : unpublished, Laboratoire Centrale des Ponts et Chaussées, LCPC, France.

Bustamante, M., and Gianeselli, L. 2006. Règles de calcul de la portance des pieux aux ELU – Méthode pressiométrique. LCPC, Laboratoire central des ponts et chaussées, Paris, France.

Bustamante, M., Gianeselli, L., and Weber, L. 1998. The bearing capacity of driven steel piles in weathered chalks. In Proceedings of the Seventh International Conference and Exhibition on Piling and deep Foundations. Vienna, Austria: DFI.

Cao, J. 2010. Modélisation numérique des problèmes d'interfaces sable-pieu pour les très grands nombres de cycles: Développement d'une méthode de sauts de cycles. University of Lille, Villeneuve d'Ascq.

Caquot, A., and Kerisel, J. 1966. Traité de mécanique des sols. In Gauthier-Villars. Paris.

Carrington, T.M., Li, G., and Rattley, M.J. 2011. A new assessment of ultimate unt friction for driven piles in low to medium density chalk. In Proceedings of the 15th European Conference on Soil Mechanics and Geotechnical Engineering. Amsterdam.

Chan, D.L.H., Buckley, R.M., Liu, T., and Jardine, R.J. 2019. Laboratory investigation of interface shearing in chalk. E3S Web of Conferences, 92: 13009. doi:10.1051/e3sconf/20199213009.

Chin, J.T., and Poulos, H.G. 1992. Cyclic axial pile loading analyses: a comparative study. Computers and Geotechnics, 13: 137–158.

Ciavaglia, F., Carey, J., and Diambra, A. 2017. Time-dependent uplift capacity of driven piles in low to medium density chalk. Géotechnique Letters, 7(1): 90–96. doi:10.1680/jgele.16.00162.

Clayton, C.R.I. 1983. The influence of diagenesis on some index properties of chalk in England. Géotechnique, 33(3): 225–241. doi:10.1680/geot.1983.33.3.225.

Coyle, H.M., and Reese, L.C. 1966. Load transfer for axially loaded piles in clays. Journal of soils Mechanics and Foundations Division, 92(SM2): 1–26.

Coyle, H.M., and Sulaiman, I.H. 1967. Skin Friction for Steel Piles in Sand. Journal of the Soil Mechanics and Foundations Division, ASCE, 93(6): 261–278.

Coyne, D., Rattley, M., Houlston, P., Alobaidi, I., Benson, A., and Russell, C. 2015. Cyclic laboratory testing of chalk to improve the reliability of piled foundation design. In Frontiers in Offshore Geotechnics III. Edited by V. Meyer. CRC Press. pp. 1185–1190.

D'Aguiar, S.C., Modaressi-Farahmand-Razavi, A., and Lopez-Caballero, F. 2011. Elastoplastic constitutive modelling of soil–structure interfaces under monotonic and cyclic loading. Computers and Geotechnics, 38: 430–447.

Dahou, A. 1995. Contribution à l'étude du comportement viscoelastoplastique d'une craie poreuse. Thèse de doctorat, Université des sciences et technologies de Lille, Lille, France.

Day, R.A., and Potts, D.M. 1994. Zero thickness interface elements - Numerical stability and application. International Journal for Numerical and Analytical Methods in Geomechanics, 18(10): 689–708. doi:10.1002/nag.1610181003.

De Gennaro, V., Delage, P., Priol, G., and Candel-Hernandis, J.V. 2003. Time-dependent behaviour of reservoir chalk: a multiphase approach. 43: 131–147.

De Gennaro, V., and Frank, R. 2005. Modélisation de l'interaction sol-pieu par la méthode des éléments finis. Bulletin des Laboratoires des Ponts et Chaussées, Paris.

Desai, C.S., Drumm, E.C., and Zaman, M.M. 1985. Cyclic Testing and Modeling of Interfaces. Journal of Geotechnical Engineering, 111(6): 793–815. doi:10.1061/(ASCE)0733-9410(1985)111:6(793).

Dessene. 1971. Etude rhéologique de la craie. Thèse Docteur Ingénieur, Université de Grenoble, Grenoble, France.

Doghman, M., Mroueh, H., and Burlon, S. 2020. A review of different pile design approaches in chalk used in France and the UK: case studies from French sites. European Journal of Environmental and Civil Engineering,: 1–25. doi:10.1080/19648189.2020.1854124.

Doremus, C. 1978. Les craies du nord de la France - Corrélations entre la lithostratigraphie, la microstructure et les propriétés mécaniques. Thèse de Doctorat, Université des Sciences et Techniques de Lille.

Doughty, L.J., Buckley, R.M., and Jardine, R.J. 2018. Investigating the effect of ageing on the behaviour of chalk putty. In Engineering in Chalk. ICE Publishing, Imperial College, London, UK. pp. 695–701.

Dührkop, J., Augustesen, A., and Barbosa, P. 2015. Cyclic pile load tests combined with laboratory results to design offshore wind turbine foundations in chalk. In Frontiers in Offshore Geotechnics III. Edited by V. Meyer. CRC Press. pp. 533–538.

Engstrom, F. 1992. Rock mechanical properties of Danish North Sea chalk. Deauville.

Fakharian, K., and Evgin, E. 1997. Cyclic Simple-Shear Behavior of Sand-Steel Interfaces under Constant Normal Stiffness Condition. Journal of Geotechnical and Geoenvironmental Engineering, 123(12): 1096–1105. doi:10.1061/(ASCE)1090-0241(1997)123:12(1096).

Florentin, J., L'Hériteau, G., Farhi, M., and Parez, L. 1961. Observations faites sur la craie comme couche de fondation. Paris, France.

FPS. 2013. The Design of Bored Piles in Chalk. Federation of Piling Specialists, London.

Frank, R. 2017. Some aspects of research and practice for pile design in France. Innovative Infrastructure Solutions, 2(1): 32. doi:10.1007/s41062-017-0085-4.

Frank, R., and Zhao, S.R. 1982. Estimation par les paramètres pressiométriques de l'enfoncement sous charge axiale de pieux forés dans les sols fins. Bulletin de Liaison du Laboratoire des Ponts et Chaussées.

Garnica-Anguas, P. 1993. Simulation numérique du frottement entre solides par équations intégrales aux frontières et modèle d'interface non linéaire. Thèse de Doctorat, Université Joseph Fourier-Grenoble I, Grenoble, France.

Gavin, K., Jardine, R., Karlsrud, K., and Lehane, B. 2015. The effects of pile ageing on the shaft capacity of offshore piles in sand. In Frontiers in Offshore Geotechnics III. Edited by V. Meyer. CRC Press. pp. 129–151.

Gourri, A. 1991. Contribution à l'étude de l'influence des conditions de drainage sur les propriétés poroélastiques des roches carbonatées. Thèse de doctorat, Université J. Fourier Grenoble.

Gutierrez, M., Oino, L.E., and Hoeg, K. 2000. The Effect of Fluid Content on the Mechanical Behaviour of Fractures in Chalk. 2(33): 93–117.

Hickman, R. 2004. Formulation and implementation of a constitutive model for soft rock. PhD thesis, Faculty of the Virginia Polytechnic Institute and State University.

Hobbs, N.B., and Atkinson, M.S. 1993. Compression and tension tests on an open-ended tube pile in chalk. 26(3): 31–34.

Homand, S., and Shao, J.F. 2000. Mechanical behaviour of a porous chalk and effect of saturating fluid. 5: 583–606.

Hoteit, N. 1990. Contribution à l'étude du comportement d'interface sable-inclusion et application au frottement apparent. Thèse de doctorat, Institut National Polytechnique de Grenoble, France.

IFSTTAR. 2015. ESSAIS DE CHARGEMENT SUR DES PIEUX REFSOL : COMPRESSION et TRACTION, Montereau-Fault-Yonne (77). Internal IFSTTAR report : unpublished, INSTITUT FRANÇAIS DES SCIENCES ET TECHNOLOGIES, DES TRANSPORTS, DE L'AMÉNAGEMENT ET DES RÉSEAUX, IFSTTAR.

Itasca. 2012. FLAC3D Version 5.0. Theory and Background. Itasca Consulting group, Inc., Minnesota, USA.

Jardine, R., Puech, A., and Andersen, k. H. 2012. Keynote Address: Cyclic Loading of Offshore Piles: Potential Effects And Practical Design. In Proceedings of the 7th International Conference: Offshore Site Investigation and Geotechnics. London, UK, Society for Underwater Technology. pp. 59–97.

Jardine, R.J., Buckley, R.M., Kontoe, S., Barbosa, P., and Schroeder, F.C. 2018. Behaviour of piles driven in chalk. In Engineering in Chalk. ICE Publishing, Imperial College, London, UK. pp. 33–51.

Jardine, R.J., Chow, F.C., Overy, R., and Standing, J.R. 2005. ICP design methods for driven piles in sands and clays. In Thomas Telford Ltd. London.

Jardine, R.J., Kontoe, S., Liu, T.F., Vinck, K., Byrne, B.W., McAdam, R.A., Schranz, F., Andolfsson, T., and Buckley, R.M. 2019. The ALPACA research project to improve design of piles driven in chalk. Proceedings of the XVII European Conference on Soil Mechanics and Geotechnical Engineering, (Geotechnical Engineering, foundation of the future): 326–333. doi:10.32075/17ECSMGE-2019-0071.

Jardine, R.J., and Standing, J.R. 2000. Pile Load Testing Performed for HSE Cyclic Loading Study at Dunkirk, France. In Offshore Technology Report OTO 2000 007. Health and Safety Executive, London.

Jardine, R.J., and Standing, J.R. 2012. Field axial cyclic loading experiments on piles driven in sand. Soils and Foundations, 52(4): 723–736. doi:10.1016/j.sandf.2012.07.012.

Jardine, R.J., Standing, J.R., and Chow, F.C. 2006. Some observations of the effects of time on the capacity of piles driven in sand. Géotechnique, 56(4): 227–244. doi:10.1680/geot.2006.56.4.227.

Jones, M.E., Bedford, J., and Clayton, C. 1984. On natural deformation mechanisms in the Chalk. 141: 9.

Karlsrud, K., Jensen, T.G., Lied, E.K.W., Nowacki, F., and Simonsen, A.S. 2014. Significant ageing effects for axially loaded piles in sand and clay verified by new field load tests. OTC, Houston, Texas. p. D041S045R001.

Kopf, T. 2019. Behavior of chalk – steel interfaces under constant normal stiffness shear conditions. Université Grenoble Alpes.

Kornes, R.I., Wersland, E., Austad, T., and Madlan, M.V. 2008. Anisotropy in chalk studied by rock sciences.: 28–35.

Kraft, L.M., Kagawa, T., and Ray, R.P. 1981. Theoretical t-z curves. Journal of Geotechnical Engineering, 107(GT11): 1543–1561.

Lafrance, N. 2016. Étude des effets de l'eau sur les phénomènes de rupture et de déformation affectant les carrières souterraines de craie. Thèse de doctorat, Université de Lorraine.

Lahrs, T., and Kallias, A. 2013. Probebelastungen von Stahlrohren in Kreide für den Offshore-Windpark Baltic 2. In Proceedings of the Pfahl symposium. Braunschweig, Germany. pp. 451–466.

Lake, L. 1975. Engineering Properties of Chalk with special Reference to Foundation Design and Performance. University of Surrey, Surrey, UK.

Lashkari, A., and Kadivar, M. 2016. A constitutive model for unsaturated soil-structure interfaces: A Constitutive Model for Unsaturated Soil-Structure Interfaces. International Journal for Numerical and Analytical Methods in Geomechanics, 40(2): 207–234. doi:10.1002/nag.2392.

LCPC. 1973. La craie. Bulletin des Laboratoires des Ponts et Chaussées.

LCPC. 2004. Essais de chargement de pieux refoulants OMEGA et ATLAS ancrés dans une craie altérée, Station d'épuration de Cambrai. Internal LCPC report : unpublished, Laboratoire Centrale des Ponts et Chaussées, LCPC, FRANCE.

Leddra, M.J., and Jones, M.E. 1989. Steady-state flow during undrained loading of chalk. In Proceeding of the International Chalk Symposium. Thomas Telford, London.

Lehane, B.M., Jardine, R.J., Bond, A.J., and Frank, R. 1993. Mechanisms of Shaft Friction in Sand from Instrumented Pile Tests. Journal of Geotechnical Engineering, 119(1): 17.

Lehane, B.M., and White, D.J. 2005. Lateral stress changes and shaft friction for model displacement piles in sand. Canadian Geotechnical Journal, 42(4): 1039–1052. doi:10.1139/t05-023.

Lord, J.A., Clayton, C.R.I., and Mortimore, R.N. 2002. Engineering in chalk. CIRIA, London.

Lord, J.A., Rheit, D., and Johlman, C.L. 1998. Is capillary suction a viable cohesive mechanism in chalk. In Proc. Eurock'98. Trondheim, Norvège. pp. 367–375.

Maleki, K. 1995. Contribution à l'étude du comportement des micropieux isolés et en groupe. Thèse de Doctorat, Ecole Nationale des Ponts et Chaussées, Paris, France.

Masson, V. 1973. Pétrophysique de la craie. LCPC.

Matthews, M.C., and Clayton, C.R.I. 1993. Influence of intact porosity on the engineering properties of a weak rock. In Geotechnical Engineering of Hard Soils - Soft Rocks. International Symposium, In, Anagnostopoulos, A., Schlosser, F., Kalteziotis, N. and Frank, R. NL. Balkema. pp. 693–702.

MELT. 1993. Fasicule 62 Titre V- Règles techniques de calcul et de conception des fondations des ouvrages de génie civil, CCTG, Texte officiel. Ministère de l'Equipement du Logement et des Transports.

Mesri, G., Feng, T.W., and Benak, J.M. 1990. Postdensification Penetration Resistance of Clean Sands. 116(7): 21.

Monjoie, A., and Schroeder, C. 1989. Caractéristiques mécaniques des craies du Crétacé Supérieur. France.

Monjoie, A., Schroeder, C., Prignon, P., Yernaux, C., da Silva, F., and Debande, G. 1990. Establishment of constitutive laws of chalkand long term tests. In Proceedings of the 3rd Sea Chalk Symposium. Copenhagen.

Mortara, G. 2001. An elastoplastic model for sand-structure interface behaviour under monotonic and cyclic loading. Ph.D. Thesis, Politecnico di Torino, Italy.

Mortara, G., Boulon, M., and Ghionna, V.N. 2002. A 2-D constitutive model for cyclic interface behaviour. International Journal for Numerical and Analytical Methods in Geomechanics, 26(11): 1071–1096. doi:10.1002/nag.236.

Mortara, G., Mangiola, A., and Ghionna, V.N. 2007. Cyclic shear stress degradation and post-cyclic behaviour from sand–steel interface direct shear tests. Canadian Geotechnical Journal, 44(7): 739–752. doi:10.1139/t07-019.

Mortimore, R.N. 2018. Developing ground models for chalk engineering: links across the disciplines. In Engineering in Chalk. ICE Publishing, Imperial College, London, UK. pp. 7–32.

Mortimore, R.N., and Fielding, P.M. 1990. 8. The relationship between texture, density and strength of chalk. In Chalk. Thomas Telford Publishing. pp. 109–132.

Mróz, Z. 1967. On the description of anisotropic workhardening. Journal of the Mechanics and Physics of Solids, 15: 163–175.

Muhammed, R.D., Canou, J., Dupla, J.-C., Palix, E., and Duc, M. 2018. Comportement hydromécanique d'une craie marine altérée. In Engineering in Chalk. ICE Publishing, Imperial College, London, UK. pp. 535–540.

Newman, G.H. 1983. The Effect of Water Chemistry on the Laboratory Compression and Permeability Characteristics of Some North Sea Chalks. Journal of Petroleum Technology, 35(05): 976–980. doi:10.2118/10203-PA.

Nguyen, H.D. 2009. Influence des interactions eau-roche sur le comportement à long terme de cavités souterraines dans la craie. Thèse de doctorat, École Nationale des Ponts et Chaussées, France.

Niemunis, A., Wichtmann, T., and Triantafyllidis, Th. 2005. A high-cycle accumulation model for sand. Computers and Geotechnics, 32(4): 245–263. doi:10.1016/j.compgeo.2005.03.002.

O'Reilly, M.P., and Brown, S.F. 1991. Cyclic loading in geotechnical engineering. In Cyclic Loading of Soils: from theory to design, O'Reilly M.P. & Brown S.F. (eds). London, Blackie. pp. 1–18.

Papamichos, E., Brignoli, M., and Santarelli. 1997. An experimental and thcoritical study of a partially saturated collapsible rock. 2: 251–278.

Papon, A. 2010. Modélisation numérique du comportement des sols sous très grands nombres de cycles: homogénéisation temporelle et identification des paramètres. Thèse de Doctorat, École Centrale de Nantes.

Pasturel, D. 1968. Essais de chargement de pieux dans la craie altérée. Bulletin des Laboratoires des Ponts et chaussées -Réf 388.

Piau, J.M., and Maury, V. 1994. Mechanical effects of water injection on chalk reservoirs. In Proc. Eurock ’94. pp. 819–828.

Pittos, G. 2014. Contribution à la proposition de lois d’interface sol-pieu sous sollicitations cycliques. Thèse Professionnelle, ENPC – École Centrale, Paris.

Porcino, D., Fioravante, V., Ghionna, V., and Pedroni, S. 2003. Interface Behavior of Sands from Constant Normal Stiffness Direct Shear Tests. Geotechnical Testing Journal, 26(3). doi:10.1520/GTJ11308J.

Poulos, H. 1989. Cyclic Axial Loading Analysis of Piles in Sand. Journal of Geotechnical Engineering, 115(6): 836–852.

Poulos, H.G. 1981. Some aspects of skin friction of piles in clay under cyclic loading. 12(1): 1–17.

Poulos, H.G. 1982. Influence of cyclic loading on axial pile response.

Poulos, H.G. 1984a. Cyclic degradation of pile performance in calcareous soils. In Analysis and Design of Pile Foundations. pp. 99–118.

Poulos, H.G. 1984b. Cyclic degradation of pile performance in calcareous soils. Anal. and Design of Pile Foundations,: 99–118.

Poulos, H.G. 1988. Cyclic Stability Diagram for Axially Loaded Piles. Journal of Geotechnical Engineering, 114(8): 877–895. doi:10.1061/(ASCE)0733-9410(1988)114:8(877).

Poulos, H.G., and Davis, E.H. 1980. Pile foundation analysis and design. John Wiley and Sons, New York, N.Y.

Pra-ai, S. 2013. Behaviour of soil-structure interfaces subjected to a large number of cycles. Application to piles. Université de Grenoble, Grenoble, France.

Pra-ai, S., and Boulon, M. 2016. Soil–structure cyclic direct shear tests: a new interpretation of the direct shear experiment and its application to a series of cyclic tests. Acta Geotechnica, 12(1): 107–127. doi:10.1007/s11440-016-0456-6.

Priol, G. 2005. Comportement mécanique différé et mouillabilité d’une craie pétrolifère. Thèse de doctorat, Ecole Nationale des Ponts et Chaussée.

Priol, G., De Gennaro, V., Delage, P., and Servant, T. 2007. Experimental Investigation on the Time Dependent Behaviour of a Multiphase Chalk. In Proceedings of the 2nd International Conference on Mechanics of Unsaturated Soil. Weimar,Germany.

Puech, A. 1982. Basic data for the design of tension piles in silty soils. In Proc. 3rd International Conference on the Behaviour of Offshore Structures. BOSS’82. BOSTON: M.I.T.

Randolph, M., and Gourvenec, S. 2011. Offshore Geotechnical Engineering. In CRC Press.

Randolph, M.F. 1983. Design considerations for offshore piles. In Proceedings of the conference on geotechnical practice in offshore engineering. Austin. pp. 422–439.

Randolph, M.F. 2003. Science and empiricism in pile foundation design. Géotechnique, 53(10): 847–875.

Randolph, M.F., and Wroth, C.P. 1978. Analysis of Deformation of Vertically Loaded Piles. Journal of Geotechnical Engineering, 104(GT12): 1465–1488.

Reese, L.C., and O'Neil, M.W. 1987. Drilled Shafts: Construction Procedure and Design Methods. US Department of TransportationFederal Highway Administration, Virginia.

Rimoy, S.P., Jardine, R.J., and Standing, J.R. 2013. Displacement response to axial cycling of piles driven in sand. Proceedings of the Institution of Civil Engineers - Geotechnical Engineering, 166(2): 131–146. doi:10.1680/geng.12.00052.

Risnes, R., and Flaageng, O. 1999. Mechanical Properties of Chalk with Emphasis on Chalk-Fluid Interactions and Micromechanical Aspects. Oil & Gas Science and Technology, 54(6): 751–758. doi:10.2516/ogst:1999063.

Risnes, R., Madland, M.V., Hole, M., and Kwabiah, N.K. 2005. Water weakening of chalk—Mechanical effects of water–glycol mixtures. Journal of Petroleum Science and Engineering, 48(1–2): 21–36. doi:10.1016/j.petrol.2005.04.004.

Robinsky, E.I., and Morrison, C.F. 1964. Sand Displacement and Compaction around Model Friction Piles. Canadian Geotechnical Journal, 1(2): 81–93. doi:10.1139/t64-002.

Rouainia, M., Boulon, M., and Garnica, P. 1992. Modelling and validation of a non linear soil-structure interface behaviour for pile problems. In Proc. Int. Symp. Num. models in Geomech. (NUMOG IV). Swansea, UK. pp. 223–230.

Saberi, M., Annan, C.-D., and Konrad, J.-M. 2019. Implementation of a soil-structure interface constitutive model for application in geo-structures. Soil Dynamics and Earthquake Engineering, 116: 714–731. doi:10.1016/j.soildyn.2018.11.001.

Sai, K. 1993. Modèles à grand nombre de variables internes et méthodes numériques associées. Thèse de doctorat, Ecole nationale supérieure des mines de Paris, Paris, France.

Said, I. 2006. Comportement des interfaces et modélisation des pieux sous charge axiale. Ecole Nationale des Ponts et Chaussées, Champs-sur-Marne.

Schlosser, F., and Guilloux, A. 1981. Le frottement dans le renforcement des sols. Revue Française de Géotechnique, (16): 65–77. doi:10.1051/geotech/1981016065.

Schroeder, C. 1995. Le "Pore Collapse": aspect particulier de l'interaction fluide-squelette dans les craies? Bruxelles,Belgium.

Schroeder, C. 2002. Du coccolithe au réservoir pétrolier. Thèse UIG, Liège.

Schroeder, C., Bois, A.P., Charlier, R., Collin, F., Cui, Y.J., Delage, P., and Maury, V. 2000. Pasachalk project: constiutive modelling, determination of parameters using secific stress paths and application to waterflooding. In Proc. 6'" Chalk Symp. JCR V. Brighton.

Shahrour, I., and Meimon, Y. 1995. Calculation of marine foundations subjected to repeated loads by means of the homogenization method. 17: 93–106.

Shahrour, I., and Rezaie, F. 1997. An elastoplastic constitutive relation for the soil-structure interface under cyclic loading. Computers and Geotechnics, 21(1): 21–39. doi:10.1016/S0266-352X(97)00001-3.

Siwak, J.M. 1994. Comportement et modélisation de la craie. Thèse de doctorat, Université des sciences et technologies de Lille.

Skov, R., and Denver, H. 1989. Time-dependence of bearing capacity of piles. In Proceedings of the 3rd international conference on the application of stress-wave theory to piles. Vancouver, Canada. pp. 879–888.

Spink, T., and Norbury, D. 1989. The engineering geological description of chalk. Brighton.

Stutz, H., and Mašín, D. 2016. Hypoplastic interface models for fine-grained soils. 41(2): 283–303.

Tabucanon, J., Airey, D., and Poulos, H. 1995. Pile Skin Friction in Sands from Constant Normal Stiffness Tests,. 18(3): 350–364.

Talesnick, M.L., Hatzor, Y.H., and Tsesarsky, M. 2001. The elastic deformability and strength of a high porosity, anisotropic chalk. International Journal of Rock Mechanics and Mining Sciences, 38(4): 543–555. doi:10.1016/S1365-1609(01)00024-7.

Tan, S.L., Cuthbertson, J., and Kimmerling, R.E. 2004. Prediction of pile set-up in non-cohesive soils. In Current practices and future trends in deep foundations, J. A. Di Maggio and M. H. Hussein. American Society of Civil Engineers (ASCE), Reston, VA, USA. pp. 50–65.

Uesugi, M., Kishida, H., and Tsubakihara, Y. 1989. Friction between sand and steel under repeated loadnig. Soils and Foundations, 29(3): 127–137.

Vijayvergia, V., Cheng, A., and Kolk, H. 1977. Design and installation of piles in chalk. In Proceedings of the 9th offshore technology conference. Houston, TX, USA. pp. 459–464.

Wernick, E. 1978. Skin friction of cylindrical anchors in non-cohesive soils. In Proceedings of the Symposium on Soil Reinforcing and Stabilizing Techniques in Engineering Practice. University of New South Wales, Sydney, Australia. pp. 201–219.

White, D.J., and Bolton, M.D. 2004. Displacement and strain paths during plane-strain model pile installation in sand. Géotechnique, 54(6): 375–397.

Wichtmann, T. 2005. Explicit accumulation model for non cohesive soils under cyclic loading. Ph.D. Thesis, Ruhr Universit¨at Bochum, Germany.

Wichtmann, T., Niemunis, A., and Triantafyllidis, T. 2010. Strain accumulation in sand due to drained cyclic loading: On the effect of monotonic and cyclic preloading (Miner's rule). Soil Dynamics and Earthquake Engineering, 30(8): 736–745. doi:10.1016/j.soildyn.2010.03.004.

Wichtmann, T., Niemunis, A., and Triantafyllidis, Th. 2005. Strain accumulation in sand due to cyclic loading: drained triaxial tests. Soil Dynamics and Earthquake Engineering, 25(12): 967–979. doi:10.1016/j.soildyn.2005.02.022.

Xie, S. 2005. Contribution à l'étude du comportement mécanique d'une roche poreuse. Thèse de doctorat, Université des Sciences et Technologies de Lille.

Yoshimi, Y., and Kishida, T. 1981. A ring torsion apparatus for evaluating friction between soil and metal surfaces. Geotechnical Testing Journal, 4(4): 145–152.

Zhang, G., and Zhang, J.-M. 2006. Monotonic and cyclic tests of interface between structure and gravelly soil. 46(4): 505–518.

Ziogos, A., Brown, M., Ivanovic, A., and Morgan, N. 2017. Chalk–steel interface testing for marine energy foundations. Proceedings of the Institution of Civil Engineers - Geotechnical Engineering, 170(3): 285–298. doi:10.1680/jgeen.16.00112.

# Appendix A

## A. Direct shear tests under monotonic loading: example of sand samples

### A.1 Comparison with experimental results

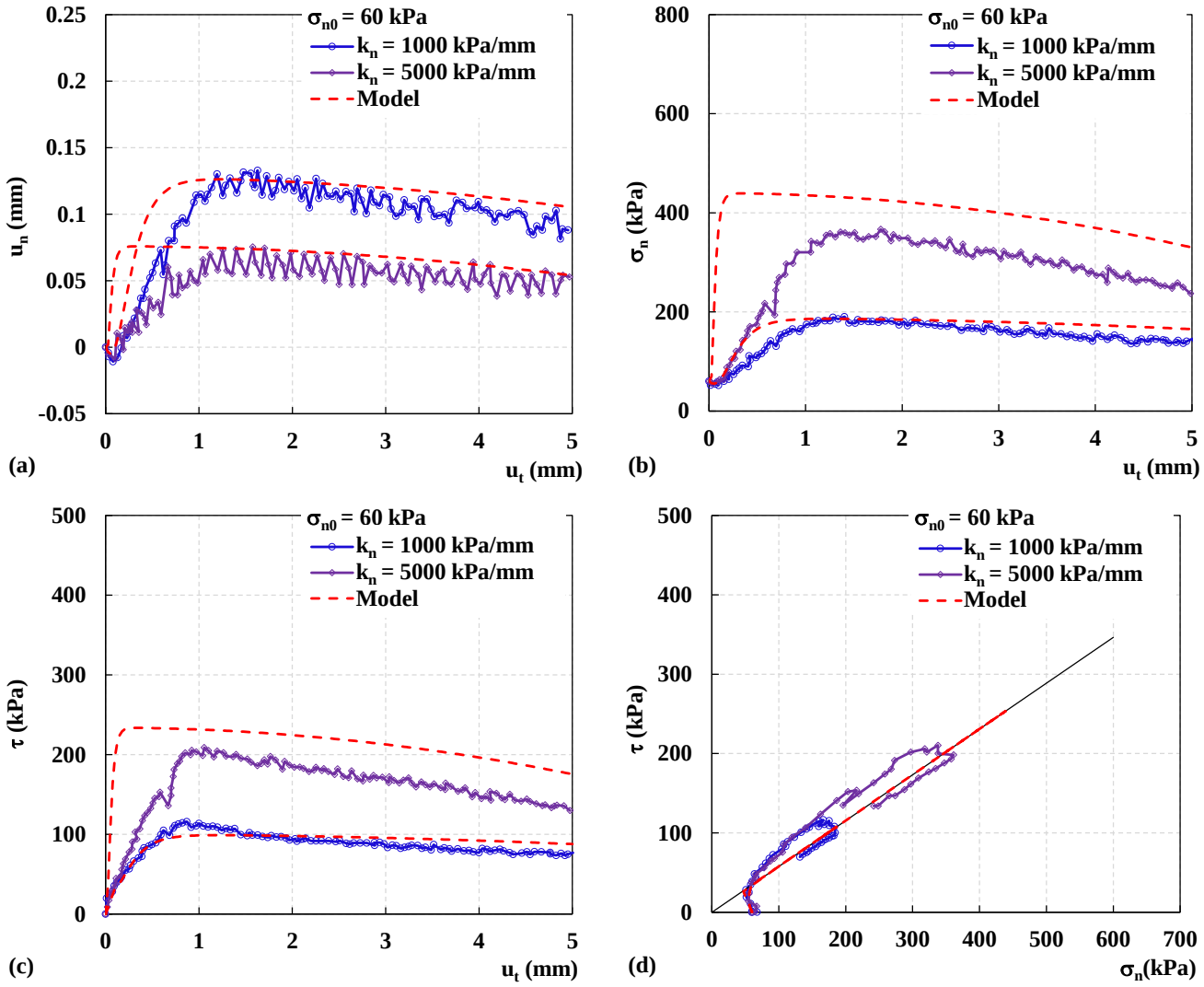


*Figure A.1 : Comparison between experimental results and model predictions, $\sigma_{n0}$=60 kPa, $k_n$=1000 and 5000 kPa/mm with rough plate and dense sand*

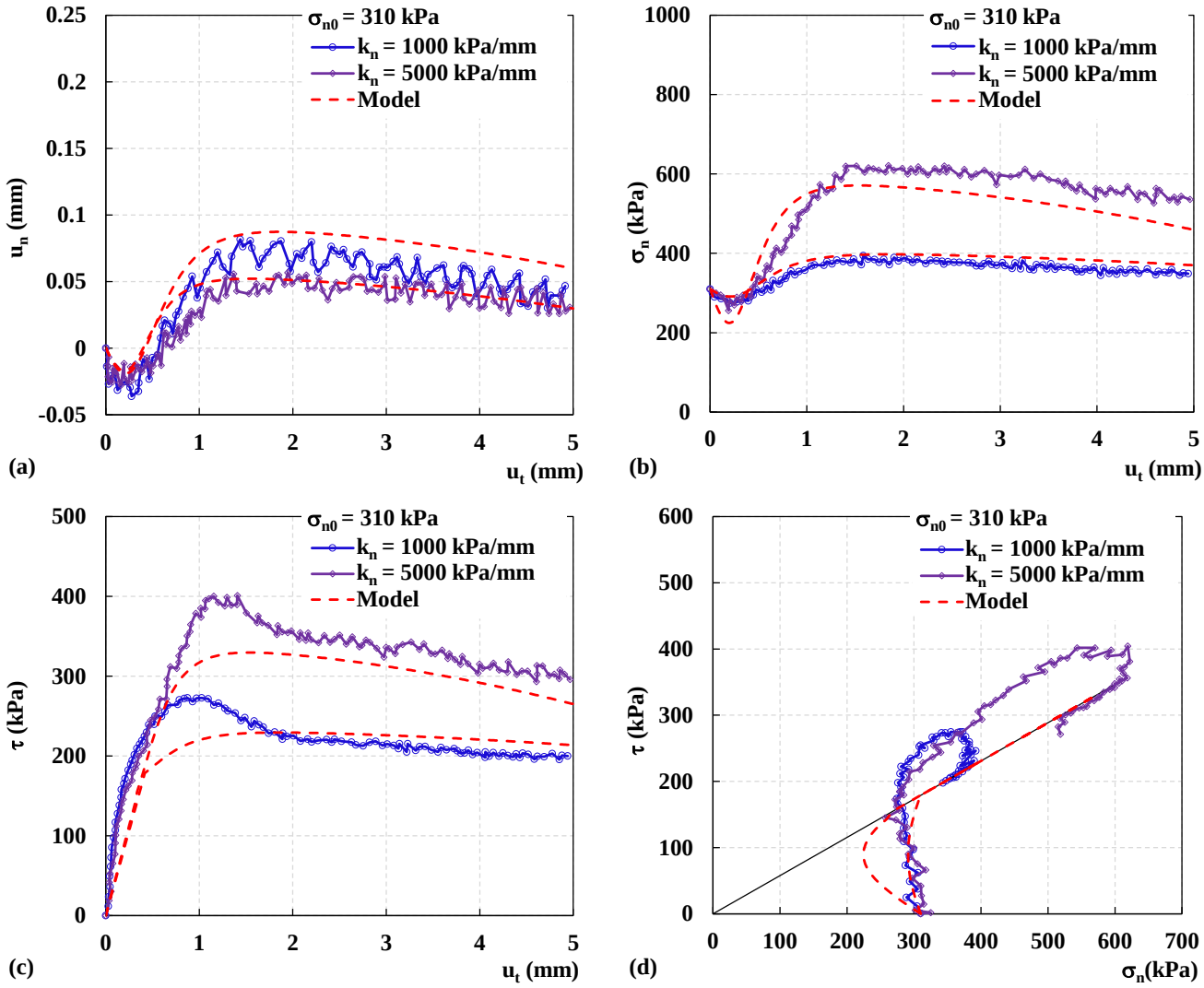


*Figure A.2 : Comparison between experimental results and model predictions, $\sigma_{n0}$=310 kPa, $k_n$=1000 and 5000 kPa/mm with rough plate and dense sand*

## A.2 Additional results

In order to identify the potentialities of the proposed model, different simulations are done with different values of normal stiffness and normal stress, always considering shear tests under CNS condition. Normal displacement is considered decreasing at the beginning of shearing (contracting phase), then increasing to pseudo-stabilisation where no additional volumetric changes will occur after the dilating phase, i.e., the parameter $A_d$ is set equal to zero.

The aim is to identify conventional observations of soil-pile interface subjected to shear loading due to axial loading at the pile head. Indeed, the effect of dilation at the interface results in an increase in the normal stress at the interface and therefore in the maximum shear stress. This explains the choice of the parameter $A_d$ adopted in these simulations.

Therefore, the monotonic interface shear tests simulations under CNS condition are performed at first with three different values of normal stiffness ($k_n$ = 1000, 2000 and 3000 kPa/mm) and a value of 300 kPa for the initial normal stress $\sigma_{n0}$. Second, normal stiffness $k_n$ is considered equal to 1000 kPa/mm and three simulations are done with three values of initial normal stress $\sigma_{n0}$, 100, 200 and 300 kPa.

Figures A.3a, A.3d, A.3c and A.3d illustrate simulation results with initial normal stress $\sigma_{n0}$ =300 kPa, it presents the influence of the normal stiffness on the interface behaviour. The calibrated parameters used in the proposed numerical equation give a relevant representation of this influence. Normal stiffness influenced principally the maximum value of the interface shear stress. When starting from the same initial normal stress, the increase of normal stiffness ($k_n$) caused an increase in maximum normal and shear stresses reached at the end of dilation. Figure A.3 shows a decreasing dilative behaviour with increasing normal stiffness. Indeed, maximum value reached by the normal displacement decreases as normal stiffness increases. This observation is related to parameter D which clearly decreases with increasing normal stiffness. By imposing the lower value of normal stiffness, the dilative behaviour is more expected and evident.

Figures A.4a, A.4d, A.4c and A.4d illustrate simulation results with normal stiffness $k_n$ =1000 kPa/mm, it presents the influence of the initial normal stress on the interface behaviour. A more compacted material tends to exhibit a less dilative behaviour. Therefore, the increase of initial normal stress ($\sigma_{n0}$) highlights a decreasing dilative behaviour. Indeed, maximum value reached by the normal displacement decreases as normal stress increases. The increase in normal stress due to dilative behaviour, depends on the initial normal stress ($\sigma_{n0}$). Considering the ratio $\sigma_{nmax}/\sigma_{n0}$, where $\sigma_{nmax}$ is the maximum normal stress reached at the end of the dilation phase,

its value was 2.23, 1.53 and 1.30 for $\sigma_{n0}$ = 100, 200 and 300 kPa, respectively. This effect is caused by the progressive decrease in the dilation rate due to the progressive increase in normal stress.

Figure A.4 shows that the increase of initial normal stress caused an increasing in maximum normal and shear stresses reached at the end of dilation.

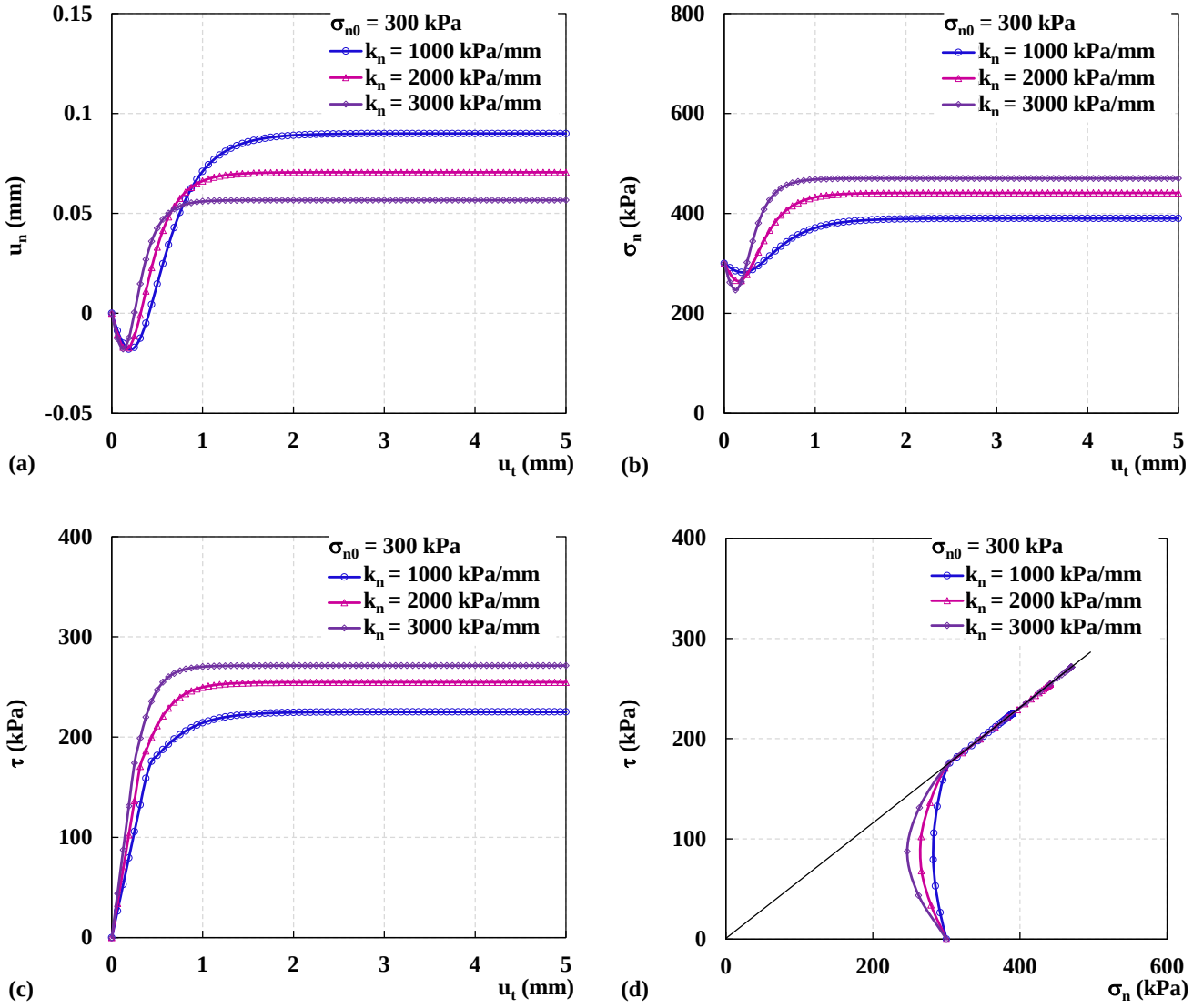


*Figure A.3 : Model predictions of monotonic CNS interface tests with three different normal stiffnesses: $k_n$=1000,2000 and 3000 kPa/mm, $\sigma_{n0}$ = 300 kPa*

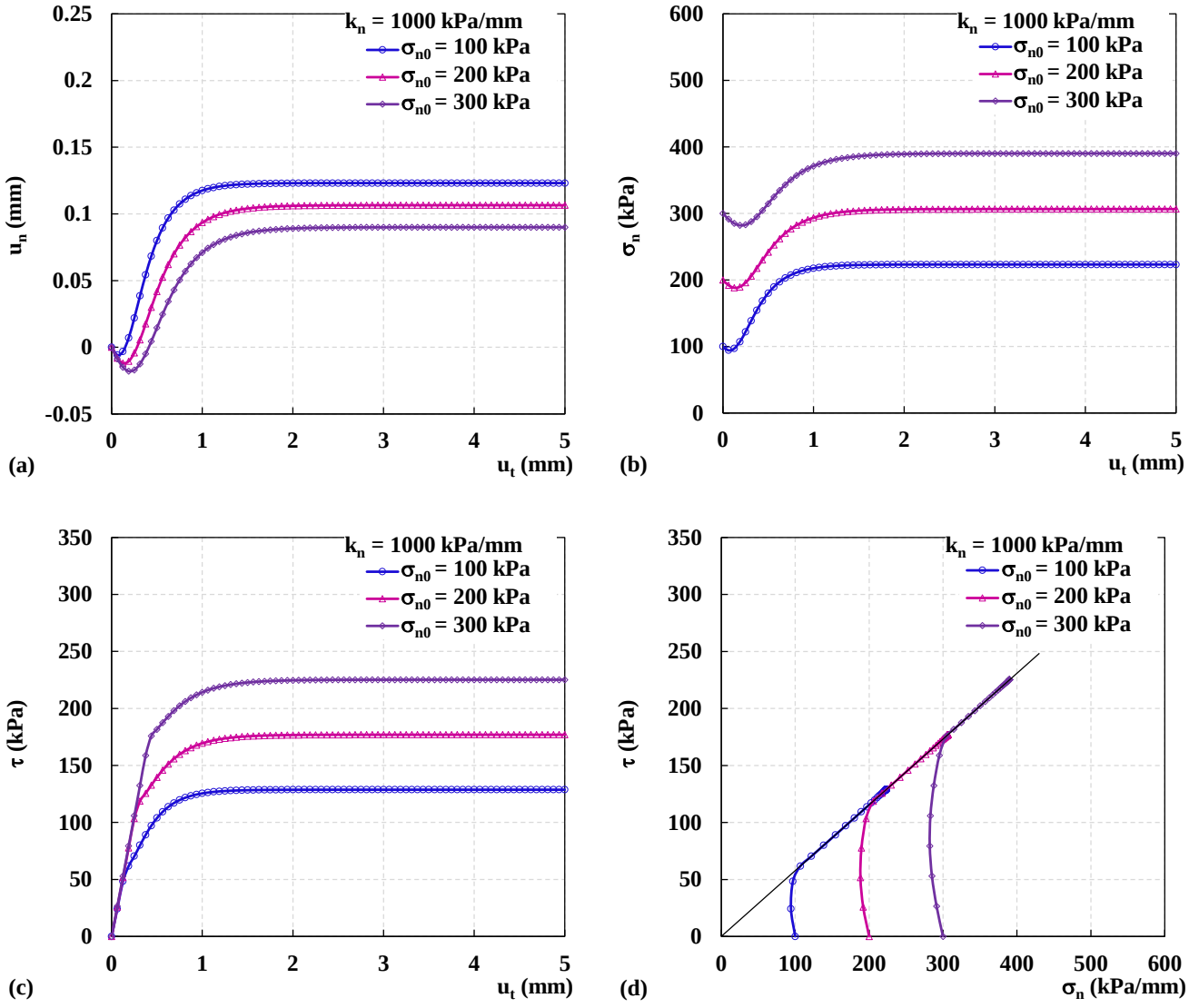


*Figure A.4 : Model predictions of monotonic CNS interface tests with three different initial normal stresses: $\sigma_{n0}$=100,200 and 300 kPa, $k_n$ = 1000 kPa/mm*

# Appendix B

## B. Direct shear tests under monotonic loading: example of sand samples

### B.1 Comparison with experimental results

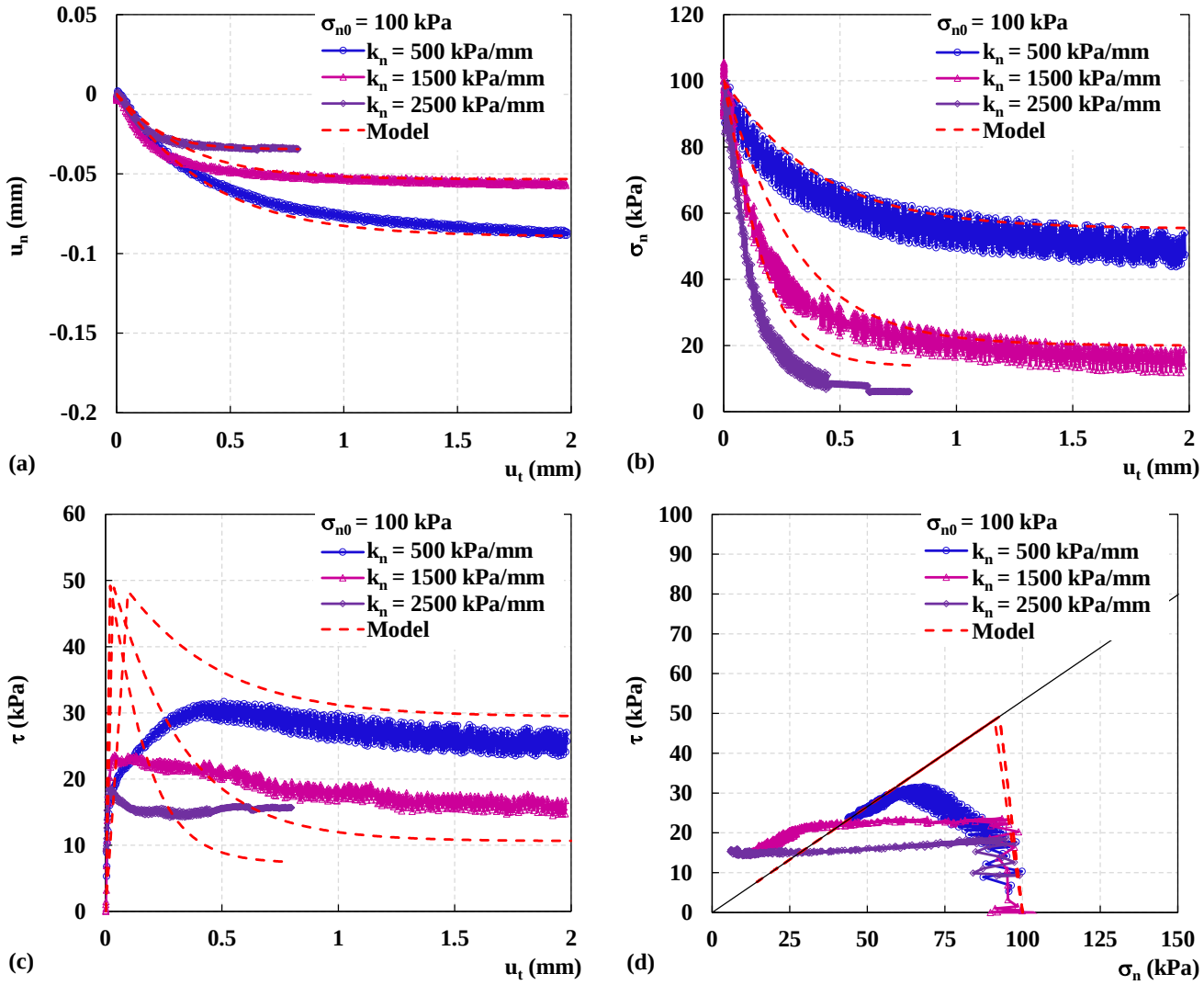


*Figure B.1 : Comparison between experimental results and model predictions, $\sigma_{n0}$=100 kPa, $k_n$=500,1500 and 2500 kPa/mm with smooth plate and chalk*

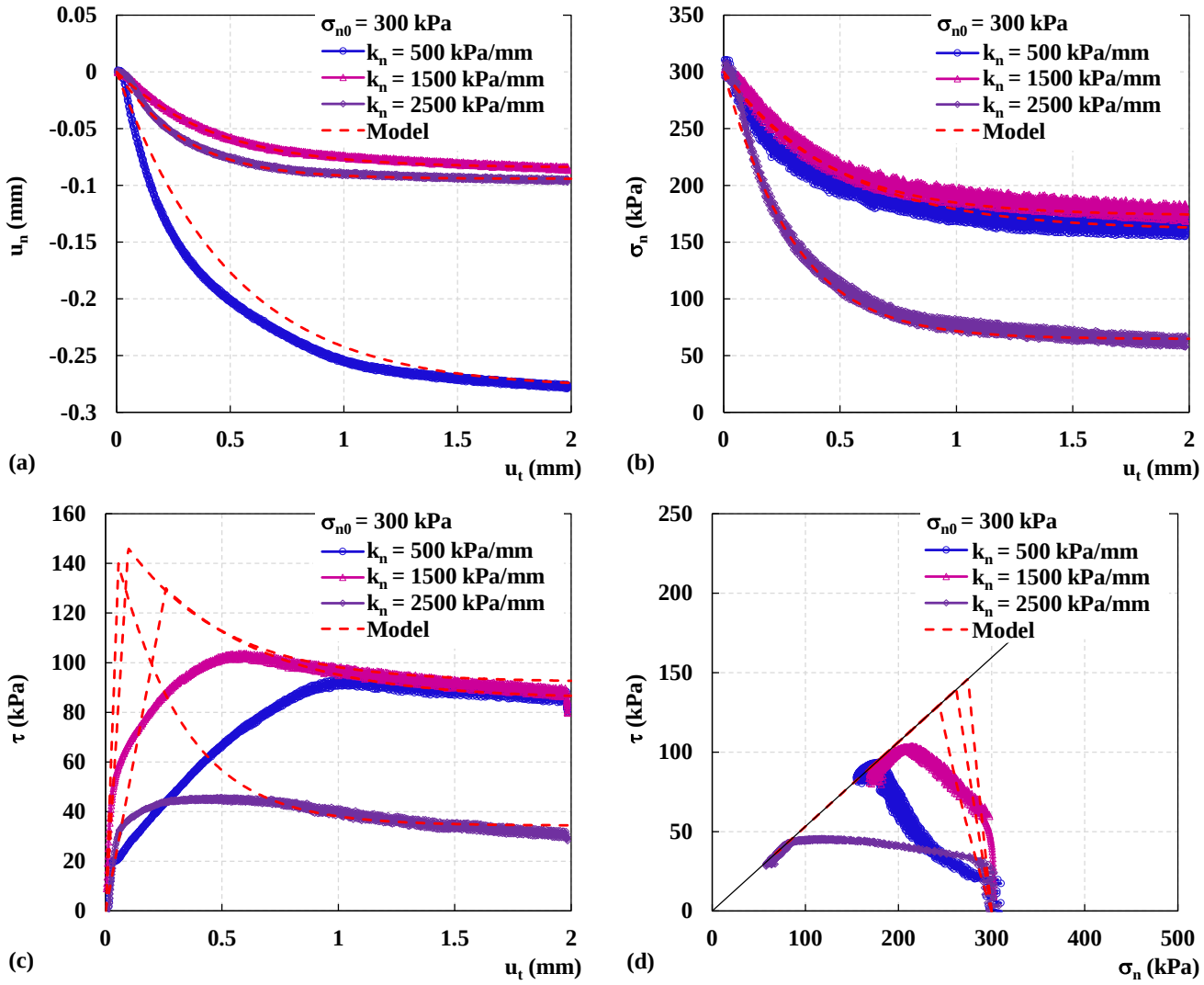


*Figure B.2 : Comparison between experimental results and model predictions, $\sigma_{n0}$=300 kPa, $k_n$=500,1500 and 2500 kPa/mm with smooth plate and chalk*

## B.2 Additional results

Calculations in this section intend to determine the capacity of the calibrated equation to present the behaviour of a contracting interface for different combinations of normal stiffnesses and initial normal stresses, that may be encountered and thus to quantify the resulted mobilised shear stress in each case.

Monotonic interface shear tests simulations under CNS condition are done at first with three different values of normal stiffness ($k_n$ = 400, 800 and 1200 kPa/mm) and a value of 100 kPa for the initial normal stress $\sigma_{n0}$. Second, normal stiffness $k_n$ is considered equal to 400 kPa/mm and three simulations are done with three values of initial normal stress $\sigma_{n0}$, 50, 100 and 150 kPa.

First calculation results, with initial normal stress $\sigma_{n0}$ =100 kPa, are presented in figures B.3a, B.3d, B.3c and B.3d. These results illustrate the effect of normal stiffness on the interface response. For the same initial normal stress $\sigma_{n0}$, the increase in normal stiffness causes a decrease in the final value reached by the normal stress as well as shear stress. During shearing, the normal stress degrades more as the normal stiffness increases. Indeed, the interface shows a decreasing contractive behaviour with increasing normal stiffness.

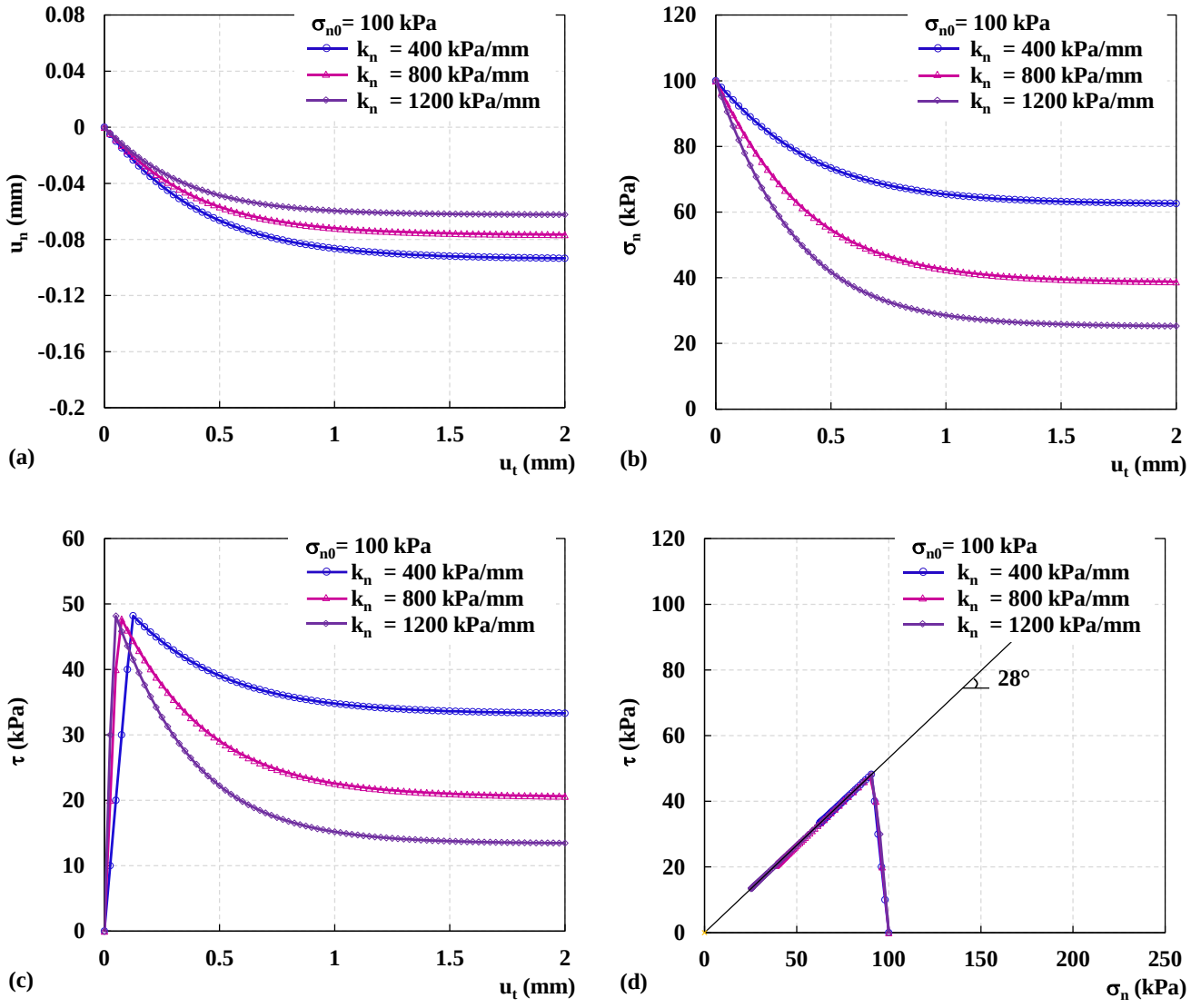


*Figure B.3 : Model predictions of monotonic CNS interface tests with three different normal stiffnesses: $k_n$=400,800 and 1200 kPa/mm, $\sigma_{n0}$ = 100 kPa*

Figures B.4a, B.4d, B.4c and B.4d illustrate calculation results with normal stiffness $k_n$ =400 kPa/mm, it presents the influence of the initial normal stress on the interface behaviour. It can be noted that the influence of initial normal stress on the evolution of normal displacement is more pronounced than the influence of normal stiffness. We can say that a more compacted soil presents a more contractive behaviour. Hence, the increase in initial normal stress exhibits an increasing contractive behaviour. Indeed, maximum value reached by the normal displacement increases as normal stress increases. The decrease in normal stress due to contractive behaviour certainly depends on the initial normal stress. Considering the ratio $\sigma_{nmin}/\sigma_{n0}$, where $\sigma_{nmin}$ is the minimum normal stress reached at the end of the contraction phase, its value is 0.7, 0.63 and

0.6 for $\sigma_{n0}$ = 50, 100 and 150 kPa, respectively. This effect is caused by the progressive decrease in the contraction rate due to the progressive decrease in normal stress.

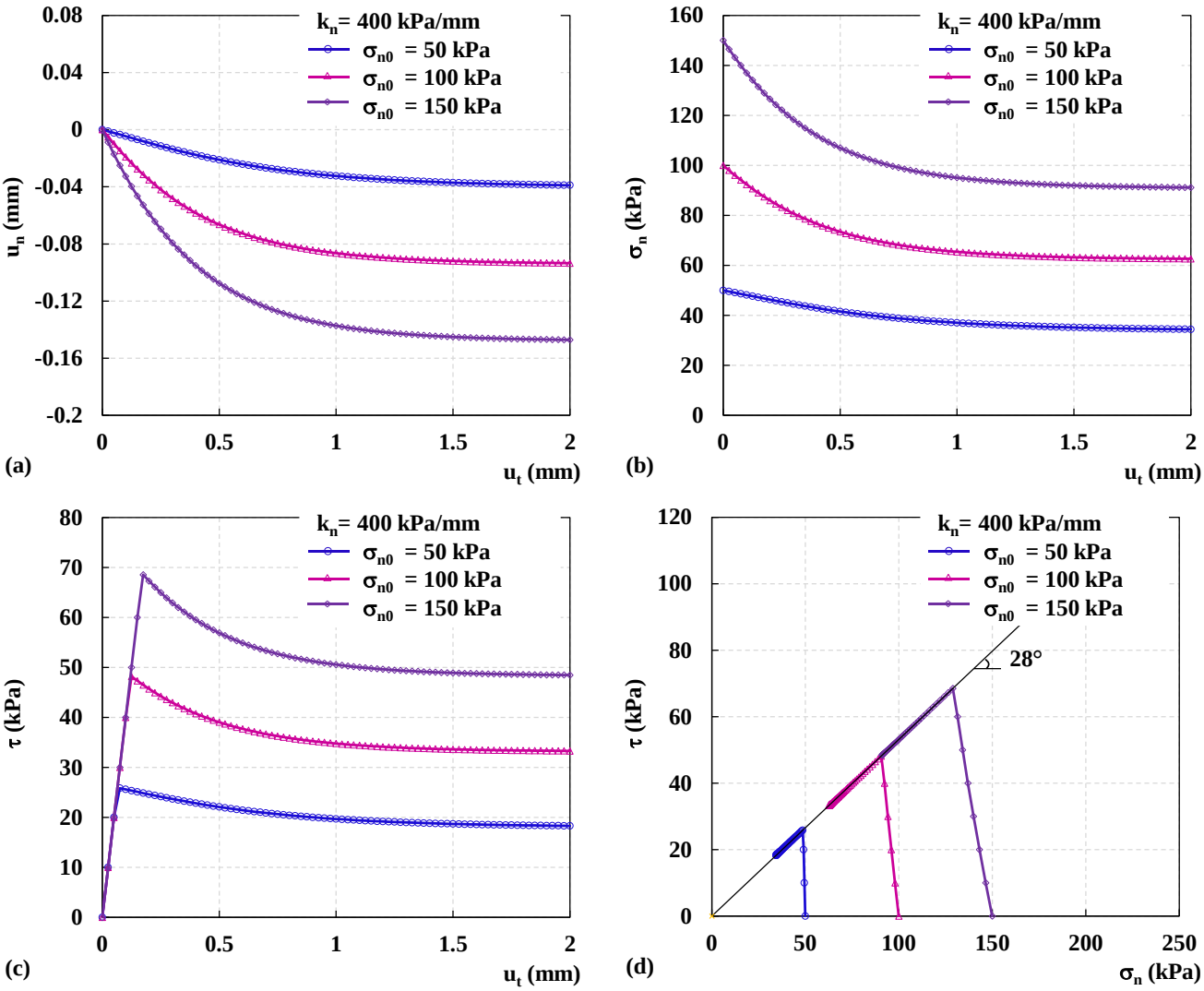


*Figure B.4 : Model predictions of monotonic CNS interface tests with three different initial normal stresses: $\sigma_{n0}$=50,100 and 150 kPa, $k_n$ = 400 kPa/mm*